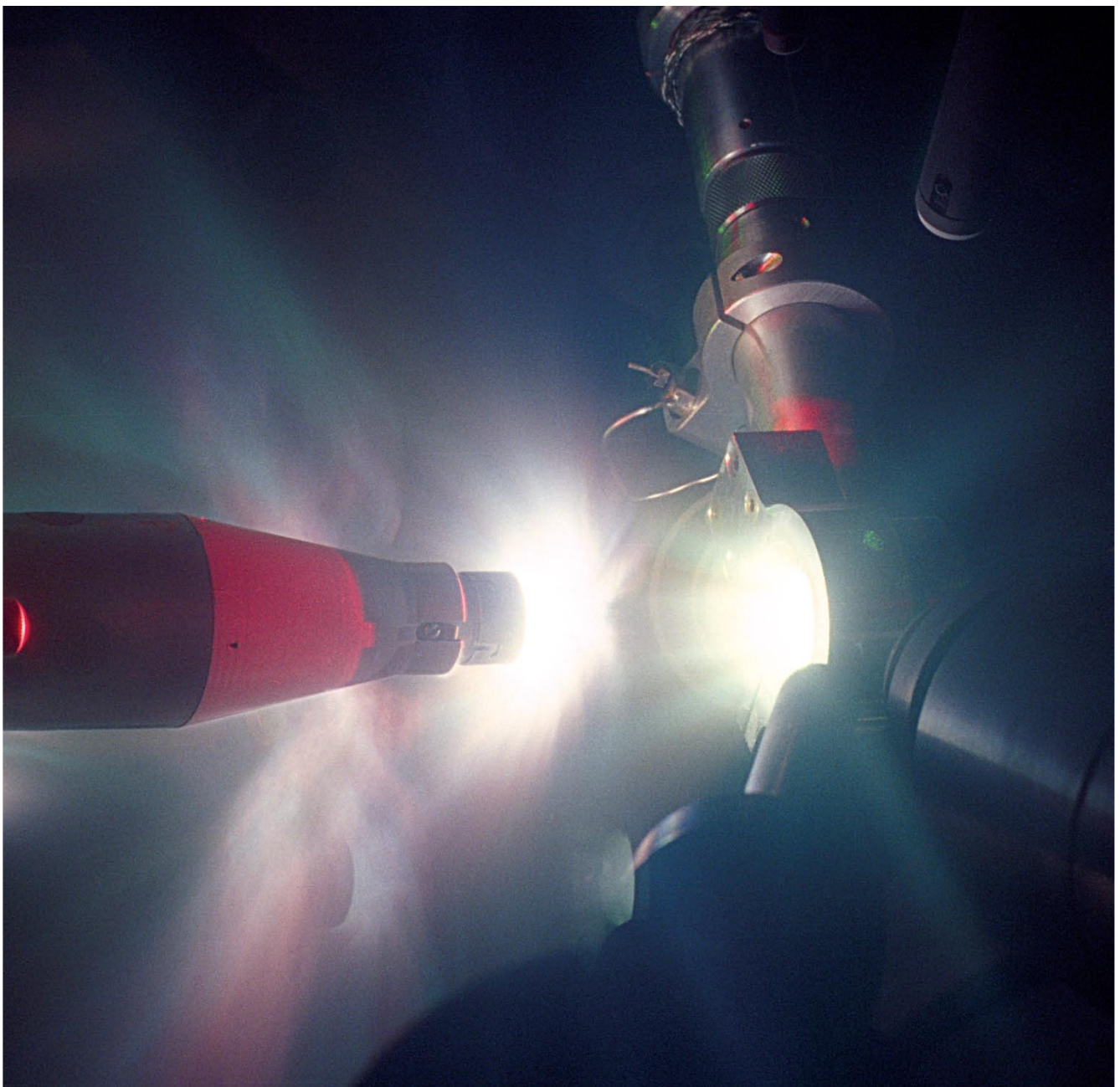




NATIONAL LASER USERS' FACILITY

# USERS' GUIDE



## Telephone Directory

### Laboratory for Laser Energetics (LLE)

Robert L. McCrory (Laboratory Director, LLE).....	(585) 275-4973
David D. Meyerhofer (Director, Experimental Division, Deputy Director, and Associate Director for Science).....	(585) 275-0255
Steven J. Loucks (Associate Director for Operations).....	(585) 275-2393
Riccardo Betti (Assistant Director for Academic Affairs) .....	(585) 275-8586
Douglas W. Jacobs-Perkins (Director, Engineering Division and Laboratory Safety Engineer) .....	(585) 275-8413
Samuel F. B. Morse (Director, Omega Facility) .....	(585) 275-9672
Stanley Skupsky (Director, Theoretical Division) .....	(585) 275-3951
John M. Schoen (Director, Administrative Division) .....	(585) 275-8296
Laboratory for Laser Energetics, Reception .....	(585) 275-5101

### National Laser Users' Facility (NLUF)

John M. Soures (Manager, NLUF and External Collaborations) .....	(585) 275-3866	
E-mail <a href="mailto:jsou@lle.rochester.edu">jsou@lle.rochester.edu</a>		
Jean Steve (Administrative Liaison, NLUF) .....	(585) 275-5286	
E-mail..... <a href="mailto:jste@lle.rochester.edu">jste@lle.rochester.edu</a>		
Facsimile .....		(585) 256-2586

Worldwide-Web Home Page: <http://www.lle.rochester.edu/>

**University of Rochester**  
**Laboratory for Laser Energetics**  
**250 East River Road**  
**Rochester, NY 14623-1299**

#### About the Cover

Optical image generated from an NLUF target shot on OMEGA is captured by Eugene Kowaluk, staff photographer and imaging specialist.

# TABLE OF CONTENTS

<b>CHAPTER 1.</b>	<b>INTRODUCTION .....</b>	<b>1.1</b>
<b>CHAPTER 2.</b>	<b>RESEARCH FACILITIES</b>	
2.1	INTRODUCTION .....	2.1
2.2	OMEGA COMPRESSION FACILITY DESCRIPTION .....	2.1
2.2.1	System Performance Requirements .....	2.2
2.2.2	Laser-Energy Performance .....	2.4
2.2.3	Top-Level Configuration .....	2.4
2.2.4	Laser-Drivers Subsystem.....	2.11
2.2.5	Amplifier Staging.....	2.13
2.2.6	Frequency Conversion and UV Transport.....	2.14
2.2.7	Optical Alignment.....	2.15
2.2.8	Laser Diagnostics .....	2.16
2.2.9	Control System.....	2.17
2.3	OMEGA FACILITY IMPROVEMENTS .....	2.24
2.3.1	Power Balance .....	2.25
2.3.2	Precision Pulse Shaping.....	2.26
2.3.3	Phase Plates.....	2.27
2.3.4	Second-Harmonic and Fourth-Harmonic Capabilities .....	2.32
2.3.5	UV Spectrometer.....	2.32
2.3.6	Target Chamber Tritium Recovery System.....	2.35
2.3.7	Software Improvements for OMEGA Operations .....	2.36
2.3.8	Support for External Users .....	2.36
2.3.9	Operational Statistics.....	2.38
2.4	OMEGA EXTENDED PERFORMANCE (EP) LASER SYSTEM.....	2.41
2.4.1	System Overview .....	2.41
2.4.2	System Performance Specifications .....	2.45
2.4.3	System Description .....	2.46
2.4.3.1	Laser sources .....	2.46
2.4.3.2	Laser amplifiers and power conditioning.....	2.49
2.4.3.3	Beamlines .....	2.54
2.4.3.4	Pulse compression, IR short-pulse transport, and diagnostics .....	2.57
2.4.3.5	Frequency conversion, UV long-pulse transport, and diagnostics .....	2.63
2.4.3.6	Target chamber and experimental systems .....	2.65
2.4.4	Control Systems .....	2.67
2.4.4.1	Overview .....	2.67
2.4.4.2	Timing systems.....	2.69
2.4.4.3	Alignment systems.....	2.71
2.4.5	Operations.....	2.73

2.5	TARGET DIAGNOSTIC CAPABILITIES .....	2.74
2.5.1	Charged-Particle Diagnostics.....	2.74
2.5.1.1	Nuclear reactions producing charged particles.....	2.74
2.5.1.2	Magnet-based charged-particle spectrometers .....	2.77
2.5.1.3	Wedge-range-filter proton spectrometers .....	2.77
2.5.1.4	High-areal-density wedge-range-filter spectrometers....	2.78
2.5.1.5	Proton temporal diagnostic.....	2.78
2.5.2	X-Ray Imaging.....	2.82
2.5.2.1	X-ray pinhole cameras .....	2.82
2.5.2.2	X-ray framing cameras.....	2.83
2.5.2.3	Kirkpatrick–Baez microscopes.....	2.84
2.5.2.4	Gated monochromatic x-ray imager (GMXI) .....	2.85
2.5.2.5	CID-camera readout system .....	2.85
2.5.3	Optical Streak Cameras .....	2.85
2.5.4	X-Ray Streak Cameras .....	2.89
2.5.5	Time-Resolved Hard-X-Ray Detector.....	2.90
2.5.6	Hard-X-Ray Spectrometer .....	2.91
2.5.7	Pinhole-Array X-Ray Spectrometer .....	2.91
2.5.8	Neutron Diagnostics .....	2.91
2.5.8.1	Activation detectors .....	2.92
2.5.8.2	Neutron time-of-flight detectors .....	2.93
2.5.8.3	Neutron temporal diagnostic .....	2.93
2.5.8.4	Neutron bang-time detectors .....	2.94
2.5.8.5	Neutron magnetic recoil spectrometer .....	2.96
2.5.9	Full-Aperture Backscatter Stations .....	2.99
2.5.10	Near-Backscatter Imaging .....	2.103
2.5.11	X-Ray Backlighter Capabilities .....	2.105
2.5.12	Short-Pulse Backlighter Development .....	2.108
2.5.13	Velocity Interferometry System for Any Reflector (VISAR) .....	2.111
2.5.14	Streaked Optical Pyrometer .....	2.113
2.5.15	Cryogenic-Target Characterization Diagnostic .....	2.114
2.5.16	External-User–Developed Diagnostics .....	2.116
2.5.16.1	HENEX (High-energy electronic x-ray diagnostic) .....	2.116
2.5.16.2	TBD (Transmitted beam diagnostic) .....	2.116
2.5.16.3	HRXI (High-resolution x-ray imaging) .....	2.117
2.5.16.4	Dante .....	2.117
2.5.16.5	DMX .....	2.117
2.5.16.6	DEMIN (Detector micromegas for neutrons) .....	2.117
2.6	TARGET FABRICATION (Under Construction) .....	2.117
2.7	REFERENCES .....	2.118

### CHAPTER 3. PROPOSAL INFORMATION

3.1	PROPOSAL PREPARATION .....	3.1
3.2	FACILITY REQUIREMENTS.....	3.1
3.3	INSTITUTIONAL COLLABORATIONS .....	3.2
3.4	PROPOSAL SUBMISSION.....	3.2

3.5	PROPOSAL REVIEW .....	3.2
3.6	FINANCIAL SUPPORT FOR USER EXPENSES .....	3.3

**CHAPTER 4. POLICIES**

4.1	USER RESEARCH GRANTS .....	4.1
4.2	SAFETY .....	4.1
4.3	TARGET DESIGNS .....	4.1
4.4	SCHEDULING OF EXPERIMENTS .....	4.1
4.5	POST-SHOT EVALUATION .....	4.2
4.6	PHOTOGRAPHIC DATA/DARKROOM POLICY .....	4.3
4.7	PUBLICATIONS .....	4.3
4.8	ACKNOWLEDGMENTS .....	4.3
4.9	RESTRICTED DATA .....	4.3
4.10	SECURITY .....	4.4
4.11	SMOKING .....	4.4
4.12	WEB SITE .....	4.4

**CHAPTER 5. TRAVEL AND HOUSING INFORMATION**

5.1	HOTELS AND HOUSING .....	5.1
5.2	AIRPORT .....	5.1
5.3	MAP .....	5.1

**APPENDIX A: LLEINST 3000F [Part I: Laser Facility Organization and Regulation Manual (LFORM)]**

**APPENDIX B: GLOSSARY OF ACRONYMS**

**APPENDIX C: NLUF PROPOSAL SUMMARY SHEET**

**APPENDIX D: FY06 LASER FACILITY REPORT**

**APPENDIX E: NATIONAL LASER USERS' FACILITY AND EXTERNAL USERS' PROGRAMS**



## 1. Introduction

The National Laser Users' Facility (NLUF) is located in Rochester, New York, at the University of Rochester's Laboratory for Laser Energetics (LLE). LLE was established in 1970 to investigate the interaction of high-power lasers with matter. The NLUF has been an integral part of LLE's activities since 1979.

This guide provides the appropriate technical references for researchers to prepare proposals for the use of the OMEGA and OMEGA EP laser facilities at LLE. Calls for proposals to use these two facilities as part of the NLUF program are issued by the Department of Energy (DOE) National Nuclear Security Administration (NNSA) through the Albuquerque Operations Office. LLE serves as the technical liaison for NLUF and as such is the primary interface for technical discussions prior to the preparation of proposals. Though some detailed information is provided in this guide to assist the potential users to formulate and field proposals on the LLE facilities, **the official DOE/NNSA solicitation contains the only formal proposal submission regulations that govern the DOE/NNSA proposal selection process.**

All potential and approved users of the facility are expected to be familiar with the contents of this handbook and the relevant references to which it points. An understanding of the general information, policies, and procedures contained herein is necessary in order to formulate, submit, and carry out a user proposal. Additional information is provided on the procedures to follow once a proposal is conditionally approved but before system shots are carried out. Finally, introductory and orientation information is provided to assist a user during visits to LLE.

The NLUF is available for experiments requiring high-intensity laser beams. Fundamental studies center around applications in high-energy-density physics.<sup>1</sup> High-energy-density physics experiments use an intense pulse of laser light focused to a diameter as small as a few tens of wavelengths of laser light. Intensities as high as  $10^{16}$  W/cm<sup>2</sup> can be created on OMEGA and much higher intensities are possible on OMEGA EP. A solid material, irradiated by such an intense laser pulse, rapidly becomes a plasma with temperatures of  $10^7$  to  $10^8$  °K and densities greater than 10 g/cm<sup>3</sup>. This point-source plasma thus provides the necessary conditions for studies of thermonuclear fusion, spectroscopy of highly ionized atoms, shock waves, laboratory astrophysics, or the fundamental physics of matter under high intensities.

The high-energy irradiation capability of the Laboratory is provided by the OMEGA facility—a 60-beam, 30-kJ, neodymium:glass laser system, operating at a wavelength of 351 nm. This facility has an experimental target chamber equipped with various diagnostics that are made available to facility users.

The University of Rochester operates NLUF under an agreement with DOE. DOE funds the operation of OMEGA, thus making it possible for researchers to conduct experiments at the

University of Rochester without direct charge. DOE provides grants directly to NLUF participants. The projects funded under this program are for the conduct of basic experimental research in high-energy-density science using the research tools and resources of the NLUF. This includes, but is not limited to, inertial fusion, plasma physics, spectroscopy of highly ionized atoms, laboratory astrophysics, fundamental physics, materials science, biology, and chemistry.

Evaluation of applications is conducted using a merit-review process in accordance with the criteria set forth in the DOE solicitation for proposals. Applications undergo a preliminary screening to determine whether the requirements of the solicitation have been met before they are subjected to detailed evaluation utilizing merit review. Applications that do not include all requested information (as specified in the DOE/NNSA solicitation) may be considered nonresponsive and may not receive further consideration.

After the preliminary review, qualifying applications are subjected to a technical peer merit review. A scientific peer committee of highly qualified individuals will evaluate the applications using the following criteria:

- (a) Scientific/technical soundness and quality of the proposed method/approach.
- (b) Overall scientific/technical merit of the experiment and its relevance to its field of research.
- (c) The competence, experience, and past performance of the principal investigator and key project personnel.
- (d) The demands of the proposal in terms of resource requirements of the LLE facilities and personnel.

The review committee (NLUF Steering Committee) is appointed by the President of the University of Rochester with the approval of DOE. The review committee recommends applications deemed worthy of laser time on the NLUF in a ranked order. Final selections is made by a designated DOE/NNSA official based on the technical merit review, cost, and funding availability. Proposal submissions and reviews are currently made biennially.

Since its inception in 1980, NLUF has received 278 proposals from prospective users of which 143 have been accepted.

Over seventy percent (70%) of the accepted proposals have come from university laboratories, including Auburn University, Brigham Young University, Harvard University, Illinois State University, Massachusetts Institute of Technology, Polytechnic Institute of New York, State University of New York at Buffalo, State University of New York at Geneseo, Syracuse University, University of California at Berkeley, University of California at Davis, University of California at Los Angeles, University of Connecticut, University of Florida, University of Illinois, University of Maryland, University of Michigan, University of Nevada at Reno, University of Pennsylvania, University of Rochester, University of Texas, University of Wisconsin, and Yale University.

## REFERENCES

1. Committee on High-Energy-Density Plasma Physics, Plasma Science Committee National Research Council, "Frontiers in High-Energy-Density Physics: The X-Games of Contemporary Science."



## 2. Research Facilities

### 2.1 INTRODUCTION

The research facilities available to NLUF participants include the OMEGA and OMEGA EP Laser Systems (operating in routine configuration), and standard laser and plasma diagnostics. DOE/NNSA also funds General Atomics, Inc. to provide limited target fabrication support to NLUF users. Detailed target fabrication requirements must be provided in the users' proposals in order to assure this support.

In addition to the OMEGA and OMEGA EP lasers and associated equipment, LLE has supporting laboratories, computing resources, shop facilities, and engineering resources. These auxiliary facilities are also made available to NLUF participants if required, but fees may be charged for their use.

### 2.2 OMEGA COMPRESSION FACILITY DESCRIPTION

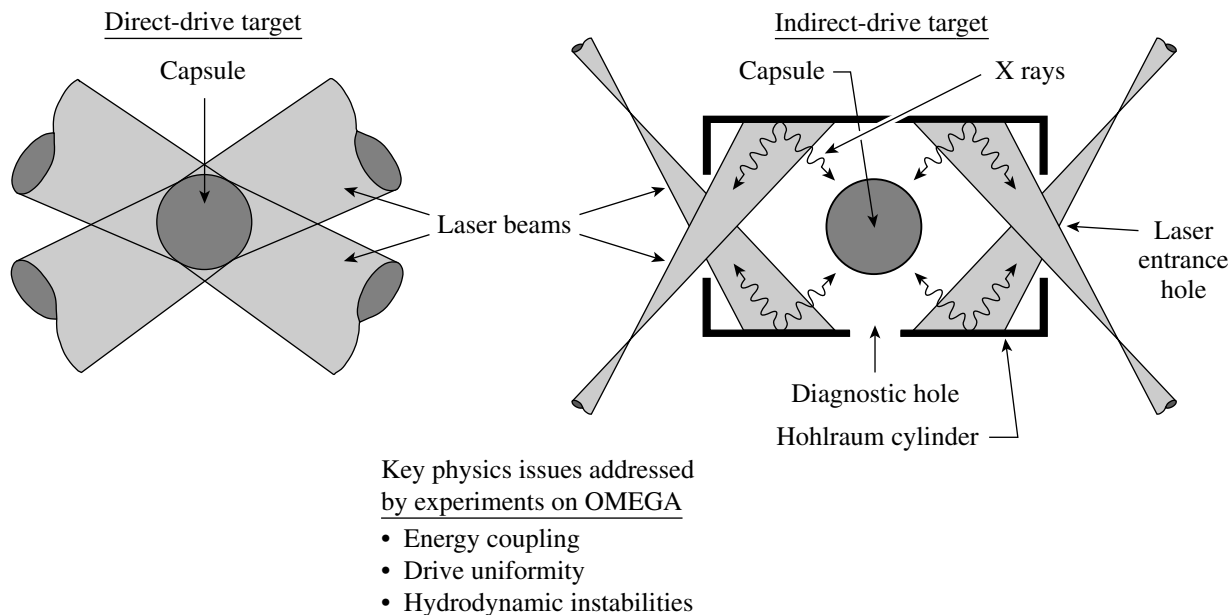
This section describes the design and summarizes the operation of the OMEGA laser system. A complete description of the system may be found at [www.lle.rochester.edu](http://www.lle.rochester.edu). An upgrade project undertaken from October 1990 to May 1995 consisted of a complete overhaul of the building and laser facility. Prior to the upgrade, OMEGA was a 24-beam, 2-kJ, 351-nm laser. After the upgrade, OMEGA has 60 beams and can deliver up to 30 kJ of 351-nm laser energy. The upgrade took 4.5 years and \$61M to complete. The OMEGA system provides a unique capability to validate high-performance, direct-drive laser-fusion targets. The ultimate goal of the Laboratory for Laser Energetics (LLE) experimental program on OMEGA is to study the physics of hot-spot formation under near-ignition conditions (ignition scaling), using cryogenic targets whose hydrodynamic behavior scales to that of high-gain targets. Performance goals of these experiments are the achievement of a convergence ratio ( $C_R$ ) = 20, compressed fuel ion temperature ( $T_i$ ) of 2 to 3 keV, and a total fuel density-radius product ( $\rho R$ ) in excess of 0.2 g/cm<sup>2</sup> for targets whose Rayleigh-Taylor growth factors are in excess of 500.

In addition to the LLE direct-drive mission, the facility time is allocated to DOE users from Lawrence Livermore National Laboratory (LLNL), Los Alamos National Laboratory (LANL), and Sandia National Laboratory (SNL). System time is also allocated for a variety of users through the National Laser Users' Facility (NLUF), which is managed by LLE. The goals of these users vary greatly but are generally focused on the physics associated with indirect-drive irradiation and on diagnostic development.

Many key physics issues associated with capsule implosions are common to both direct and indirect drive. Studies of drive uniformity, hydrodynamic instabilities, and energy coupling to the

\*The detailed configuration of the OMEGA Laser Facility is evolving as new capabilities and improvements are implemented. The user is advised to consult the facility manager regarding any detailed system specifications and experimental requirements prior to the detailed design of an experiment.

capsule are relevant to either approach. [Direct and indirect drive refers to the way the laser couples to the target (see Fig. 2.1)]. The OMEGA facility is central to developing an early understanding of the expected target performance under conditions that will be available with the National Ignition Facility (NIF), a 192-beam laser currently under construction at LLNL.



E6426bJ1

Figure 2.1

Direct-drive targets are driven by laser irradiation that impinges directly on the capsule. Indirect-drive targets are compressed by x rays generated when the laser impinges on a cylindrical “hohlraum” that surrounds the target.

### 2.2.1 System Performance Requirements

The system is installed in the space previously occupied by the 24 beam OMEGA laser and capitalizes on the experience gained over three decades of system operations. The uniformity, total-energy, and pulse-shaping requirements for the ignition-scaling experiments call for a 60-beam system to produce 30 kJ on target in temporally shaped pulses with peak powers of up to 45 TW. The top-level specifications are given in Table 2.1.

The on-target energy goal is dictated by the requirement to conduct hydrodynamically equivalent capsule implosions that produce diagnostic signatures sufficient to adequately diagnose the fuel-core performance. Short-wavelength (351-nm) ultraviolet laser light has long been attractive as a laser-fusion driver due to its enhanced absorption and reduced hot-electron production. The use of Nd:glass was set by the requirement of upgrading the original 24-beam OMEGA system. The Nd:glass master-oscillator/power amplifier system produces 60 beams of infrared energy (1054 nm). Each beam is converted to the ultraviolet at the end of the amplifiers prior to being

delivered to the target. The optical assembly that performs this conversion is referred to as the frequency-conversion crystal (FCC) subsystem.

The uniformity of the laser has two parts; first, each beam must produce a uniform spot on target, and second, the beam-to-beam power variation on target must be kept to a minimum. On-target uniformity benefits from the 60-beam configuration because the power delivered to any given point on a spherical target has contributions from many beams. As a result of the beams overlapping on target, a beam-to-beam energy balance of 3%–4% is sufficient to produce an on-target irradiation uniformity of 1%–2%. Power balance is achieved by ensuring that the time history of the arrival of the energy at the target is the same for each beam. This is achieved by minimizing the beam-to-beam variation of the gain produced by each amplification stage and by equalizing the time of arrival on target.

The instantaneous uniformity of the energy within a given beam spot on the target is optimized by the application of the three smoothing techniques listed in Table 2.1. Smoothing by spectral dispersion (SSD) is a technique that modulates the wavelength of the master-oscillator pulse. This causes the speckle points within the on-target spot to move during the period of irradiation. Polarization smoothing is achieved by passing the UV beam through a distributed phase rotator (DPR) optic as it propagates to the target. This effect works in conjunction with a distributed phase plate (DPP) optic to produce multiple focus spots on the target.

A versatile capability to produce temporally shaped pulses is also needed to minimize hydrodynamic instabilities in the implosions. Finally, the system repetition rate of one shot per hour facilitates a productive experimental program.

Table 2.1: OMEGA Specifications

Energy on target	Up to 30 kJ in a 1-ns square pulse
Wavelength	351 nm (third harmonic of Nd:glass)
Lasing medium	Nd-doped phosphate glass
Number of beams	60
Irradiation nonuniformity	1%–2%
Beam-to-beam energy balance	Less than 4% rms on target
Beam-to-beam power balance	<1% @ peak
Beam smoothing	<ul style="list-style-type: none"> <li>• Spectral dispersion</li> <li>• Polarization smoothing</li> <li>• Phase smoothing</li> </ul>
Pulse shaping	0.1- to 4-ns arbitrary shapes with 40:1 contrast
Repetition rate	One shot/h
Laser and diagnostic pointing	Any location within 1 cm of chamber center

### 2.2.2 Laser-Energy Performance

A variety of ultraviolet (UV) pulse shapes that tailor the target drive for a specific experiment are available. While the infrared (IR) performance is relatively independent of the pulse shape, UV power is strongly dependent on shape because the conversion to UV is a nonlinear, intensity-dependent process. The system performs nearly optimally with a 1-ns square pulse, which is to say that maximum UV energy can be delivered to the target with a 1-ns square pulse.

The overall energy performance predicted for a 1.0-ns square pulse on OMEGA is shown in Table 2.2. This table outlines the performance for the cases of no-SSD bandwidth and for 1.0-THz-SSD bandwidth at nominal system peak power and with the best IR to UV conversion setting. The energies quoted are summed over the 60 beams and reflect 0.84-kJ IR per beam prior to conversion. The UV on-target numbers include a 4.1% loss at the UV diagnostic pickoff and an additional 8% loss due to the transport system, including transport mirrors, DPR's, DPP's, focus lenses, vacuum windows, and debris shields. The average fluence is the maximum average fluence in the pulse including the effects of gain saturation and the radially-varying gain profile of the system. The peak fluence is taken as 1.78 times the maximum average fluence based on experience at LLE and elsewhere. Although FCC's have been upgraded to enhance broad-bandwidth frequency-conversion efficiency, there is nearly a 25% energy penalty for 1-THz operation.

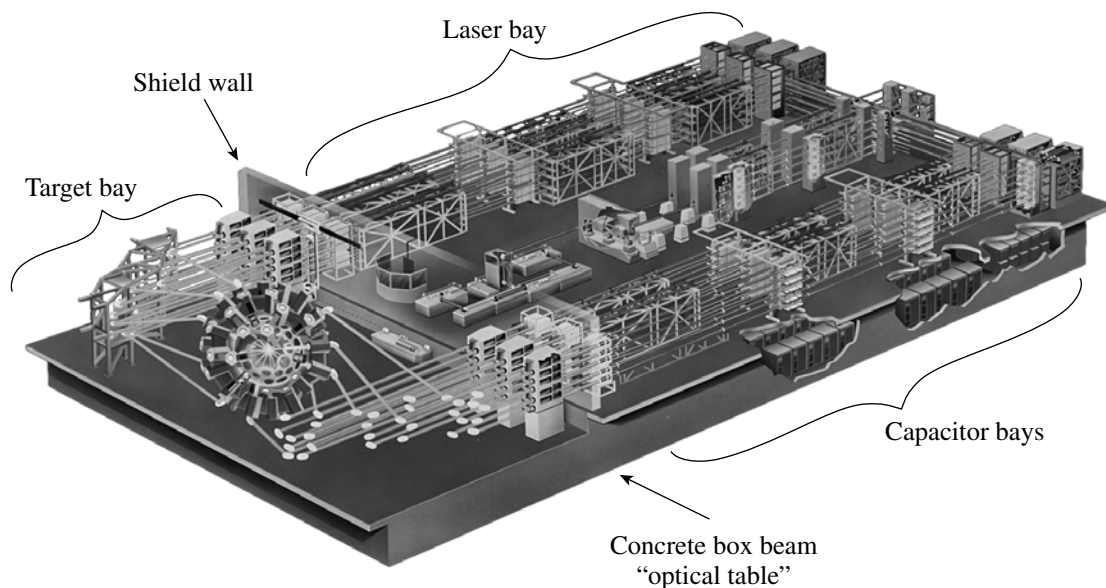
Table 2.2: Energy Performance of OMEGA with a 1.0-ns square pulse.

	No SSD bandwidth	1.0-THz SSD
Peak power of main pulse	31.2 TW	23.8 TW
UV energy on target (kJ)	31.2	23.8
UV energy after FCC (kJ)	35.2	27
Average fluence after FCC ( $J/cm^2$ )	1.13	0.87
Peak fluence after FCC ( $J/cm^2$ )	2.02	1.55
Conversion efficiency	70%	55%
IR energy before FCC (kJ)	50.4	50.4
IR avg. fluence before FCC ( $J/cm^2$ )	1.59	1.59
IR peak fluence before FCC ( $J/cm^2$ )	2.84	2.84

### 2.2.3 Top-Level Configuration

The OMEGA laser system is installed in the same facility that formerly housed the 24 beam OMEGA system. A significant feature of the facility is the concrete box beam structure [67 m long, 29 m wide, and one story (4.9 m) high] that serves as an "optical table" on which the laser is built. This optical table rests on a bed of gravel and is structurally independent from the laboratory building enclosing it. As shown in Figure 2.2, the OMEGA laser system is installed on the optical table in two bays separated by a neutron-absorbing shield wall. The shield wall includes a viewing

area called the “Visitors Gallery,” which looks into both bays. The western bay contains the IR laser components and is called the Laser Bay. The eastern bay is dominated by the target mirror structure (TMS) and target chamber (TC) and is called the Target Bay (TB). The Laser Bay and Target Bay are climate controlled and designed to operate as Class-1000 clean rooms, but actually perform to nearly Class-100 conditions. The area inside the facility below the Laser Bay contains the capacitor bays, which house the power conditioning system that powers the laser amplifiers. The Pulse Generation Room (PGR) is also below the Laser Bay. The area below the Target Bay, called LaCave, contains support systems for experimental diagnostics and the target insertion portion of the Cryogenic Target Handling System (CTHS). Supporting systems, such as the laser spatial filter vacuum piping, deionized (DI)/glycol cooling piping, and nitrogen gas piping, are also installed beneath the laser bay. The Control Room is located in the laboratory building just north of the Laser/Target Bays. The laboratory building also houses offices, laboratories, and supporting services.



TC2998J1

Figure 2.2

The OMEGA laser system is built on a concrete structure that is independent of the surrounding building.

Figure 2.3 is a schematic representation of the elements that make up the OMEGA system. Figure 2.4 illustrates the physical layout of the same elements. The laser drivers subsystem produces the shaped seed pulses and delivers them to the stage-A splitter in the Laser Bay. The remainder of the beam-handling equipment, up to the target itself, is referred to as the optomechanical subsystem. It includes the laser optical system and six power amplifier stages. These components amplify the pulses, divide them into 60 beams, and control arrival time at the target, energy, polarization, and spatial distribution of each beam. The optomechanical system also includes the frequency-conversion crystals, which triple the frequency of the IR beams to produce UV energy and target bay subsystems, which transport the beams to the target, and align and focus them precisely. The experimental system

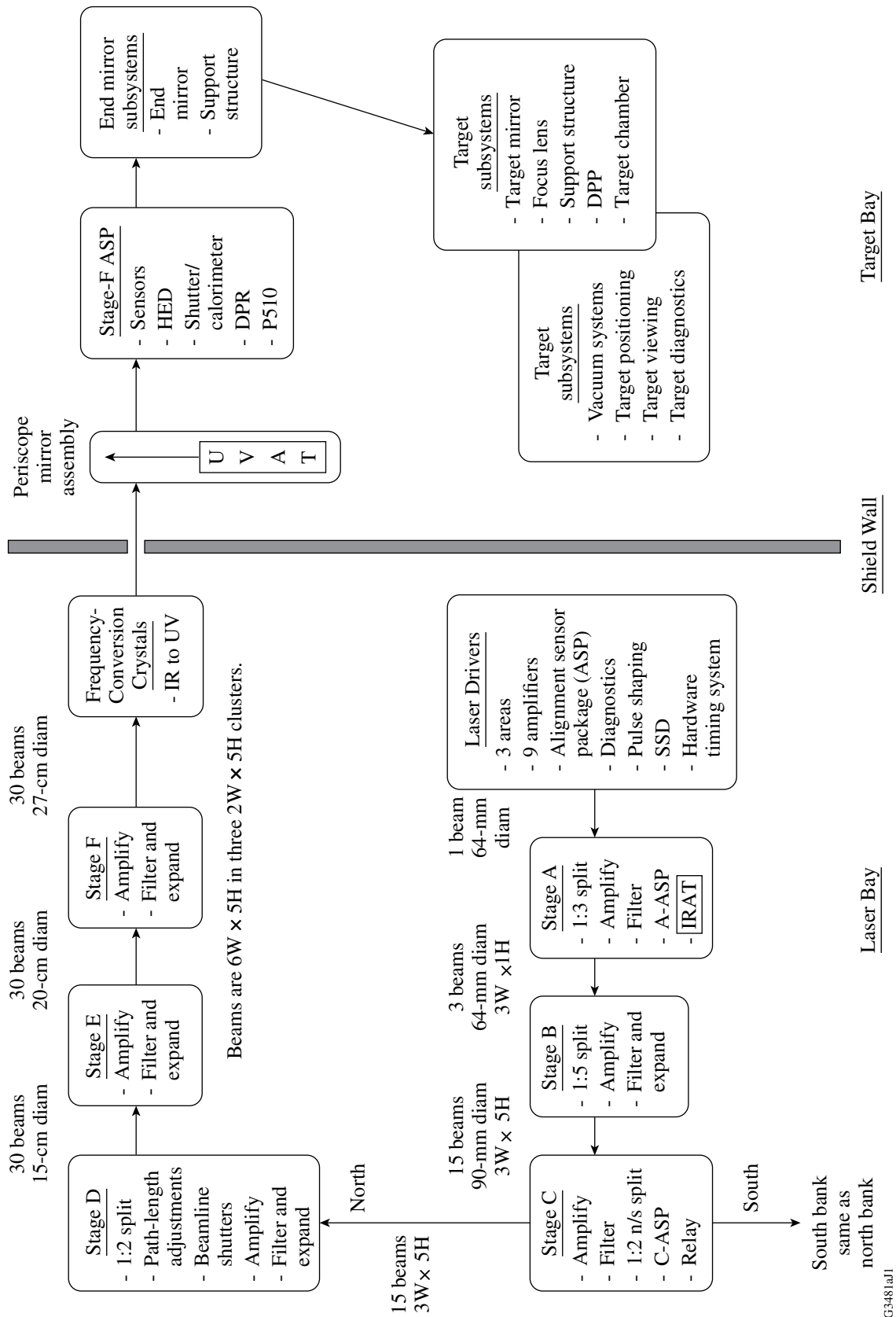


Figure 2.3  
A schematic of OMEGA. IRAT and UVAT are the IR and UV alignment tables; ASP's are alignment sensor packages.

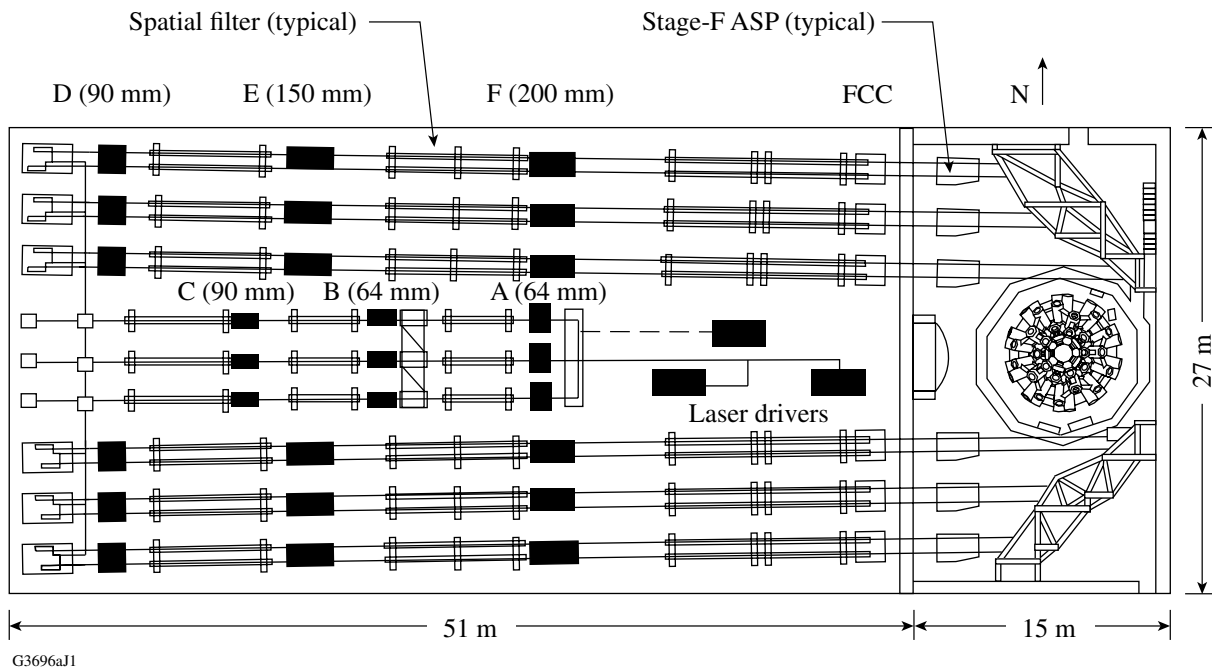


Figure 2.4

The physical layout of OMEGA. The location of four stages of rod amplifiers (A–D), two stages of disk amplifiers (E, F), and the frequency-conversion crystals (FCC’s) are indicated.

includes the target subsystems, which establish and maintain a vacuum within the target chamber and insert and position the targets, and the experimental diagnostic instruments that acquire data during shots.

The laser beams originate in the Driver Electronic Room (DER) located below the laser driver area in the Laser Bay. The shaped pulses produced in the DER are sent via optical fiber to the PGR, which is located adjacent to the DER. The PGR is the facility where the laser beam is spatially formed and, in the case of the SSD driver, modified substantially to improve the on-target laser uniformity. The driver beams go through a periscope to the laser bay where they are distributed to three separate amplifier systems: the SSD, main, and backlighter large-aperture ring amplifiers (LARA). After amplification in the LARA, each beam is spatially filtered and propagates westward into the stage-A beam splitter. As is detailed in the next section, these three sources can be configured to produce a variety of target irradiation conditions. Only the basic, single-driver configuration is described here.

The single driver beam is split three ways at the A-split. All of the beam splitters are configured with polarization-control wave plates that provide the ability to accurately control the energy balance between beams. After the A-split, each beam is amplified and split five ways (B-split), resulting in 15 beams. These beams, now at 1/5 the output energy of the A amplifiers, are amplified again. The stage-A and stage-B amplifiers are 64-mm rod amplifiers. The 15 beams are then expanded and propagated through 90-mm amplifiers (stage C).

Each beam is then split four ways at the end of the bay. The resulting 60 beams pass through assemblies that permit path-length adjustment needed to compensate for unavoidable differences in transport paths to the target chamber or to provide precision beam-timing delay for experiments. This adjustment allows control of individual beam arrival times to ~10 ps. A range of travel of 9 ns available on each beam permits intentional mistiming of beams for special experimental configurations.

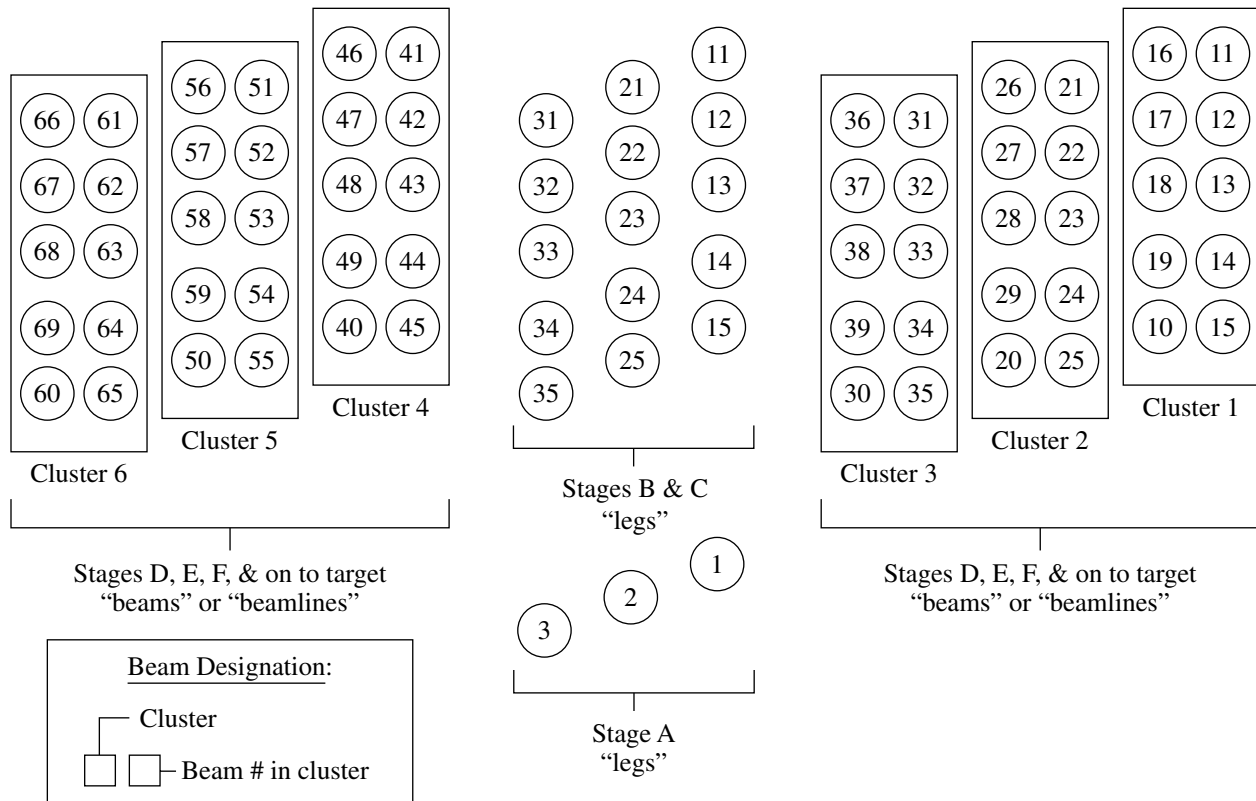
The 60 beams then propagate eastward, back down the length of the laser bay, 30 beams on the north side and 30 beams on the south side of the Laser Bay. The beams are arrayed in six clusters of ten beams (two wide, five high). Each beam passes through a second 90-mm rod amplifier (stage D) before being amplified by the stages-E and -F disk amplifiers. (These feature clear-aperture diameters of 150 mm and 200 mm, respectively.) Both the 64-mm and 90-mm rod amplifiers are modified versions of the original OMEGA amplifiers and are pumped by 12 longitudinal flashlamps along the barrel of the rod. In the disk amplifiers, the laser gain media is a face-pumped disk geometry because rod amplifiers are not feasible at the larger apertures. The disk amplifiers are termed single-segment amplifiers or SSA's because each amplifier is dedicated to a single beam. The disk amplifiers were designed and prototyped at LLE prior to deployment on OMEGA; their performance is described in Chap. 3.

The 30 beams propagating toward the Target Bay on each side of the Laser Bay are all mutually parallel but are angled  $0.75^\circ$  toward the center of the Laser Bay. This angle is required to map the 60 beams onto the spherical target chamber using only two mirrors per beam while limiting the incident angle on the mirrors to  $60^\circ$  or less. Additional advantages of this wedged configuration are that it minimizes the in-air path length of the UV transport system to a total of 18 meters propagation in air. Minimization of in-air path length is required to stay below the thresholds where stimulated rotational Raman scattering (SRRS) will occur. SRRS is a phenomenon that can degrade the performance of the system and/or damage transport optics.

At each stage of the laser, spatial filtering is used to remove high-spatial-frequency noise in the beam and to ensure correct image relaying. Image relaying is critical to the performance of laser beams with SSD because it prevents excessive excursions of different frequencies across the beam aperture. Spatial filtering mitigates the beam degradation that would otherwise result from the frequency-dependent, grating-induced differences in propagation directions. Image relaying and spatial filtering also prevent intensity modulation caused by interference effects and nonlinear, intensity-dependent phase errors.

The power-amplified beams are spatially filtered and magnified to a clear aperture of 280 mm. They then propagate through thin-film polarizers before reaching the FCC's. The polarizers maximize conversion efficiency by ensuring that the correct linear polarization is incident upon the crystals. UV light reflected from the target is prevented from propagating backward through the laser system by a UV-absorbing window on the input of the frequency-conversion cells. Frequency conversion to the third harmonic (351 nm) is carried out using the polarization-mismatch method developed at LLE. After frequency conversion, the beams pass through holes in the 76-cm-thick concrete shield wall and enter the Target Bay.

Each beam has a unique identification; the 15 beams propagating west are referred to as “legs.” The 60 beams that emerge from the stage-D splitter are called “beams.” Figure 2.5 shows the OMEGA beam-numbering convention.



G5626J1

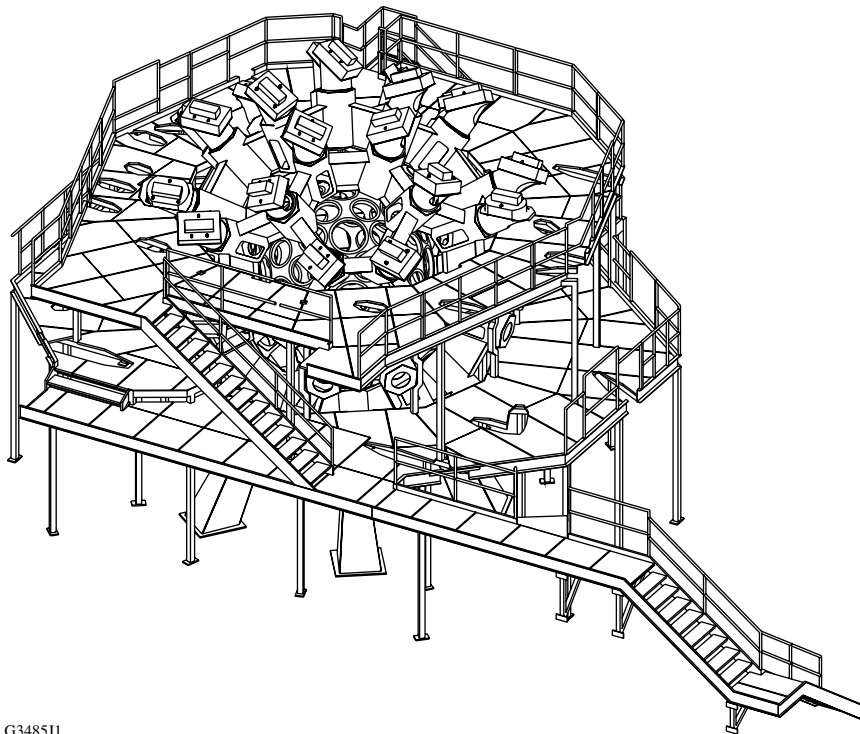
Figure 2.5  
OMEGA beam designations as viewed from the Target Bay.

In the Target Bay, each beam encounters a stage-F alignment sensor package (F-ASP), which provides the alignment reference for the laser beamlines. The F-ASP’s are housed in six structures constructed of a cast epoxy/granite composite. These massive structures (20,000 kg each) ensure the thermal and vibrational stability necessary for the required  $\sim 1\text{-}\mu\text{rad}$  system-alignment accuracy. Also in these structures are optical pickoffs that distribute a fraction of the beam energy to the alignment, energy, and pulse-shape diagnostics.

The F-ASP’s provide the reference to which IR and UV beams are aligned. Both IR and UV alignment beams are referenced to the same position on the F-ASP camera. The periscope mirror assembly (PMA) is a moving gantry system that can insert a full-aperture UV beam from the UV alignment table (UVAT) into any of the 60 beamlines aligned to the F-ASP camera.

The F-ASP's also provide a sample of each beam via fiber optic to the harmonic energy detector (HED) and to the P510 UV streak camera system. The HED system consists of integrating spheres that capture and measure a small fraction of the laser beam energies at the fundamental (1054-nm), second (527-nm), and third (351-nm) harmonics produced by the FCC's. HED diagnostic data is the primary laser-energy diagnostic for OMEGA. The P510 cameras can measure the temporal pulse shape of all ten beams from each cluster. Comparisons between beam-intensity profiles are used to characterize the power balance and infer the time instantaneous target irradiation uniformity.

In the Target Bay, the linear geometry of the laser transitions to the spherical geometry of the target chamber. Each beam is transported to the target chamber via two mirrors: the end mirror on the beam axis and the target mirror on the target mirror structure (TMS). The focus lens assembly (FLAS), which holds the focus lens and the DPP for each beam, is mounted on the chamber. The focused beam enters the evacuated target chamber through a flat blast window assembly (BWA), which has two optics, a vacuum window, and a thin debris shield. The TMS supports the target mirrors, the target chamber, and its ancillary systems and is surrounded by the TMS platform for personnel access. These are shown in Fig. 2.6.



G3485J1

Figure 2.6  
Target mirror structure and personnel platform.

### 2.2.4 Laser-Drivers Subsystem

The laser drivers subsystem consists of the equipment that provides the temporally shaped seed pulses to the beamlines subsystem and a “fiducial” pulse train that provides a timing reference for many of the laser and target diagnostics. The precision electronic timing system, called the Hardware Timing System (HTS), that is used to trigger time-critical functions throughout the OMEGA system is also part of the laser drivers subsystem.

The three separate seed pulse drivers are called the main, the SSD, and the backlighter. The subsystem is configured so that either the main or the SSD driver can be injected into the stage-A splitter, where it would normally continue on to feed each of the three stage-A legs and all 60 beamlines. The backlighter driver can be injected into any one of the stage-A legs, where it can feed 20 beamlines. When this is done, the main or the SSD driver can feed the other two stage-A legs and the remaining 40 beams.

The names applied to the three driver systems that can seed OMEGA are explained below:

- The “main” driver is the most streamlined source. It has all of the basic necessities for generating a round beam of the appropriate pulse shape and timing needed for shots. It does not include the SSD feature needed for advanced beam smoothing on target and, therefore, is generally of greater utility to indirect-drive experiments.
- The “SSD” driver is similar to the main driver but has additional equipment to smooth the profile of the beam on target. The SSD smoothing is accomplished by more than 100 components including electro-optical modulators and in-house-fabricated holographic diffraction gratings. Because the SSD modulation effect can be quickly applied to or removed from the pulses provided by this line, the SSD driver has become the primary source for OMEGA.
- The “backlighter” driver equipment is so named because its intended primary use is to seed beams that may be pointed at separate target elements used to produce x rays that backlight the primary target for diagnostic purposes. Because this line does not have an amplifier after its LARA, it is capable of seeding only one 20-beam OMEGA leg. When the backlighter driver is injected into an OMEGA leg, the resulting 20 beams may be directed to all of the same target or diagnostic destinations as beams that are seeded by the other two drivers. This line has no SSD capability.

The laser-driver subsystems, outlined in Fig. 2.7, are located in the DER, the PGR, and the driver line area of the Laser Bay. In addition, a laser driver system in the Target Bay is used to generate a timing reference (“fiducial”) pulse for diagnostic systems. This fiducial laser is a diode-pumped amplifier, but it produces a comb of pulses. This independent but synchronous laser provides IR, green, and deep UV pulses to instruments located throughout the laser facility.



To decouple the sensitive PGR optical configuration from heat and electromagnetic interference (EMI) sources, much of the associated electronic equipment is housed in the DER. The various timing circuits, regen cooling system, and majority of the PGR power supplies are located in this room.

The 0.1-mJ outputs from each regen are separately directed upward, via a vertically mounted periscope, to the next set of amplifiers, which is located on the Laser Bay level. These amplifiers are 40-mm, large-aperture ring amplifiers (LARA's). One is provided for each of the main, SSD, and backlighter pulses. Each LARA provides a gain of about 10,000 in four round-trips.

Either the SSD or main driver is selected by the position of a kinematic mirror for propagation to OMEGA. Prior to leaving the driver area, the selected driver (main or SSD) is amplified to 4.5 J by a 64-mm rod amplifier. The pulse is then spatially filtered and propagated to the stage-A beam splitter, where the driver-line pulses are split three-ways and injected into the OMEGA power amplifiers.

The backlighter driver generates a 1.5 J laser pulse capable of driving one of the three legs from the A-split in lieu of the main or SSD driver pulses. The backlighter pulse arrives at the stage-A splitter by a path that is separate from that used by the other two drivers.

### 2.2.5 Amplifier Staging

The power amplifier section of OMEGA has a 64-mm input aperture and a 20-cm output aperture. The output aperture of the final amplifier was initially determined by the number of beams, the total energy requirement, and damage thresholds for the optical coatings. The amplifier staging comprises four stages of rod amplifiers (A–D) and two stages of disk amplifiers (E and F), all separated by spatial filters. Figure 2.8 provides the details of the final stages. The final aperture of the beam is increased to 28 cm to reduce the fluence on the UV transport optics.

A total of 93 rod amplifiers are used in stages A–D. The rod amplifier design evolved from the original OMEGA system and incorporates significant mechanical and thermal improvements. Rod amplifiers use de-ionized water cooling for the flashlamps and feature a separate DI/glycol cooling channel along the barrel of the rod. The disk amplifiers for the last two stages are of a new design utilizing conventional box geometry with a 15-cm aperture at stage E followed by a 20-cm aperture at stage F. Each amplifier contains four Nd:glass laser disks. The clear aperture of the final amplifier is set by damage constraints; specifically, the antireflection coating on the input lens of the final spatial filter will damage if the laser pulse reaches  $9.8 \text{ J/cm}^2$ . The 15-cm stage provides a small signal gain of 4.2:1, and the 20-cm stage a gain of 3.0:1.

The disk amplifiers, like the rod amplifiers, use water-cooled flash lamps that facilitate operation at a high storage efficiency. The benefits of this are outlined in Chap. 3. Both the 15- and 20-cm amplifier stages utilize the same power-conditioning and pulse-forming network (PFN). The cooling times for the disk amplifiers permit a 1-h shot cycle. The modular nature of the design allows for the rapid change of flash-lamp pump modules within this shot cycle.

Stage	C output	D	E	F
Amplifier size		90-mm rod	150-mm disk	200-mm disk
Beam diameter		86 mm	143 mm	191 mm
Nominal energy	25 J	130 J	428 J	1000 J
Nominal fluence	0.6 J/cm <sup>2</sup>	2.6 J/cm <sup>2</sup>	2.8 J/cm <sup>2</sup>	3.6 J/cm <sup>2</sup>

G3376bJ1

Figure 2.8

The amplifier staging of the OMEGA laser consists of four stages of rod amplifiers and two stages of disk amplifiers. The early stages compensate for the 1:60 splitting; the last three stages (shown here) provide ~97% of the beamline energy.

## 2.2.6 Frequency Conversion and UV Transport

Conversion of the 1054-nm IR energy produced by the laser amplifiers into the 351-nm UV energy that is delivered to the target is achieved in the frequency-conversion crystal (FCC) subsystem, located in the Laser Bay at the end of each cluster just before the shield wall. Each of the 60 FCC assemblies has an input polarizer and a cell assembly that includes three crystal optics made from potassium dihydrogen phosphate (KDP) and a UV absorption window. With the correct combination of polarization angle, crystal axis orientation, and crystal temperature, the first KDP crystal, called the “doubler,” doubles the frequency of part of the incoming 1054-nm beam. The second crystal, called the “tripler,” combines the resulting green photons with the remaining IR photons to efficiently produce UV photons. A second “tripling” crystal provides a capability for efficiently converting terahertz (THz) SSD bandwidth. The gimbal mount that holds the crystal assembly is provided with a three-axis motorized positioner. The temperature of each FCC is kept stable by an insulated enclosure and is sensed to allow for angular tuning of the gimbal axes in response to minor changes in temperature. The temperature tuning is achieved through the computer control system and provides for maximum efficiency of frequency conversion.

After the IR beam is converted to the UV by the FCC's in the Laser Bay, it passes through the shield wall and through the Stage F-ASP. The UV transport system utilizes two mirrors (an end mirror and a target mirror) per beam to direct the UV beam exiting the F-ASP to the target chamber. The beams are focused onto the target using 1.8-m-focal-length,  $f/6.7$ , fused-silica aspheric lenses. These lenses are mounted in precision mounts that allow accurate control of the lens position for

focusing. This subsystem is called the focus lens adjustment system or FLAS. A distributed phase plate (DPP) can be mounted on the input end of the FLAS. The DPP optics create a uniform, repeatable spot approximately the size of a typical fusion capsule. Because some experiment campaigns do not irradiate spherical capsules, these optics are removable. Different designs are available to create different irradiation conditions.

The F-ASP's and periscope mirror assembly (PMA) are located along the shield wall, and the north and south ends of the Target Bay are filled with the end-mirror structures (EMS). A personnel platform surrounds the target mirror structure (TMS) and provides three working levels, allowing access to all of the ports on the target chamber, as well as the transport optics. The north EMS platform supports the fiducial laser, and a laser diagnostic station has been deployed on the south EMS platform.

Central to the target area is the TMS, which supports the target mirrors and target chamber. The 3.3-m-diam chamber is the heart of the experimental system, where targets are irradiated and the various diagnostics are supported. The diagnostic suite has both fixed and flexible diagnostic platforms. Fixed diagnostics include plasma calorimeters that measure absorbed laser energy, x-ray pinhole cameras that capture time-integrated images of the target emission, Kirkpatrick-Baez (KB) microscopes, and x-ray and neutron streak cameras that record time-resolved target events.

Flexible accommodations for experimental diagnostics are provided by ten-inch manipulators (TIM's). Six of these subsystems are currently installed on the target chamber. Each provides mechanical, vacuum, and electrical/control support and positioning for any compatible instrument that needs to be positioned near the center of the target chamber. Also installed on the chamber are the target viewing systems, the system used to position ambient temperature targets, the upper and lower pylon elements of the Cryogenic Target Handling System, and the cryogenic pumps used to create the high vacuum environment.

### 2.2.7 Optical Alignment

Because the high-energy pulsed beam is converted from IR to UV part way through the OMEGA system, the OMEGA alignment system must include both IR and UV sources. A hand-off between the two alignment sources takes place at the 60 F-ASP's. These utilize achromatic optics so that they can function at both wavelengths and are located in the Target Bay just prior to the end mirrors. Each F-ASP includes a special full-aperture pick-off optic that reflects 4% of the beam energy into the diagnostic subsystem while allowing the remainder to propagate onward to the end mirror. During the alignment process, a 4% sample of the alignment beam being used is directed to the alignment sensor. On a shot, the 4% sample of the high-energy pulse is directed to beam performance diagnostics.

The IR portion of the OMEGA system is aligned using a 1054 nm Nd-doped yttrium lithium fluoride (Nd:YLF) laser that is located on the infrared alignment table (IRAT) and is injected into the system at the A-Splitter. The beam train is aligned in a progression towards the target using a sensor package the A-Splitter, 15 sensor packages at stage C, and ending at pointing references in each of the 60 F-ASP's.

The UV portion of the system is aligned using a 351 nm cw laser that is mounted on the UV alignment table (UVAT) on the centerline of the system near the west wall of the Target Bay. The UVAT optics project separate full-aperture alignment beams northward and southward from the table into corresponding periscope mirror assemblies (PMA's). Each PMA functions to position movable mirrors at specific locations on the shield wall. These mirrors inject the alignment beam into one beamline at a time one each side of the bay.

Co-alignment of the IR and UV alignment beams in each beamline is achieved by steering the PMA mirrors to point the UV alignment beam to the pointing reference in the F-ASP. The portion of the UV alignment beam that passes through the pick-off optic is then steered to the target by moving the transport mirrors. The UV reflections from a surrogate target are transmitted back to an alignment sensor package on the UVAT to guide this process. The north/ south symmetry allows one north side and one south side beam to be aligned simultaneously.

### 2.2.8 Laser Diagnostics

Beam-energy measurements are required at various points in the laser chain. The most important measurement is made just after the FCC's, where a second-order Fresnel reflection from two uncoated optical surfaces transports 0.16% of the beam energy into a harmonic energy diagnostic (HED) package. The first uncoated surface is the primary pickoff that passes 96% of the energy to the target. The second is on a flip-in optic that directs 4% of the first 4% to an integrating sphere via an evacuated optical relay. The optical layout ensures that the beam image plane is relayed to the rear surface of an integrating sphere. A fiber optic pickup in each sphere transfers the light to a spectrometer coupled to a scientific CCD camera. There is one spectrometer/CCD unit for the 30 beams on each of the north and south sides of the Target Bay. The HED spectrometers are calibrated using 60 full-aperture calorimeters that can be inserted into the beam to measure its total energy. These calorimeters are of a conventional absorber/thermopile design.

The UV delivered to target is equal to the energy measured by the HED multiplied by the passive transmission of the UV transport optics. Each beam has two UV high-reflector mirrors, a distributed phase plate, a focus lens, a vacuum window, and a debris shield. An instrument called the OMEGA Transport Instrumentation System (OTIS) measures the cumulative transmission of the ten optical surfaces and four substrates. OTIS consists of a CCD-based ratiometer embedded in the UVAT and special reflective sphere inserted into the target chamber. This system is capable of characterizing the UV transport with better than 1% precision.

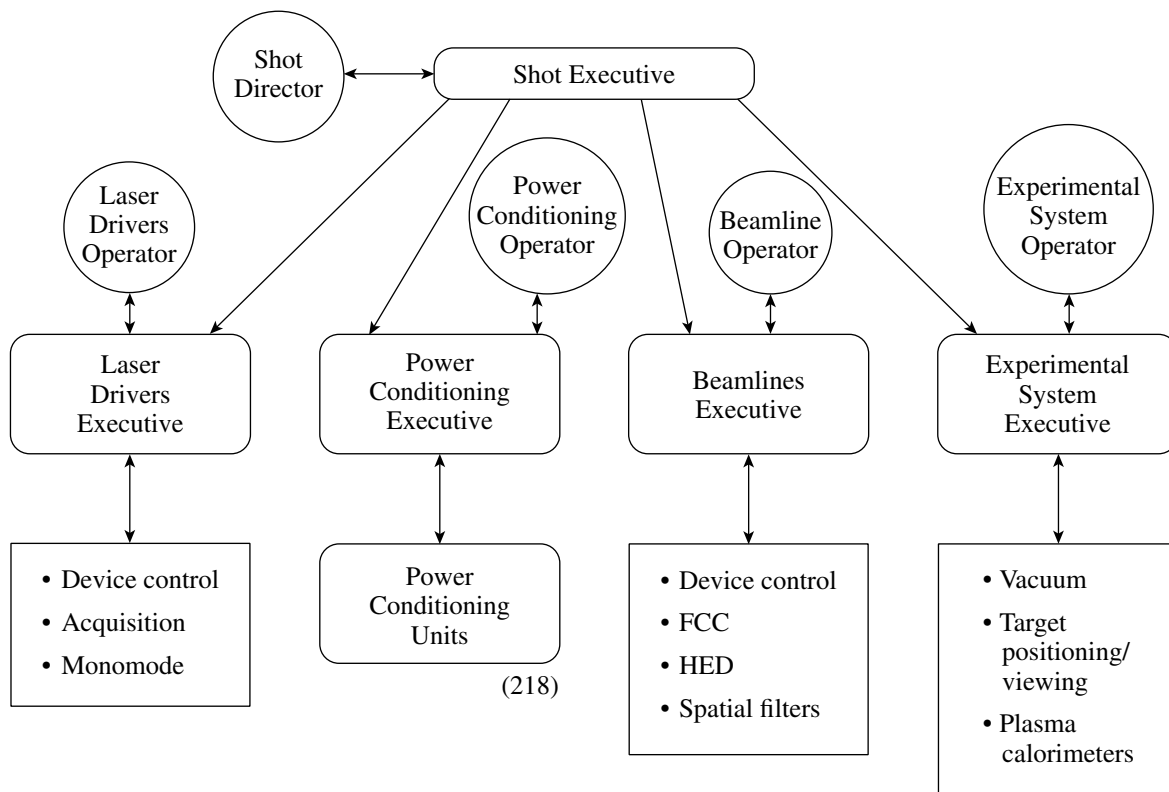
An instrument called the P510 streak camera measures temporal pulse shapes of the output of each of the 60 beams. The instrument system consists of six separate instruments, each of which measures the ten beams from a cluster. These cameras have very high temporal bandwidth for a high-fidelity time history of the irradiation on target. Because the UV shape on target is one of the critical parameters that an investigator conducting experiments on OMEGA is interested in, this system is calibrated frequently for optimal performance.

### 2.2.9 Control System

The OMEGA control system provides the system operators with remote control of subsystems, displays of sensor data, and safe sequencing of key processes. The control system also collects and records information about each shot. Operator interfaces are provided in the Control Room and throughout the facility.

#### (a) *Functional Subsystems*

The control system architecture reflects the hierarchical subsystem configuration of OMEGA. Four autonomous consoles in the Control Room allow each subsystem to be operated by the respective trained operators. During shot operations, the subsystem functions are coordinated by a Shot Director who uses a fifth, supervisory, control station. Figure 2.9 illustrates this arrangement.



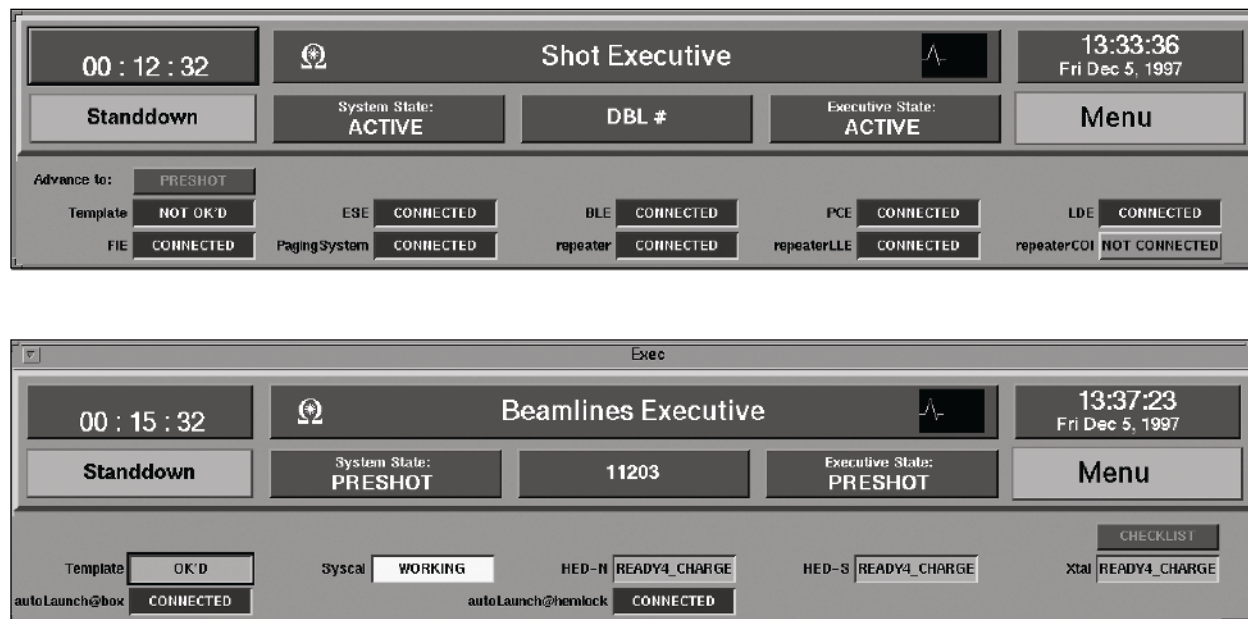
G4518cJ1

Figure 2.9

The top-level architecture of the OMEGA Control System. (Circles represent human operators; boxes represent applications running on computer workstations.) Three levels of computers are used to provide a system with appropriately distributed processing capabilities. Operators use executive and subsystem-specific applications to operate numerous microprocessor-controlled devices via local networks. The shot director monitors and coordinates the subsystem activities.

Communication between the operators and the supporting technicians is facilitated by a headset-based intercom and a facility public address system. This verbal communication is supplemented by messages that pass between the application programs running on the computers. High-level application-to-application communication uses a standardized OMEGA intercommunication protocol (OIP) that conveys limited system status and control information in both directions. Figure 2.10 shows two examples of the “generic executive” graphical user interface that portrays the status information to the operators. Specific versions of the generic executive are configured as the Shot Executive (SE), Laser Drivers Executive, Beamlines Executive, and Experimental Executive. [Although the Power Conditioning Executive (PCE) is functionally similar, it is not based on the same generic code as the other executives. Yet another variation is the Facility Interlock Executive, which is used, primarily by the Shot Director, to manage room access and warnings.]

Each executive provides a top-level operator interface for the subsystem and controls and receives information from devices in the bays by communicating with one or more “intermediate” processors over bus extensions, the Ethernet, or other standard communication links. These intermediate computers serve to relieve the executive of routine computation and downward communication tasks. Each of the subsystem executives monitors the applications required for configuring and executing a shot at that console. All executive processors are synchronized to the shot sequence by the Shot Executive.



G4582J1

Figure 2.10 Each Control Room operator is provided with a standardized display of the status of the overall OMEGA system and of the sub-tier processes critical to his or her functions. Two examples are shown here.

(b) *Control Room and Control Stations*

The OMEGA Control Room, on the second floor of the laboratory building, is the focus of operations. Figure 2.11 is a layout of the Control Room that shows the space allocations for control, operations, and planning and data analysis activities. The equipment is arranged to allow the operators to work together and to minimize distractions.

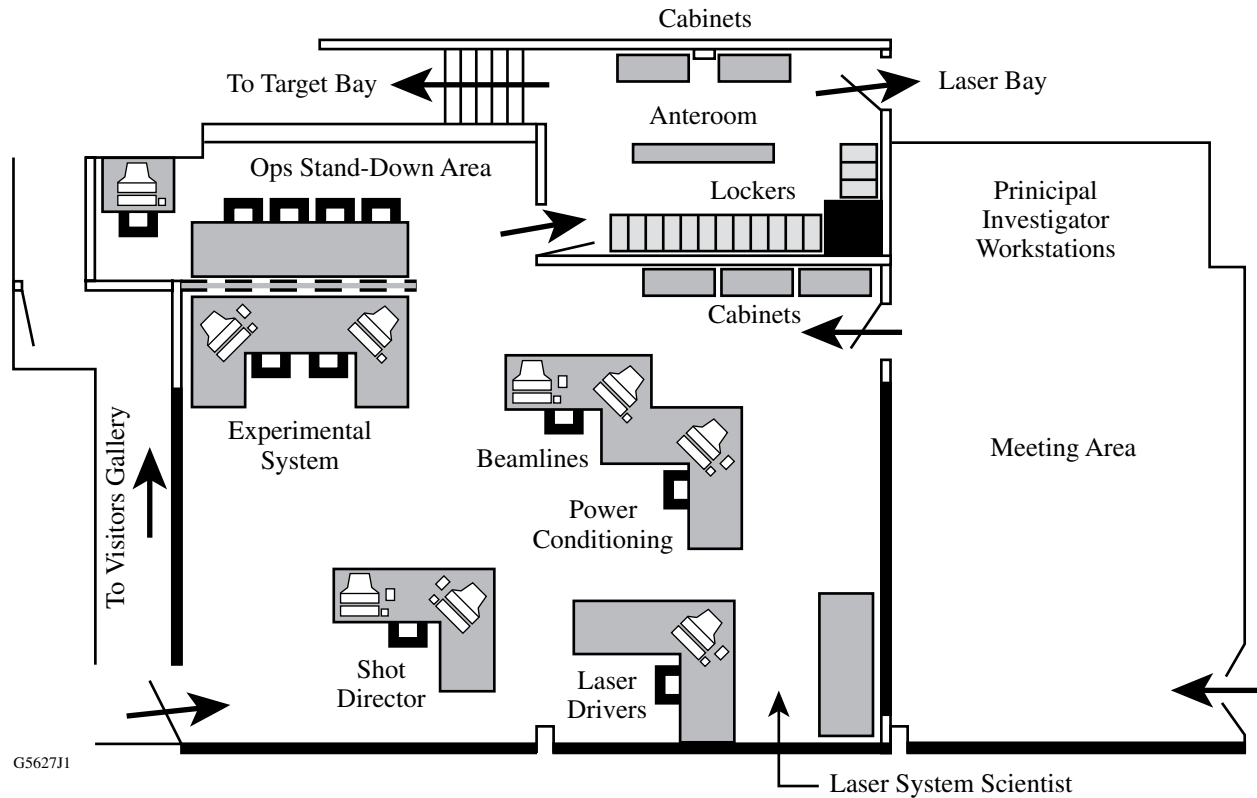


Figure 2.11

The five Control Room workstations are arranged to allow the operators to work together with minimal distraction. A separate conference room is used for briefings, data assessment, and planning. The Target and Laser Bays are accessed through the Control Room.

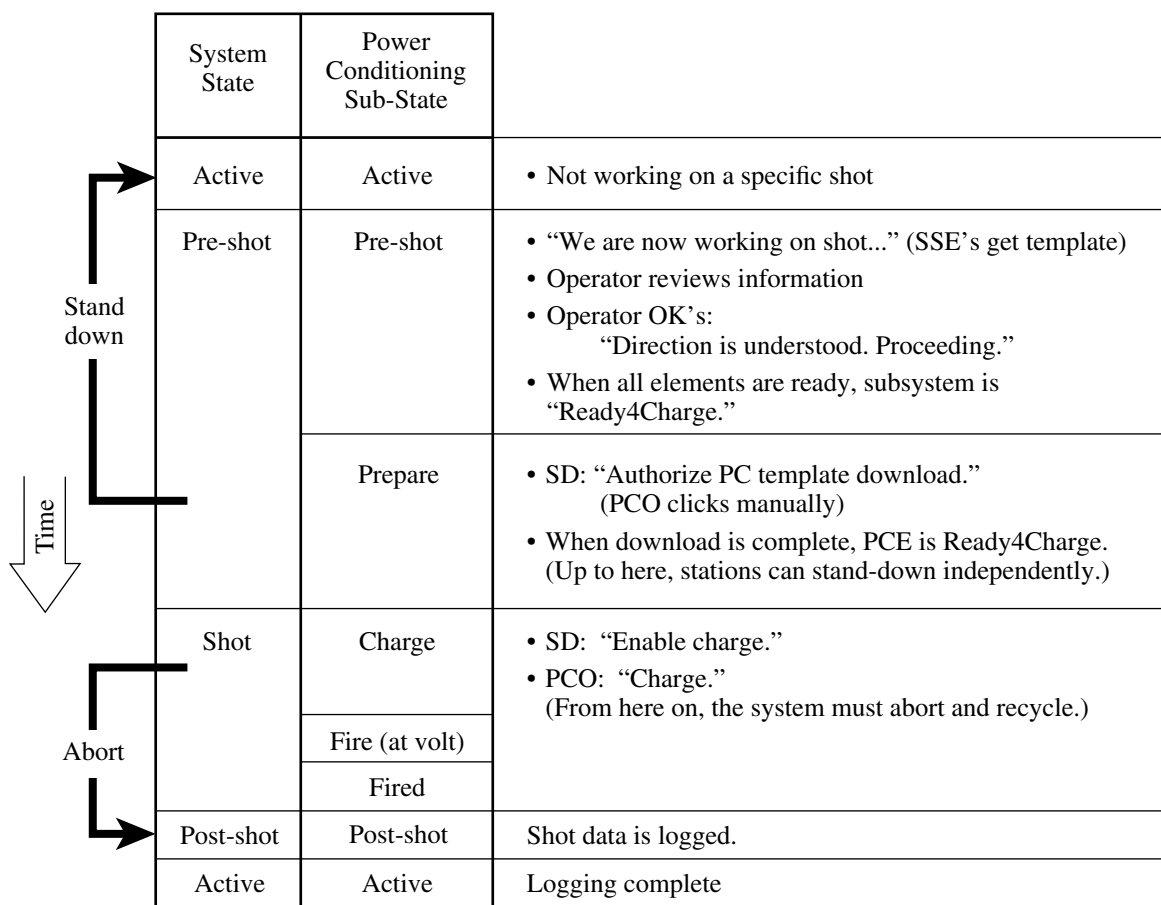
(c) *Shots and System States*

The control system facilitates the operational activities that maintain the system, prepare it for a shot, execute the shot, and record the shot results. Computer network communication is used to coordinate actions requiring synchronization to within about one second. The precision timing required to execute and diagnose a shot is provided by the hardware timing system (HTS). A “handoff” between the two levels of timing control takes place 20 seconds before a shot is triggered.

The approach to system operations makes use of the concept of a “shot cycle,” consisting of a sequence of “system states” and a number of distinct “shot types.” The system states partition the activities into known situations for communications and coordination. The shot types identify the extent to which the high-energy pulsed beam is propagated and the degree of system-wide coordination that is required.

Figure 2.12 illustrates the system state sequence that is executed for every type of shot. In the “active” state, the system is not formally preparing for a specific shot and the subsystems are operated independently for maintenance or setup. Formal preparations for a shot are initiated by the Shot Director (SD) who uses the Shot Executive (SE) to specify a shot type and other key parameters and to communicate them to the other operators via the subsystem executives. The act of transmitting this “master template” information marks the transition of the system from the active state to the “pre-shot” state. The SE also transmits a “shot number,” which is the index to be used when the data from the intended shot is logged. Each subsystem operator reviews the setup information, signals approval to the SD, and proceeds to prepare for the shot.

When a subsystem has been readied, the operator signals the SD using a “checklist” button on the executive GUI. The SD then reviews key details of the setup with the operator before signifying



G4523aJ1

Figure 2.12 The OMEGA shot cycle is a sequence of system states. In the “active” state, the system is not formally preparing for a specific shot and the subsystems are operated independently for maintenance or setup. The pre-shot/shot/post-shot sequence is repeated for each shot attempt. The power conditioning subsystem has sub-states.

concurrency on the Shot Executive. In the special case of the power conditioning subsystem, this process consists of the SD reviewing and approving the power conditioning “template” that details the online/offline status of the power conditioning units (PCU’s) and the voltage commands that will be sent to them for the shot. When this critical safety check is complete, the SD authorizes the transmission (“download”) of the template values.

When all necessary subsystems are ready for the shot, the SD authorizes the power conditioning operator to charge the PCU’s. This marks the transition from the pre-shot state to the “shot” system state. Within the shot system state, the power conditioning subsystem has sub-states that are not reflected in the other processes. These track the major steps of the power conditioning subsystem sequence. Once the charge command has been issued, the power conditioning subsystem controls the laser system to within ten seconds of the shot and then enables the key system elements to proceed on the basis of electrical master timing signals from the HTS.

The events synchronized by network messages include activation of high-voltage diagnostic power supplies, acquisition of background data, and “arming” elements so that they will respond to hardware triggers. The events synchronized by the hardware timing signals include selection of the optical pulses in the laser-drivers subsystem, triggering the electrical discharges that drive the flash lamps in the laser amplifiers, and the operation of diagnostic instruments.

Once the software and hardware sequencing has proceeded through the issuing of the shot triggers, the system enters the “post shot” state and each of the system elements that has acquired shot-related data proceeds to log that data to the system database. As the logging is completed, each element effectively reverts to its “active” state. When all of the elements have completed this process, the system is formally in the active state and ready to initiate another shot cycle.

(d) *Stand-down and Abort*

The shot cycle can be interrupted by either a “stand-down” or an “abort.” If a problem arises or a change of plans occurs prior to the system entering the “shot state” (the PCU’s have not started to charge), the system can “stand down” to the active state. When the situation is cleared up, a new shot cycle can be initiated. Each subsystem can also stand down independently. In this case, the system remains in the pre-shot state, and the subsystem will automatically advance into its pre-shot state as soon as it is ready to do so. Because a stand-down does not cause shot data to be logged, the “shot number” is not incremented.

If a critical problem arises after charging has started, the shot is normally stopped by the abort process: Each of the executive GUI’s has an ABORT button that can be used to initiate the process by signaling the PCE to execute an abort. All of the other software elements are also notified so that they can respond as needed. When an abort is signaled, the PCE immediately prevents the HTS from issuing the critical triggers and issues commands that dump the energy in the capacitors in the PCU’s. Power conditioning and other subsystems then log data and the system proceeds to the active state. In this case, the “shot number” is used and the next shot attempt will be associated with the next sequential number.

The Shot Director can also stop a shot by pressing a switch that is hard-wired to the electric power substation that powers the PCU's, shutting off all of its output. This, in turn, dumps the energy in the capacitors and renders the system safe, even if a software or communication failure has occurred.

While the software-based abort and the hard-wired dump are effective in stopping a shot up to within about one second before the shot trigger, some conditions that necessitate preventing a shot can be detected only in the area of 10 to 100 milliseconds before the shot trigger. These include the target moving or not being in the correct location near the center of the target chamber or an error in the removal of the shroud from a cryogenic target. A mechanism that spoils the seed pulse in the laser drivers subsystem is used to address these conditions. This "driver abort" is automatically initiated by computer logic associated with a target detection subsystem. The action is to interrupt the trigger for the regenerative amplifier in the driver. The pulse that then propagates to the power amplifiers is too low in energy to be amplified to normal levels in the remainder of the system. This prevents laser damage due to energy passing through the target chamber.

(e) *Shot Types*

Not all shots on OMEGA are target shots used for physics research. Many are used for system preparation, checkout and evaluation, or laser technology research and development. This has made it necessary to consider categories, or types, of shots. The seven "shot types" that have been defined are:

<u>Type</u>	<u>Description</u>
1	driver only
2	non-propagating (no driver)
3	propagating to the stage-A splitter
4	propagating to the stage-D splitter
5	propagating to the stage-F alignment sensor package
6	target shot with low (or no) neutron yield
7	target shot with high neutron yield expected

The shot type establishes which of the executive processes must be involved in the shot, the location at which propagation stops, and which bays must be closed to access.

In addition, each of the seven may be simulated as a "trigger test" shot: the system-state sequence is executed as it would be for an actual shot and the HTS triggers are produced, but no PCU's are charged and the seed pulse is not amplified beyond the driver regenerative amplifiers. The two variations are

- Null Template Trigger Test: No PCU's are included in the Power Conditioning Template.
- Zero Volts Trigger Test: One or more PCU's are included, but the charge voltages are set to zero.

It is also possible to produce the HTS triggers without executing the system-state sequence. This is called a “Timing Test.”

(f) *Shot Request Forms*

Execution of effective and safe experimental shots requires complete and detailed specification of the facility configuration and laser-operating parameters, extensive advance planning, and many hours of system preparation prior to and during the actual shot day. The Shot Request Form (SRF) is the primary vehicle for recording and communicating the specifications for a shot. A separate SRF is used for each target shot. Supplemental tools and forms are also generally used in planning and communicating about the sequences of related shots that are referred to as “campaigns.”

The SRF is a database object that is created within the LLE computer system primarily via inputs made at a web-based SRF user interface. This interface consists of a series of pages or screens called “forms” that collect information of various types. The forms include

- General - PI's, campaign identification, planned date, planned order, ...
- Driver - pulse shape, SSD modulation, ...
- Target - characteristics, unique identifier, ...
- Beams - groups defined by energy, pointing, focus, ...

Target diagnostics are specified via a hierarchical series of groupings and setup forms.

Each SRF is automatically assigned a unique, sequential, identifying number at the time it is created. Appropriate controls are applied to limit both read and write access to the records. Figure 2.13 illustrates some of the relationships between the SRF, the database, and OMEGA operations.

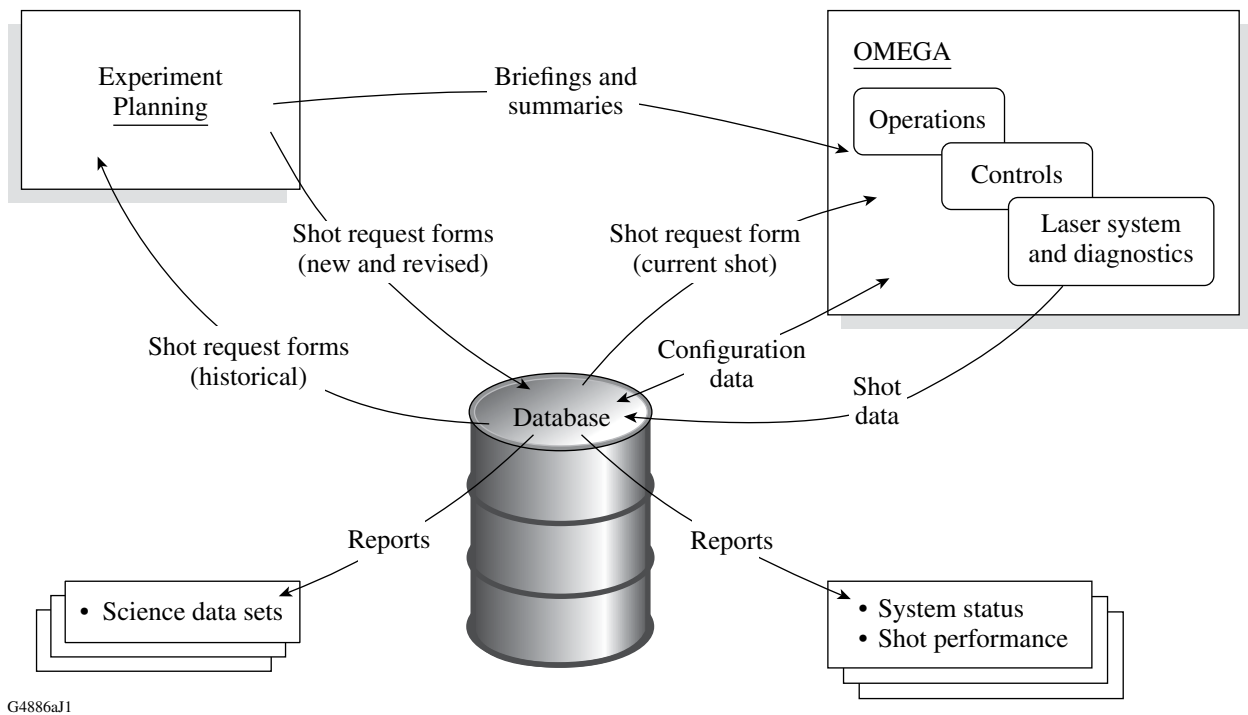
The SRF can be viewed or printed, in part or whole, to provide a standard format for review and implementation. On shot day, SRF data values are also accessed directly by the OMEGA Control System and used to assist the operators in preparing for and executing the shot. Once a SRF has been used to specify a system shot, it is considered expended and will not be reused. The SRF data values are retained indefinitely. The SRF values, indexed by the unique identifying number, may be retrieved for use in data assessment and can be copied to create new SRF's.

(g) *Data Acquisition and Archiving*

Both system configuration and diagnostic sensor data are logged for each shot. The system configuration data consists of all of the parameters that are sensed by the computer system and all of the parameters that can be altered by inputs to the software. Diagnostic data is generally stored locally during a shot and transferred to the archive within minutes after the shot.

(h) *Data Reduction*

A standard set of data reduction routines is used in support of system operations to allow assessments to be made immediately after the shot. Detailed reduction of most target diagnostic data is performed by the investigators well after the shot.



G4886aJ1

Figure 2.13

The OMEGA database plays a significant role in the planning, execution, and evaluation of shots. The detailed plans for experimental campaigns are embodied in Shot Request Forms (SRF's), which are stored in the database. SRF data is used to configure the OMEGA system for the shot. On-the-shot data acquired by the system and the laser and target diagnostics is recorded in the database.

## 2.3 OMEGA FACILITY IMPROVEMENTS

Improvements to the OMEGA facility have continued to maintain it as a unique resource for performing a wide variety of precision experiments. Direct-drive implosion experiments have benefited from improvements to the power balance (Sec. 2.3.1), advances in pulse-shaping technology (Sec. 2.3.2), and the implementation of a new set of phase plates (Sec. 2.3.3). Section 2.3.3 also describes a set of elliptical phase plates that have enhanced the quality of indirect-drive experiments carried out under the National Ignition Campaign. Plasma physics experiments have benefited from the addition of optics enabling one OMEGA beam to be diverted and focused on target as either a second-harmonic beam for laser–plasma interaction experiments or a fourth-harmonic beam for Thomson scattering (Sec. 2.3.4).

OMEGA laser performance diagnostics have been enhanced by the addition of a novel UV spectrometer with a separate channel for each OMEGA beam (Sec. 2.3.5). The spectrometer monitors the performance of the high-bandwidth SSD system on OMEGA, detects misalignment of frequency-conversion crystals, and diagnoses self-phase modulation within the laser system.

A new Target Chamber Tritium Recovery System has been installed to support high-activity cryogenic DT targets (Sec. 2.3.6). Improvements have been made to OMEGA Operations software to accommodate both new OMEGA capabilities and requirements related to OMEGA EP (Sec. 2.3.7). Significant effort continues to be directed to supporting external users, who account for approximately 50% of OMEGA shots (Sec. 2.3.8). Operational statistics (Sec. 2.3.9) show that high levels of system reliability and experimental effectiveness have been maintained.

### 2.3.1 Power Balance

OMEGA was designed to achieve very low beam-to-beam variations in both power and energy on target. Very tight tolerances were placed on a number of important subsystems, including energy measurement and power conditioning. The performance of these subsystems meets or exceeds the specifications. As a result, the system meets its power balance specification of 5% rms beam-to-beam.

Energy balance is necessary to ensure power balance, but it is not sufficient. Due to the intrinsically nonlinear nature of the laser system, two beamlines can generate the same energy with different output pulse shapes, even though all beamlines are fed with the same input pulse shape derived from the single master oscillator. To obtain good power balance, it is necessary to match the gains and losses of all beamlines at each stage, and to control the optical splitters with which the driver beam is successively divided into 60 individual beams. The gains are measured by firing a single stage of the system and recording the signal using a special pickoff in the final (stage F) spatial filter that feeds an additional set of fibers attached to the harmonic-energy-diagnostic system.<sup>1</sup> This signal, divided by the signal from a reference shot taken without firing the stage being measured, provides the relative small signal gain of the stage. Major differences in gain generally represent faults in the amplifiers that are corrected. Minor differences in gain are corrected by making adjustments to the charge voltage for the amplifier. Using this procedure, the small signal gains of the amplifiers can be matched to better than 1%.

While the inter-stage losses are difficult to measure directly, the specifications on the optics and their maintenance ensure that losses between stages are matched to better than the required 2% per stage.

Once the amplifier gains are matched, the split ratios are adjusted to balance the output energies. Due to unavoidable differences among the beamlines, it is not optimum to exactly balance the input energies. The matching of the splits is determined by firing subsets of the system and measuring the output energies. Using this data as input, the splits are then set using an automated adjustment system.

A test shot with only stages A through D fired is used to evaluate the quality of the split adjustment. Residual errors are compensated by adjusting the gains of the D amplifiers. Based on a full-system shot, the gains of the F amplifiers are then adjusted to match the IR energies input to the frequency-conversion crystals. This technique is a variation of that described in Ref. 1. IR energy balance into the frequency-conversion crystals is typically at the 0.6% level after this procedure, with

the UV out of the crystals matched to 2.2%. The on-target energy balance that results is typically at the 3.5% level or better, this higher number reflecting variations among beamlines in the transport optics from the crystals to the target.

Simulations of the system, combined with selected measurements from the P510 streak cameras and system energy measurements, indicate that after power balancing the required 5% beam-to-beam power matching at the output of the frequency-conversion crystals is almost certainly being obtained, even for strongly shaped pulses. At present this level of power balance cannot be fully confirmed with streak-camera measurements since not all 60 channels of the P510 system have the required precision. The three final P510 streak cameras are being upgraded for this purpose.

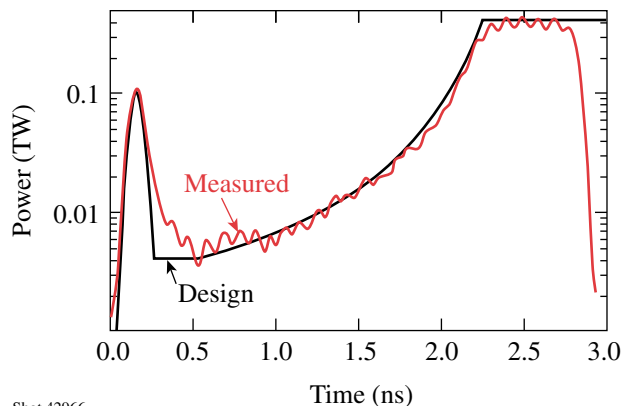
Refinements to the data reduction software are needed to obtain the required time-base accuracy and handle bandwidth mismatches (different cameras generate different amounts of spreading of the sharp rising and falling edges of the pulses). This is an ongoing effort. The single-master-oscillator configuration of the OMEGA laser allows certain kinds of measured imbalance to be readily identified as arising from instrumental error. Time-base variations and bandwidth mismatch among the channels are readily apparent. By eliminating those channels that clearly suffer from these defects, it is possible to use a subset of the measurements to confirm the model's predictions of power balance.

There are several optics between the energy- and power-measurement pickoffs and the target. To obtain the UV energy and power balance on target, the losses due to these optics must be measured. This is done by propagating the UV alignment laser beam through these optics to the target chamber and back and using the very consistent Fresnel reflection from a glass sphere placed at target chamber center. This allows absolute transport measurements to be made with an accuracy of better than 1%. Based on these measurements, transport optics are replaced in such a way as to maximize the uniformity of the net beam-to-beam transport. Transport matching to about 1% is generally obtained.

The power balance strategy outlined above tends to provide the best balance at the time in the pulse when two thirds of the energy has been delivered. This is typically at the peak power level for shaped pulses. It is generally considered preferable to have the best power balance occur in the foot of the pulse. When the P510 data reduction is improved to the point that sufficiently good power measurements can be made in the foot, this data will be used to adjust the gain of the F amplifiers to optimize balance in the foot of the pulse. This can be accomplished with very little degradation of the power balance later in the pulse.

### **2.3.2 Precision Pulse Shaping**

Several advances have been made in precision pulse shaping on the OMEGA Laser System. An Integrated Front End Source has provided shaped pulses with higher reliability than previous systems. Figure 2.14 shows the design template and the measured ultraviolet laser pulse produced on target for a low-adiabat pulse shape. This includes a narrow picket pulse (~80 ps) on top of a low-intensity foot followed by a high-intensity drive pulse. Such pulses are required for ignition-



Shot 42966  
U557JX

Figure 2.14

Designed and measured single-beam pulse shapes for a low-adiabat cryogenic target implosion on OMEGA (shot 42966).

scaled cryogenic target experiments. The agreement between the designed and measured shapes is excellent, particularly for the picket energy, the 100:1 contrast between the foot and drive pulses, and the rising edge of the drive pulse.

The capability to routinely produce a picket with stable width and amplitude combined with a shaped pulse is now standard on OMEGA. A method for generating stable double pickets has also been developed and has been used in target experiments on OMEGA.

### 2.3.3 Phase Plates

A major requirement for successful laser fusion is the uniform irradiation of fuel capsules. For high-power, solid-state laser drivers, the major source of irradiation nonuniformity is the intensity distribution of the individual frequency-tripled beams at the target plane. The beams' irradiation nonuniformities are caused primarily by spatial variations in the near-field phase front that accumulate as the pulse propagates through the air, the amplifiers, and the transport optics. Phase plates at the end of a laser beam<sup>2-4</sup> modify the beam's spatial coherence, changing its focusing properties and shifting the on-target energy toward the higher spatial frequencies that can be smoothed using temporal beam-smoothing techniques such as SSD.<sup>5,6</sup> Phase plates limit the effect of shot-to-shot phase errors arising from the amplifiers on the 60-beam on-target irradiation profile. Phase plates also allow the on-target intensity distribution to be shaped according to the needs of different experiments.

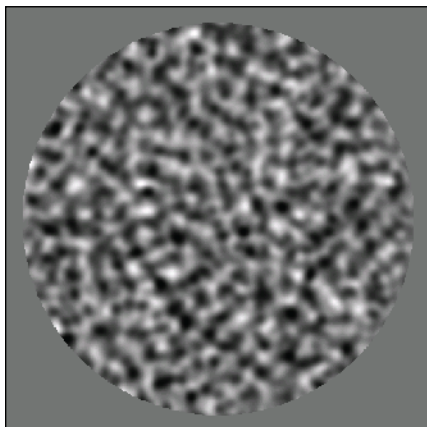
Most experiments carried out on OMEGA require a specific configuration of phase plates. The latest phase-plate design, implemented on all 60 OMEGA beams for spherical target implosion experiments, has an irradiance envelope  $I(r)$  approximated by a rotationally symmetric super-Gaussian profile [ $I(r) \propto \exp(-r/r_0)^n$ , where  $r$  is radius,  $r_0 = 380 \mu\text{m}$ , and  $n \approx 7$ ]. When combined with SSD and polarization smoothing, these phase plates (known as "SG4" phase plates since  $n$  is effectively 4 after smoothing) produce the most uniform irradiation conditions available for spherical implosions to date. Other experiments conducted on OMEGA rely on a wide variety of available phase plates. These provide alternative spatial profiles for flat-target experiments with 100-, 200-, 300-, and 800- $\mu\text{m}$  spot diameters, some with elliptical profiles for oblique incidence, and some with continuous one-dimensional patterns of a specific spatial frequency.

Phase plates made over the last five-year period are more efficient, uniform, and reproducible due to improvements in lithography, etching, and, more recently, advances in magnetorheological finishing. A goal of phase-plate design is to generate the desired far-field spatial profile while minimizing wide-angle scattering outside this profile. Improved design techniques, based on simulated annealing and phase-retrieval algorithms, have been developed to improve the shape and profile of the phase-plate focal spot. Greater experience in the design process has resulted in better control of the correlation length in the near-field phase distribution. This allows the selection of one phase-plate design over another on the basis of overall performance and manufacturability.

For the continuous phase plates currently used,<sup>4</sup> the phase retardation is distributed over the surface by introducing optical path differences (OPD's) in the form of a continuously varying thickness  $t(x,y)$  of a material with refractive index  $n$ . The OPD is given as  $t(x,y)(n-1)$ . Since the correlation length of the phase plate is much larger than the wavelength of light, the surface relief refracts the light a similar amount for all frequencies, making the on-target spot size relatively independent of wavelength. (This is in contrast to the original phase plates used for fusion applications,<sup>7,8</sup> whose surfaces were made of discrete elements of different thicknesses and suffered from diffraction from the discontinuities.)

Optical lithography is used to generate complex surface-relief structures that are subsequently etched into a glass that is compatible with high-irradiance UV laser light. Mask fabrication, photoresist patterning, and ion-beam etching have been significantly improved at LLE to fabricate 310-mm-diam continuous phase plates for use in OMEGA. Improved photolithographic masks, such as the mask shown in Fig. 2.15, were made using an LVT photographic film writer developed by Eastman Kodak in Rochester, NY. The accurate masks, together with a uniform ultraviolet light source, ensures that the mask transmittance at a point multiplied by the material removal function of the photoresist is linearly related to the phase difference required by the phase-plate design.

The final fabrication step involves the transfer of the surface relief into a suitable UV-compatible material. After extensive development of ion-beam etching, the transfer of photoresist masters into fused-silica glass has become highly reproducible. The fabrication of phase plates is



E14636JX

---

Figure 2.15  
Surface relief (shown in gray level) on one side of a glass  
substrate used to form a continuous phase plate.

---

performed in class-100 to class-1000 clean-room conditions to limit contamination that can cause losses due to surface-relief scattering, material scattering, and material absorption. An alternative manufacturing process using magnetorheological finishing, a technique originated at LLE, has been developed by outside vendors to fabricate high-quality phase plates for applications requiring small focal spots,<sup>9</sup> for which the gradients of  $t(x,y)$  are small. This process produces very little far-field scatter and defect-free near-field irradiance. It is the baseline process being used to make the NIF indirect-drive phase plates, but its ability to make direct-drive phase plates [which require larger gradients of  $t(x,y)$ ] has still to be determined.

Phase plates are characterized using the OMEGA ultraviolet diagnostic table, which provides a laser-beam characterization capability for up to four beamlines. The table is located on top of the south end-mirror structure, where it has access to beamlines 46, 52, 56, and 57 without conflicting with target chamber access, other diagnostics, or maintenance activities. The on-target irradiation distribution from a single focused laser beam is measured with an equivalent-target-plane CCD (charge-coupled device) camera.<sup>10,11</sup>

Examples of equivalent-target-plane images are given in Fig. 2.16(a) for the “SG4” phase plates recently installed on OMEGA for implosion experiments and the “SG3” phase plates previously used on OMEGA. In both cases 2-D SSD<sup>6</sup> with 1-THz bandwidth<sup>12</sup> and polarization smoothing<sup>13</sup> were used. Lineouts through the images [Fig. 2.16(b)] show that the SG4 phase plates produce significantly flatter profiles than the previous phase plates.

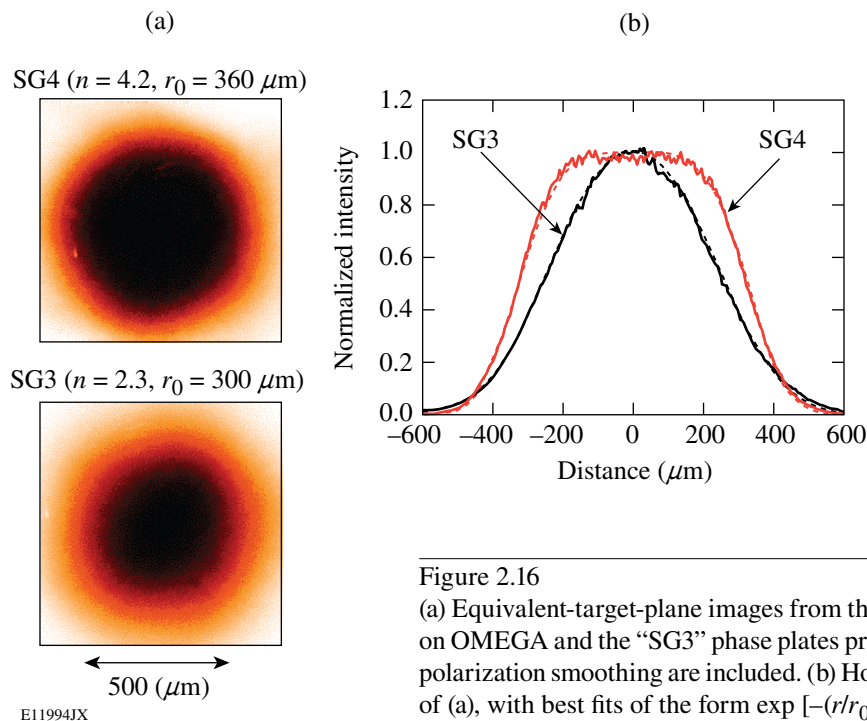


Figure 2.16

(a) Equivalent-target-plane images from the “SG4” phase plates currently used on OMEGA and the “SG3” phase plates previously used on OMEGA. SSD and polarization smoothing are included. (b) Horizontal lineouts through the images of (a), with best fits of the form  $\exp[-(r/r_0)^n]$  shown dashed.

The focal spot from an SG4 phase plate has been characterized outside the focal plane. As seen in Fig. 2.17(a), the azimuthally averaged beam initially becomes less flat as the distance from the best focus increases to 5 mm. As  $z$  increases farther, the profile becomes flatter and then approaches the near-field irradiance profile for very large focal shifts. The measured profiles agree well with ray-tracing simulations.<sup>14</sup> The only significant deviation occurs in a small area near the center of the beam for  $z = 5$  mm, where nonuniformities resulting from phase errors in the near field (not included in the calculation) may not be averaged out effectively; also, speckle in the beam makes it difficult to define a meaningful azimuthal average near the center of the beam. The width of the beam, defined on the basis of the radius encircling 90%, 95%, or 99% of the laser energy, is shown as a function of  $z$  in Fig. 2.17(b).

The profiles shown in Fig. 2.17(a) are for a beam without SSD or polarization smoothing. The  $z = 0$  lineout is a little narrower than the SG4 lineout shown in Fig. 2.16(b) because the angular dispersion associated with SSD (imposed by diffraction gratings early in the laser system) and the far-field displacement between the two polarization components resulting from polarization smoothing cause the beam envelope to be broadened in both directions.

A set of 40 phase plates has recently been made for indirect-drive experiments on OMEGA. These phase plates are designed to reach a peak envelope intensity of  $10^{15}$  W/cm<sup>2</sup>. Their shapes are elliptical to provide approximately circular spots when projected onto the laser entrance hole of the hohlraum target. A measured far-field intensity distribution and beam envelope are shown in Fig. 2.18. These phase plates were successfully fabricated by the Zygo Corporation<sup>15</sup> in collaboration with the Lawrence Livermore National Laboratory, using magnetorheological finishing.

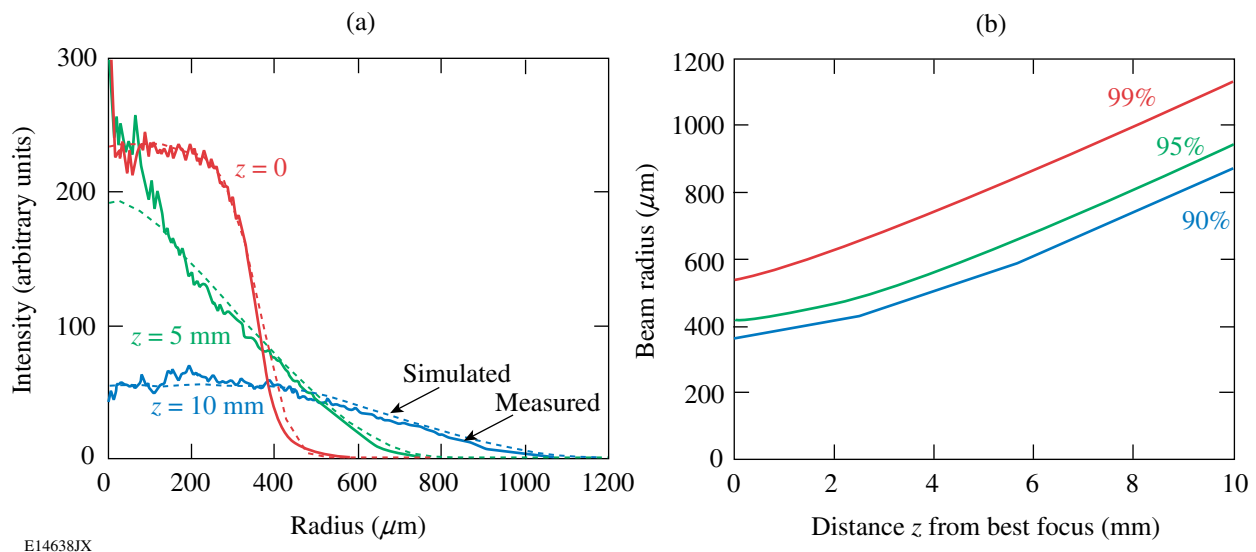


Figure 2.17

(a) Azimuthally averaged radial lineouts of an SG4 phase plate intensity distribution (without SSD or polarization smoothing) at three distances  $z$  from best focus. The dashed curves are ray-tracing simulations. (b) Radii of the SG4 beam as a function of  $z$  based on the 90%, 95%, and 99% encircled energy contours.

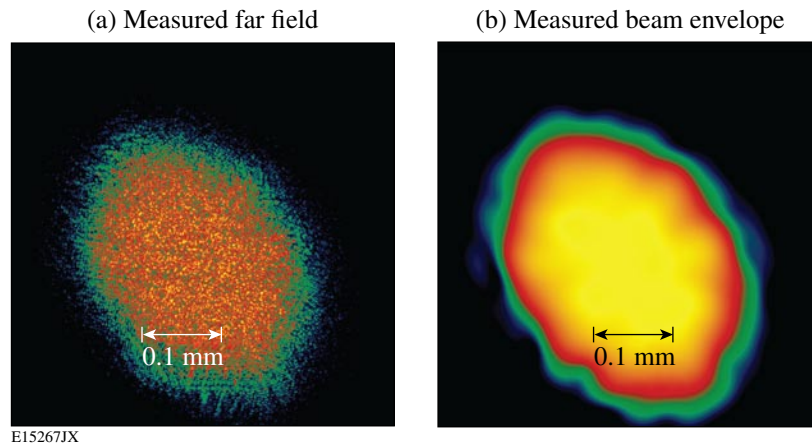
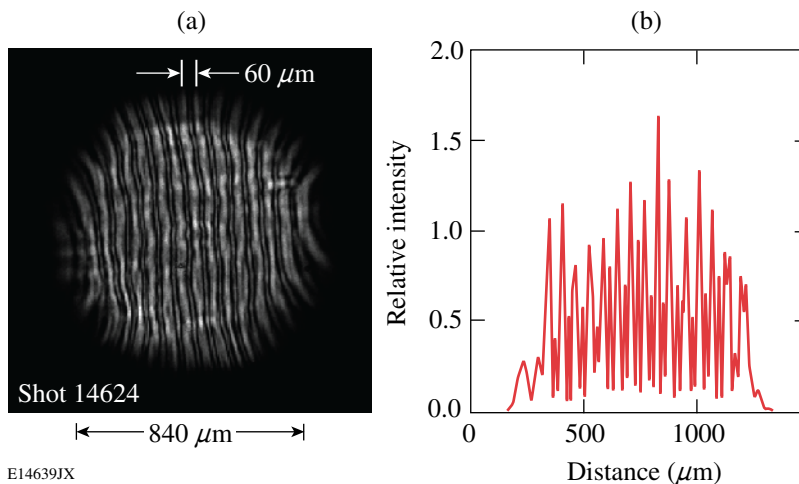


Figure 2.18  
 (a) Measured far field produced with the elliptical phase plate E-IDI-300 and (b) measured beam envelope. The average intensity  $I_{50}$  is  $1 \times 10^{15}$  W/cm<sup>2</sup>, the peak intensity  $I_{95}$  is  $3.8 \times 10^{15}$  W/cm<sup>2</sup>, the super-Gaussian power  $n$  is 4.1, the  $1/e$  minor diameter is 212  $\mu\text{m}$ , and the  $1/e$  major diameter is 290  $\mu\text{m}$ .

Several other phase plates are available for target experiments on OMEGA. “SG8” phase plates provide focal spots of diameter  $\sim 800 \mu\text{m}$  with a very flat central portion of diameter  $\sim 400 \mu\text{m}$ ; they may be approximated as super-Gaussians with  $r_0 = 412 \mu\text{m}$  and  $n = 4.7$ . These phase plates are used for many planar-target experiments including stability, equation-of-state, and long-scale-length-plasma experiments. A set of similar phase plates produces 800- $\mu\text{m}$ -diam, elliptically shaped spots relative to the beam axis so as to produce circular spots on target when used at irradiation angles of 23°, 48°, and 60°. A small number of phase plates with 100- $\mu\text{m}$  and 200- $\mu\text{m}$  diameter provide very high irradiance for plasma physics experiments. Another set of phase plates produces 300- $\mu\text{m}$ -diam, elliptically shaped spots for use at irradiation angles of 23° and 48°. Finally, a novel phase plate design has produced the one-dimensional pattern in the target plane shown in Fig. 2.19 for use in several laser-imprint experiments on OMEGA. Phase plates with intensity perturbations of 30- $\mu\text{m}$  or 60- $\mu\text{m}$  wavelength are available for studying hydrodynamic instabilities.



E14639JX

Figure 2.19  
 (a) Equivalent-target-plane image and (b) one-dimensional lineout of a phase plate designed to provide a 60- $\mu\text{m}$ -wavelength intensity perturbation.

### 2.3.4 Second-Harmonic and Fourth-Harmonic Capabilities

A second-harmonic ( $2\omega$ ) capability has been implemented on OMEGA. It is available by detuning the triplers in the frequency-conversion cell of one of the OMEGA beams (beam 25) and redirecting the beam to port P9 on the target chamber using kinematic mirrors. (A separate port was needed because a new,  $2\omega$  focus lens was required.) Beam pointing, focusing, energy diagnostics, and a dedicated  $2\omega$  phase plate (with a  $200\text{-}\mu\text{m}$  spot diameter) are included. The  $2\omega$  beam can be converted to the fourth harmonic ( $4\omega$ ) by inserting a KDP quadrupler into the beam. A half-wave plate can be inserted into the  $4\omega$  beam to rotate its polarization to the desired orientation.

The  $2\omega$  beam is used for  $2\omega$  laser–plasma interaction experiments,<sup>16–18</sup> and the  $4\omega$  beam is used as a probe for Thomson-scattering experiments.<sup>19,20</sup> The  $2\omega$  and  $4\omega$  capabilities were installed as a collaborative effort between LLNL and LLE and were funded through LLNL's LDRD (laboratory-directed research and development) program. A full-aperture backscattering station operating at  $2\omega$  has also been implemented, together with Thomson-scattering diagnostics operating at  $4\omega$  that measure the absolute, spectrally resolved scattering from the target.

### 2.3.5 UV Spectrometer

A 63-channel, ultraviolet (UV) spectrometer<sup>21</sup> has been installed on OMEGA. This instrument replaces the previous spectrometer, which was limited to four beams. With an input energy of  $1\ \mu\text{J}$  per channel, 63 spectra can be acquired simultaneously on a single multibeam laser shot. The spectrometer has a dispersion at the detector plane of  $8.6 \times 10^{-2}$  picometers (pm)/ $\mu\text{m}$  and a spectral window of 2.4 nm at  $\lambda = 351$  nm. The wavelength resolution varies from 2.5 pm at the center of the field of view, three times better than that of the previous spectrometer, to 6 pm at the edge.

The primary function of the spectrometer is to diagnose the spectral broadening that is imposed on the OMEGA laser beams as part of the implementation of two-dimensional smoothing by spectral dispersion (SSD).<sup>6,12</sup> To maximize the available bandwidth, limited by the acceptance bandwidth of the potassium-dihydrogen-phosphate (KDP) crystals used for frequency tripling,<sup>22</sup> a second tripler crystal was added to each OMEGA beam, with the two tripler crystals angularly detuned by specified amounts with respect to the direction of propagation.<sup>23,24</sup> To maintain the highest conversion efficiency, the angular detuning of these crystals must be controlled to approximately  $100\ \mu\text{rad}$ . Mistuned crystals decrease the UV conversion efficiency and change the spectra of the converted light. While a procedure has been developed to tune the crystals by monitoring the conversion efficiency over a series of nine laser shots, the tuning can drift with time and checks of individual beamlines have revealed that the spectra are different. One goal of the new spectrometer is to make it possible to determine the tuning state of all the crystals on a single shot and to correct any misaligned crystals, thereby improving the power balance on OMEGA. An improved tuning procedure based on the UV spectrometer is being implemented.

A secondary motivation for building the spectrometer was the need to understand and control an intrinsic source of bandwidth on the OMEGA system due to self-phase modulation. If the intensity of a laser pulse varies in time, the nonlinear index of refraction produces a time-varying

phase.<sup>25</sup> This phase, known as the “*B* integral,” is equal to  $\int n_2 I ds$ , where  $n_2$  is the nonlinear index of refraction,  $I$  is the laser intensity,  $ds$  is an element of the path length, and the integral is over the entire beam path. When this phase varies in time, it produces a frequency shift.

These dual missions determined the specifications of the spectrometer. The spectrometer acquires complete spectra for all OMEGA beams on a single shot. To allow for the possibility of corrupt channels and to incorporate *in-situ* wavelength calibration, the system was constructed with 63 channels. Each channel spans a 0.6-nm bandwidth around  $\lambda = 351$  nm to view the entire SSD-broadened spectrum. With SSD turned off, the spectrometer can resolve spectral features of the order of 3 pm. The light that feeds the spectrometer comes from the small fraction of the light from each beamline that is split off for diagnostics purposes. To accommodate total UV energies per beamline of 10 to 500 J, the detection system is designed to handle signal levels that vary by a factor of 50, from 20 nJ to 1  $\mu$ J.

A schematic of the spectrometer is shown in Fig. 2.20. Light from a 63-channel fiber bundle passes through a  $3 \times 21$  slit array and a collimating lens pair before reflecting off three mirrors and three gratings. A second lens pair focuses this light onto a CCD. Many spectrometers use reflective optics to image the light through the instrument to avoid chromatic aberrations associated with the refractive elements. However, since this instrument has a limited spectral range, the spectral dispersion in the fused silica can be ignored. The advantage of using refractive optics is that the imaging can be done on axis, allowing a wider field of view than possible with off-axis imaging. The large field of view is required because the spatial extent of the fiber head is  $21 \times 25$  mm<sup>2</sup>.

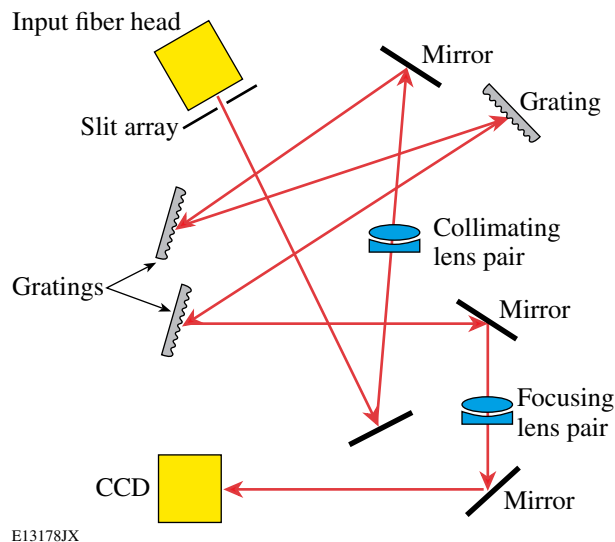
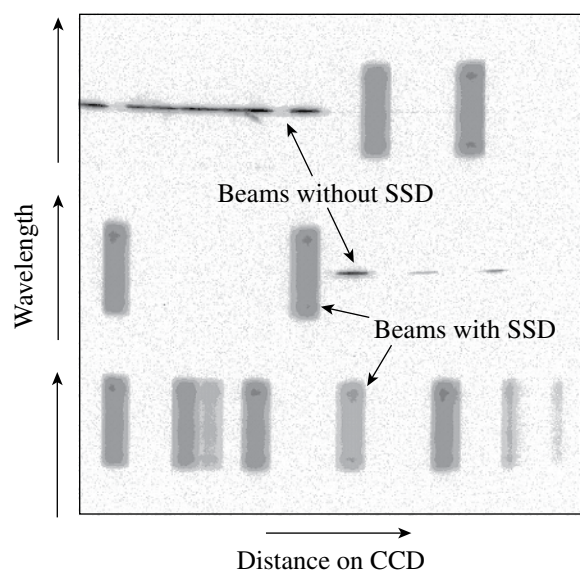


Figure 2.20

Schematic of the 63-channel UV spectrometer. The slit array (one slit per channel) is imaged onto the CCD with spectral dispersion in one direction.

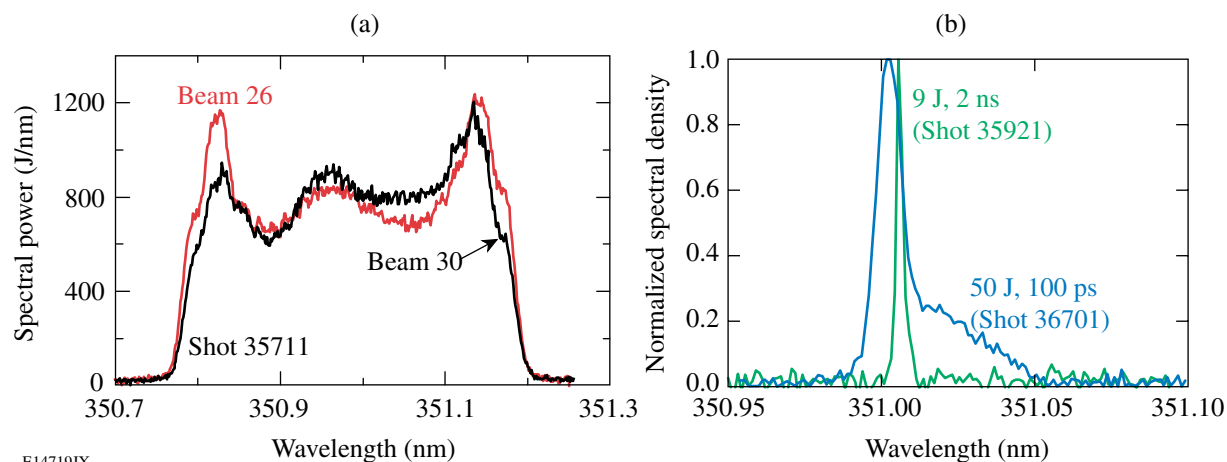
A typical CCD image from the UV spectrometer is shown in Fig. 2.21. The image includes spectra for some beams with SSD and some without. The SSD beams, represented by large rectangular spectra (dispersed in the vertical direction), have approximately the same energy and 80 times the bandwidth of the narrow-linewidth beams. The 37 missing channels would be interspersed among the 23 channels shown.

Some representative spectra obtained from images such as those illustrated in Fig. 2.21 are shown in Fig. 2.22. The spectra of Fig. 2.22(a) are from beams with 1-THz SSD and show the characteristic three peaks of the two-tripler frequency-conversion system used on OMEGA.<sup>24</sup> They are produced from a region of the CCD with  $570 \times 100$  pixels by averaging along the 100-pixel



E13175JX

Figure 2.21  
A UV-spectrometer CCD image from shot 37038 showing 23 of the 60 beams, some with and some without SSD. The density is logarithmic.



E14719JX

Figure 2.22

(a) Spectra from two beams from a single shot with 1-THz SSD. (b) Spectra from a low-intensity pulse (9 J, 2 ns) and a high-intensity pulse (50 J, 100 ps), both recorded on beam 61, the channel with the highest resolution.

spatial direction and show that the spectrum differs from beam to beam. Since the detailed shapes of these spectra depend on the tripler-crystal alignment, the UV spectrometer can potentially aid in crystal tuning.<sup>26</sup>

In Fig. 2.22(b), two spectra taken without SSD are compared. The narrow spectrum, from a low-intensity pulse, is expected to be transform limited and represents the instrument response to a single frequency. The other spectrum, from a high-intensity pulse, illustrates the largest allowed intrinsic spectral broadening on the OMEGA system (due mainly to the *B* integral). Larger bandwidths can damage the system. The spectrum is asymmetrical because the rising edge of the pulse, which generates the red-shifted wavelengths, is faster than the falling edge, which generates the blue-shifted wavelengths.

### 2.3.6 Target Chamber Tritium Recovery System

To support high-activity cryogenic DT targets (~0.24 Ci each) while maintaining tritium emissions within environmental release limits (2.2 Ci per year), a Target Chamber Tritium Removal System (TC-TRS) has been added to the OMEGA target chamber's vacuum-pump exhaust line. This exhaust line also serves the Cryogenic Target Handling System Cart Maintenance Room and tritium scrubber.

The TC-TRS uses molecular sieves to collect tritiated water (HTO) from the exhaust effluent before transferring the gas to the building exhaust stack. A catalytic reactor converts tritium gas (HT) to HTO prior to the molecular sieve stage. The molecular sieves are automatically regenerated *in situ*. Three molecular sieve beds are installed, allowing continuous availability even during regeneration cycles. Input and output tritium and moisture monitors verify performance of the removal system and support a predictive maintenance plan that ensures high reliability and availability. To date, bed regenerations have yielded ~80 liters of tritiated water condensate containing 6 Ci of activity. The TC-TRS traps tritium in the exhaust from mechanical vacuum pumps used on the OMEGA target chamber.

The TC-TRS also receives effluent from the tritium scrubber. This is a small system that is dedicated to removing concentrated elemental tritium in the effluent from OMEGA cryogenic vacuum pump regenerations. Most of the tritium released into the target chamber is collected by these pumps. The tritium scrubber employs zirconium-iron at elevated temperatures to reversibly adsorb elemental tritium. Effluent from the scrubber is then polished by the TC-TRS to remove residual tritium.

The target chamber's vacuum system and the auxiliary vacuum systems (e.g., for the ten-inch manipulators and the target positioner) have been modified to support decontamination cycles of the target chamber and antechambers. Modifications include the addition of purge-gas intake valves; a direct, atmospheric pressure path to the TC-TRS; and software and operating procedures to support automated decontamination of the target chamber and its antechambers. This operating mode allows equipment that has been exposed to tritium in the target chamber's vacuum envelope to be safely serviced while minimizing personnel exposure to tritium and preventing contamination of the Target Bay environment.

The TC-TRS also receives effluent from Moving Cryostat Transfer Carts (MCTC's) as the result of decontamination activities in the Cart Maintenance Room. MCTC's are subjected to vent/pump cycles using room air to remove tritium from internal spaces. Effluent from the pump-out portion of the cycle is directed to the TC-TRS. Approximately 100 cycles are required over a period of two days to reduce concentrations to acceptable maintenance levels. Highly contaminated MCTC's have been observed to yield as much as 500 millicuries during the decontamination process.

The TC-TRS modification allows OMEGA to shoot high-activity DT targets while providing a high degree of personnel safety and ensuring minimal release of tritium to the environment.

### **2.3.7 Software Improvements for OMEGA Operations**

OMEGA operations are supported by an array of software and database applications that capture the principal investigator's shot specifications, categorize shots by their impact on the operational configuration, orchestrate the shot itself, collect and archive shot data, and provide data reduction for initial assessments. This system includes executive-level programs that communicate on an internal computer network and coordinate the activities of all shot-related programs. For example, the "Shot Executive," which is at the top of the executive-level hierarchy and operated by the Shot Director, propagates messages that transition the entire laser system from one well-defined state to the next. As the shot approaches, a precision hardware timing system counts down, fires the laser, and triggers all diagnostics for data acquisition.

During the period FY03–FY07, the software suite has continued to evolve as new capabilities have been added to the OMEGA Laser System and as computer-aided setup and monitoring have been applied to existing elements. The software framework has been extended and improved to accommodate joint shots using OMEGA EP. Significant improvements have been realized in the areas of object-oriented design; intra-program communication facilities; code development that employs mature, industry-recognized libraries; and source code control. The new laser system will employ the same operational concepts as used on OMEGA and, from the outset, will benefit from the software maturity of the older system.

While the two systems use separate databases for configuration and shot-data archiving, a common shot request system will serve to link the databases for shot preparation and data retrieval. The same executive-level software modules are used in both systems so that the "look and feel" of functions, terminology, and the user interface are shared.

### **2.3.8 Support for External Users**

Approximately 50% of OMEGA shots are currently assigned to outside users. The support for these users is virtually the same as for LLE users and is centered around shot scheduling and planning, the integration of user-developed diagnostics, and user access to shot data.

(a) *Shot Planning*

A yearly OMEGA schedule is formulated three months before the beginning of the fiscal year. This allows principal investigators to prepare and submit experimental proposals to the Facility Advisory and Scheduling Committee (FASC) for approval two months in advance of the experiment. Target requests are typically made to the target support contractor (GA) four months in advance of the planned experiments.

Subsequently, the communication of the detailed requirements and specifications is accomplished through an automated shot request form (SRF) prepared by the principal investigator for each shot. Video conferences or face-to-face meetings between LLE Operations Group leaders and external users are required both two weeks and one week prior to a campaign to review the SRF's. This ensures the accurate communication of user requirements and system capabilities.

(b) *Support for User-Developed Equipment*

A large number of instruments developed by external users have been deployed successfully on OMEGA. To permit the efficient integration of these subsystems, LLE provides standardized logistical support, a well-defined and reviewed entry and integration path, and extensive local support. Logistical support for external-user-developed diagnostics includes a standard interface into the target chamber [the ten-inch manipulator, or TIM, power and trigger feeds, a calibrated timing monitor system, and network connections and software interfaces to the OMEGA Control System. As necessary, on-site setup and calibration facilities are implemented to support the operation of diagnostics developed by external users.

The smooth integration of instruments developed by external users is ensured by a uniform development/entry path for equipment being deployed on OMEGA. This procedure, which includes a Critical Equipment Qualification Checklist (CEQC), supplements the developer's project management program. The CEQC provides a series of waypoints and reviews with key LLE personnel to ensure that the new equipment will interface with OMEGA, will perform to required specifications, will not inhibit other system functions, and will not pose a safety hazard to personnel or other equipment on OMEGA.

The CEQC procedure ensures readiness of the new equipment by disseminating vital information about the instrument's operation. This is accomplished through written procedures and documentation and the training of operations personnel. Fit and function tests outlined by the CEQC verify proper operation of the new equipment.

Frequently the expertise of the external user's technical staff is critical to the operation of the user's equipment. It has been necessary to provide for the qualification of these personnel to operate and repair their equipment while it is installed on OMEGA. This program, designated Outside User's Training, ensures that the external user is aware of relevant safety and system issues prior to working in the OMEGA environment.

(c) *Data Access*

Standard shot data (e.g., laser performance information) are presented to the user in a package following each shot. Film records are available directly to the user.

Two means of accessing digital data are available. While on-site, the user may be issued an account that allows direct access to relevant data files. On- and off-site, the user may access authorized data files using a Web-based interface.

**2.3.9 Operational Statistics**

OMEGA capabilities, efficiency, and effectiveness have continued to improve, and OMEGA continues to be NNSA's principal laser facility for performing high-energy-density physics experiments.

At the start of FY03, to accommodate increased demand from the national laboratories and the outside user community, LLE converted ten normal weeks (including three 12-hour shot days) into "super-extended" weeks (including two 12-hour shot days, one 16-hour day, and one 8-hour day). This allowed OMEGA to increase its nominal annual shot rate to 1450. Figure 2.23 shows the number of OMEGA target shots per year since commissioning and their breakdown by user.

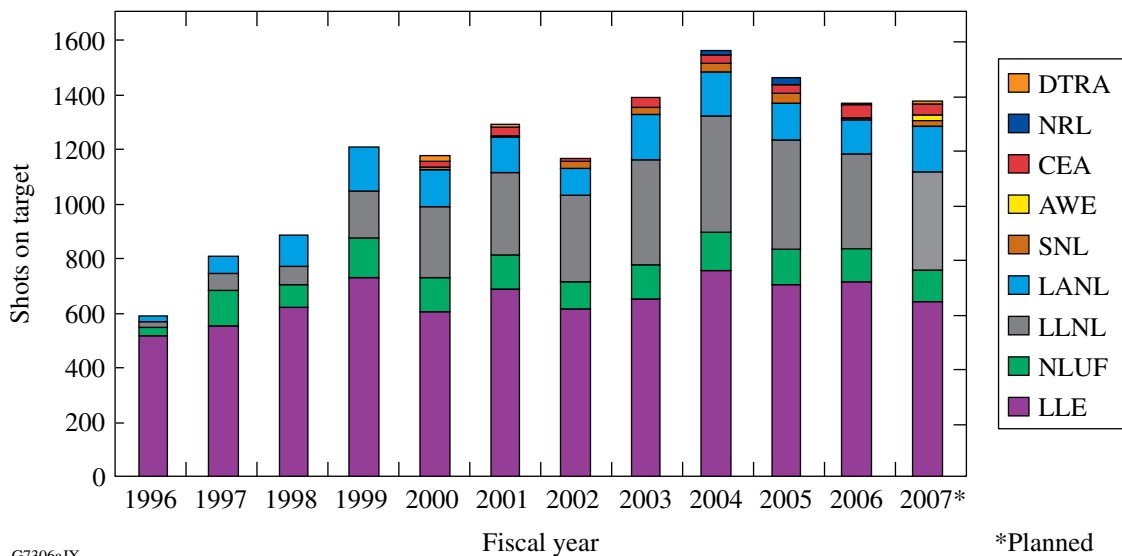
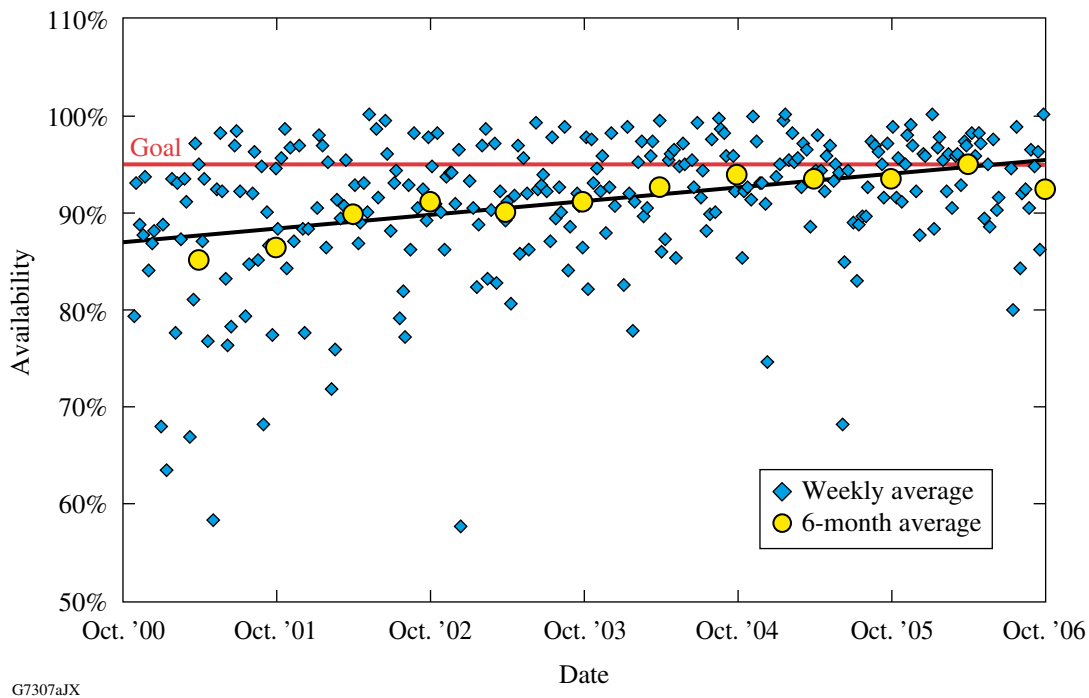


Figure 2.23  
 OMEGA target shot production FY96 to FY06. (DTRA: Defense Threat Reduction Agency; NRL: Naval Research Laboratory; CEA: Commissariat à l'Énergie Atomique; AWE: Atomic Weapons Establishment; SNL: Sandia National Laboratories; LANL: Los Alamos National Laboratory; LLNL: Lawrence Livermore National Laboratory; NLUF: National Laser Users' Facility; LLE: Laboratory for Laser Energetics)

A total of 1558 target shots were taken on OMEGA in FY2004. This was a record for OMEGA and is the highest number of target shots ever taken in a single year by a comparable-sized facility. Over 50% of these shots were conducted for external users including the National Laboratories (LLNL, LANL, and SNL).

OMEGA’s reliability is measured by an availability statistic that quantifies the percentage of time during the scheduled operating hours that the system was ready for use. For the system availability to be 100%, the first daily target shot must occur by 9 AM with subsequent shots each hour thereafter. Each delay is categorized by subsystem and reason, and analysis is performed to identify operational and system improvements. Figure 2.24 tracks the system availability over the past ten years. The trend in the six-month averages (yellow circles) indicates that the goal of 95% has been achieved.

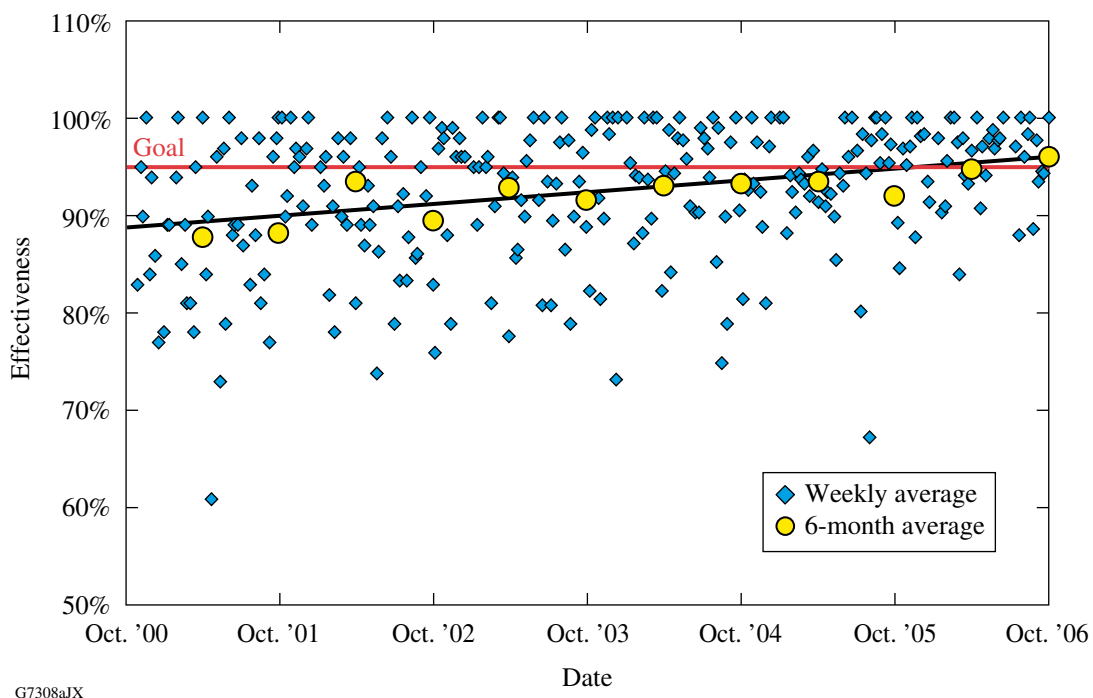


G7307aJX

Figure 2.24  
Average OMEGA system availability per shot week from October 2000 to September 2006. The yellow circles indicate averages over the previous six months and show progress toward the goal of 95% (red line).

OMEGA's experimental effectiveness is measured by the principal investigator evaluating the performance of the laser (energy, pulse shape, and timing), experimental diagnostics, and the target after each shot. The effectiveness of each shot is reviewed in real time to determine issues that require attention. Additionally, these statistics are analyzed to determine systematic issues to be addressed. Figure 2.25 tracks the experimental effectiveness over the past ten years. Again, the trend in the six-month averages indicates that the goal of 95% has been achieved.

Overall, the statistics presented in this section illustrate that OMEGA operations are meeting the required shot schedules and setting a high standard for performance and reliability.



G7308aJX

Figure 2.25

Average OMEGA experimental effectiveness per shot week from October 2000 to September 2006. The yellow circles indicate averages over the previous six months and show progress toward the goal of 95% (red line).

## 2.4 OMEGA EXTENDED PERFORMANCE (EP) LASER SYSTEM

The OMEGA Extended Performance (EP) Laser System (Fig. 2.26) will provide a major enhancement to the experimental facilities at LLE. It will be completed in April 2008. It includes four NIF-scale beamlines, two of which can be compressed to short pulse (1 to 100 ps) in a grating compressor chamber. The compressed pulses can be propagated to the OMEGA target chamber or the OMEGA EP target chamber. Alternatively, all four OMEGA EP beams can be frequency converted to the third harmonic and propagated to the new chamber as long-pulse beams. The many combinations of beam paths, pulse widths, and wavelengths built into the OMEGA EP design greatly increase the diversity of experiments that can be performed at LLE, including short-pulse backlighting, fast-ignition physics, high-energy-density physics, and ultra-intense laser-matter interactions. It is possible to send two compressed 1053-nm pulses and two long-pulse, 351-nm pulses into the OMEGA EP target chamber on the same shot for short-pulse interactions with preformed plasmas.

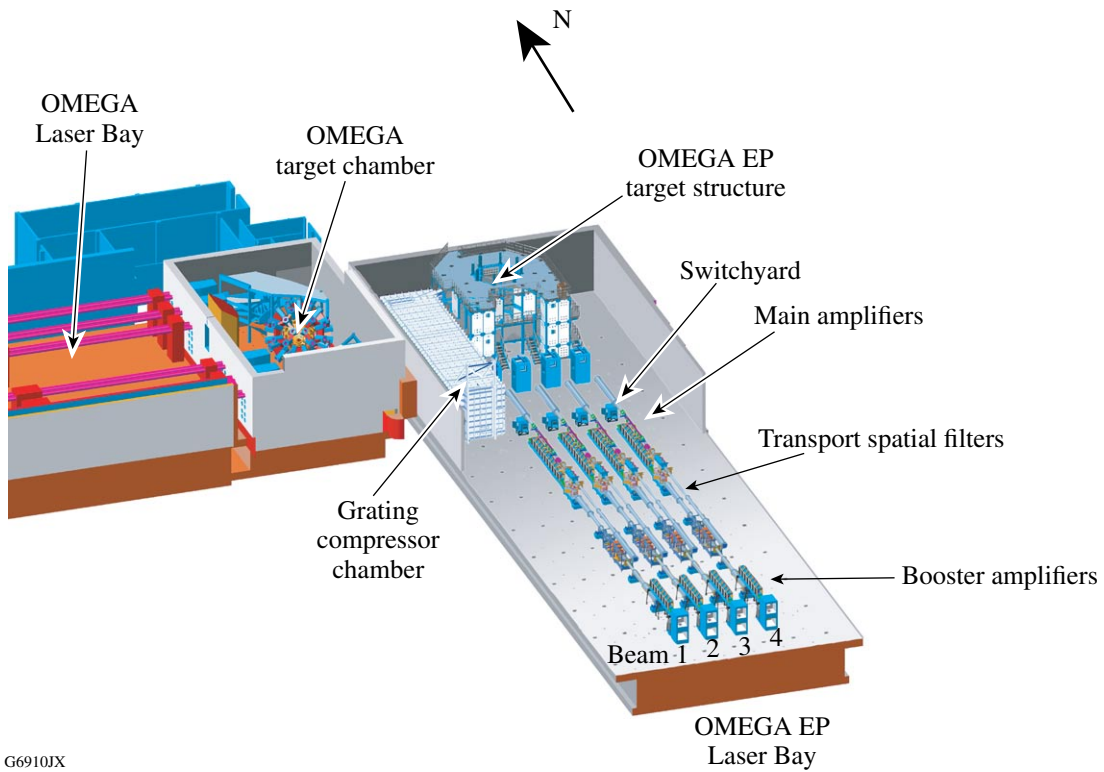
This section describes the OMEGA EP Laser System.<sup>27,28</sup> Section 2.4.1 provides an overview of the system. The performance specifications in the various possible configurations are given in Sec. 2.4.2. A more detailed description of the system is given in Sec. 2.4.3, including laser sources, amplifiers, and power conditioning; the beamlines and their alignment and diagnostics systems; the pulse compression of the IR beams and the frequency conversion of the long-pulse beams; and the target chamber and experimental systems. Control systems are covered in Sec. 2.4.4 and operations in Sec. 2.4.5.

### 2.4.1 System Overview

This section provides an overview of the OMEGA EP Laser System. The new facility (Fig. 2.26) is housed in a building attached to the south side of the existing LLE building that was provided by the University of Rochester. The OMEGA EP target chamber is due east of the existing OMEGA target chamber. The most significant structural feature of the building constructed for the new laser system is an 83-ft-wide, 263-ft-long, one-story-high (14-ft) concrete box-beam. The first and second floors of this structure are 30-in.-thick slabs that serve as a rigid optical table. The lower floor rests on a bed of compacted gravel and is structurally independent from the building that encloses it. This structural approach was based on the success of the original OMEGA facility design. It provides the high degree of vibration isolation that is necessary for precision laser operations.

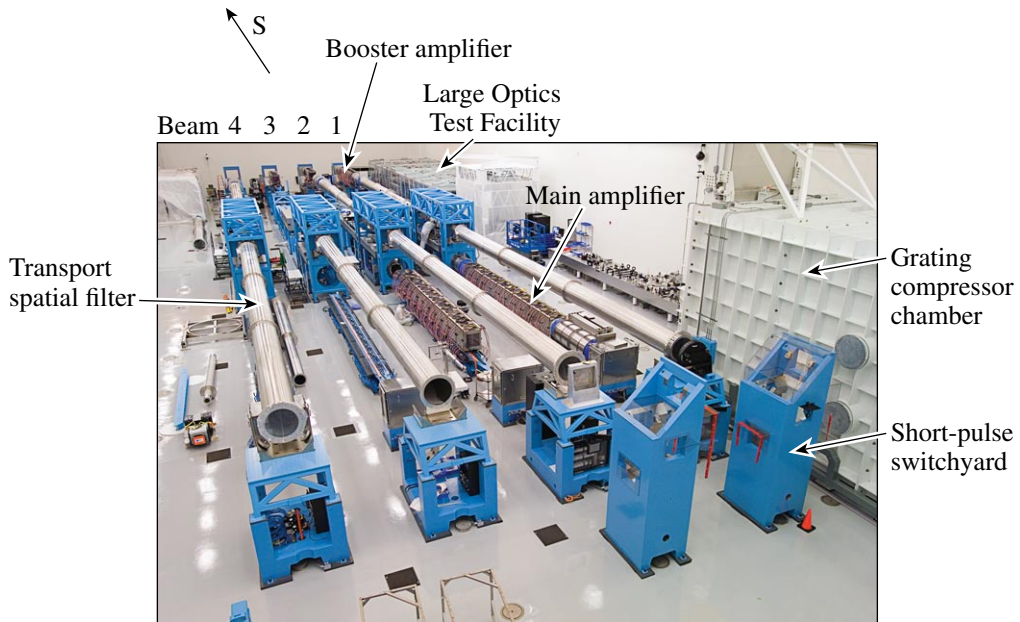
The area inside the box-beam on the lower level contains the Diagnostic Bays, the Sources Bay, and two Capacitor Bays that house the laser-amplifier power conditioning system. The Sources and Laser Bays are climate controlled and designed to operate as Class-1000 clean rooms but perform to nearly Class-100 conditions. A control room is provided on the second floor to the east of the Laser Bay and a viewing gallery is located at the north end of the Laser Bay.

The four laser beamlines are arranged horizontally across the floor to the south of the grating compression chamber and the target chamber and its supporting structure (Figs. 2.26 and 2.27). Beams 1 and 2 may be diverted by mirrors in the short-pulse switchyard into the grating compressor chamber and temporally compressed to short-pulse IR beams.



G6910JX

Figure 2.26  
 A simplified view of the OMEGA EP Laser Bay showing the four beamlines, grating compressor chamber, and target area structure relative to the OMEGA Laser System.



G7534JX

Figure 2.27  
 OMEGA EP beamlines as seen from the target area structure looking south (November 2006).

A schematic diagram of the main components of a beamline is shown in Fig. 2.28. The system architecture is modeled on the National Ignition Facility (NIF).<sup>29</sup> Each beamline is “folded” into two levels: an upper level that includes a 7-disk booster amplifier and transport spatial filter and a lower level that forms a cavity between the cavity end mirror to the south and the deformable mirror. The cavity includes an 11-disk main amplifier, a cavity spatial filter, and a plasma-electrode Pockels cell (PEPC). The deformable mirror corrects wavefront errors in the laser pulse that originate from aberrations in the optics and from prompt-induced distortion of the laser disks produced when the amplifiers fire. The PEPC is an electro-optical switch that uses polarization rotation to trap the laser pulse in the cavity, providing an additional double pass through the main amplifier to increase the gain.

The seed laser pulse (generated in the Laser Sources Bay) is injected into the transport spatial filter via a periscope. For short-pulse experiments in either target chamber, the seed pulses of Beams 1 and/or 2 are generated as  $\sim 2.4$ -ns chirped pulses using optical parametric chirped-pulse amplification (OPCPA). The injected pulse passes through the booster amplifier and is reflected off the fold mirror to a Brewster-angle polarizer (POL1 of Fig. 2.28) and into the main amplifier. The pulse makes two round-trips through the cavity to gain the required energy, then returns through the booster amplifier and transport spatial filter, and propagates to the switchyard. In the switchyard (Fig. 2.29), the beam is directed into the grating compressor chamber for temporal pulse compression or to frequency-conversion crystals (FCC’s) for conversion to the UV. A second polarizer (POL2 of Fig. 2.28) is inserted between the PEPC and the cavity spatial filter during short-pulse operation to prevent light reflected from the target from re-entering the main amplifier.

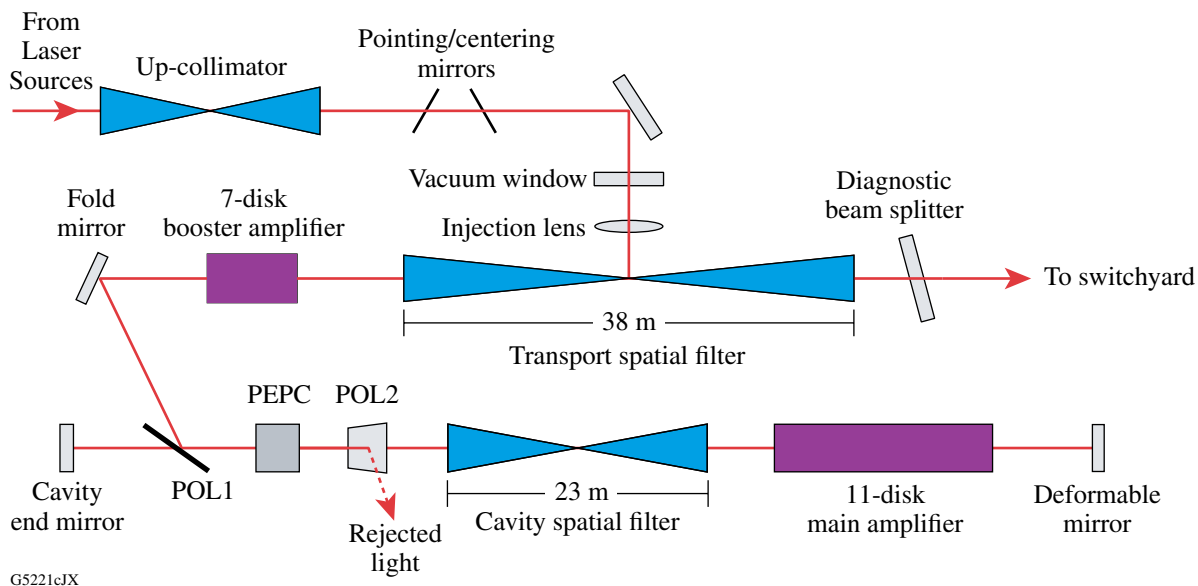


Figure 2.28

Optical components for the injection and amplification portions of an OMEGA EP beamline (PEPC: plasma-electrode Pockels cell; POL: polarizer). Beamlines 3 and 4 do not have short-pulse capability and therefore do not require POL2.

Depending on the individual beamline and experimental conditions, the amplified pulse emerging from the transport spatial filter may take one of several paths, as shown in Fig. 2.29. For short-pulse experiments, Beam 1 and Beam 2 may be routed to the upper and lower compressor, respectively, in the grating compressor chamber, where four matched multilayer-dielectric tiled grating assemblies temporally compress the pulse. A deformable mirror after the fourth tiled grating assembly provides static wavefront correction, primarily for grating phase errors. After passing through their individual compressors, the beams can be co-aligned through a polarizing beam splitter known as

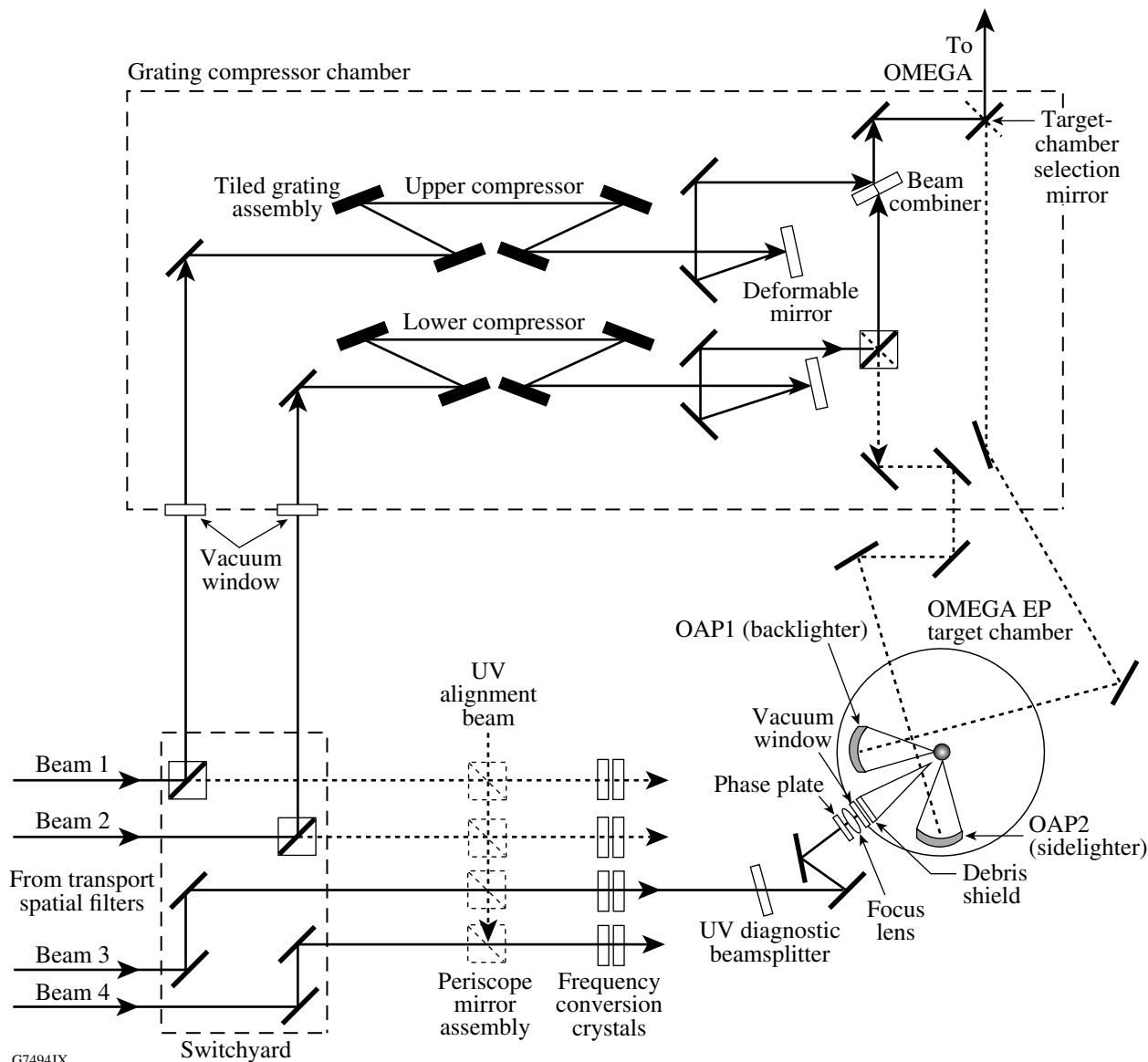


Figure 2.29  
 Beam paths through the switchyard, grating compressor chamber, and frequency-conversion crystals to the OMEGA and OMEGA EP target chambers. The short-pulse beams in the OMEGA EP target chamber can be focused from orthogonal directions with off-axis parabolas OAP1 and OAP2.

the beam combiner. Beam 1 is reflected off this optic in *s* polarization while Beam 2 is transmitted in *p* polarization. The co-aligned beams are routed to one of the target chambers using the target-chamber selection mirror and focused using an *f*/1.8 off-axis parabolic mirror. Transport from the grating compressor chamber is in an evacuated beam transport tube connected to the target chamber being used. Alternatively, after the compressed pulses reflect off their respective deformable mirrors, the beam from the upper compressor may be directed to the OMEGA EP “backlighter” port and the beam from the lower compressor independently to the OMEGA EP “sidelighter” port. This allows targets irradiated by long-pulse, 351-nm beams to be radiographed from two orthogonal directions on the same shot and targets irradiated by the compressed, backlighter pulse to be radiographed by the sidelighter pulse.

### 2.4.2 System Performance Specifications

The short-pulse beams can be compressed to pulse widths in the range of 1 to 100 ps. The top-level specifications for these beams are given in Table 2.3 for (1) a 1-ps beam providing the maximum on-target intensity; (2) a 10-ps fast-ignition beam; and (3) a co-propagated channeling beam. For short-pulse backlighting, the pulse width and spot size depend on the requirements of the specific experiment.

The parameters in Table 2.3 arise because the system performance is limited by the damage threshold of the multilayer dielectric reflection gratings. The laser itself, even at the relatively short output stretched pulse length of 1.13 ns, is capable of producing >4.0 kJ of energy at the input to the compressor. The final grating is critical as it sees the fully compressed pulse and will damage first. At a 1-ps pulse duration the grating damage threshold is reduced, limiting the 1-ps beam to ~1 kJ. When Beam 2 is co-propagating with Beam 1, its pulse width at full energy is limited by the *B*-integral accumulated in the beam combiner in the grating compressor chamber, resulting in a power of 26 TW and a maximum on-target intensity of  $\sim 3 \times 10^{18}$  W/cm<sup>2</sup>. The co-propagated beam can be operated with a shorter pulse width provided that the energy is scaled to maintain constant power. The *B*-integral also reduces the focusability of the beam, leading to a spot radius of 20  $\mu$ m. A higher *B*-integral can be tolerated for experiments that require a larger spot radius.

Table 2.3: Performance parameters for the 1053-nm chirped-pulse-amplification beams. Note that the beams can be used for backlighting at all pulse widths from 1 ps up to 100 ps. When Beam 2 is not co-propagating with Beam 1, it has the same parameters as Beam 1.

Baseline performance	Beam 1		Beam 2
	Maximum intensity	Fast-ignition beam	Channeling beam co-propagated
Pulse width (ps)	1	10	100
Focal spot radius ( $\mu$ m)	10	10	20
Energy on target (kJ)	$\sim 1.0^{(a)}$	2.6	2.6
Intensity on target (W/cm <sup>2</sup> )	$\sim 3 \times 10^{20}$	$\sim 6 \times 10^{19}$	$\sim 3 \times 10^{18(b)}$

<sup>(a)</sup>Limited by the grating damage threshold at 1 ps.  
<sup>(b)</sup>Limited by the *B*-integral in the beam combiner.

The long-pulse performance parameters are given in Table 2.4. For the shorter pulse widths the energy is limited by *B*-integral considerations in the IR portion of the laser. For the longer pulse widths ( $\geq 4$  ns) the energy is limited by the damage threshold of high-reflector UV mirrors. Ongoing development will lead to the “potential” energies quoted.

Table 2.4: Performance parameters of the 351-nm long-pulse beams for flat temporal profiles (quantities refer to a single beam). The “baseline” UV energies are what can be obtained with existing technology. The “potential” UV energies are possible with reasonable optical technology developments. The quoted intensities are averages over the focal spot and use the baseline UV energies.

Pulse width (ns)	0.1	1.0	4.0	8.0	10.0
UV on-target energy (kJ):					
Baseline	0.25	2.5	3.7	4.5	5.0
Potential	0.25	2.5	4.8	6.0	6.5
Intensity ( $\text{W}/\text{cm}^2$ ) for 1-mm spot diameter	$3 \times 10^{14}$	$3 \times 10^{14}$	$1.2 \times 10^{14}$	$7 \times 10^{13}$	$6 \times 10^{13}$
Intensity ( $\text{W}/\text{cm}^2$ ) for 100- $\mu\text{m}$ spot diameter	$3 \times 10^{16}$	$3 \times 10^{16}$	$1.2 \times 10^{16}$	$7 \times 10^{15}$	$6 \times 10^{15}$

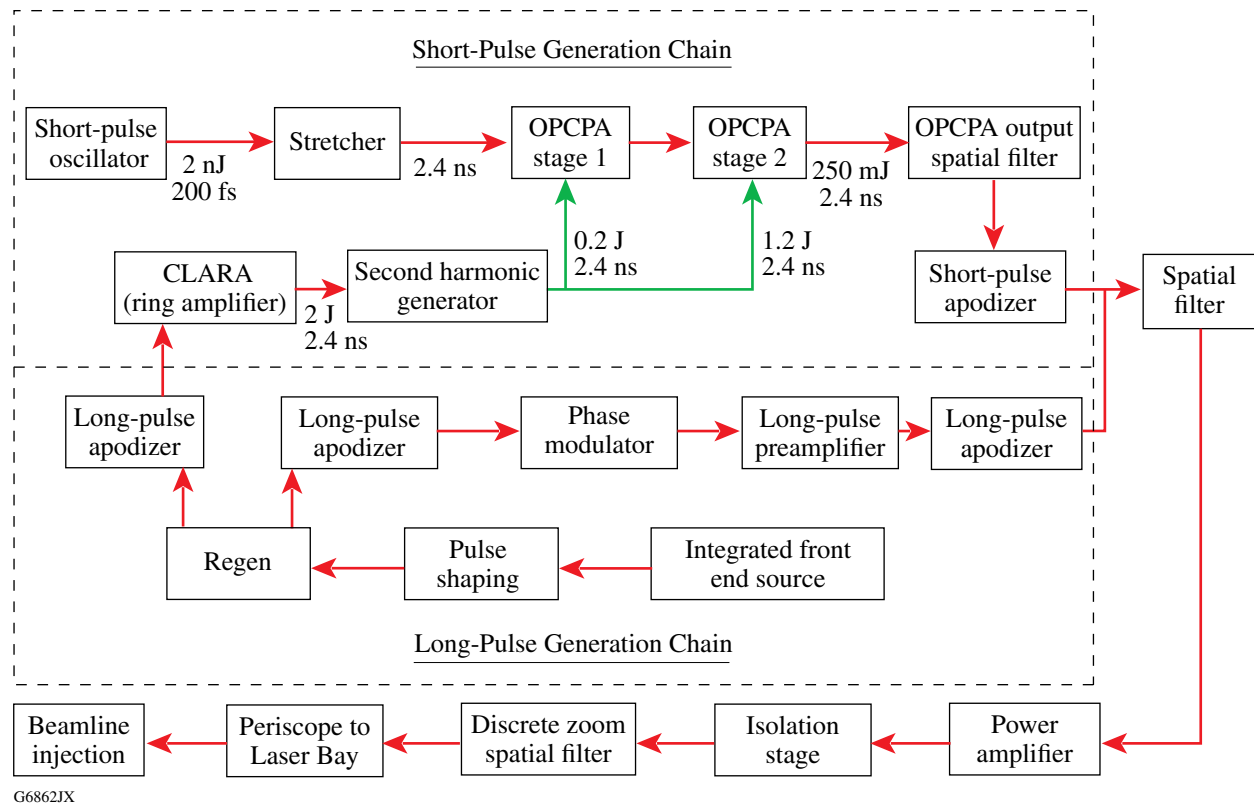
## 2.4.3 System Description

### 2.4.3.1 Laser sources

The Laser Sources Bay (Fig. 2.30) is located between the north and south capacitor bays on the first floor of the facility. Each beam in OMEGA EP has its own dedicated set of laser drivers, referred to as “laser sources.” Two different designs are used, one that produces both short and long seed pulses for Beams 1 and 2 (Fig. 2.31) and another that produces just long seed pulses for Beams 3 and 4 (Fig. 2.32). The long-pulse sources are largely based on existing OMEGA technology, with some modifications made to the regenerative amplifier (regen) to allow for pulse widths up to 10 ns. The short-pulse source is based on optical parametric chirped-pulse amplification (OPCPA)<sup>30</sup> to accommodate the required bandwidth.

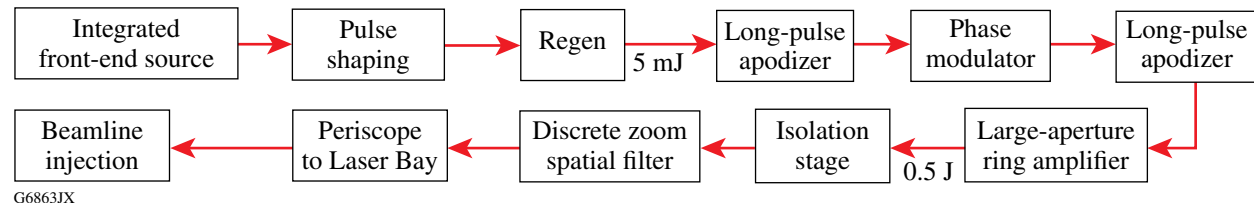


Figure 2.30  
Laser Sources Bay.



G6862JX

Figure 2.31  
Block diagram of the Laser Sources subsystem for Beams 1 and 2. These sources support both short-pulse (1 to 100 ps) and long-pulse (0.1 to 10 ns) operation.



G6863JX

Figure 2.32  
Block diagram of the Laser Sources subsystem for Beams 3 and 4. Long pulses of 0.1- to 10-ns duration are provided.

The short-pulse beams (Fig. 2.31) are seeded with a commercial Time Bandwidth Products<sup>31</sup> mode-locked oscillator that produces pulses with a  $\sim 200$ -fs duration and 8-nm bandwidth. These pulses are stretched to  $\sim 2.4$  ns (FWHM) in an optical system that uses a diffraction grating to impose different delays on different frequency components.<sup>32</sup> The resulting “chirped” beam is spatially shaped before being amplified using an optical parametric amplifier. This OPCPA stage is critical to the performance of the short-pulse beams. Attractive features of OPCPA include a broad gain bandwidth, high gain in a short optical path, and reduced amplified spontaneous emission. These features are exploited to preserve the bandwidth of the signal beam and provide a gain of  $\sim 10^9$ .

Optical parametric amplification is a nonlinear optical process wherein energy is down-converted from a (pump) beam of higher frequency into two beams of lower frequency, known as the signal and idler beams. For OMEGA EP, the pump beam is a frequency-doubled, 527-nm-wavelength, Nd:YLF laser. Lithium triborate (LBO) crystals are used as the parametric-amplification media. The signal beam is the input to each OPCPA stage, and the amplified signal beam is the output. The idler (1053 nm, like the signal) is generated in the LBO crystals and separated after each OPCPA stage. The sum of the (chirped) signal and idler frequencies equals the pump frequency for each temporal portion of the pulse. Optical parametric amplification is essentially the reverse of sum-frequency mixing, where two lower frequencies combine to form a higher frequency as in the third-harmonic frequency-conversion crystals, and is described by the same equations.<sup>33</sup> OPCPA is a special case of optical parametric amplification where the signal beam is frequency chirped.

The OPCPA pump laser starts with the same components as the long-pulse beam up to and including the regen and produces a beam that is flat in time. The beam emerging from the regen is spatially shaped using an apodizer to produce a square cross section to match the shape of the beamline optics. It is then amplified to  $\sim 2$  J/pulse in a high-repetition-rate (5-Hz) power amplifier (CLARA, crystal large-aperture ring amplifier<sup>34</sup>) and converted to 1.4-J, second-harmonic pulses using a frequency-doubling cell. The pump laser, flat in both space and time, is critical to the overall performance of the short-pulse beams. The OPCPA system has reliably produced energies of 400 mJ, exceeding the required energy of  $\sim 250$  mJ at 5 Hz in a 1-cm square beam. The beam emerging from the OPCPA stage passes through a second apodizer that adjusts its spatial shape to precompensate for the spatial gain variations in the disk amplifiers. It is then amplified using the same Nd:glass power amplifier that is used in long-pulse mode. This amplifier employs 15-cm disks similar to those used on OMEGA. The output of the OPCPA stage can also be propagated through the main portion of the laser system to establish optical alignment, verify compressor performance, and align the beam transport and focusing systems.

In long-pulse mode, the same systems are used for all beams (Figs. 2.31 and 2.32). The optical signal from the integrated front-end laser source originates from a commercial distributed-feedback fiber laser.<sup>35</sup> The oscillator produces a continuous wave output (at 1053.044 nm) that is sliced and shaped so that the desired on-target temporal profile will be generated after the nonlinear processes of amplification and frequency conversion. The pulse-shaping system uses either aperture-coupled-strip-line (ACSL)<sup>36</sup> or arbitrary-waveform-generator (AWG)<sup>37</sup> technology, depending on the pulse-length and bandwidth requirements for a given experiment. The temporally shaped pulse is amplified in a regenerative amplifier that produces  $\sim 5$ -mJ laser pulses at 5 Hz. An apodizer shapes the spatial profile of the beam from round to square. A small amount of frequency-modulation bandwidth is imposed to suppress stimulated Brillouin scattering that could otherwise threaten large optics such as the focus lenses. The bandwidth of  $0.5 \text{ \AA}$  ( $\sim 15$  GHz) is applied at a modulation frequency of 3 GHz using a bulk microwave lithium niobate ( $\text{LiNbO}_3$ ) modulator. The pulse is passed through a second apodizer to precompensate for spatial gain variations in the disk amplifiers. The pulse is further amplified in a Nd:glass power amplifier and expanded (to 57-mm square) in a spatial filter before injection into the transport spatial filter of the beamlines. The image plane of the long-pulse apodizer is relayed throughout the system.

The Laser Sources Bay includes diagnostics that are used for shot preparation and to acquire on-shot laser performance. Measured parameters include energy, temporal pulse shape, spatial profile, spectrum, prepulse contrast, and pulse timing. Energy measurements are accomplished with a centralized 100-channel instrument that is capable of measuring all of the 5-Hz signals, including all of the OPCPA pump-beam energies, and acquiring each of the beam energies on-shot. The energy diagnostic also acquires the beamline output energy from the beamline diagnostic packages. The energy diagnostic is calibrated using absorbing calorimeters at each sample point. Temporal pulse profiles are measured with a multichannel ROSS streak camera. Spatial profiles of the laser beams are captured electronically using 16-bit scientific cameras<sup>38</sup> that image the output plane of each of the laser sources. Beam spectral characteristics are measured with two six-channel, 1/2-meter spectrometers.<sup>39</sup> Prepulse contrast is measured by 7-GHz transient digitizers.<sup>40</sup> An optical time-domain reflectometer<sup>41</sup> uses photodiodes and an oscilloscope to measure stray light that returns to the laser sources after the pulses are delivered to the beamlines. This instrument is used to understand the sources of stray light and their relative magnitude.

#### 2.4.3.2 Laser amplifiers and power conditioning

The disk amplifiers and their associated power conditioning units are the basic building blocks of the laser, providing the necessary gain and resulting infrared energy. This section describes the booster and main 40-cm disk amplifiers that are located in the Laser Bay. The amplifiers use xenon-flash-lamp-pumped, Brewster-angle, Nd-doped glass disks<sup>42</sup> to provide high and relatively uniform gain across their aperture while avoiding thermal gradients transverse to the laser propagation direction. The basic staging of the 40-cm main and booster amplifiers is similar to that of the NIF.<sup>29</sup> This approach allows the OMEGA EP Laser System to use a modern multipass design and to benefit from experience gained on the Beamlet<sup>43</sup> and NIF lasers.

The OMEGA EP amplifiers differ from those of the NIF in three ways: (1) OMEGA EP uses a more modular mechanical-design approach than the highly integrated line-replaceable-unit concept<sup>44</sup> used in the NIF, reducing the dependence on expensive robotic handling equipment; (2) the OMEGA EP amplifiers use water-cooled flash lamps<sup>45</sup> to improve the thermal recovery rate; (3) OMEGA-like power conditioning is used to drive the amplifier flash lamps, taking advantage of the commonality with existing OMEGA parts, procurements, and training. A main amplifier consisting of 11 laser disks and a booster amplifier (Fig. 2.33) consisting of 7 disks are used for each of the four beamlines to produce sufficient energy to meet the program's science requirements.

The square beam shape matches the aperture of the amplifiers (Fig. 2.34), maximizing compatibility with the amplifier, adaptive optics, and other components developed for the NIF. The transverse beam cross section is close to being a "flat top" at the end of amplification to maximize the aperture fill factor<sup>46</sup> and the frequency-conversion efficiency, and to minimize the risk of damage due to excessive amplitude modulation. The beam fits within the 40-cm-sq clear aperture of the amplifiers and the beamline optics, with allowances for alignment tolerances and the lateral beam shift accumulated on each pass through the amplifier due to the angular multiplexing of the disks.

A measured contour plot of the gain within a typical disk is shown in Fig. 2.35(a). Significant variations in the horizontal direction are evident. A nominal gain of ~5%/cm is achieved at the center

of the disk, while the edges produce only ~3% to 4%/cm. The problem is magnified because the beam passes through 58 disks in the multipass configuration (two passes through the booster amplifier and four through the main amplifier). Figure 2.35(b) shows the normalized gain along a horizontal lineout after being raised to the 58th power, equivalent to the pulse traversing 58 laser disks.

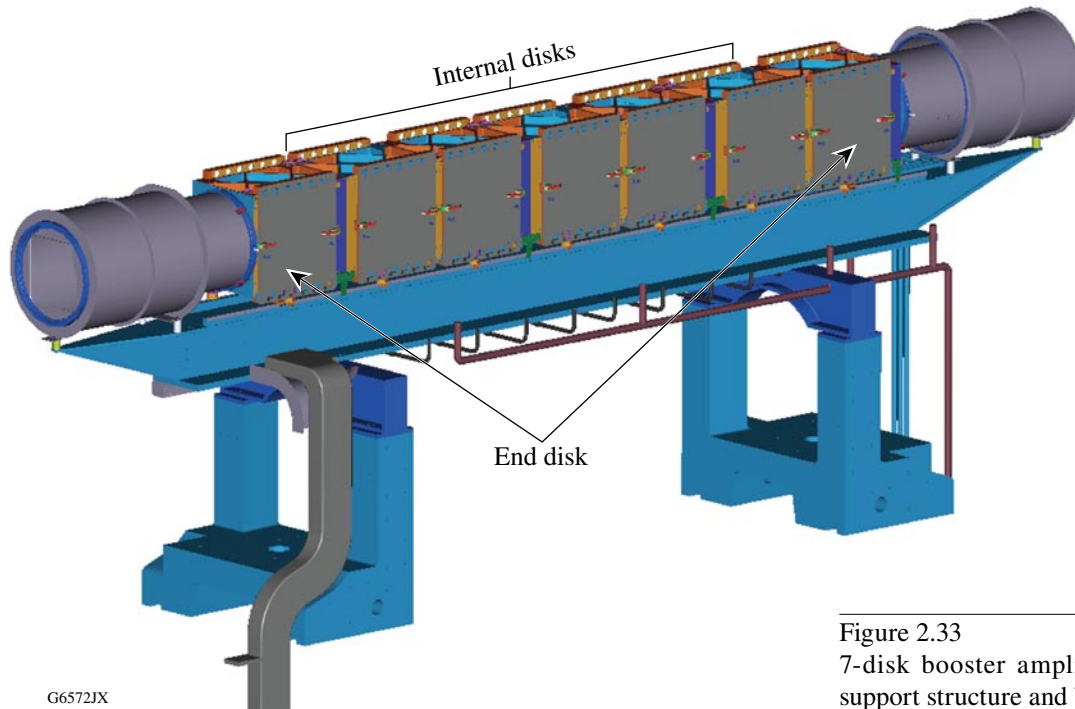


Figure 2.33  
 7-disk booster amplifier including support structure and beam tubes.

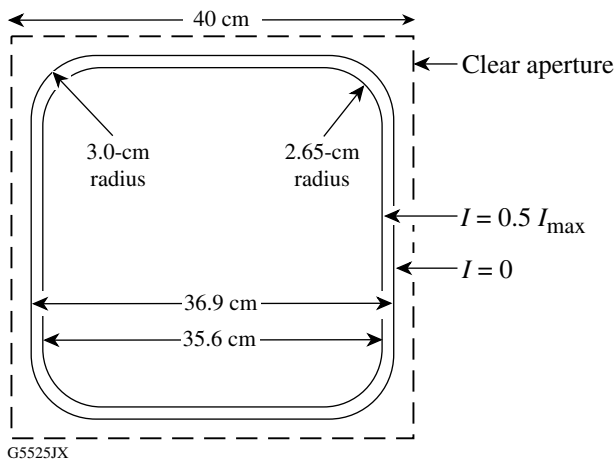


Figure 2.34  
 40-cm-amplifier beam cross section, showing contours of intensity  $I = 0$  and half the maximum intensity  $I_{\max}$ .

The injected pulse is apodized to compensate for this nonlinear gain profile. Figure 2.36 shows the calculated injection beam shape, with a peak-to-valley ratio of 12.3. The apodizers in Laser Sources, used primarily to make the beam square (following a 40th-order super-Gaussian), filter the energy in the center of the pulse to compensate for the high gain in the center of the amplifier. This ensures that the beams entering the pulse compressor and the frequency conversion crystals have flat spatial profiles.

Most features of the OMEGA EP amplifier modules are similar to those of OMEGA with one notable difference. Each OMEGA disk-amplifier module contains four laser disks, whereas each OMEGA EP amplifier module contains a single disk. This achieves maximum modularity of amplifiers, allowing an economy of scale for procurement. Each amplifier module consists of three major subassemblies: the amplifier frame assembly, the disk frame assembly, and the pump module,

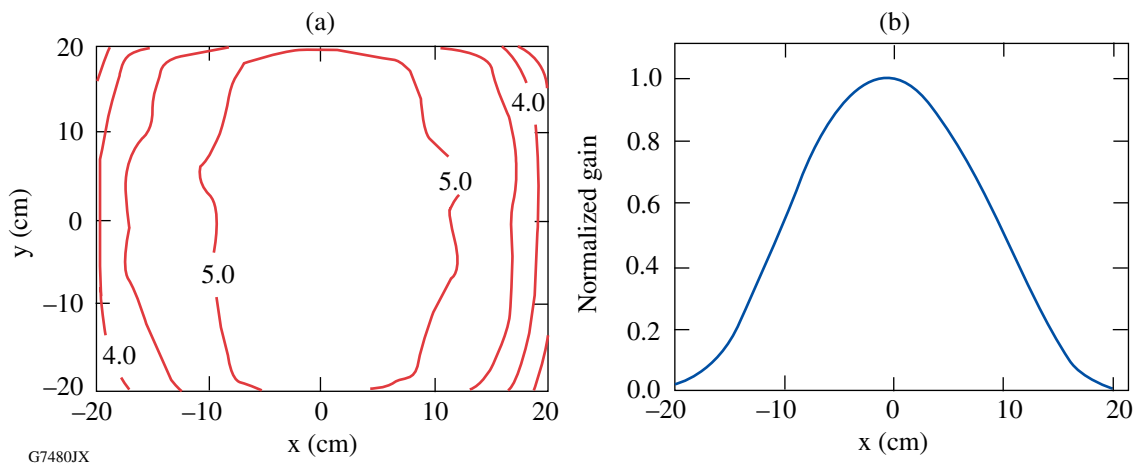


Figure 2.35  
 (a) Contour plot of gain (in units of %/cm) for an internal disk. (b) Normalized gain along a horizontal slice ( $y = 0$ ) accumulated through 58 disks.

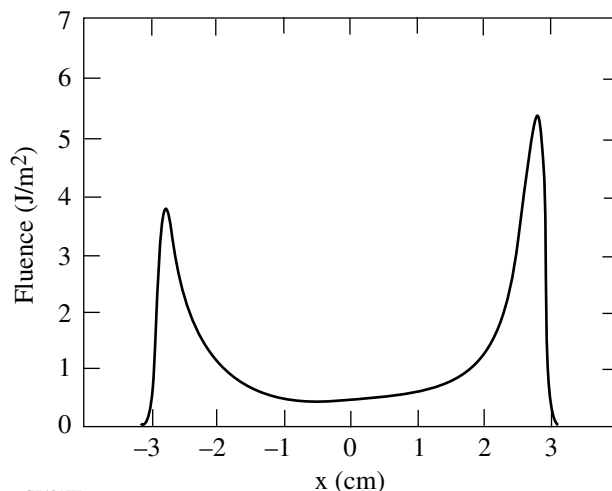


Figure 2.36  
 Nominal injection beam shape for the four-pass mode of operation.

as shown in Fig. 2.37. The pump module system is similar to that of OMEGA and features water-cooled flash lamps. A water-cooled flash-lamp assembly is shown in Fig. 2.38. It consists of a flash lamp, a Pyrex water jacket, and two flash-lamp connector assemblies. The connector assemblies provide the electrical connections to the flash lamp as well as the means for moving cooling water into and out of the assembly.

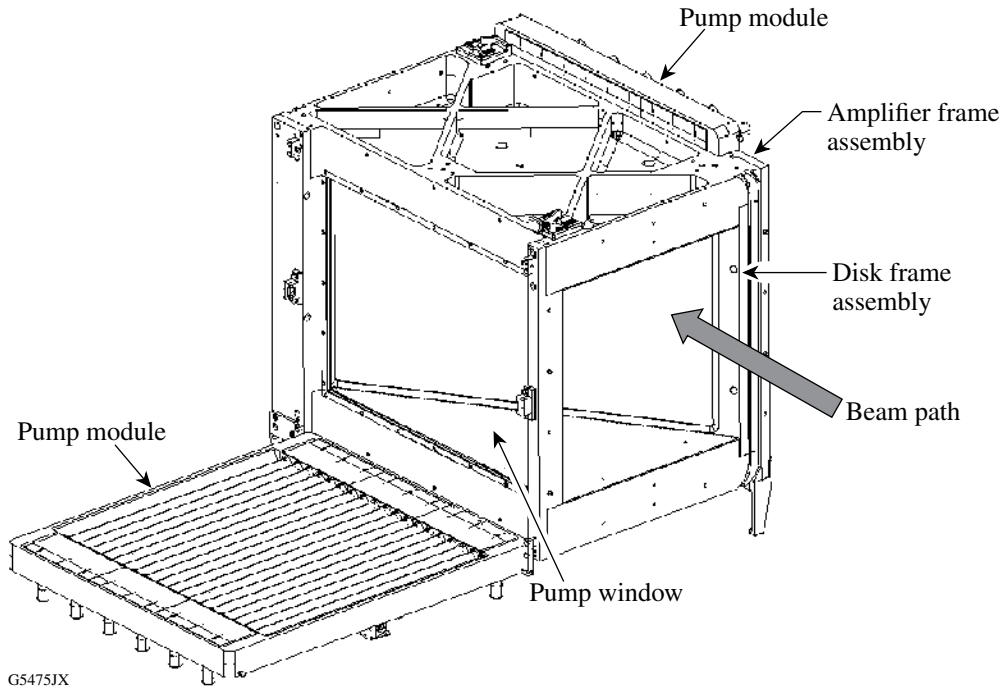
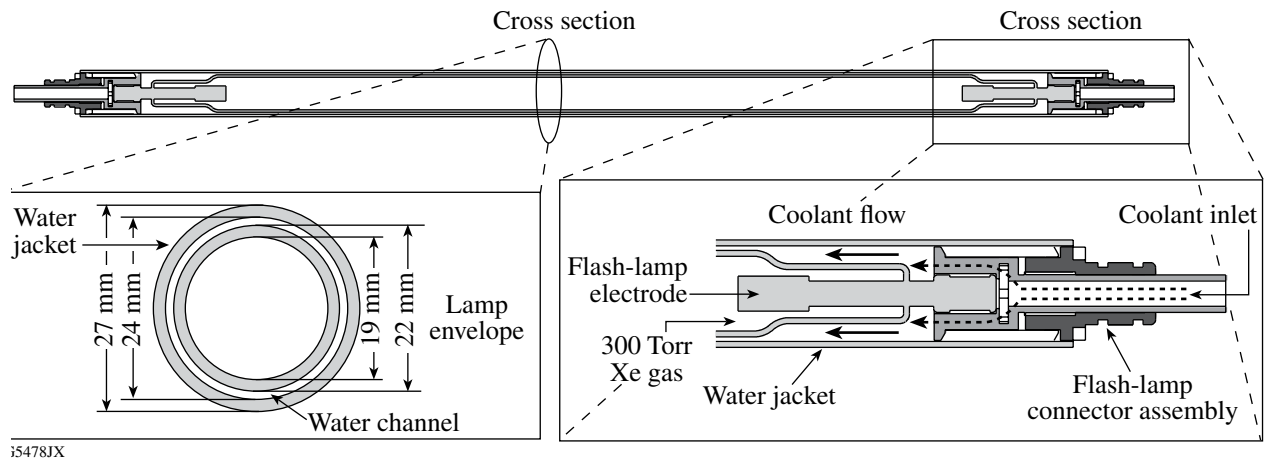


Figure 2.37  
 Isometric view of an OMEGA EP amplifier module showing the three major subassemblies (amplifier frame assembly, disk frame assembly, and pump module). The path of the laser beam is also shown.



i5478JX

Figure 2.38  
 Sectional view of a water-cooled flash-lamp assembly.

The power conditioning system provides the electrical energy that energizes the laser amplifiers. A 500-kVA substation supplies power to the power conditioning unit (PCU, Fig. 2.39) at 208 V. This power is converted to high voltage and used to charge a bank of capacitors for subsequent discharge into the flash lamps in the laser amplifiers. The power-conditioning control module in the PCU times this discharge, diagnoses the performance of the equipment during the shot, and provides data to the Power Conditioning Executive software. Each amplifier disk has an associated PCU. The PCU is the building block of the power conditioning system. There are 77 PCU's in the capacitor bays on the first floor of the facility, one for each of the 76 glass amplifier disks and an additional PCU used to support testing. There are seventy-two 40-cm disk amplifiers in the OMEGA EP Laser Bay (eighteen per beam). Laser Sources use four smaller glass amplifiers, each supported by a single PCU.

Each PCU is a self-contained, pulsed-power system that includes (1) a high-voltage power supply to convert incoming ac to high-voltage dc; (2) pulse-forming networks (PFN's) for energy storage and pulse shaping; (3) preionization and lamp check circuits (PILC's); (4) high-energy switching devices to discharge the energy; and (5) an embedded controller with associated control circuits and diagnostics to safely sequence the charge and discharge functions. The pulsed-power circuits are nearly identical to those of OMEGA except that inductance is added to the PILC circuit to generate a pulse with a reduced rise time. Each pulse-forming network powers three amplifier lamps connected in series and is a critically damped circuit made up of a single inductor, capacitor, and resistor. Each PCU is supplied with power from a 2-kW, high-voltage power supply with a 15-kV dc output. The pulse-forming-network capacitors are constructed using metalized polypropylene film technology. This is the industry standard for energy-storage capacitor construction and provides high energy density and excellent reliability compared with the layered-paper and metal-foil construction



G6593JX

Figure 2.39  
Power conditioning unit. (PFN: pulse-forming network; PILC: preionization and lamp check)

used in older designs. The switching-style power supplies, used to charge these capacitors, are mounted within each PCU enclosure. The A-size (e.g., Richardson<sup>47</sup> NL-7218H-100) ignitron switches energy for the PILC pulse, and the D-size (Richardson NL8900R) ignitron switches energy into the flash lamps for the main pulse. These ignitrons are used in the OMEGA Laser System and are proven, robust, and reliable devices. The OMEGA EP power conditioning units contain stand-alone trigger generator modules located at both the PILC and pulse-forming-network ignitrons. These modules enable the power conditioning control module to trigger each of the ignitrons at the appropriate time.

### 2.4.3.3 Beamlines

The optical components in the injection and amplification portions of one beamline are almost identical for long- or short-pulse operations. Referring to Figs. 2.28 and 2.40, the input laser beam (up to 0.58 J for 2-ns long pulses, 3.5 J for 10-ns long pulses, and 0.55 J for short pulses) is injected into the transport spatial filter, where it expands to a ~37-cm-square aperture. The injection lens (Fig. 2.28) is color corrected with a negative-dispersion diffractive optic that precompensates chromatic aberration accumulated from large-aperture beamline lenses. After the expanded beam makes an initial pass through the seven-disk booster amplifier, it is reflected down 1.5 m to the lower beam level by a fold mirror and a Brewster's angle polarizer (POL1) to enter the main laser cavity. This represents a layout change from the NIF to fit the beamlines into a smaller building. The fold mirror is smaller than that of the NIF and has a different coating requirement because of the reduced angle of incidence. The transport spatial filter is shorter than that of the NIF as the image relay distances to the target area are smaller.

The beam must be *p*-polarized relative to the disks in both amplifiers. The amplifier disks are mounted lengthwise on edge to minimize stress, requiring a horizontal orientation of the electric field. The electric field is *s*-polarized relative to the fold mirror and the Brewster's angle polarizer POL1, resulting in maximum reflectance from the polarizer surface.

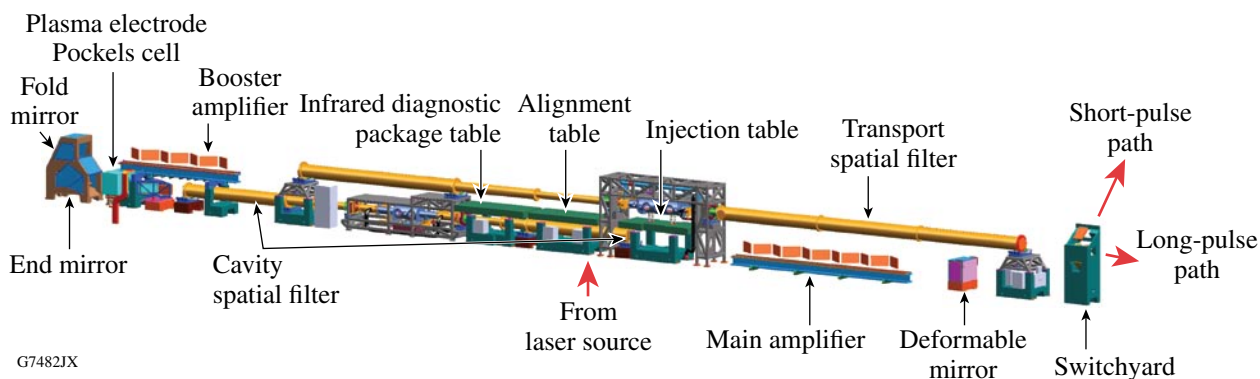


Figure 2.40

Main portion of an OMEGA EP beamline. The laser cavity is formed on the lower level (1.0 m from the floor) between the end mirror and the deformable mirror. The input beam from Laser Sources is injected into the transport spatial filter on the upper level (2.5 m from the floor).

To permit four passes through the main amplifier, the polarization of the beam must be rotated to prevent the beam from being reflected out of the cavity following the second pass. The plasma-electrode Pockels cell (PEPC) accomplishes this. It is an electro-optic device that rotates the electric-field vector of plane-polarized radiation by  $90^\circ$ . The LLE unit is based on the design developed at LLNL for the NIF. For four-pass operation, the PEPC is initially in its “off” state. After the pulse has passed through the PEPC, the device is switched to its “on” state by applying a high voltage ( $\sim 20$  kV). The returning beam is then rotated to a vertical polarization state, making it  $p$ -polarized relative to the Brewster’s angle polarizer POL1, resulting in high transmission through the polarizer. The beam then reflects from the cavity end mirror and returns through the polarizer and the PEPC. The PEPC rotates the beam’s polarization another  $90^\circ$  back to its initial, horizontal orientation. The voltage on the PEPC is then turned off, and, following the fourth pass, the beam is switched out of the cavity by POL1 and returns to the upper portion of the beamline.

The deformable mirror<sup>48</sup> at one end of the laser cavity corrects for low-spatial-frequency aberrations (of length scale  $\geq 33$  mm) introduced by the amplifier disks. A sample of the output beam, taken immediately after the transport spatial filter, is reflected to a Shack–Hartmann wavefront sensor. The output of the wavefront sensor is used to generate error-correction signals sent to the 39 actuators on the deformable mirror.

The cavity and transport spatial filters use a pair of aspheric lenses housed at the ends of evacuated tube assemblies to spatially filter the light between amplifier passes and to provide relay-plane imaging. The cavity spatial filter relays the image plane of the front-end apodizer to the deformable mirror. North of the transport spatial filter assembly there is a diagnostic beam-splitter mirror that provides a path to beam diagnostics that include shot and alignment sensors. In both the cavity and transport spatial filters, the beam passes through a different pinhole on each pass through the spatial-filter focal plane. This “angular multiplexing” reduces the likelihood of pinhole closure in the cavity spatial filter. There are four pinholes in each assembly, one for each pass. Angular multiplexing is used in the transport spatial filter to allow the seed beam to be injected into the main beamline.

In short-pulse mode, the Brewster’s-angle polarizer POL2 in combination with the PEPC (Fig. 2.28) prevents back-reflected pulses from the target from re-entering the main amplifier. (Back-reflected pulses could extract gain from the amplifiers and damage the injection mirror in the transport spatial filter.) The PEPC is pulsed “on” after the main pulse exits the cavity and prior to the arrival of the back-reflected pulse. Back-reflected light that re-enters the beamline has its polarization rotated by the PEPC and is rejected from the system by POL2 into a beam dump before it can reach the main amplifier disks and deformable mirror. A compensator plate, also at Brewster’s angle, is placed next to POL2 to avoid the spatial shift in the beam centerline that results from passage through a single obliquely oriented optic. The polarizer POL2 is not needed in long-pulse mode since any UV light reflected from the target will not reflect off the IR transport mirrors and cannot re-enter the beamline. It is removed from the cavity to avoid damage in this mode of operation.

The components of the beamline are interconnected with nitrogen-filled beam tubes (not shown in Fig. 2.40). This prevents oxygen from degrading the internal silver reflecting surfaces

at the ends of the main and booster amplifiers and maintains the low-relative-humidity working environment required by the polarizer coatings. The tubes and amplifiers are positively pressurized to ~0.1 in. of water. A monitoring system determines the oxygen percentage and relative humidity and can provide an out-of-specification alarm in the Control Room.

An IR diagnostic package containing a suite of diagnostic instrumentation is dedicated to each of the beamlines (Fig. 2.41). This package provides comprehensive information about system performance in preparation for and during a target shot. During a shot, measurements are made of the beam energy, the near-field and far-field spot profiles, and the full-aperture beam wavefront. A spectrometer and a streak camera are used to measure the temporal pulse shape. Prior to taking a shot, alignment diagnostics are used to point and center the beam from the source injection point to the beam emerging from the end of the transport spatial filter.

The source beam for the IR diagnostic package comes from the first-surface reflection of the IR diagnostic beam splitter—a flat, wedged plate oriented at  $0.10^\circ$  relative to the beam normal and located at the output end of the transport spatial filter (Fig. 2.41). Approximately 0.2% of the incident light is reflected from the front surface of this plate and down-collimated by the transport-spatial-filter output lens and a lens on the pinhole table within the transport-spatial-filter vacuum vessel.

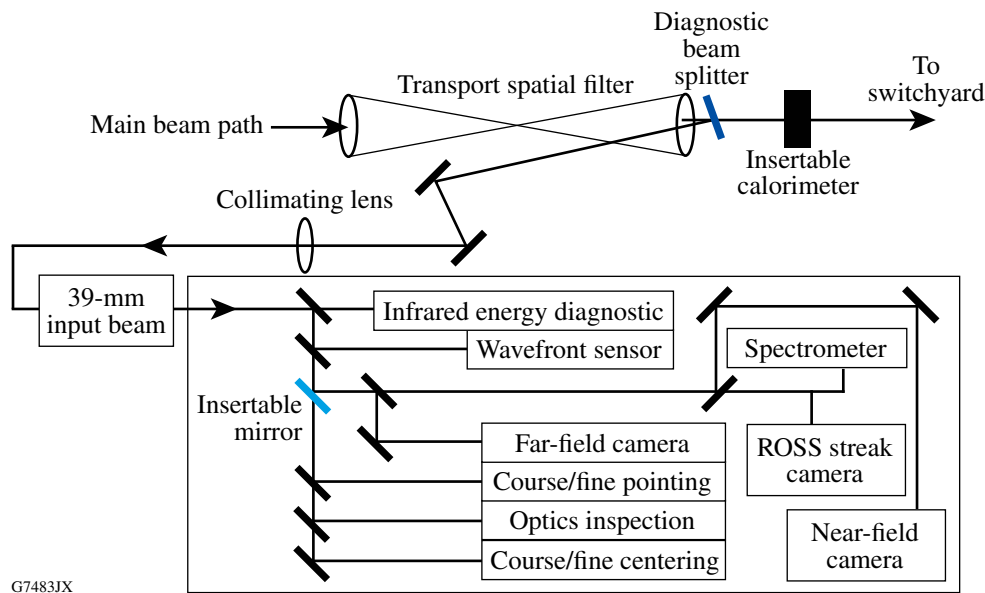


Figure 2.41

Schematic layout of the infrared diagnostic package (placed on a 5-ft  $\times$  12-ft optical table near the transport-spatial-filter injection point), identifying the beam paths to the nine individual instruments. The beam is sampled after emerging from the transport spatial filter. The insertable mirror is removed during alignment procedures prior to a laser shot.

#### 2.4.3.4 Pulse compression, IR short-pulse transport, and diagnostics

The pulse-compression grating systems are located in the grating compressor chamber—a large rectangular vacuum chamber in the northwest corner of the Laser Bay (Fig. 2.42). An equipment entry door on the south end facilitates insertion of large pieces of equipment, while two smaller entry doors located on the north and south ends provide personnel access.

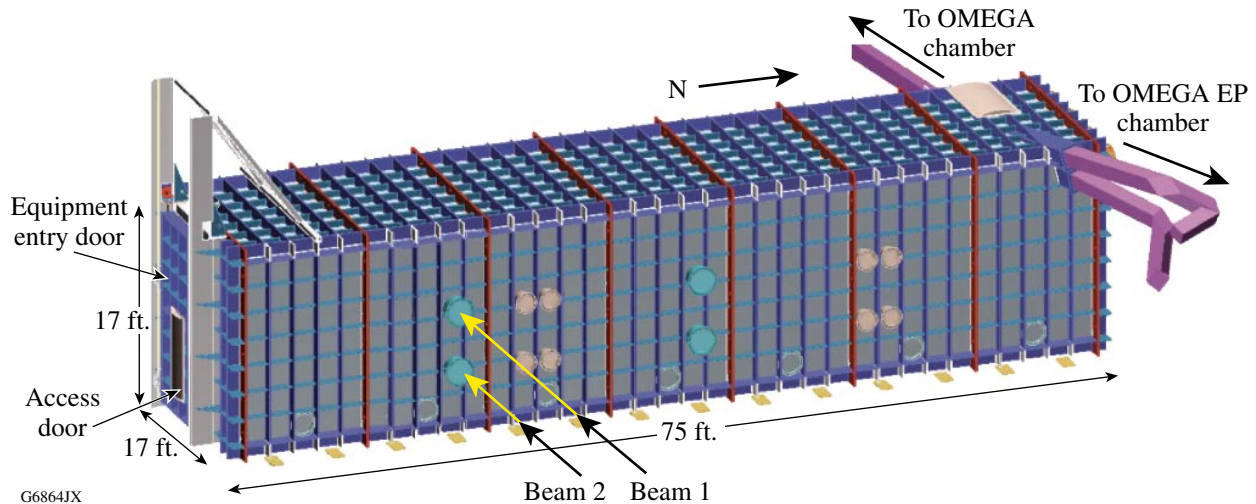


Figure 2.42

Grating compressor chamber (GCC), showing the main equipment access door to the south and the beam exit ports to the north.

Referring to Figs. 2.43 and 2.44, the grating compressor chamber houses two independent pulse compressors, deformable mirrors, compressor alignment mirrors, transport mirrors, a beam combiner, and transport optics to the short-pulse diagnostic package table. Each pulse compressor comprises four tiled grating assemblies (G1 to G4), each of which comprises three tiled gratings. A pair of interferometers align the tiles of each tiled grating assembly. Full-aperture calorimeters may be inserted to measure the energy of the high-intensity pulses. There are 14 optical tables within the grating compressor chamber.

The optical path of the upper compressor is shown in Fig. 2.44. Beam 1 from the switchyard enters via a vacuum window located on the east side of the grating compressor chamber and is directed toward the first grating assembly, G1, at an incidence angle of  $72.5^\circ$ . The diffracted beam (at  $61.5^\circ$ ) encounters the second grating assembly (G2) at  $61.5^\circ$  and emerges at  $72.5^\circ$ . After similar paths through G3 and G4, the pulse has been temporally compressed by up to 300 ps/nm. Emerging from G4, the pulse reflects off the compressor deformable mirror, which corrects for aberrations in the compressor optics and the short-pulse transport and focusing optics. The diagnostic mirror directs 0.5% to 1% of the energy to the short-pulse diagnostic table. The remainder of the pulse reflects off the surface of the beam-combiner mirror to the target-chamber selection mirror. The design of the lower compressor is virtually identical; however, after the diagnostic mirror, the pulse may follow two paths. It may transmit through the beam combiner, where it becomes co-aligned with

the pulse from the upper compressor and is directed either to the OMEGA target chamber or to the “backlighter” port of the OMEGA EP target chamber. Alternatively, it may be routed independently to the “sidelighter” port of the OMEGA EP target chamber.

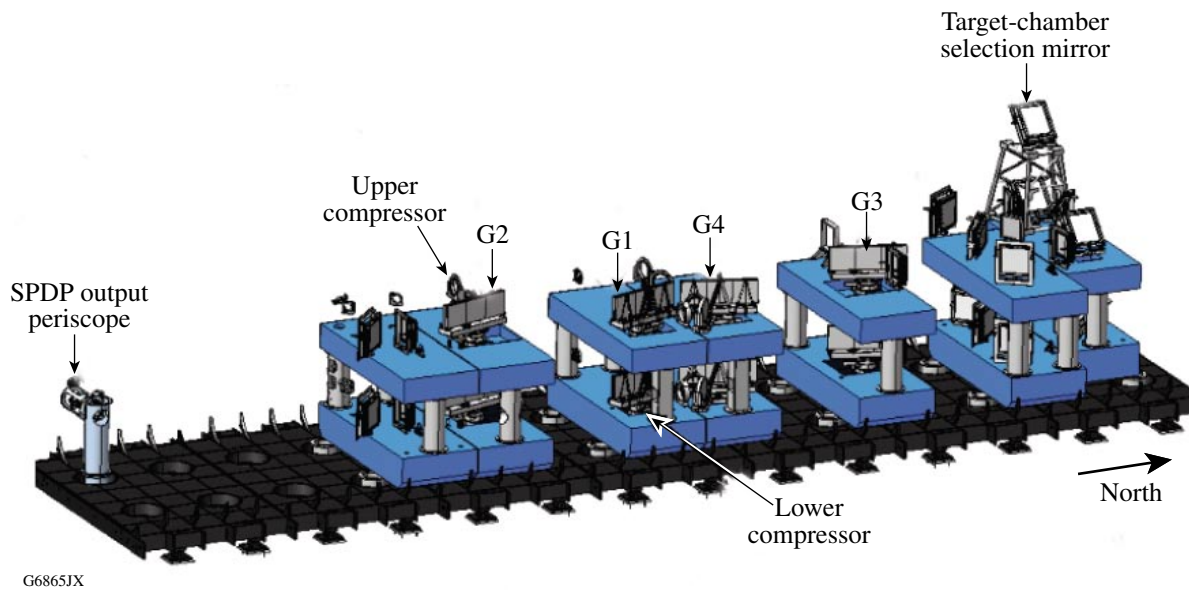


Figure 2.43

Internal components of the GCC, including the tiled grating assemblies (G1 to G4) and the target-chamber selection mirror. The upper and lower compressors, for Beams 1 and 2, respectively, are aligned atop one another. Diagnostic beams exit the GCC via the short-pulse-diagnostic-package (SPDP) output periscope.

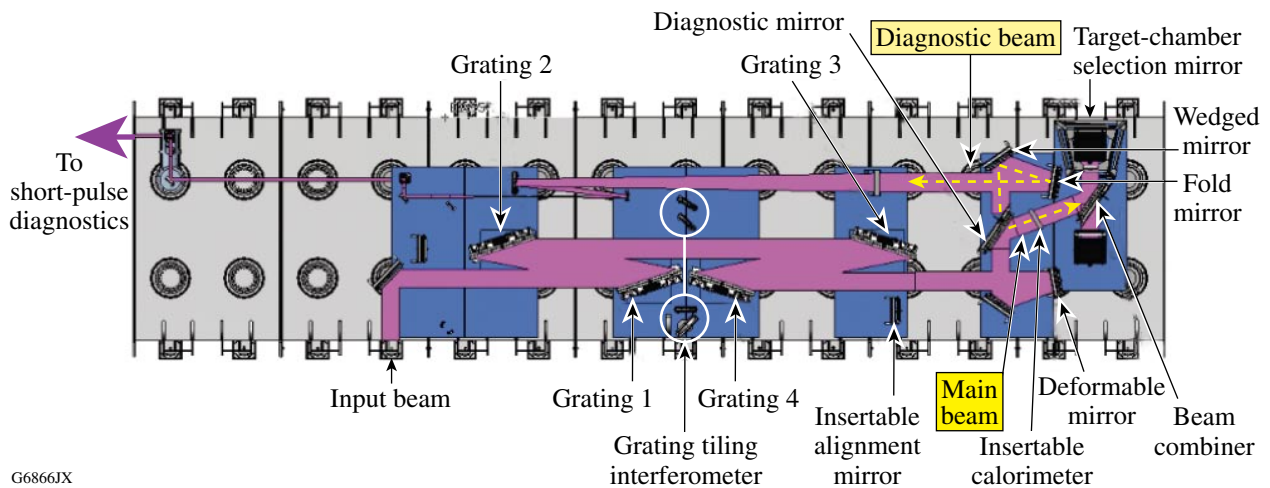
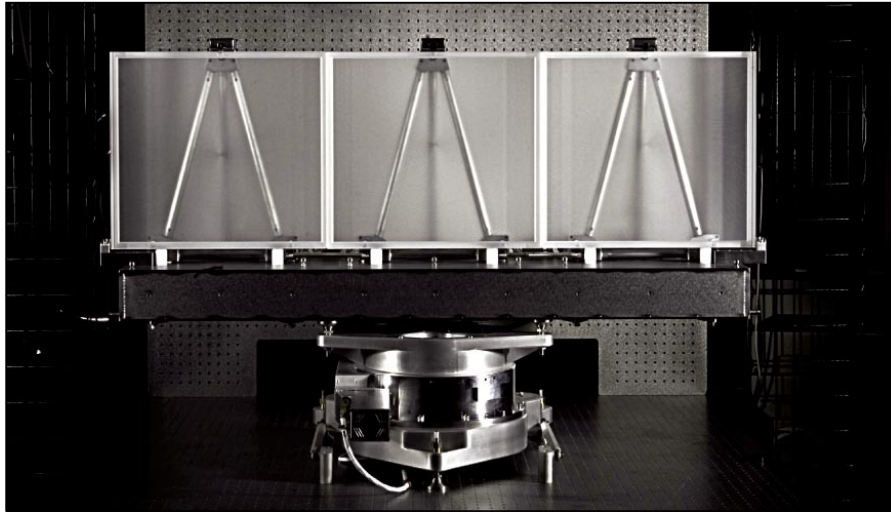


Figure 2.44

Optical path of the upper compressor. The diagnostic mirror provides a 1% pickoff for the short-pulse diagnostic beam, shown exiting the chamber to the left. The optical configuration of the lower compressor is almost identical. The circles are the internal structure mounting points. (Note: The final design differs from this figure in some minor details.)

A photograph of a grating assembly is shown in Fig. 2.45. The width of the assembly accommodates the beam footprint at  $72.5^\circ$ . Three smaller gratings (47 cm wide by 43 cm high), rather than one large grating, were designed to facilitate their manufacture. The grooves of the gratings are aligned with the vertical and have a pitch of 1740 grooves/mm. The outer tiles are precision aligned to the center tile to control tip, tilt, rotation, piston, and shift using an interferometer incorporated into the compressor, minimizing errors in the combined wavefront. The tiles rest upon a precision six-axis stage for compressor alignment.



G6867JX

---

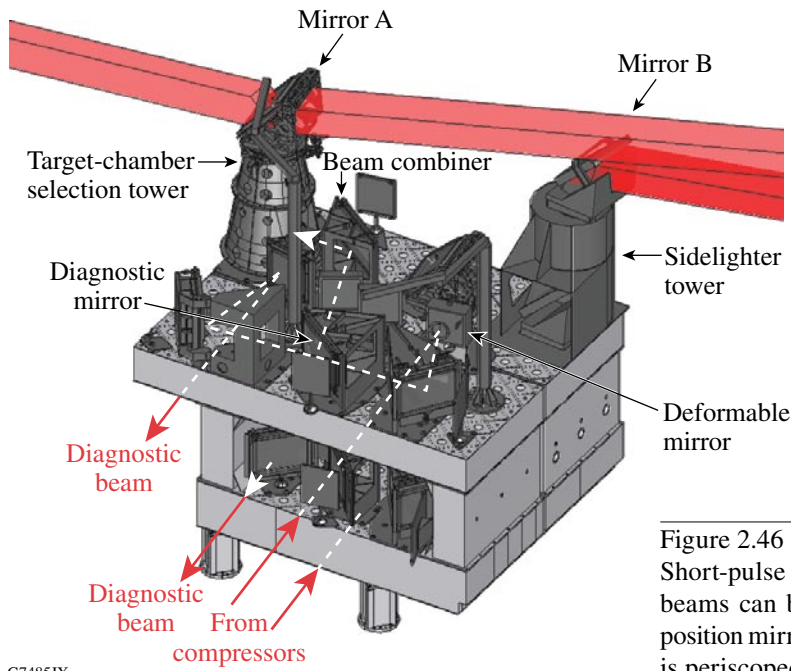
Figure 2.45

Grating assembly, comprising three tiled gratings on a tile support beam placed on a six-axis base used for compressor alignment. Each of the outer grating tiles has a precision control system used to align the beam wavefront to that of the center tile.

---

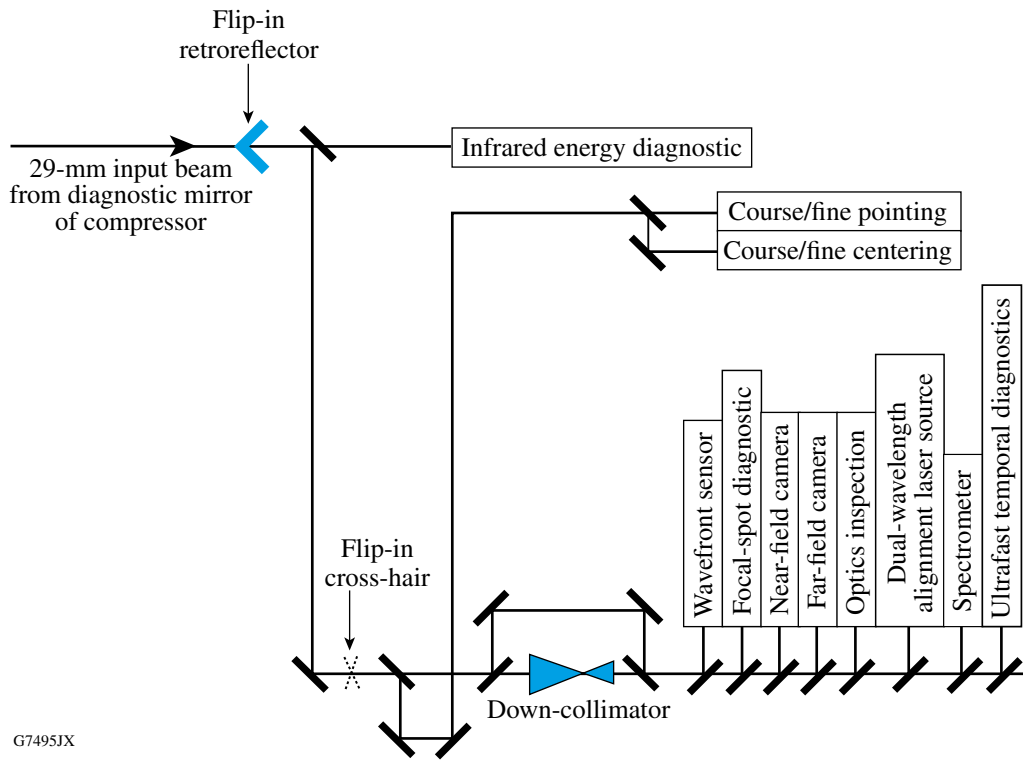
The components on the two optical tables to the north of the compression gratings comprise the short-pulse switchyard. Configuration flexibility allows for the short-pulse beams to be delivered to the OMEGA or OMEGA EP target chambers. The different configurations are obtained by positioning the upper mirrors of two periscopes to the desired locations (Fig. 2.46).

The instruments in the short-pulse diagnostic package (Fig. 2.47) diagnose the properties of the beams before they are co-aligned. They measure the beam quality, energy, alignment, spectrum, optical component damage, output wavefront, pulse width, and pulse contrast. For the upper beam, the transmitted light through the diagnostic mirror in the grating compressor chamber is directed to a near-normal-incidence optic with a slight wedge. The first surface of the wedge is uncoated, providing a 4% reflection, while the rear surface of the wedge is highly reflective. The small pointing difference between the beams reflecting off the front and rear surfaces of the wedge allows an operator to select either a low- or a high-transmission path. This flexibility enables greater attenuation for the highest-intensity ( $\sim 1$  ps) short-pulse beams, providing a low-energy diagnostic beam and minimizing



G7485JX

Figure 2.46  
 Short-pulse switchyard. Co-propagated or individual beams can be diverted to either chamber by the two-position mirror (A). The beam from the lower compressor is periscoped up to the upper table, where it is directed by the two-position mirror (B) either through the beam combiner or to the sidelighter tower.



G7495JX

Figure 2.47  
 Layout of the short-pulse diagnostic package. There is one of these systems for each of the two compressed beams.

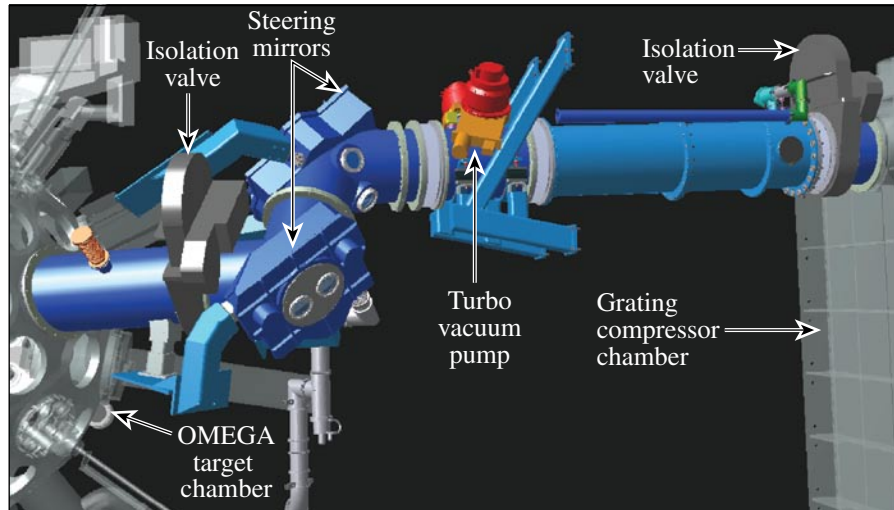
the  $B$ -integral for on-shot measurements. The lower compressor generally operates at 10 to 100 ps and does not need an attenuation wedge. A single  $45^\circ$  fold mirror in the lower compressor beam replaces the wedge and fold mirror pair. In both compressors the diagnostic beam is downcollimated by a pair of lenses.

The diagnostic package includes a dual-wavelength IR alignment laser (1053 nm and 1047 nm) that can illuminate the short-pulse transport paths to the target and the Fizeau interferometers in the grating compressor chamber. This laser allows alignment and setup of the pulse compressors to be conducted independently of the main beamline. Two wavelengths are used in the alignment procedure to ensure that the grating assemblies are aligned for broadband compression. The short-pulse diagnostic package sends this laser beam into the compressor counter-propagating to the pulsed beams. Insertable alignment mirrors in the compressor allow for fine positioning of each of the grating degrees of freedom. One of these alignment mirrors directs the dual-wavelength laser back to the target chamber along the short-pulse transport path. The diagnostics and laser source are located on a 5-ft  $\times$  32-ft optical table adjacent to the compressor vessel. The instruments in the short-pulse diagnostics package (Fig. 2.47) are nearly the same as those on the infrared diagnostic package at the output of the transport spatial filter. Alignment sensors, near- and far-field cameras, energy sensors, wavefront sensors, and inspection systems are also used. Unique to this area are the focal-spot diagnostic and the ultrafast temporal diagnostic package. The focal-spot diagnostic uses pre- and on-shot wavefront sensors and near-field spatial-profile instrumentation to characterize the spatial irradiance pattern on target. A far-field camera with two fields of view is used pre-shot (in narrow field) to confirm grating tiling alignment and on-shot (in wide field) to characterize any noise passing through the pinholes. The temporal instruments consist of a fast streak camera and an autocorrelator used in combination to measure the pulse duration and shape. The flip-in retroreflector in Fig. 2.47 is used for various alignment procedures.

After the laser pulses are compressed in the grating compressor chamber, they are transported to target by reflections off mirrors within a vacuum environment. Each of the three available beam paths includes at least two steering mirrors and one focusing mirror, an  $f/1.8$  off-axis parabola with a 1-m focal length. The path from the grating compressor chamber to the OMEGA target chamber is shown in Fig. 2.48 and the path to the OMEGA EP target chamber in Fig. 2.49. The vacuum vessels have gate valves at either end to isolate the tube and mirror enclosures to direct the beam to the focusing parabola.

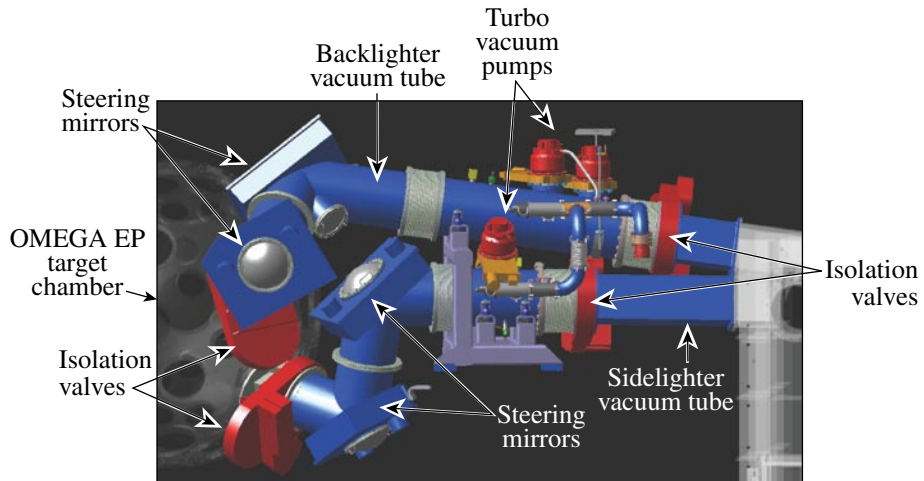
The off-axis parabola requires precise alignment to the optical axis of the system, accomplished using the vacuum-compatible parabola alignment diagnostic (shown in Fig. 2.50). This diagnostic is placed in a ten-inch manipulator. It includes a linearly polarized, fiber-coupled laser apodized to the OMEGA EP spatial profile with its polarization rotated by a waveplate to match the incoming beam. This alignment beam can be counter-propagated through any of the transport paths and directed by an insertable compressor alignment mirror into the short-pulse diagnostic package. The alignment diagnostic also senses the wavefront of the short-pulse diagnostic package beam using a lenslet array and a CCD camera, and the beam pointing using a lens and CCD camera. Wedges in the parabola alignment diagnostic compensate for the keystone distortion of the off-axis parabola. The parabola alignment diagnostic is positioned to the desired focus of

the short-pulse beam and a target-chamber-referenced autocollimator, bringing the beam onto the target along the proper axis.



G7484JX

Figure 2.48  
 Short-pulse path from the grating compressor chamber to the OMEGA target chamber.



G7533JX

Figure 2.49  
 Short-pulse path from the grating compressor chamber to the OMEGA EP target chamber.

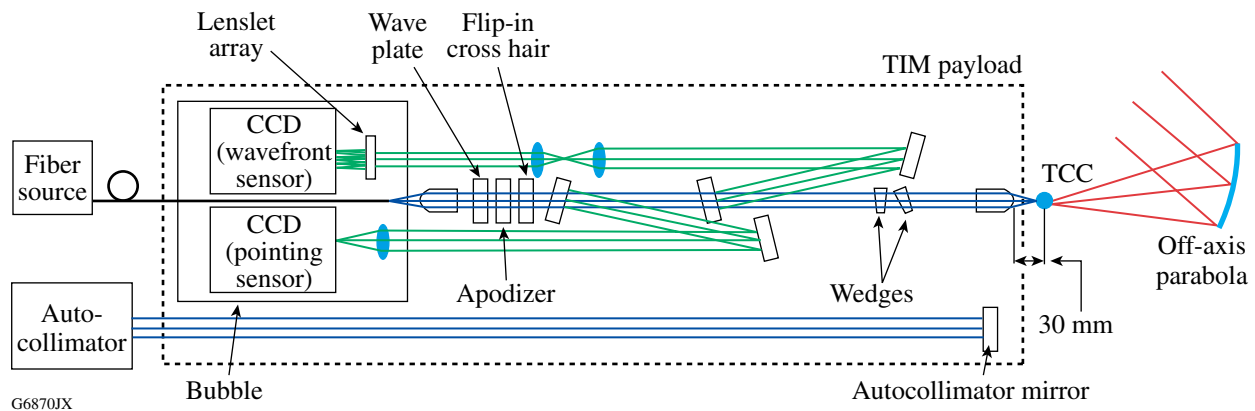


Figure 2.50

Parabola alignment diagnostic (PAD), a self-contained TIM-based diagnostic, portable between target chambers. A Shack–Hartmann sensor uses a lenslet array to measure the wavefront reflected off the off-axis parabola, the autocollimator monitors angular displacement of the PAD optics, and a pointing diagnostic determines the location of target chamber center (TCC).

#### 2.4.3.5 Frequency conversion, UV long-pulse transport, and diagnostics

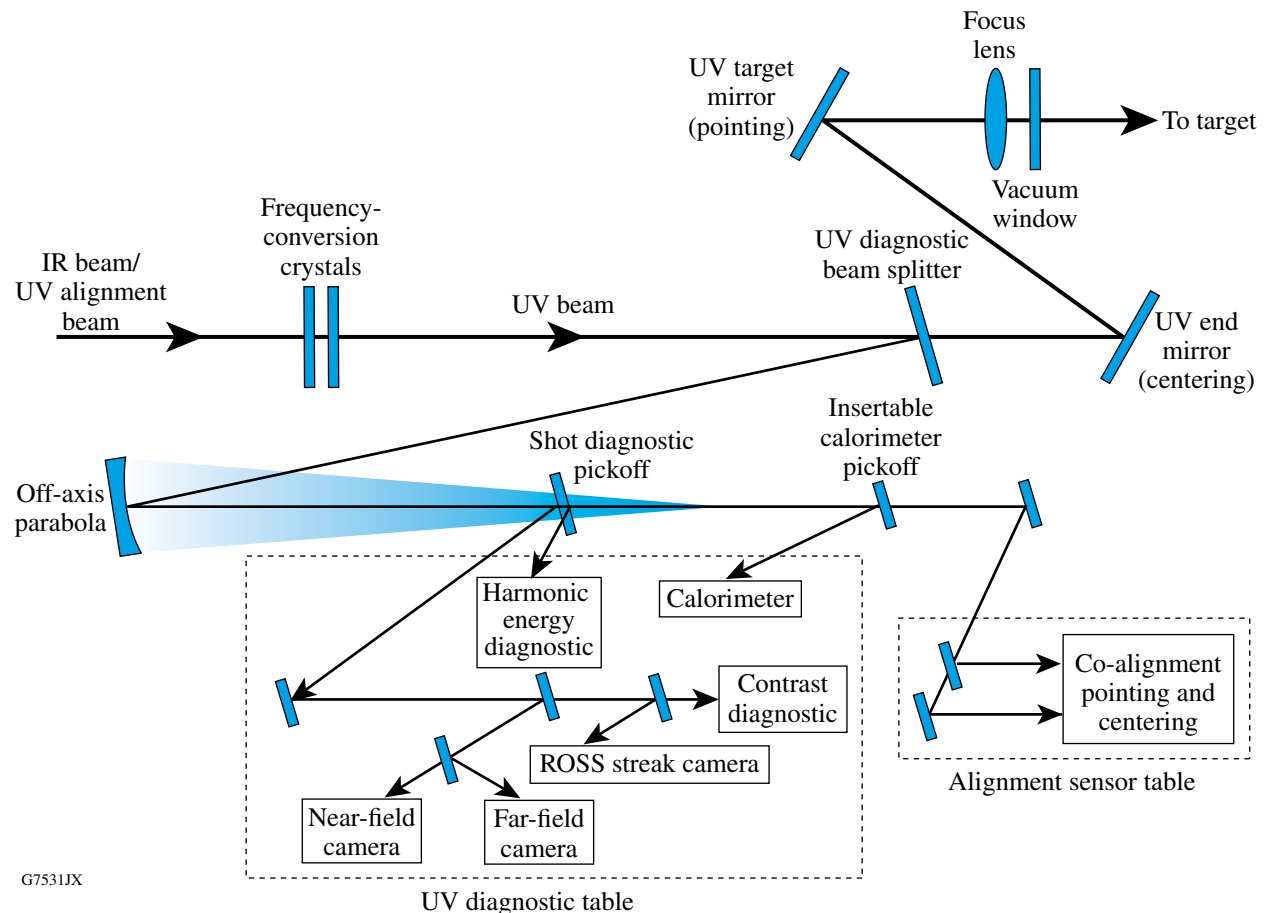
For experiments requiring long-pulse (1 to 10 ns) beams, the 1053-nm beams are frequency tripled to 351 nm using potassium-dihydrogen-phosphate (KDP) and deuterated-potassium-dihydrogen-phosphate (KD\*P) frequency-conversion crystals (FCC's) and transported to the OMEGA EP target chamber (Fig. 2.29). They cannot be directed to the OMEGA target chamber. Each beam is focused onto the target using an  $f/6.5$  aspheric lens of 3.4-m focal length followed by a vacuum window and a thin debris shield. A phase plate can be inserted before the lens to smooth and tailor the target-plane profile. The beams are directed to ports at a  $23^\circ$  angle of incidence with respect to a common central axis that is typically aligned with the target normal.

The frequency-conversion system is based on the type-I/type-II angle-detuning configuration originated at LLE<sup>22</sup> and implemented on the NIF.<sup>49,50</sup> The NIF design has been adopted because it is optimal for OMEGA EP. Two  $40 \times 40$ -cm crystals are used: an 11-mm-thick, type-I KDP doubler that converts approximately 67% of the IR to its second harmonic followed by a 9-mm-thick KD\*P tripler to mix this second harmonic with unconverted IR to form the third harmonic. Compared with the type-II/type-II polarization-mismatch scheme<sup>22</sup> used on OMEGA, this configuration has the advantage that a polarizer is not needed before the crystals but the disadvantage of a tighter alignment requirement on the doubler for the highest operating intensities. The choice of configuration is forced because transmission polarizers at the IR fluences of the NIF or OMEGA EP are unavailable. An additional consideration is that the type-I cut is more favorable for doubling a square beam due to boule-size considerations.<sup>49</sup>

The frequency-conversion performance is diagnosed with a 4% diagnostic pickoff located after the FCC's in an arrangement similar to that used successfully on OMEGA (Fig. 2.51). The pickoff diagnostics include alignment sensors for co-aligning a UV alignment source to the IR alignment source. Each of the four beamlines has its own UV diagnostic and alignment table, located near the

target chamber on the target-area structure (Fig. 2.52). The UV alignment source is located on its own table on the Laser Bay floor in front of the target area structure, and its output beam is introduced just before the FCC's with a periscope mirror assembly similar to that on OMEGA (Fig. 2.29). The UV alignment beam is sequentially propagated through each of the four pulsed beam paths. The placement of the FCC's before the target chamber (rather than on the target chamber as in the NIF) permits more convenient beam diagnostics and allows for the rejection of unconverted light by the transport mirrors.

The UV diagnostic packages provide comprehensive information about the system performance, both in preparation for and during a target shot. Measurements are made of the beam energies at all three harmonics, the near-field (IR and UV) and far-field spot profiles, and the contrast. The IR beam energies before the FCC's are measured in the IR diagnostic package (Fig. 2.41).



G7531JX

Figure 2.51  
Layout of the UV diagnostic table and alignment sensor table.

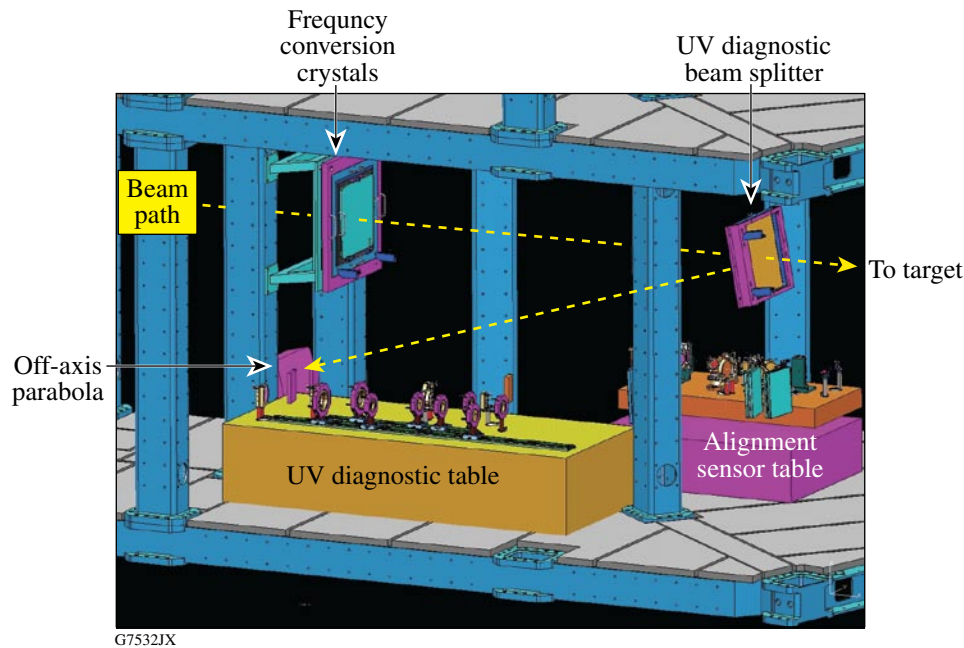


Figure 2.52

Location of the UV diagnostic table and alignment sensor table on the target-area structure.

Co-alignment of the IR and UV alignment beams is achieved by steering the periscope mirrors to point the UV alignment beam to the pointing and centering alignment sensors on the UV diagnostic table. These sensors use achromatic optics so that they can function at both wavelengths. The portion of the UV alignment beam that passes through the UV diagnostic beam splitter is then steered to the target by moving the transport mirrors (Fig. 2.51). The beam is confirmed to be aligned by retroreflection back to sensors adjacent to the laser source. This method of UV system alignment is the same as used on OMEGA. A minor difference is that the UV beam is injected prior to the FCC's on OMEGA EP.

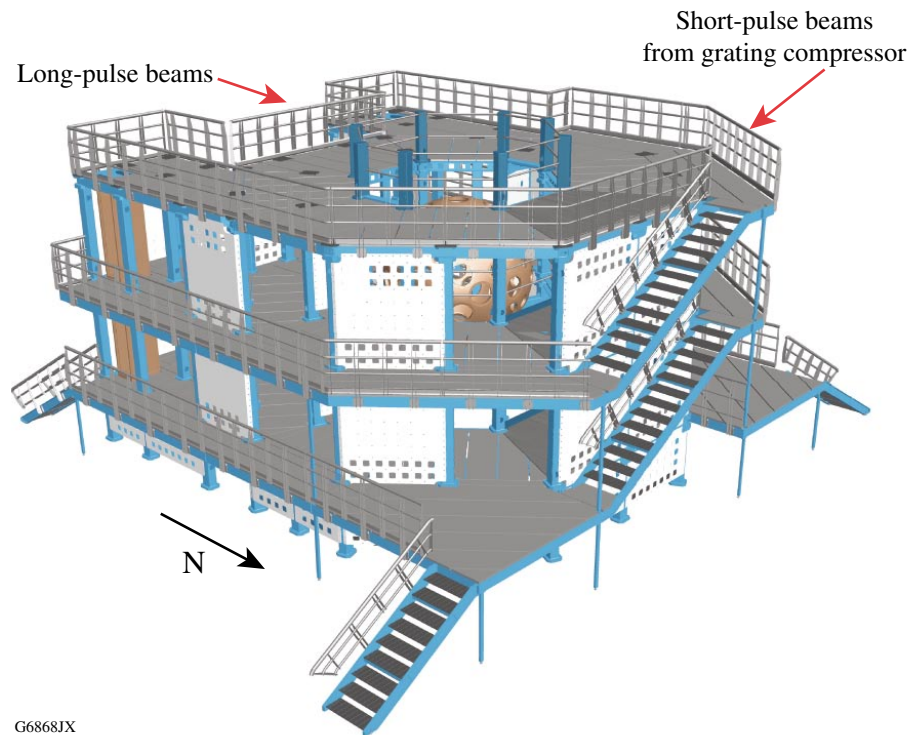
#### 2.4.3.6 Target chamber and experimental systems

The OMEGA EP target chamber is similar in design to the OMEGA target chamber and has the same 3.3-m diameter. The chamber is located within the target area structure (Fig. 2.53) located at the north end of the Laser Bay. A diagram of the ports as viewed from the Laser Bay is shown in Fig. 2.54.

The target chamber design takes advantage of the substantial infrastructure developed for the OMEGA Laser System and allows for the full compatibility of existing diagnostic instrumentation. The target chamber will support six ten-inch-manipulator (TIM) diagnostic shuttles (three initially), a target positioning system, a target viewing system, and other support items based on their OMEGA equivalents. The top and bottom ports are reserved for the addition of a planar cryogenic target system. The target chamber has two TIM-like off-axis-parabola inserter/manipulators. Beam transport tubes from the grating compressor chamber enter the target chamber from the west. The short-pulse beams

propagate to their respective off-axis parabolas that focus them along orthogonal paths, with the parabolas placed in the “backlighting” and “sidelighting” ports. The target-area structure supports the IR transport mirrors, the periscope mirror assembly, the frequency-conversion crystals, the UV diagnostic beam splitters, the UV diagnostic tables, the alignment sensor tables, and the UV end and target mirrors.

The diagnostic suite has both fixed and flexible diagnostic platforms. Fixed diagnostics include plasma calorimeters, x-ray pinhole cameras (Sec. 2.5.2.1), Kirkpatrick–Baez microscopes (Sec. 2.5.2.3), and x-ray streak cameras (Sec. 2.5.4). Flexible accommodations for experimental diagnostics are provided by the TIM's. Each TIM provides mechanical, vacuum, and electrical/control support and positioning for any compatible instrument that needs to be positioned near the center of the target chamber.



G6868JX

---

**Figure 2.53**

Target-area structure with the target chamber located within. Beam-transport tubes from the grating compressor chamber enter the target chamber from the west (not shown).

---

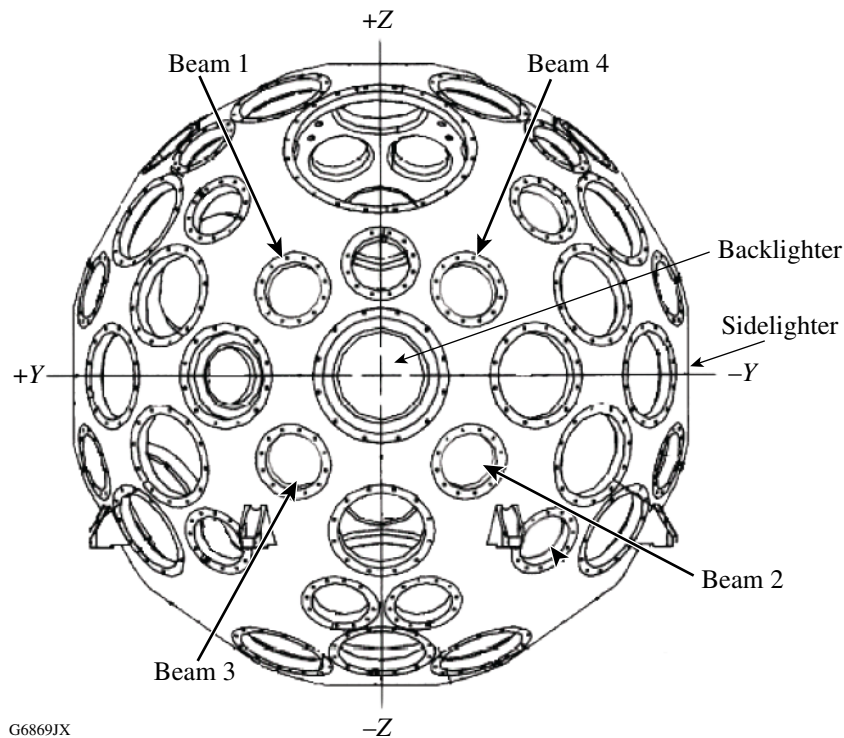


Figure 2.54

South elevation view of ports on the OMEGA EP target chamber. The long-pulse UV beams enter through ports  $23^\circ$  from the central port. The backlighter off-axis parabola resides in that central port (“-X”), and the sidelighter off-axis parabola resides in the “-Y” equatorial location.

## 2.4.4 Control Systems

### 2.4.4.1 Overview

The control system for OMEGA EP is nearly identical to that used on OMEGA. Applications are grouped by functional area and run under a software executive that continuously monitors software status. The control system architecture (Fig. 2.55) shows the hierarchical structure of executive software and the connectivity path that functions when the OMEGA EP beams are used in the OMEGA target chamber. For shots on OMEGA that require OMEGA EP, the OMEGA EP system is treated as a single additional control connection. Operations staffing places control of the executive software under the direction of a single individual in a centrally located control room. The control room for OMEGA EP (Fig. 2.56) has four primary workstations with fixed functions and three flexible workstations for the scientific oversight of operations, maintenance operations, and (on an as-needed basis) concurrent alignment, diagnostic setup, or other testing needs.

The primary control systems consist of beam motion controls for moving devices, video for alignment, and the hardware timing system. These applications and hardware are replicas of the systems in use on OMEGA. Specialized systems have been developed to deal with new technologies including the deformable mirrors, the plasma-electrode Pockels cells, Shack–Hartmann wavefront

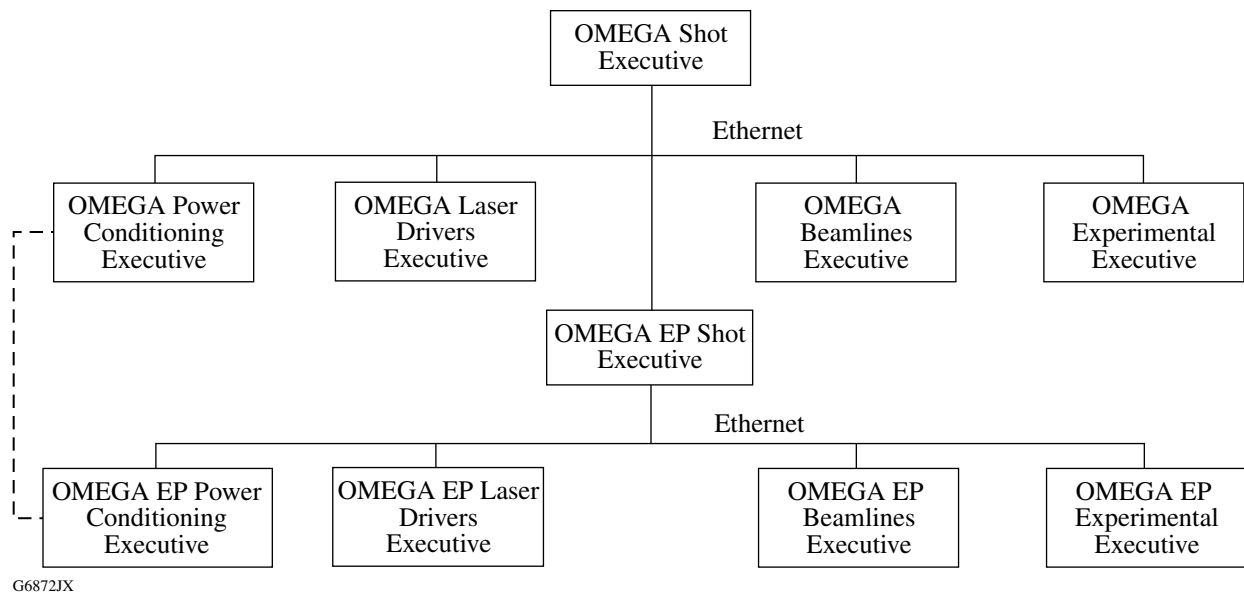


Figure 2.55

Top-level architecture of the laser control system, indicating OMEGA as the senior system when used in joint shot operations. The lines connecting the executives represent the LLE Ethernet and the software hierarchy. Power conditioning executives share information during shot set-up to coordinate charge sequences.

sensors, grating alignment, and a higher precision timing system. The control system architecture has been modified to reflect OMEGA EP as a subordinate system to OMEGA when in the “joint” shot mode. When not shooting jointly, the two laser systems are completely independent.

As on OMEGA, the laser control system facilitates the operational activities that maintain the system, prepare it for a shot, execute the shot, and record the shot results. A network communication system coordinates actions requiring synchronization to within about one second. The timing required to execute and diagnose a shot is provided by the hardware timing system. A “handoff” between the two levels of timing control takes place 20 s before a shot is triggered. As on OMEGA, the operations system makes use of the concept of a “shot cycle,” consisting of a sequence of “system states” and “shot types.” The system states partition the activities into known situations for communications and coordination. The shot types identify the configurations in which the high-energy, pulsed beams are propagated and the degree of system-wide coordination that is required. The Shot Executive controls the transitions from one state to the next and ensures that the required sub-executives are performing satisfactorily.

The Shot Director in the OMEGA EP Control Room operates the Shot Executive and the OMEGA EP Power Conditioning Executive. The Power Conditioning Executive is a software program that controls the 76 amplifier power conditioning units through a shot sequence. It is similar to the OMEGA power conditioning executive in appearance and function. For shots into the OMEGA target chamber, the OMEGA Power Conditioning Executive is superior, and the charge sequence starts at the command of the OMEGA Shot Director.

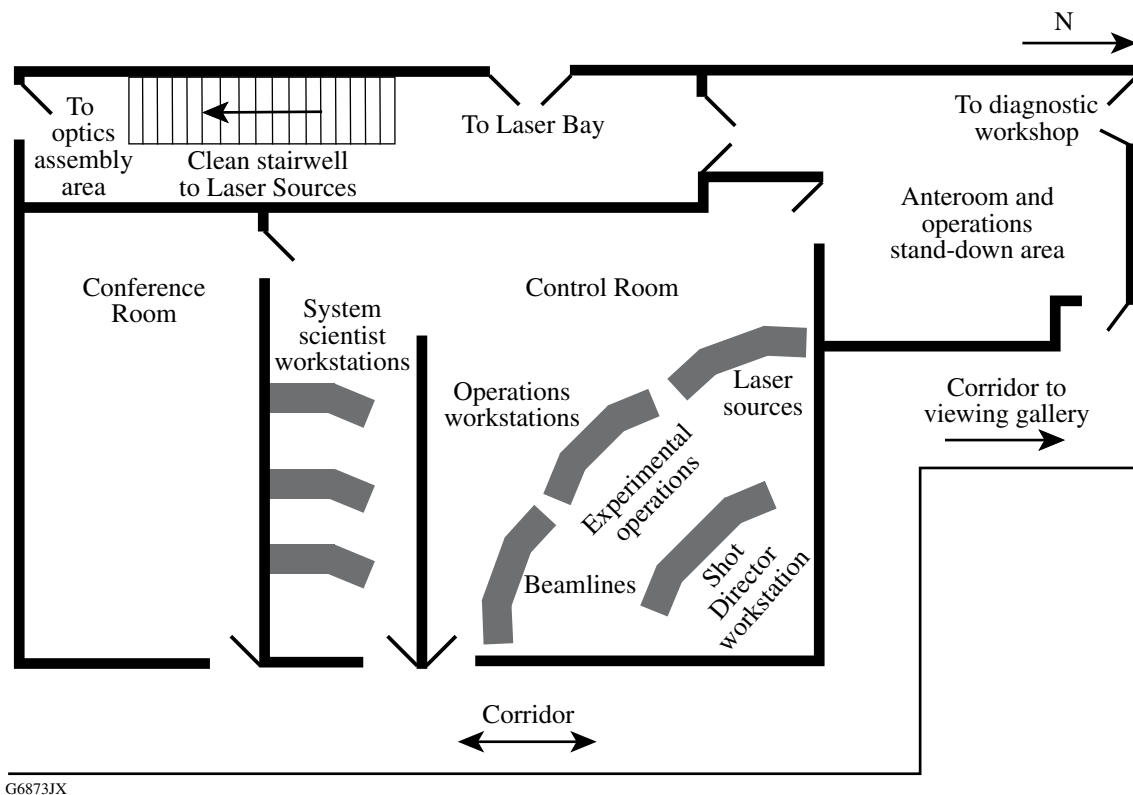


Figure 2.56

Layout of the OMEGA EP Control Room, anteroom, and conference area. Workspace is provided for the system scientists and principal investigators.

#### 2.4.4.2 Timing systems

Figure 2.57 shows the timing and shot control configuration for the two laser systems. The reference frequency generator (RFG) is common to both systems, and the 38-MHz sine wave from the RFG is distributed to both facilities. This signal is used in the Laser Sources subsystems and as the precision clock source in each of the timing crates in both facilities. It is used by the master timing generator (MTG) to produce a digital trigger that repeats at a 0.1-Hz rate. This signal is distributed to all of the timing crates along with the signal from the RFG. The 5-Hz signal and other timing signals produced by the timing crates are based on the 38-MHz clock and are synchronized to the MTG 0.1-Hz signal. The Power Conditioning Executive causes the MTG to produce T-10 and T-0 shot triggers synchronized to the 0.1-Hz signals at the correct times in the shot cycle.

The 38-MHz RF and the other (digital) signals used by the Hardware Timing System are distributed throughout the OMEGA and OMEGA EP facilities. The rate regenerator module in each timing crate accepts the RF signal, the 0.1-Hz rate, and the T-10 and T-0 digital signals from the MTG and provides them to quad-channel delay modules. Each delay module has four independent channels that can each be set to implement a precision delay and provide a trigger at the desired amplitude, duration, and rate to one of the seven output signals.

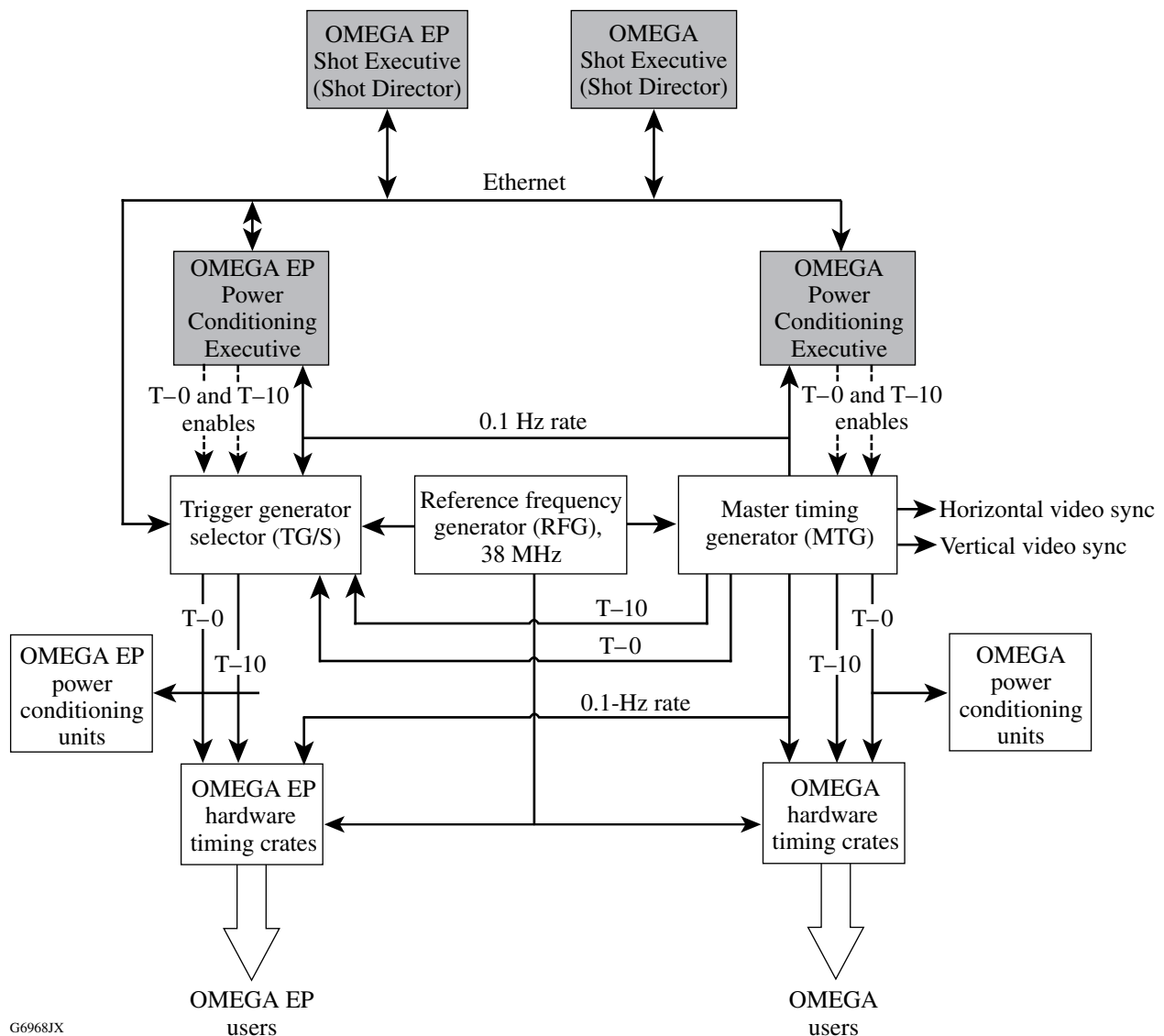


Figure 2.57

Block diagram of the timing control system for joint shot operations. The reference frequency generator is common to both OMEGA and OMEGA EP systems. The shot triggers used in the OMEGA EP system are distributed by a trigger generator/selector unit that has separate modes for independent and joint operations. In the independent mode, the trigger generator/selector passes synchronized T-10 and T-0 shot triggers for OMEGA EP only. In the joint mode, the signals generated by the master timing generator are used in both systems.

Timing of the laser shot is accomplished by the synchronization of the front-end sources in OMEGA and OMEGA EP using high-bandwidth, ultrafast ROSS streak cameras.

Using streak cameras in the IR at the front end and in the UV at the output, the on-target beams can be timed to 10 ps as on OMEGA. A fiducial pulse can be simultaneously streaked with the main beam. The fiducial is used to determine the relative timing of each of the beamlines with

respect to each other and to the OMEGA beamlines. The fiducial also provides a set of evenly spaced pulses that are used to check the accuracy of the streak-camera time base.

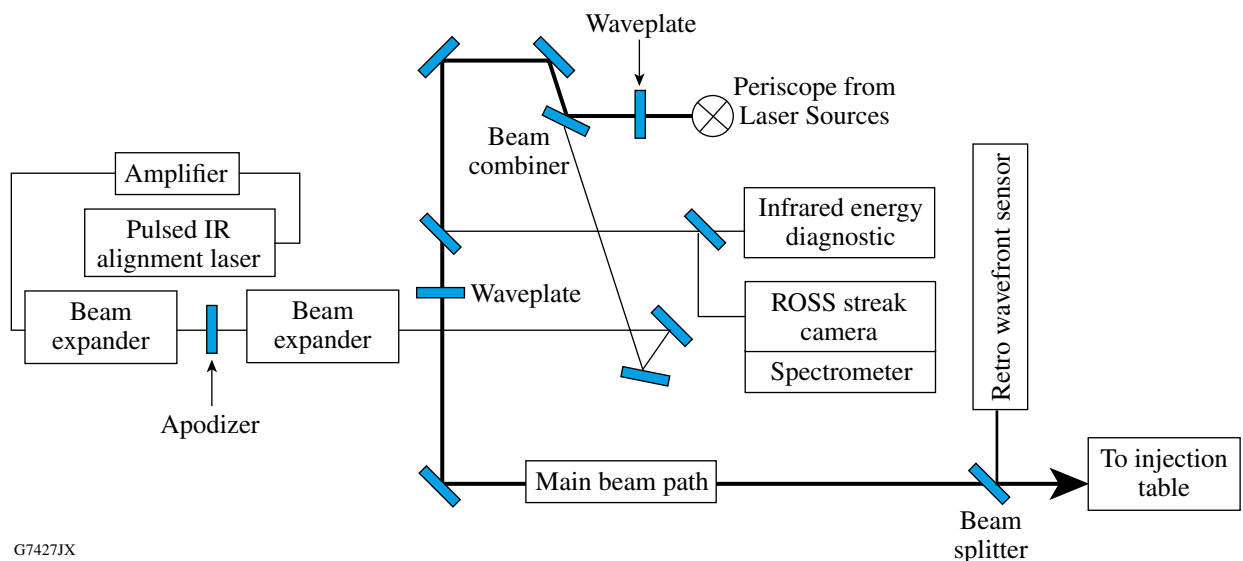
The Precision Optical Timing and Triggering System (POTTS) is an all-fiber-optic signal delivery system that provides precision trigger signals (to 10-ps rms) to the ultrafast diagnostics and pulse-shaping systems as well as ultrafast timing fiducials. Each short-pulse beamline is equipped with a POTTS system that provides eight ultrafast pickets with 40-ps spacing.

### 2.4.4.3 Alignment systems

Laser alignment begins as the beam emerges from the fiber optics in the Laser Sources area and continues to the target. The OMEGA EP alignment system partitions this activity into four distinct sections: (1) laser sources; (2) beamline to transport-spatial-filter output; (3) compressor and short-pulse transport; and (4) frequency-conversion crystals to target. The alignment systems rely on sensor systems and control points modeled on the OMEGA system, largely centering the beam on a single cross hair and then aligning the crosshair to other crosshairs while maintaining the pointing of the laser beam with far-field detectors.

Pointing and centering cameras are used at each of three stages in the laser sources, along with computer-actuated mirrors that can be used to compensate for small amounts of alignment drift. Throughout the system, including the laser sources, large alignment errors at any stage require corrective maintenance.

Each of the main beams has an alignment laser at 1053 nm located on the infrared alignment table (IRAT), shown in Fig. 2.58. The IRAT tables are located adjacent to the injection tables, just



G7427JX

Figure 2.58  
Layout of the infrared alignment table. Either the beam from Laser Sources or the IR alignment laser can be selected for injection into the beamline via the injection table.

south of the transport-spatial-filter vacuum vessels. The main beam passes sequentially through the IRAT, the injection table, and the transport spatial filter. The alignment beam is injected into the main beam path through the beam combiner on the IRAT and is propagated through the beamline. A series of crosshairs align the beam using video and beam-motion control systems. For the short-pulse beamlines, the alignment beam enters the grating compressor chamber, where it traverses either the upper or lower compressor to the table containing the short-pulse diagnostics. The IRAT tables also contain a number of diagnostics to measure quantities such as the beam energy, temporal shape, and spectrum.

The beam from the IRAT proceeds to the injection table (Fig. 2.59). A small fraction (0.5%) of the beam is transmitted through a leaky mirror to a number of diagnostics including pointing and centering alignment sensors. The alignment detectors are video-rate CCD cameras that capture pulsed data for analysis with computer software identical to that used on OMEGA. Each of the alignment sensors features low- and high-resolution settings so that both coarse and fine alignment can be electronically sensed. Another portion of the beam is routed to a megapixel scientific (16-bit) near-field camera. A test shot illuminating the system crosshair is captured on this camera. The image is reduced for beam quality as well as alignment prior to executing shots.

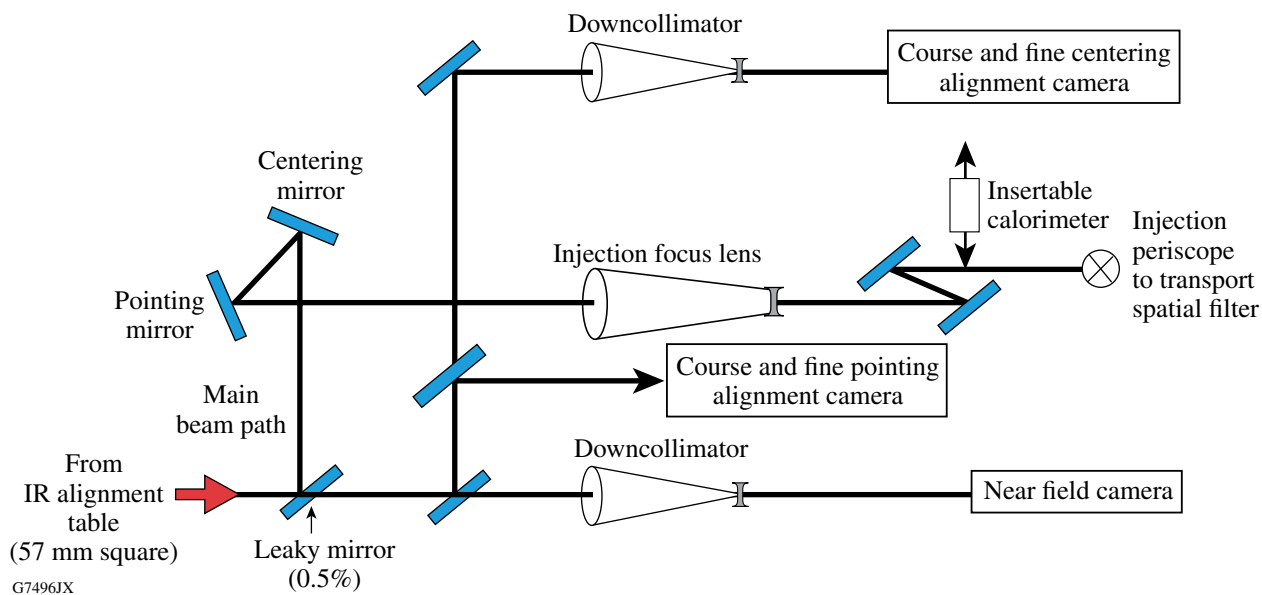


Figure 2.59

Layout of the injection table, indicating the locations of the alignment sensors and the beam path to the transport spatial filter located directly above.

## 2.4.5 Operations

OMEGA EP will be operated in the same way as the OMEGA Laser Facility. Existing LLE infrastructure includes specific instructions for operations that are directly extensible to the OMEGA EP architecture. The Laser Facility Organization and Regulation Manual<sup>51</sup> addresses critical operations issues and specifies how scientific programs are allocated system time, how system time is scheduled, and how training and safety programs within the facility are conducted. The OMEGA EP Facility uses a four-volume set of documentation for configuration management and control of operations procedures. Volume VII describes the system architecture, Volume VIII contains all of the written procedures for operations, Volume IX describes the startup and shutdown procedures, and Volume X addresses the periodic maintenance program. These volumes are available from the “OMEGA Operations” page of the LLE Web site.

Execution of effective and safe laser and experimental shots requires a complete and detailed specification of the facility configuration. It includes detailed laser operating parameters, extensive advance planning, and many hours of system preparation prior to and during the actual shot day. The Shot Request Form (SRF) is the primary vehicle for recording and communicating the specifications for a shot. The SRF's are handled identically between laser systems via a common SRF Web page. The SRF enables the requestor to specify whether the shot is an OMEGA, OMEGA EP, or joint system shot.

Supplemental tools and forms are used in planning and communicating the sequences of related shots that are referred to as “campaigns.” The SRF is a database object that is created within the LLE computer system primarily via inputs made through a Web-based SRF user interface on the “OMEGA Operations” page of the LLE Web site. This interface consists of a series of pages or screens known as “forms” that collect information of various types. The SRF pages for OMEGA EP include

- General: laser system, PI's, campaign identification, planned date, planned order
- Sources: short/long pulse width, pulse shape, etc.
- Target: characteristics, unique identifier, etc.
- Beams: groups defined by energy, pointing, focus
- Diagnostics: fixed and re-entrant instruments, timing, filtration, alignment, etc.

On the shot day, SRF data values are also accessed directly by the Laser Control System and assist the operators in preparing for and executing the shot. Once an SRF has been used to specify a system shot, it is considered expended and is not reused. The SRF data values are retained in the database indefinitely but may be retrieved for use in data assessment or for the creation of new SRF's.

## 2.5 TARGET DIAGNOSTIC CAPABILITIES

This section surveys the large number of experimental diagnostics available on the OMEGA Laser System to support the full range of experimental activities. Recent enhancements to these diagnostics are highlighted. This unique set of diagnostics will provide a basis for the experimental activities planned for the next five-year period. **Potential NLUF users should note that some of the diagnostic systems require significant effort to field and analyze. Thus, not all of the diagnostic systems are made routinely available to NLUF users.**

### 2.5.1 Charged-Particle Diagnostics

Nuclear reactions in the fusion fuel produce energetic neutrons and a variety of charged particles including  $p$ , D, T, and  $^4\text{He}$ . The primary diagnostics used on OMEGA to measure these charged particles are two magnet-based charged-particle spectrometers and a number of wedge-range-filter proton spectrometers, which have all been installed in collaboration with the MIT Plasma Science and Fusion Center.

The nuclear reactions and the information that they can provide are surveyed in Sec. 2.5.1.1. Section 2.5.1.2 describes the charged-particle spectrometers, Secs. 2.5.1.3 and 2.5.1.4 the wedge-range-filter proton spectrometers, and Sec. 2.5.1.5 the proton temporal diagnostic, which measures the time history of protons produced by fusion reactions. **The track-based charged-particle-diagnostic systems are available to external users only by special arrangement. Please consult the NLUF Manager if you need to use these diagnostics.**

#### 2.5.1.1 Nuclear reactions producing charged particles

Charged particles and energetic neutrons arise from a number of nuclear reactions:

(a) *Primary Reactions from DT Fuel*



The 14.1-MeV neutron yield is routinely measured using copper activation and scintillator-based detectors (Sec. 2.5.8). Alpha particles ( $^4\text{He}$ ) undergo substantial energy loss in the compressed plastic shells of typical non-cryogenic OMEGA targets and therefore cannot routinely be used as a diagnostic. For very thin shells the alpha particles escape with little energy loss since the areal densities are very small ( $\sim 1 \text{ mg/cm}^2$ ). In this case, a cross-calibration has been made directly between the neutron detectors and the charged-particle spectrometers using the implosion of thin glass-shell targets filled with DT.<sup>52</sup>

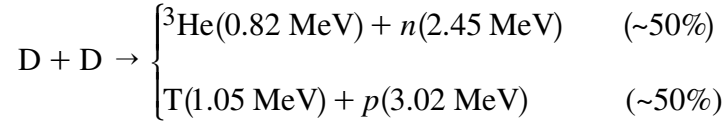
A second branch of the DT reaction emits a 16.7-MeV gamma ray,<sup>53</sup> with a branching ratio of  $<10^{-4}$ :



The gammas are produced via the decay of  $^5\text{He}$  from an excited state to a ground state.

(b) *Primary Reactions from  $D_2$  Fuel*

In  $D_2$  fuel, the primary nuclear reactions comprise two branches with approximately equal probabilities:



The neutron yields, measured using indium activation and scintillator-based detectors (Sec. 2.5.8), are routinely used to diagnose the yield of the DD implosions.

(c) *Secondary Reactions from  $D_2$  Fuel*

The  ${}^3\text{He}$  and triton products from the above two reactions [Eq. (2.5.3)] can combine with fuel deuterium in the following “secondary” reactions:



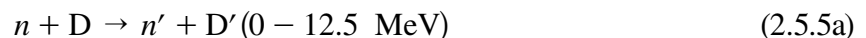
where  $\text{T}^*$  and  ${}^3\text{He}^*$  indicate tritons and  ${}^3\text{He}$  nuclei that can have energies less than their corresponding birth energies [Eq. (2.5.3)] due to slowing down in the target.

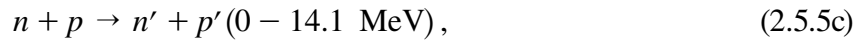
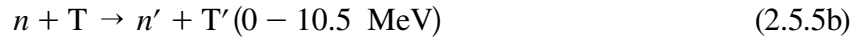
With models of the fuel region, neutron and proton yields from these reactions can be used to estimate the fuel areal density  $(\rho R)_F$ .<sup>54–60</sup> The estimated value depends on the model used. For example, the  $(\rho R)_F$  obtained from an “ice-block” model (a uniform fuel and source) is  $\sim 34\%$  larger than that obtained from a hot-spot model (a point source surrounded by uniform fuel).<sup>54,58</sup> *LILAC* simulations suggest that the ice-block model is more appropriate for current OMEGA experiments.

Information about the shell areal density can be inferred from the proton spectra. The downshift of the energetic protons [Eq. (2.5.4b)] is relatively insensitive to temperature (for gas-filled and cryogenic targets on OMEGA) and depends primarily on the shell areal density.<sup>54</sup> Secondary proton spectra measured using the charged-particle spectrometers and the wedge-range-filter proton spectrometers (Sec. 2.5.1.3) have been used to provide information about the shell areal density.<sup>54</sup>

(d) *Knock-On Reactions in DT-Filled Targets*

Up-scattered DT fuel nuclei (“knock-ons”<sup>61</sup>) and knock-on protons from the shell<sup>62</sup> are produced in the following reactions:





where  $n$  indicates the 14.1-MeV neutron from the DT reaction and  $T'$ ,  $D'$ , and  $p'$  indicate tritons, deuterons, and protons, respectively, at energies in the ranges shown in parentheses. Triton and deuteron spectra measured using the charged-particle spectrometers<sup>63</sup> have been used to identify the fuel and shell areal densities in the target. The number of each of these particles in the high-energy peak in the spectrum is proportional to the fuel areal density, and the downshift of this peak provides a measure of the shell areal density.<sup>61,63,64</sup>

For areal densities  $\rho R \lesssim 100 \text{ mg/cm}^2$ , the proton knock-on yield in a suitably chosen energy range (10.5 to 12.0 MeV) is proportional to the areal density of the shell.<sup>65</sup> Proton knock-on spectra have been measured using the charged-particle spectrometers and wedge-range-filter spectrometers.<sup>63,64,66</sup>

(e) *Tertiary Reactions from DT Fuel*

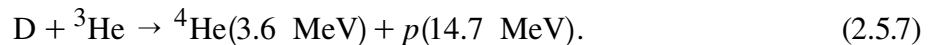
“Knock-on” tritons and deuterons can further interact with thermal DT fuel nuclei, producing the “tertiary” reactions:<sup>67–69</sup>



where  $D'$  and  $T'$  indicate the knock-on particles.

(f) *Primary Reactions from D<sup>3</sup>He Fuel*

Primary nuclear reactions from D<sup>3</sup>He fuel comprise the primary DD reactions [Eq. (2.5.3) above] plus the following reaction:

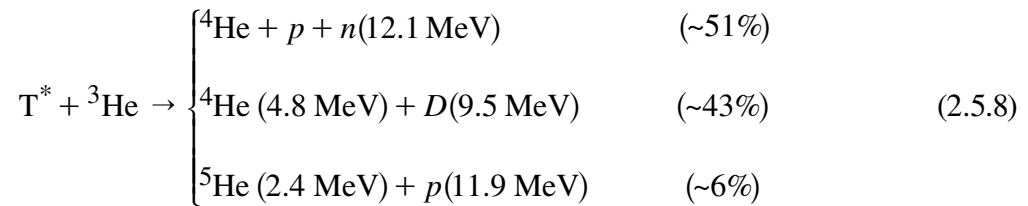


Similar to the secondary protons, the downshift of the primary D<sup>3</sup>He protons<sup>70</sup> is proportional to the total areal density of the compressed target. Being relatively insensitive to temperature for the areal densities of interest in OMEGA implosions, this diagnostic has been successfully used to infer compressed-shell areal densities in D<sup>3</sup>He-filled targets.<sup>64,70–74</sup> The range of these protons limits this diagnostic to values of areal density up to  $\sim 300 \text{ mg/cm}^2$  (Refs. 70 and 73).

The temperature of the fuel ions at burn time can be estimated from the ratio of DD neutrons [Eq. (2.5.3a)] to D<sup>3</sup>He protons.<sup>73</sup>

(g) *Secondary Reactions from D<sup>3</sup>He Fuel*

In addition to the DD secondary reactions of Eq. (2.5.4), the following secondary reactions can occur in D<sup>3</sup>He-filled targets:



However, with their very low reaction rates, the T<sup>3</sup>He reactions provide observable signals only in special circumstances. For example, the implosion of a thin, T<sup>3</sup>He-filled glass shell can reach very high temperatures, leading to an observable signal for the 9.5-MeV deuterons. In this case, due to the relatively low areal densities, the emergent deuterons are relatively monoenergetic and consequently have been used to calibrate the two charged-particle spectrometers.

**2.5.1.2 Magnet-based charged-particle spectrometers**

Two charged-particle spectrometers (CPS's) on OMEGA can measure the spectra of several particle species (e.g., *p*, D, T, <sup>3</sup>He, <sup>4</sup>He) simultaneously. They use 7.6-kG permanent magnets for energy discrimination and CR-39 for particle detection (see Refs. 52, 75, and 76 for detailed descriptions of these instruments). The design of the magnet and the system geometry makes possible the study of a very wide range of particle energies (0.1 to 30 MeV for protons), while the CR-39 detectors count individual particles and provide discrimination among different particle types. The dynamic range of a CPS is determined by the size of the entrance aperture, the distance from the target, and the minimum and maximum number of particles per unit area that can be measured with CR-39; particle yields from ~10<sup>7</sup> per MeV to at least 10<sup>16</sup> per MeV can be accommodated. The energy resolution is better than 4% and the absolute energy calibration is better than 0.1 MeV.

The range of particle types, energies, and yields covered by a CPS has made possible the study of many types of implosions. Of particular importance are (1) knock-on D and T spectra from room-temperature and cryogenic DT-filled targets, allowing the study of fuel areal density;<sup>63</sup> (2) knock-on proton spectra from DT-filled CH targets for the study of shell areal density;<sup>63</sup> and (3) D<sup>3</sup>He and DD protons from D<sup>3</sup>He-filled targets for the study of shell areal density.<sup>73</sup> The fact that there are two CPS's viewing the implosion from different directions makes possible rudimentary symmetry measurements.

**2.5.1.3 Wedge-range-filter proton spectrometers**

A second type of spectrometer, known as the wedge-range-filter (WRF) spectrometer, was developed specifically for the study of protons.<sup>72,52,54</sup> This simple and compact spectrometer uses a CR-39 detector, which records the tracks of individual particles and has energy discrimination for protons in the range of 0.5 to 8 MeV, behind a filter whose thickness varies with position (with a wedge-shaped cross section). The energy of each detected particle is measured, and the thickness of the filter it passed through is used to calculate the energy the particle had before it encountered the

filter. Theoretically, a filter with an appropriate range of thicknesses could be used to find the spectra of protons from 0.5 MeV up to an arbitrarily high energy. The first-generation WRF spectrometers, deployed in 2001, used Al filters with thickness varying from 400 to 1800  $\mu\text{m}$  to provide coverage of proton energies from 8 to 18 MeV.

Unlike the CPS's, these spectrometers cannot measure spectra of different particle species simultaneously and cannot cover a large energy range. However, they can measure proton spectra at much lower yields than the CPS's (by more than two orders of magnitude) and at many different angles simultaneously (an experiment using six is described in Sec. 2.3.4.4). As a result, they have allowed several important areas of study. Their high sensitivity has made possible the accurate measurement of secondary  $\text{D}^3\text{He}$  protons from  $\text{D}_2$ -filled targets, which generally have yields lower than the CPS limit. This has led to the WRF spectrometer becoming the standard instrument for the study of shell areal density for  $\text{D}_2$ -filled targets (Ref. 54). The high sensitivity allows the measurement of primary  $\text{D}^3\text{He}$ -proton spectra in cases where the yield is low (e.g., in mix experiments involving a pure  $^3\text{He}$  fill in shells having CD sublayers<sup>77</sup> and in indirect-drive experiments using  $\text{D}^3\text{He}$ -filled targets<sup>78</sup>). The fact that many WRF spectrometers can be deployed simultaneously has made possible many studies of areal density symmetry with  $\text{D}_2$ -filled targets,<sup>54</sup>  $\text{D}^3\text{He}$ -filled targets,<sup>71,79,62,74</sup> and DT-filled targets.<sup>246</sup>

#### 2.5.1.4 High-areal-density wedge-range-filter spectrometers

The 8- to 18-MeV energy range of the original WRF spectrometers proved to be satisfactory until recently, when low-adiabat experiments with  $\text{D}_2$ -filled targets and thick CH shells (Secs. 2.3.5.2, 2.3.5.4, and 2.3.8.5) began to result in areal densities high enough to require a low-energy measurement limit well below 8 MeV. For several years it has been anticipated that the areal densities of cryogenic  $\text{D}_2$  targets would approach 200  $\text{mg}/\text{cm}^2$  and result in secondary proton energies as low as 3 MeV.

As a consequence, a new WRF design has been developed utilizing a wedge filter that expands the energy coverage from 3 to 25 MeV. The material used for the filter is zirconia, with a thickness varying from 15  $\mu\text{m}$  to 1600  $\mu\text{m}$  (used in conjunction with a 25- $\mu\text{m}$  Al blast shield). Twenty five of these have been fabricated, and they have performed well. Final calibration of the new WRF's using data from OMEGA and from the MIT accelerator is underway.

#### 2.5.1.5 Proton temporal diagnostic

A proton temporal diagnostic (PTD) has been developed to record the fusion reaction-rate history of protons generated from the thermonuclear burn of  $\text{D}^3\text{He}$ - and  $\text{D}_2$ -fueled targets on OMEGA.<sup>79</sup> The primary purpose of the PTD is to measure the temporal history of primary  $\text{D}^3\text{He}$  protons generated via Eq. (2.5.7) with an energy of 14.7 MeV. The PTD is also sensitive to secondary protons (12.6 to 17.5 MeV) and primary neutrons (2.45 MeV) from  $\text{D}_2$ -fueled targets, according to Eqs. [2.5.4(b)] and [2.5.3(a)], respectively.

The PTD detector system, shown schematically in Fig. 2.60, was developed as a modification of the existing OMEGA neutron temporal diagnostic—the cryoNTD.<sup>80</sup> The PTD was designed to operate in one of the OMEGA ten-inch manipulators (TIM's). It is based on a fast scintillator (BC-422) that acts as a proton-to-light converter shielded by two thin (100- to 200- $\mu\text{m}$ ) Al and Ta foils

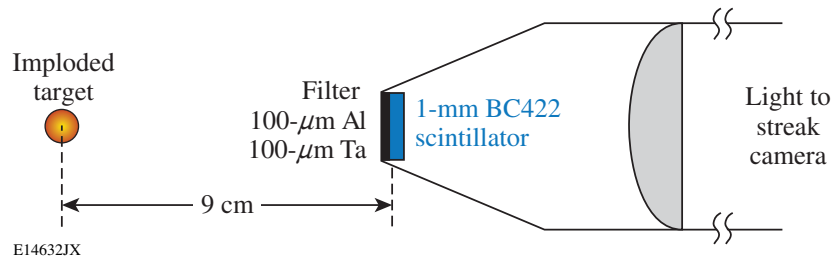


Figure 2.60

Schematic of the proton temporal diagnostic (PTD) detector system on OMEGA. The detector is based on a fast scintillator that acts as a proton-to-light converter protected by Al and Ta foils against x-ray and direct laser illumination. An optical system transfers the scintillator light to a streak camera.

against x-ray and direct laser illumination. An optical system, including 11 lenses and 2 mirrors,<sup>80</sup> transfers the scintillator light through the TIM and the vacuum window along a 3.5-m optical path to a high-speed optical streak camera.<sup>81</sup> The front end of the optical system is mounted in the TIM and inserted close to the target. Since the PTD uses the existing cryoNTD optics and mechanical assembly, the PTD scintillator is located 9 cm from the target, the required standoff distance for OMEGA cryogenic target operations. With additional optics, the PTD scintillator can be placed closer to noncryogenic targets to improve the temporal resolution. A simultaneously recorded optical fiducial provides a reference for accurate timing with respect to the incident laser pulse.

Figure 2.61(a) shows a sample image, recorded by a charge-coupled-device (CCD) camera attached to the streak camera, for a  $D^3He$  implosion with a proton yield of  $5.7 \times 10^7$ . The fiducial train is at the top of the image and the scintillator output is in the center. After the PTD signal is averaged across the central portion of the scintillator, the streak-camera flat-field and geometric distortions are removed and the CCD background from the bottom portion of the image is subtracted to create the final temporal trace [Fig. 2.61(b)]. This trace has three distinct components: an early x-ray peak resulting from hard x rays<sup>82</sup> of energy  $>30$  keV, presumed to originate via bremsstrahlung from suprathermal electrons created by the two-plasmon instability in the target corona, and the shock and compression proton peaks. In contrast to the NTD, where the neutron yield at shock convergence is  $\sim 100$  times smaller than the yield at peak compression, the shock and compression proton peaks of the PTD are comparable for  $D^3He$  implosions (because of the stronger temperature dependence of the proton-production cross section).

The BC-422 scintillator has a very fast rise time ( $<20$  ps) and a decay time of  $\sim 1.2$  ns, as seen in the x-ray peak of Fig. 2.61(b). The scintillator decay from x rays creates a background for the proton signal. Since it is difficult to calculate this background level, the filter thickness was optimized experimentally. The PTD background depends on many parameters such as the laser energy, pulse shape, and target design. The filter-thickness optimization required a series of identical shots where all parameters except the filter thickness were fixed.

The nose cone is the main difference between the PTD and the cryoNTD.<sup>80</sup> The design of the PTD nose cone satisfies several criteria: (1) it is light tight to prevent direct laser illumination;

(2) it survives ablation, target debris, and the thermal impulse from the target implosion; (3) it is transparent to protons with energies larger than 10 MeV; and (4) it absorbs as much of the soft-x-ray radiation as possible. Tantalum was chosen as the PTD filter material because of its strength and hardness and because 25-mm-diam tantalum foil disks are commercially available.<sup>83</sup> An additional 100- $\mu\text{m}$  Al filter placed in front of the Ta foil reduces a spurious PTD signal caused by hard x rays generated from suprathermal electrons hitting the foil; this filter reduces the hard-x-ray background by a factor of four, while the proton signal is reduced only 10% to 20% depending on the proton energy. A 0.3-mm-thick plastic spacer ring is inserted between the filter foils and the scintillator to prevent the scintillator from melting due to the heating of the filters by light, x rays, and plasma from the target. It is possible to change the PTD nose cone to the cryoNTD nose cone or to change the PTD filter-foil/scintillator combination within the 45-min OMEGA shot cycle. Tests done with 100- $\mu\text{m}$  Ta foils placed 9 cm from the target show that these foils survive more than 50 direct-drive OMEGA shots without damage.

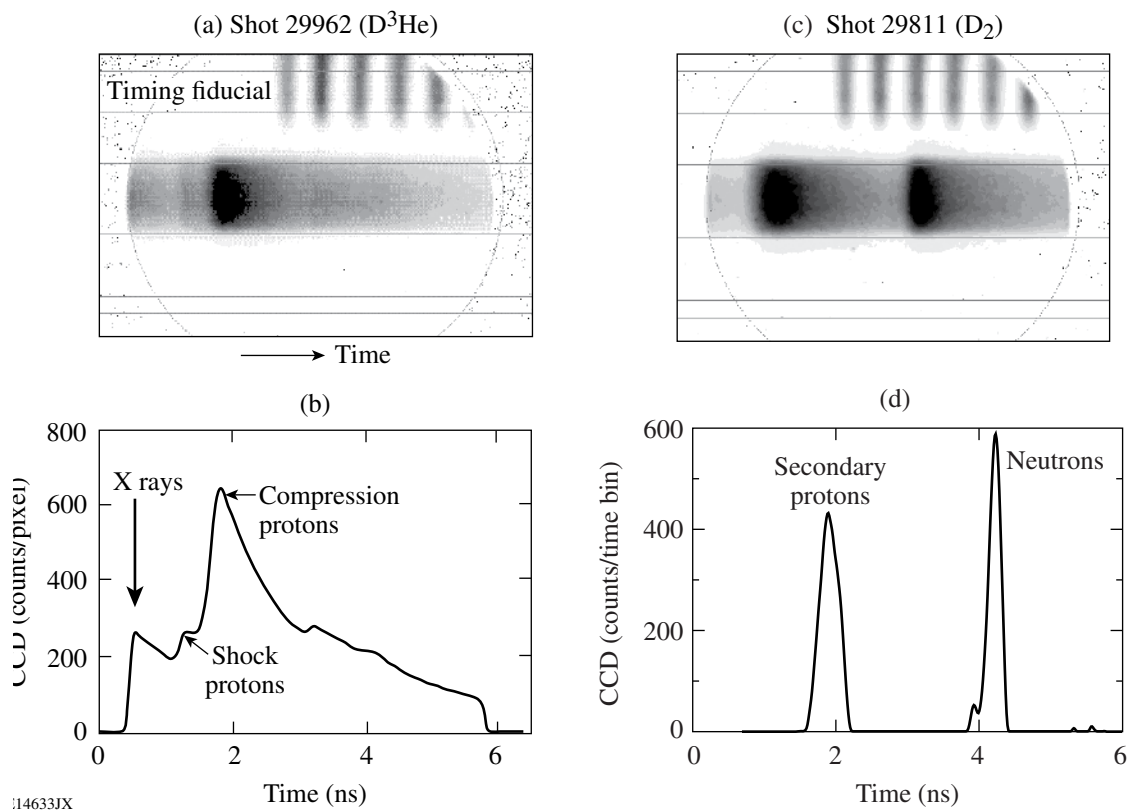


Figure 2.61

(a) The PTD streak camera image from shot 29962, in which a 24- $\mu\text{m}$ -thick plastic shell filled with 18 atm of D<sup>3</sup>He was imploded on OMEGA with a 1-ns pulse shape and 23 kJ of energy. (b) The PTD signal averaged across the central portion of the scintillator with the CCD background subtracted and with the streak-camera flat-field and geometric distortions taken into account. (c) Same as (a) but for shot 29811, in which a 20- $\mu\text{m}$ -thick plastic shell was filled with 15 atm of D<sub>2</sub>. (d) Same as (b) but for shot 29811 and with correction made for the 1.2-ns scintillator decay time.

Absolute timing is established using the OMEGA fiducial system. The OMEGA fiducial beam consists of a series of eight  $0.53\text{-}\mu\text{m}$  pulses spaced 548 ps apart and is synchronized to the OMEGA laser pulse with a jitter of less than 20 ps. The optical fiducial is amplified separately from the main laser pulse, split, and distributed to various diagnostic instruments for precision timing. The fiducial pulse train is recorded on the P510 ultraviolet streak cameras<sup>84</sup> that are used to record the laser pulse shapes for each of OMEGA's 60 beams. The common optical fiducial serves as a reference for both the proton signal and the laser pulse, enabling very accurate timing of PTD signals relative to the laser pulse. The recorded fiducial pulse [Fig. 2.61(a)] is fit by a train of eight Gaussian pulses spaced at a well-characterized period of 548 ps.<sup>84</sup> This reduces the influence of noise on the determination of the timing reference.

The PTD is designed for multiple fusion-reaction products and multiple standoff distances. Its fiducial has ten delay fibers with nominal delays from 1 ns to 10 ns in steps of 1 ns. These fibers were characterized at the Lawrence Livermore National Laboratory with an accuracy of better than 3 ps using 45-ps-FWHM,  $0.53\text{-}\mu\text{m}$  laser pulses (the same wavelength as the OMEGA fiducial). The PTD streak camera has  $3\times$ ,  $5\times$ , and  $10\times$  sweep cards that create approximately 3-ns, 5-ns, and 10-ns time windows with pixel resolutions of 7.5 ps, 13 ps, and 23 ps, respectively.

While the PTD is primarily intended for use with  $\text{D}^3\text{He}$  implosions, it is also used for  $\text{D}_2$  implosions. A typical PTD streak camera image for a  $\text{D}_2$  implosion with a neutron yield of  $1.3 \times 10^{11}$  is shown in Fig. 2.61(c) with its deconvolved signal in Fig. 2.61(d). In a  $\text{D}_2$  implosion, the first PTD peak is the signal from secondary protons with energies of 12.6 to 17.5 MeV and the second peak is the signal from the 2.45-MeV DD neutrons. (The structure near the start of the neutron signal indicates shock-produced neutrons.) Although the yields of secondary protons and primary neutrons differ by a factor of 1000, the PTD signals are comparable due to the different interaction mechanisms of protons and neutrons within the scintillator.

The PTD neutron signal from a  $\text{D}_2$  implosion is used to determine the time of peak neutron production (the bang time) similar to the NTD.<sup>85</sup> The bang times measured by the two instruments correlate to  $\sim 30$  ps (rms).

The secondary-proton peak in the PTD signal seen in Fig. 2.61(d) is used to measure the secondary-proton yield in  $\text{D}_2$  implosions above  $1 \times 10^7$ . The average energy downshift of these protons is routinely used on OMEGA to measure the total areal density of the target<sup>72</sup> (see also Sec. 2.5.1.3). The average energy downshift of the secondary protons is inferred from the PTD, based on the time-of-flight difference between the secondary-proton and the primary-neutron peaks. From the secondary proton's energy downshift, the total areal density can be calculated by using plasma-stopping formulas<sup>86</sup> as with wedge-range-filter spectrometer data (Sec. 2.5.1.3). A comparison with the total-areal-density data inferred from the charged-particle spectrometers shows significant differences,<sup>87</sup> probably due to known areal-density asymmetries<sup>54</sup> on OMEGA.

Protons emitted from the  $\text{D}^3\text{He}$  reaction lose energy when passing through the compressed capsule shell. The areal density of target material through which the protons pass determines the amount of energy loss. Therefore, by measuring the proton-production history with the PTD and

simultaneously a time-integrated proton-energy spectrum by charged-particle spectroscopy, the temporal evolution of the target areal density can be inferred. The areal-density evolution in  $D^3He$  implosions was first studied in Ref. 87 with the assumption that the  $D^3He$  proton-production history is proportional to the  $D_2$  neutron-production history. With the development of the PTD, the areal-density evolution can now be inferred using the proton-production history.<sup>79</sup>

Further information on the PTD can be found in Ref. 87.

## 2.5.2 X-Ray Imaging

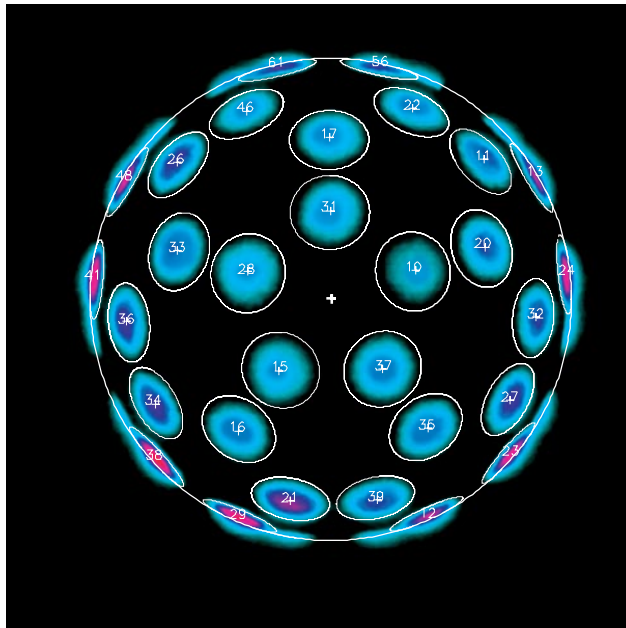
Imaging of laser-generated plasma x-ray emission can be used to determine the size, shape, temperature, and areal density of compressed plasmas on OMEGA. X rays are imaged using pinhole cameras (Sec. 2.5.2.1), framing cameras (Sec. 2.5.2.2), Kirkpatrick–Baez (KB) microscopes<sup>88</sup> (Sec. 2.5.2.3), and a gated monochromatic x-ray imager (Sec. 2.5.2.4). Some pinhole cameras used on OMEGA are fixed on the target chamber; others are deployable in the ten-inch-manipulators (TIM's). TIM's can also be used to deploy multiple-image, time-resolving, x-ray framing cameras. The images from these diagnostics are recorded either with film or electronically with CCD cameras or other x-ray-sensitive cameras (Sec. 2.5.2.5).

### 2.5.2.1 X-ray pinhole cameras

X-ray pinhole cameras are routine diagnostics on the OMEGA target chamber and are typically used on every target shot where the UV intensity is sufficiently high ( $>10^{14}$  W/cm<sup>2</sup>) to generate x-ray emission from the laser target. There are sufficient pinhole cameras that spherical alignment targets can be viewed from several directions (typically six to eight), allowing each focused beam spot position to be measured accurately.

Laser-drilled pinholes in thin metal (Ta) substrates provide the desired x-ray imaging. The pinhole diameters are currently 10  $\mu\text{m}$ , with a typical target-to-pinhole distance of 17 cm and a 68-cm pinhole-to-image distance (a magnification of 4). The TIM-based pinhole cameras can be operated with a magnification of 1 to 8. The pinhole camera resolution is limited to  $\sim 11$   $\mu\text{m}$  by geometrical blurring. The pinhole cameras are outfitted with electronic readout using charge-injection devices<sup>89</sup> (CID's), providing near-instantaneous images of target x-ray emission.

Figure 2.62 shows an example of an image obtained on a 60-beam pointing shot. The target is a 4-mm-diam, Au-coated plastic sphere. Each beam produces an x-ray spot  $\sim 600$   $\mu\text{m}$  in diameter by conversion of the absorbed UV light into x rays. By correcting for view-angle and conversion-efficiency effects, the original UV light fluence distribution (beam shape) is obtained, allowing for both the beam shape and the beam position to be accurately inferred.<sup>90</sup> After analysis, the beam alignment can be determined and any large pointing errors corrected. It is possible to reduce the beam-pointing errors to  $<10$   $\mu\text{m}$  (rms) using this method.<sup>91</sup> Using similar targets, a method by which the beam-to-beam, peak on-target intensities are determined and rebalanced (made equal) has been developed.<sup>90</sup> This relies upon images obtained with cross-calibrated, CID-equipped pinhole cameras.



E14702JX

Figure 2.62

CID-recorded image from an x-ray pinhole camera taken on an OMEGA pointing shot. The target is a 4-mm-diam, Au-coated plastic sphere. Analysis of the x-ray image allows the beam position (pointing), shape, and peak fluence to be inferred.

The CID-equipped pinhole cameras are used in the analysis of cryogenic target implosions to determine the target position at shot time.<sup>92</sup> This relies on determining the target center in fixed pixel positions in the CID-recorded images. By using the five fixed pinhole cameras it is possible to determine the target position at the start of the laser pulse to an accuracy of  $\sim 2 \mu\text{m}$  by triangulation. The cryogenic target position is determined relative to a room-temperature target shot with the target fixed on a stalk. Due to the presence of a sealed vacuum window and the large pinhole standoff distance (17 cm), the pinhole cameras can be used on all shots with targets containing DT.

### 2.5.2.2 X-ray framing cameras

X-ray framing cameras<sup>93-99</sup> are used for two-dimensional, time-resolved, x-ray imaging. Four framing cameras are available, of which two are operated with a temporal resolution of  $\sim 40$  ps and two with 80, 200, 300, 400, 500, or 1000-ps resolution by the use of interchangeable pulse-forming modules. The framing cameras are operated from ten-inch manipulators (TIM's).

The key component of a framing camera is a microchannel plate (MCP) that has a gold photocathode coated onto its surface in the form of a microstrip line. A two-dimensional x-ray image is formed on the photocathode, producing photoelectrons that are accelerated down the channels of the MCP and multiplied by a short-duration, high-voltage pulse propagated along the microstrip line. Different sections of the microstrip line are sequentially gated. The electrons exiting the MCP strike a phosphor plate, producing an optical image.

The optical image is recorded with either film or CCD camera arrays<sup>100</sup> with  $4096 \times 4096$  pixels of  $9\text{-}\mu\text{m}$  size. Currently, four of the six TIM's on the OMEGA target chamber are outfitted to accept CCD recording systems, and up to three CCD cameras can be used simultaneously during one shot. In the future, all TIM's will be capable of using CCD's simultaneously. The CCD cameras

are cooled to about  $-20^{\circ}\text{C}$  during shot operations to reduce the CCD dark-current noise. All the framing cameras are now configured with remote electronic controls that allow changes to the camera's timing and MCP voltages through a computer interface, eliminating the need to cycle the framing camera to atmosphere every time these changes are required.

The two fast framing cameras are configured with a four-strip MCP, but the slow framing cameras can be configured to operate with a four-strip, two-strip, or single-strip MCP depending on the needs of the particular experiment. A single-strip MCP is available for use, while a two-strip MCP can be made available with sufficient lead time.

### 2.5.2.3 Kirkpatrick–Baez microscopes

The Kirkpatrick–Baez (KB) microscopes used on OMEGA are derived from an original LLE design.<sup>101</sup> The optic consists of four mutually perpendicular, stacked concave mirrors with a radius of curvature of  $\sim 27$  m. Five KB optics are available for use on OMEGA. Their properties and uses are summarized in Table 2.5 and are more fully described elsewhere.<sup>102–106</sup> Three are currently in use, fixed on the chamber as indicated in the table, and two are designed to couple to the PJX streak camera (Sec. 2.5.4). The resolution of the KB optic is limited by aberrations, primarily spherical, which depend on the mirror size. The smaller mirrors have better on-axis ( $\sim 3$   $\mu\text{m}$ ) and off-axis resolution, but subtend smaller solid angles.

The energy range of the optic is determined by the coating on the reflecting surfaces. For optimum broadband imaging, three of the KB optics are coated with Ir, which has the best high-energy response of any elemental amorphous coating. Optic #1 (KB1) is used for simple time-integrated broadband imaging (2 to 8 keV) as is optic #3 (KB3). Both can accept a grating for use in obtaining space-resolved continuum spectra of target core emission.<sup>105</sup> Optic #2 is identical to optic #1 and is installed in the gated monochromatic x-ray imager (GMXI),<sup>103</sup> which is capable of recording monochromatic images of target emission as described in Sec. 2.5.2.4. Another optic (#4) is uncoated (bare Zerodur<sup>102</sup>) to provide for an energy throughput with no appreciable response above 3 keV.

Table 2.5: KB optics available for use on OMEGA.

Optic #	OMEGA chamber location	Mirror size (mm)	Coating	Best resolution ( $\mu\text{m}$ )	Mag	Solid angle	Energy range (keV)	Comments
1	KB1 (H8)	9	Ir	5	12.9	$4 \times 10^{-7}$	2 to 8	4-channel filter pack on film
2	KB2, GMXI (H9)	9	Ir	5	13.6	$4 \times 10^{-7}$	2 to 8	Uses WB4C ( $2d = 26.5 \text{ \AA}$ ) diffractors for monochromatic imaging
3	KB3 (H13)	4.5	Ir	3	20.3	$1 \times 10^{-7}$	2 to 7	High-resolution core imaging; uses grating for continuum spectroscopy
4	—	4.5	None	3	13.6	$1 \times 10^{-7}$	1.5 to 3	High-resolution, low-energy imaging
5	—	9	WB <sub>4</sub> C $2d = 140 \text{ \AA}$	5	13.6	$4 \times 10^{-7}$	7 to 9	High-energy imaging

This optic is suited for the radiography of targets such as driven CH foils.<sup>102</sup> Optic #5 (Ref. 106) has a high-energy response defined by the multilayer coating applied to the reflecting surfaces ( $\text{WB}_4\text{C}$ , with the Bragg plane spacing  $2d = 140 \text{ \AA}$ ) and the standard grazing angle ( $0.7^\circ$ ). This optic is useful for imaging high-opacity targets with higher x-ray energies (7 to 9 keV).

Work has recently begun on a 16-image version of a KB microscope.<sup>107</sup> A framing camera is also under development that will allow gated images of target x-ray emission to be obtained using the 16-image KB optic as the imaging device.<sup>107</sup> The framing camera images will be obtained outside the vacuum system, allowing the instrument to be used on high-yield DT target experiments.

#### 2.5.2.4 Gated monochromatic x-ray imager (GMXI)

The GMXI is an instrument capable of simultaneously resolving x-ray emission from ICF targets in space, time, and spectrum.<sup>103</sup> Jointly developed by LLE and LANL, the GMXI consists of a KB microscope and two monochromator/imager pairs.  $\text{WB}_4\text{C}$  multilayers (with  $2d = 26.5 \text{ \AA}$ ) coated onto smooth Si(111) substrates allow the imaging of narrow energy bands ( $\Delta E \sim 10 \text{ eV}$ ) with no additional blurring due to the monochromator. The imagers can be film packs, CID cameras, or framing cameras. When used in the time-integrated mode, both film packs and CID cameras can be used simultaneously, or up to four CID cameras can be used. Each monochromator turret holds two monochromators at the same angle and can be tuned to a different energy. The optic used in the GMXI (optic #2 of Table 2.5) has a useful energy range from 2 to 8 keV.

#### 2.5.2.5 CID-camera readout system

The CID-camera readout system provides up to 18 electronically recorded, time-integrated x-ray images of an OMEGA target shot. Charge-injection devices<sup>89</sup> (CID's), electronic detectors similar to CCD's, directly record the spatially dependent x-ray flux distribution in imaging instruments. The current cameras use  $800 \times 600$ -pixel arrays with  $38.5 \times 38.5\text{-}\mu\text{m-sq}$  pixels. The cameras are interfaced to all the fixed x-ray pinhole cameras, all the TIM-based, time-integrated x-ray diagnostics (including x-ray spectrometers and NLUF user-supplied instruments), and the KB microscopes (including the GMXI). The image shown in Fig. 2.62 was recorded on a CID camera. Due to their electronic architecture<sup>108</sup> these cameras are durable detectors suited to the extreme radiation conditions that can be generated in the OMEGA target chamber. They provide data even on shots producing high neutron yields (up to  $\sim 10^{14}$  for DT) with the cameras located within the outer radius (1.8 m) of the target chamber.

### 2.5.3 Optical Streak Cameras

The Diagnostic Development Group has operated six optical streak cameras for the past seven years as part of LLE's UV power-balance diagnostic program.<sup>84</sup> Two other cameras have been used to diagnose the laser system's driver lines. All of these cameras use a P510 streak tube<sup>109</sup> with either an S-20 or an S-1 photocathode. These cameras have operated with a reliability in excess of 99.9% on over 7000 shots during the past seven years. The cameras have also accumulated over 70,000 streaks each for system calibration in support of the data analysis. The quality of the data has enabled the OMEGA system to realize high-precision laser pulse shaping as the peak power in each beamline can be measured to 2% accuracy over a 10-ps time interval.

With over 500,000 streak acquisitions to prove the technology and demonstrate its reliability, these streak cameras have provided a successful test bed for the Rochester Optical Streak System (ROSS),<sup>110</sup> a new, complete streak camera system designed and built at LLE with some initial mechanical and optical engineering support from LLNL. The ROSS camera features many system upgrades including significant improvements in the precision focusing and calibration of the system. Since the success of the LLE streak cameras had generated significant interest from other ICF laboratories, the redesign and packaging were also directed toward commercialization. A technology transfer has been negotiated with Sydor Instruments<sup>111</sup> in Rochester that includes licensing of LLE's patented slow-scan calibration technique.<sup>112</sup>

One of the goals for the new system was to build a camera whose performance is limited by the streak-tube electron optics. One distinctive feature of the camera is that it can accept the P510, P820, and PJX tubes from Photonis,<sup>107</sup> as well as the ST-R tube from Photek.<sup>113</sup> The design is general enough that any streak tube with an outer diameter less than 5 in. can be packaged into the camera.

The ROSS camera design incorporates major upgrades to the recording system, the EMI (electromagnetic interference) shielding, and the closed-loop voltage control. The standard recording system now comprises a 1:1 fiber-coupled, back-illuminated CCD. The system gain has been increased to over 100 CCD electrons per 15-keV streak-tube photoelectron and the system noise is less than 10 CCD electrons for background-subtracted frames. This ensures that single photoelectron events are unambiguously detected. The streak tubes' potting shells have been upgraded to mu-metal<sup>114</sup> cylinders. The magnetic field from the 60-Hz radiation from the local power grid had complicated the acquisition of flat-field calibration data. Further shielding has been built into the camera by housing the HV switching supplies for the tube electrodes in mu-metal boxes. Closed-loop voltage control has been implemented on all HV circuits, maintaining voltage stability to better than 0.02% rms. All new streak tube purchases include a baffle electrode that shields the phosphor screen from scattered electrons, significantly reducing the signal-induced noise from pre- and post-streak inputs.

New capabilities in the ROSS camera include (1) remote control for focusing the input optics and inserting the reticles; (2) the addition of an air path for coupling in signals from external sources; (3) a built-in GHz comb generator for time calibrations; and (4) a fiber switchyard for directing fiber-coupled signals to various data channels. The upgraded input optics for the ROSS cameras are shown in Fig. 2.63. The optical inputs are coupled to the streak tube via an Offner triplet.<sup>115</sup> Twelve stepper motors and their control system are installed in the optical calibration module of the camera to allow remote adjustments of the input optics and input slit positions. The fiber input has four-axis ( $x$ ,  $y$ ,  $z$ ,  $\theta$ ) controls. The air path (via the flip-in mirror) has  $y$ ,  $z$ , and slit-width adjustments. The secondary mirror is in a three-point flexure mount behind a motorized iris for aperture control. The final motor translates the selected reticle into position.

A selection of reticles may be inserted at the slit location for spatial resolution verification or flat-field and geometric-distortion calibrations. The acquisition of calibration data has been greatly simplified with the motorized controls and full remote access. The typical geometric distortion calibration dataset shown in Fig. 2.64, comprising the raw data and the corrected image, can be

generated in less than 1 minute. This data was acquired on a slow-scan streak with one of the reticles illuminated by the internal LED (light-emitting diode) in pulsed mode. The point spread function at different locations in the image plane can also be determined from these images.

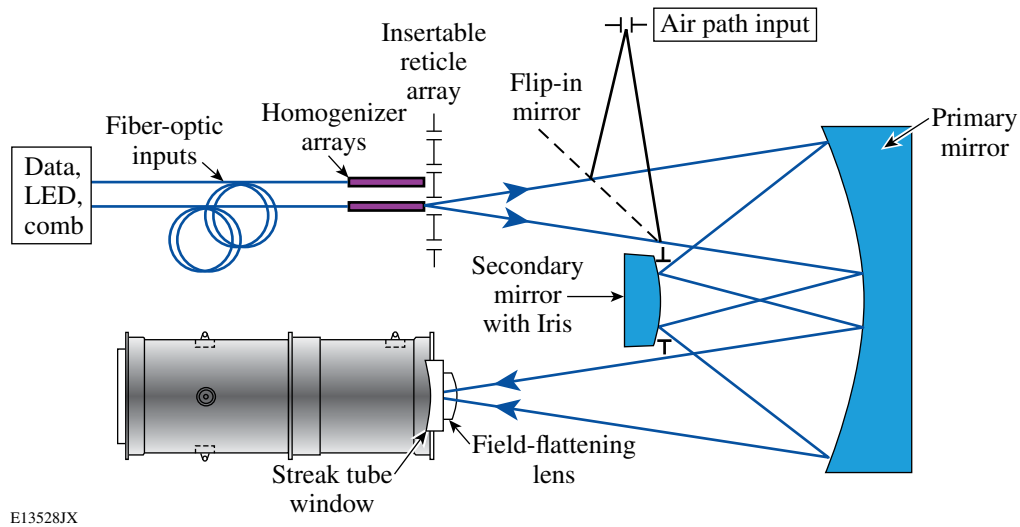


Figure 2.63  
Input optics of the ROSS streak system. A variety of optical inputs are coupled to the streak tube via the primary and secondary mirrors of an Offner triplet. Reticle arrays may be inserted for spatial calibration. Twelve remotely controlled stepper motors are used for precision setup.

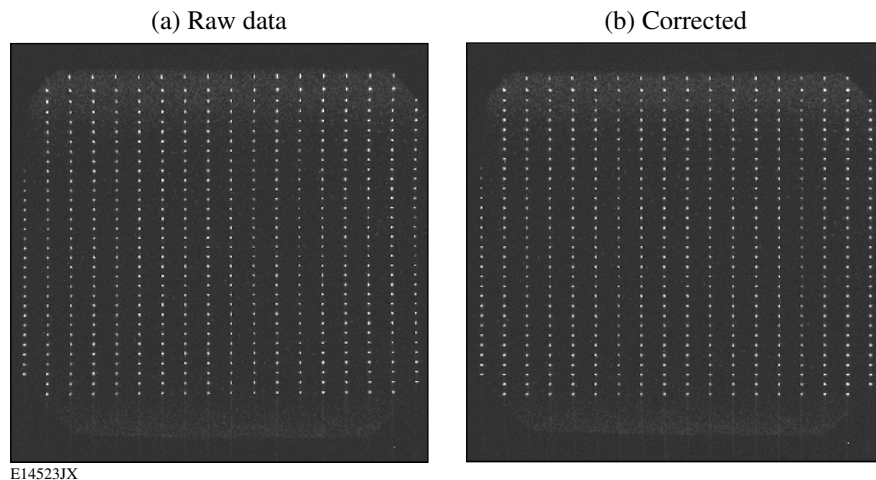


Figure 2.64  
A typical geometric calibration dataset: (a) raw data showing some pincushion distortion; (b) corrected image with the points aligned to  $0.5 \pm 0.3$  pixels. The data were generated on a slow-scan streak with one of the reticles illuminated with the internal LED in pulsed mode.

A motorized flip-in mirror (Fig. 2.63) has been added to the camera to direct a signal from a slit on the side wall of the camera to the photocathode. This allows external sources to be coupled into the camera. The mirror can be sized to allow the air path and the fiber path to be used simultaneously. Time calibrations are performed with the internal 2-GHz comb generator. This is a 664-nm vertical-cavity surface-emitting laser producing 1- to 2- $\mu$ s-duration trains of 30-ps pulses. The comb frequency can be reduced to 500 MHz for calibrating the slower streak speeds. A fiber switchyard has been added so that the internal comb and/or an external comb can be directed to a single channel or multiple data channels. The switchyard is very flexible, with multiple configurations of discrete  $1 \times 2$  and  $2 \times 2$  switches and  $1 \times N$  splitters.

The ROSS is a comprehensive streak camera, with extensive auto-focus and self-calibration capability. It is fully operational from a remote site and therefore may be located in relatively inaccessible places. The self-contained sources and remote functionality ensure optimized system performance in advance of the shot. A base P510-ROSS camera (without the optical calibration module) has been collecting time-resolved backscatter spectra from OMEGA targets for the past year. The system signal-to-noise ratio and dynamic range are significantly improved in comparison with the previous streak camera system.

The PDF-ROSS is the first LLE camera utilizing a P820 streak tube.<sup>109</sup> This tube has better spatial and temporal resolution than the P510 streak tube, but its photocathode length is only 10 mm. The peak current-handling capability of the P820 (0.6 mA) is slightly less than that of the P510 tube (1.0 mA). The peak current increases to 1.8 mA, however, when the tube is operated in inverse mode by reversing the polarity on the quadrupole electrode. The PDF-ROSS has been used to measure IR pulses with a full width at half maximum (FWHM) of 3 to 15 ps on the LLE MTW laser system. It will be used for laser pulse characterization on OMEGA EP, specifically when the pulse duration exceeds that measurable with autocorrelation systems. A train of 5-ps-FWHM laser pulses separated by 70 ps recorded with the PDF-ROSS in inverse mode is shown in Fig. 2.65. The data, recorded at a sweep speed of 0.65 ps/pixel, span almost three decades of dynamic range and have a peak signal-to-noise ratio in excess of 75. The time resolution of this camera is currently limited by the streak speed. Work is in progress on the development of faster drivers with the aim of reaching the 1-ps level.

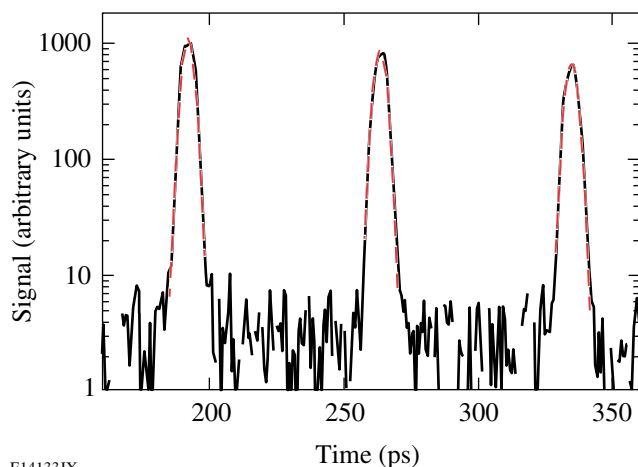


Figure 2.65  
PDF-ROSS (inverse mode) streak record of a train of 5-ps-FWHM laser pulses separated by 70 ps. The data, recorded at a sweep speed of 0.65 ps/pixel, span almost three decades of dynamic range and have a peak signal-to-noise ratio in excess of 75. The dashed curves (red) are Gaussian fits.

All of the optical and x-ray streak cameras can be cross-timed to  $\pm 25$  ps by recording the timing comb (eight pulses separated by 548 ps) from a timing fiducial laser alongside the data. The fiducial laser is a small Nd:glass laser located in the Target Bay that is synchronized to the OMEGA laser to within  $\pm 100$  ps. The fiducial system outputs at the first, second, and fourth harmonics are distributed throughout the OMEGA facility via optical fibers.

#### 2.5.4 X-Ray Streak Cameras

Time-resolved x-ray imaging and x-ray spectroscopy both provide powerful tools for exploring the dynamics of ICF targets. The suite of x-ray streak cameras available on OMEGA includes units built at LLE and fielded in ten-inch manipulators (TIMS's) and six-inch-manipulator streak cameras that were used on Nova.<sup>116</sup> The TIM-based cameras can be outfitted with either imaging optics or Bragg diffraction crystals for spectroscopy. All of the cameras include a fourth-harmonic (263 nm) timing-fiducial channel that is recorded simultaneously with the x rays, allowing cross timing of the x-ray emission with the incident laser pulse to  $\pm 25$  ps. Work is underway to convert all of the x-ray streak cameras to record on CCD's instead of film.

The TIMPJX camera is the first LLE diagnostic to reside in an air bubble when mounted in the TIM boat. The tube body, power supplies, control electronics, and CCD are contained inside the bubble. Communication to and from the bubble is via optical fibers. Power is supplied on a single 28-V dc line and chilled water is circulated to stabilize the internal temperature. There are many advantages to this system: (1) thermal instability issues associated with operating power supplies in a vacuum are avoided; (2) the EMI (electromagnetic interference) shielding is better; (3) vacuum-incompatible materials may be used for high-voltage insulation; and (4) tritium decontamination is simplified as only external surfaces of the bubble are exposed.

The TIMPJX has been successfully deployed on multiple OMEGA campaigns as an imaging diagnostic. It has been coupled to a high-resolution, x-ray imager comprising a 2-D Kirkpatrick–Baez microscope operating at 1.5 keV that relays a target-plane resolution of  $< 5 \mu\text{m}$  at  $6\times$  magnification to the PJx tube operating in inverse mode (Sec. 2.5.2.3). This diagnostic was instrumental in validating dynamic overpressure stabilization of ablation-front perturbation growth.<sup>117</sup> The TIMPJX operating in standard mode has been mated to a multiple imager system consisting of an inline array of pinholes. The line of pinholes is tilted slightly to the photocathode axis so that each pinhole image is through a different chord at the target plane. The resultant streaked images can then be sliced and re-assembled into a movie showing 2-D images with 10-ps time resolution.<sup>118</sup> The 60-mm-long photocathode allows 19 pinhole images to be streaked simultaneously.

The six-inch-manipulator x-ray streak cameras are TIM-based cameras that are used predominantly for spectroscopy, although they have been fitted with imaging front ends for Rayleigh–Taylor experiments where the pointing tolerance is greatly relaxed. Time-resolved x-ray spectroscopy has been used extensively on OMEGA for ablation studies,<sup>119</sup> to investigate mix,<sup>120,121</sup> and to follow the time history of the core temperature and density. While the spectral range of significance extends from 1.35 keV for the Mg K-shell lines to the 13.5-keV Lyman- $\alpha$  line of Kr, the greatest interest has been focused on the K-shell spectra of Ti (used as a shell dopant) and Ar (used as a fuel dopant). The

x-ray streak cameras are an essential component of integrated experiments where spectroscopically determined quantities are compared with the time-dependent measurements of other diagnostics via the timing fiducial.

The current Ultrafast X-Ray Streak Camera project involves building a second TIM-based camera in an air bubble. It will use an x-ray version of the P820 tube and use the ROSS camera electronics and control system. The camera's time resolution will initially be about 3 ps, but it should approach 1 ps with an improved ramp driver. This camera will be an important diagnostic for the short-pulse OMEGA EP Laser System.

### 2.5.5 Time-Resolved Hard-X-Ray Detector

The multichannel, time-resolved hard-x-ray detector (HXRD)<sup>122</sup> is based on the combination of a scintillator and a photomultiplier tube as shown in Fig. 2.66. Each of the four HXRD channels is filtered by a single high-pass filter to provide spectral resolution. The cutoff energies are 20, 40, 60, and 80 keV, respectively. Assuming an exponentially falling hard-x-ray spectrum with intensity  $I \sim \exp(-h\nu/kT)$ , where  $h$  is Planck's constant,  $\nu$  is the x-ray frequency, and  $k$  is Boltzmann's constant, the temperature  $T$  can be inferred by fitting the expected signals on the four detectors given their spectral sensitivities.

The HXRD has been modified to improve the shielding against Compton-scattered photons by the addition of a lead base plate (Fig. 2.66). If not absorbed, Compton-scattered photons would bypass the filter in front of the detector, increasing the signal in the high-energy channels and making it impossible to obtain reliable measurements of the hot-electron temperature.

The HXRD has been used successfully in several experimental campaigns, in particular to infer the amount of laser energy coupled to the target as suprathermal electrons for direct-drive implosions.<sup>82,123,124</sup>

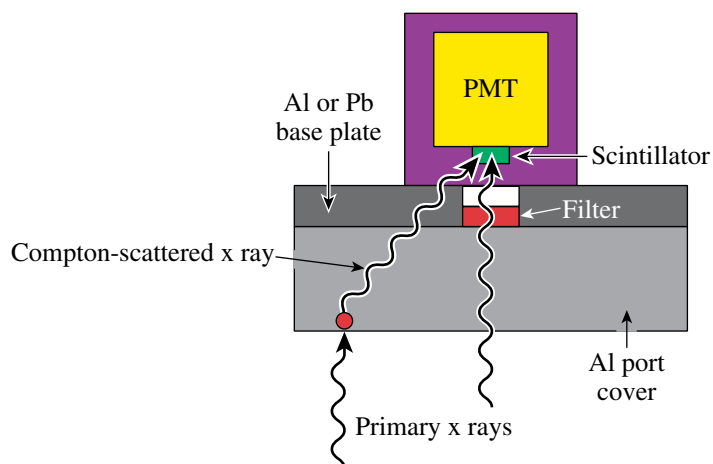


Figure 2.66  
Schematic of one channel of the hard-x-ray detector (HXRD), indicating the use of a Pb base plate to absorb Compton-scattered x rays. The HXRD uses a scintillator coupled to a photomultiplier tube (PMT) with different filtering in different channels.

### 2.5.6 Hard-X-Ray Spectrometer

A high-resolution, hard-x-ray spectrometer,<sup>125</sup> developed by NRL in collaboration with LLE, has been successfully fielded on OMEGA for several scientific campaigns.<sup>126,127</sup> The experience on OMEGA has been crucial in developing a similar instrument (HENEX,<sup>127</sup> Sec. 2.5.16.1) for the National Ignition Facility.<sup>128</sup>

### 2.5.7 Pinhole-Array X-Ray Spectrometer

The pinhole-array x-ray spectrometer consists of an array of pinholes in front of a flat-crystal x-ray spectrometer, yielding about 200 two-dimensional, quasi-monochromatic, time-integrated x-ray images covering a wide range of x-ray wavelengths.<sup>129</sup> Typically the image-center photon energy changes by approximately 10 eV between adjacent images. The spectrometer is used to diagnose the cold, compressed shell without backlighting by imaging the target on a single spectral line and subtracting an image at a nearby photon energy.<sup>129</sup> It is also used to study modulations in the areal density ( $\rho\Delta R$ ) of imploded shells by comparing core images obtained below and above the K edge of a dopant material in the shell.<sup>130,131</sup> This instrument has been used by external users of OMEGA to obtain temperature and density maps of implosion plasmas, using line and continuum x-ray radiation from Ar-doped targets.<sup>132,133</sup>

A modified version of this instrument incorporating a framing camera is used to obtain time-gated measurements. K-edge filters and multilayer mirrors are used instead of flat crystals to provide the increase in signal necessary for time resolution. With these modifications, the time evolution of shell modulations during spherical implosions has been measured around the time of peak compression for shells with titanium-doped layers.<sup>134</sup>

Recently, the pinhole-array spectrometer played a crucial role in the diagnosis of the areal density of highly compressed targets through the measurement of the x-ray spectrum emitted by the central hot spot.

### 2.5.8 Neutron Diagnostics

A large suite of neutron diagnostic systems are operational on OMEGA to routinely diagnose spherical implosion experiments. They are listed in Table 2.6 with the parameters that they measure and their ranges of applicability. The reactions that result in neutron production are described in Sec. 2.5.1.1.

The primary neutron yield is measured by two sets of diagnostics, one based on copper and indium nuclear activation and the other using current-mode neutron time-of-flight (nTOF) detectors. The yield range of these diagnostics covers ten orders of magnitude. The secondary neutron yield is measured using copper activation and scintillator/photomultiplier nTOF detectors.<sup>60</sup> Some of the nTOF detectors have sufficient sensitivity and temporal resolution to determine the burn-averaged ion temperature.

Table 2.6: Neutron diagnostics for the OMEGA laser. (PMT: photomultiplier tube; MCP: microchannel plate; CVD: chemical vapor deposition; NTD: neutron temporal diagnostic; NBT: neutron bang time; HYNBT: high-yield NBT.)

Measured Parameter	Instrument	Applicable Yield Range
Neutron yield	Cu activation In activation Scintillator/PMT	$1 \times 10^8 < Y < 1 \times 10^{16}$ (DT) $1 \times 10^9 < Y < 1 \times 10^{12}$ (DD) $5 \times 10^4 < Y < 1 \times 10^{15}$
Fuel areal density	Secondary yield (scintillator/PMT)	$5 \times 10^5 < Y < 1 \times 10^{11}$
Fuel ion temperature	Scintillators/(MCP-PMT) and CVD diamond detectors	$Y > 2 \times 10^8$ (DD) $Y > 1 \times 10^9$ (DT)
Neutron-emission time history	Scintillator/streak camera (NTD)	$1 \times 10^9 < Y < 3 \times 10^{13}$
Neutron bang time	Scintillator/PMT (NBT) CVD diamonds (HYNBT)	$1 \times 10^7 < Y < 1 \times 10^{11}$ $5 \times 10^{10} < Y < 1 \times 10^{15}$

The neutron burn history of both room-temperature targets and cryogenic DT targets is measured on OMEGA with the neutron temporal diagnostic (NTD).<sup>85</sup> The neutron burn history of cryogenic D<sub>2</sub> targets is measured with the “cryoNTD”<sup>80</sup> located in a ten-inch-manipulator. A neutron bang-time detector (NBT)<sup>135</sup> determines the time of peak neutron production for shots with low neutron yields. A high-yield neutron bang-time detector (HYNBT)<sup>136</sup> is used to measure the bang time for high-yield shots.

### 2.5.8.1 Activation detectors

The activation systems include copper activation [<sup>63</sup>Cu(n,2n)<sup>62</sup>Cu with a 10.9-MeV threshold and a decay by positron emission] to detect 14.1-MeV neutrons from DT fuel experiments and indium activation [<sup>115</sup>In(n,n'<sup>γ</sup>)<sup>115m</sup>In, with a 330-keV threshold and a decay with the emission of a 336.2-keV gamma ray] to detect 2.45-MeV neutrons from D<sub>2</sub> fuel. Before a shot, the Cu activation sample is manually placed in a pneumatic retractor holder and inserted into the target chamber 40 cm from the target. Immediately after the shot, the activated sample is retracted from the chamber and dropped via a plastic tube to a pickup basket in a room under the Target Bay. The operator picks up the activated Cu sample from the basket and delivers it to a counting room. The time from the shot to the start of counting is 3 to 5 minutes. The indium activation sample is manually inserted and retracted using a ten-inch-manipulator port. The indium sample is located at 9.4 cm from the target. Two different systems are used to count the activation samples.

The positrons resulting from copper activation are detected using an NaI coincidence system, consisting of two 7.6-cm × 7.6-cm NaI(Tl) detectors and associated electronics. This system measures coincident 511-keV gamma rays from positron annihilation. Using copper disks of different mass, the copper activation diagnostic can measure neutron yields from DT-filled targets from  $1 \times 10^8$  to  $1 \times 10^{16}$ .

The activation of the indium samples is detected with a high-resolution gamma-ray spectrometer that uses a high-purity-germanium (HPGe) detector. The indium activation measures the neutron yield from  $1 \times 10^9$  to  $1 \times 10^{12}$ .

Both the indium and the copper activation systems have been absolutely calibrated using several methods. All agree within 10%, determining the error in the absolute yield. The relative shot-to-shot error for activation systems is dominated by the counting statistics and is below 3% for high-yield shots.

### 2.5.8.2 Neutron time-of-flight detectors

Several current-mode scintillator/photomultiplier-based detectors or chemical-vapor-deposition (CVD) diamond detectors<sup>137,138</sup> with overlapping, staggered sensitivities measure the full range (ten orders of magnitude) of primary and secondary neutron yields on OMEGA. Some detectors can measure both the primary and secondary yields, while others can measure only the primary yield. They complement the activation diagnostics. The scintillator yield measurements are calibrated *in situ* by comparison with the activation systems for both 2.45-MeV and 14.1-MeV neutrons.

The scintillators have various volumes and are mounted at various distances from the target. Each detector is shielded from prompt x-ray and  $n-\gamma$  radiation by lead that varies in thickness between detectors from 1.27 cm to 5 cm. Two CVD diamond detectors have 10-mm-diam, 1-mm-thick CVD wafers and are located at 2.8 and 5.3 m from the target. The signal from each detector is split and recorded on two channels of a 1-GHz, 5-GS/s Tektronix TDS-684 digital oscilloscope.<sup>139</sup> For all target shots, PC-based data acquisition programs record the data from the oscilloscopes. An on-line program analyzes this data and makes the results available about ten minutes after the shot.

Several of the scintillator/photomultiplier-based detectors can measure the thermal broadening of the neutron signal, enabling an ion-temperature measurement.<sup>140</sup> They use fast microchannel-plate photomultiplier tubes (MCP-PMT's) coupled to quenched plastic scintillators. Two CVD diamond detectors are also used for ion-temperature measurements at high DT yields. The time-of-flight signals are fit up to their trailing half-maximum to exclude the contribution at later times due to  $\gamma$  rays from  $n-\gamma$  reactions.

### 2.5.8.3 Neutron temporal diagnostic

The neutron temporal diagnostic (NTD) determines the fusion reaction-rate history by measuring the emission time of neutrons from DT- and D<sub>2</sub>-filled targets. This instrument was previously operated on the Nova laser at LLNL<sup>85</sup> before being moved and adapted to the OMEGA facility. The instrument is based on a fast-rise-time, commercially available plastic scintillator and has a temporal resolution of 25 ps. Neutron collisions with the scintillator convert their kinetic energy to light with a wavelength between 350 and 450 nm. The light is collected and transported by an  $f/2$  zoom-lens optical system to the photocathode of a fast streak camera, whose output image is recorded by a CCD camera. The recorded target burn history is synchronized to the incident laser pulse through simultaneously recorded timing fiducial pulses. The absolute time calibration has been determined to an accuracy of 50 ps (Sec. 2.5.3). The NTD needs neutron yields greater than 10<sup>9</sup> to obtain a usable burn history because of neutron statistics. Compared with the neutron bang-time detector (Sec. 2.5.8.4), the NTD has better temporal resolution but lower sensitivity because a streak camera is used instead of a photomultiplier tube.

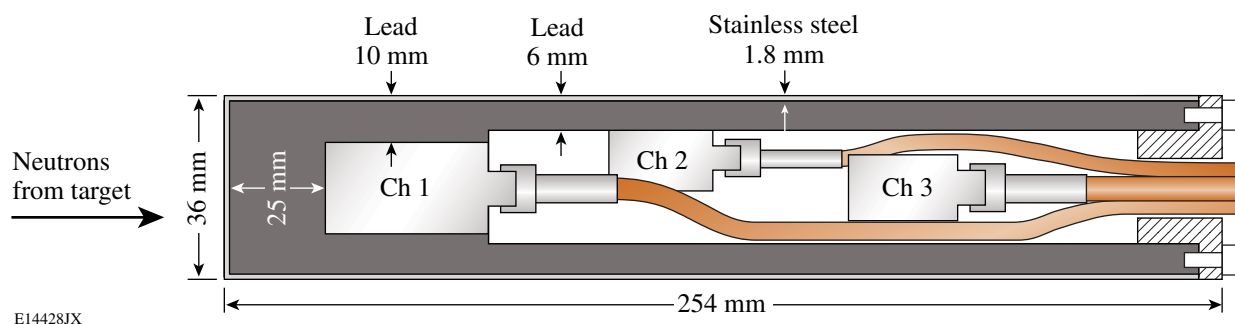
The new, cryoNTD<sup>80</sup> has been developed to measure the fusion reaction history of D<sub>2</sub> cryogenic targets. The NTD needs to be withdrawn to a distance of 20 cm during cryogenic shots to avoid interference with the cryogenic equipment. As a result the NTD has insufficient sensitivity for D<sub>2</sub> cryogenic implosions, motivating the development of the cryoNTD. The cryoNTD is placed in a ten-inch-manipulator port and uses a ~30-mm-diam scintillator placed at 9 cm from target chamber center. The cryoNTD uses the same fast scintillator as the NTD along with a similar streak camera and fiducial and similar analysis software. The cryoNTD sensitivity and temporal resolution are comparable to those of the NTD. The cryoNTD cannot be used for high-yield DT cryogenic implosions because its streak camera is not shielded against neutrons. However, for cryogenic DT targets, the sensitivity of the NTD at 20 cm from target chamber center is sufficient to measure the temporal burn history.

#### 2.5.8.4 Neutron bang-time detectors

The time interval from the beginning of the laser pulse to the peak of the neutron emission (the bang time) is an important parameter in inertial confinement fusion experiments. The neutron bang time is very sensitive to the energy absorption and the hydrodynamic response of the target and can be directly compared with numerical simulations.

The neutron bang-time detector (NBT) on OMEGA<sup>135</sup> uses fast quenched scintillators and fast photomultiplier tubes and can be used for yields up to  $10^{11}$ . A new detector, the high-yield neutron bang-time detector (HYNBT), has been developed to measure the bang time in high-yield experiments. The HYNBT is also a continuation of prototype diagnostic development work<sup>141</sup> for the National Ignition Facility.

The HYNBT detector is shown in Fig. 2.67. It consists of three chemical-vapor-deposition (CVD) diamond detectors of different sizes and sensitivity placed in a lead-shielded housing. The HYNBT uses “optical quality” polycrystalline DIAFILM CVD wafers purchased commercially.<sup>142</sup> The CVD wafers are disks with the following dimensions: Ch1 10-mm diam, 0.5-mm thick; Ch2 5-mm diam, 0.25 mm thick; and Ch3 2-mm diam, 0.5-mm thick. The electrical contacts, consisting of 10-nm-thick Cr and 50-nm-thick Au, were deposited on each side of the CVD wafer. Each wafer was assembled in a separate, simple aluminum housing with an SMA connector. The separate housing



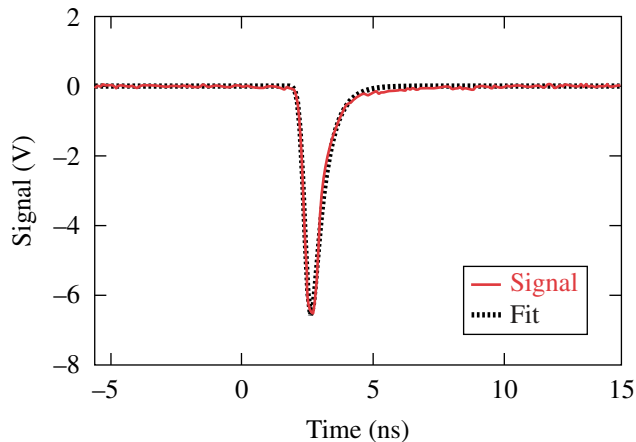
E14428JX

Figure 2.67  
Design of the high-yield neutron bang-time (HYNBT) detector.

for each channel allows pre-testing of the individual CVD diamond detectors. The HYNBT thin-wall stainless steel cylinder acts as a Faraday cage, decreasing electromagnetic pulse (EMP) noise. The HYNBT lead shielding protects the CVD diamond detectors from hard x rays. This shielding is not necessary for current experiments on OMEGA but it has been installed in anticipation of a higher level of hard x rays produced by the interaction of the short OMEGA EP laser pulse with the gold cone or the fuel shell in fast-ignition experiments.<sup>143</sup> Double-braided RG-142 coaxial cables are used to deliver the signals to an oscilloscope due to their low sensitivity to neutron-induced signals.<sup>144</sup> The HYNBT is used alternatively in the same re-entrant tube as the NBT at 50 cm from the target chamber center. The RG-142 cables are 10 m long and are followed by 22-m-long LMR-400 cables. Inside the OMEGA Target Bay the cables are routed in the radial direction as much as possible to minimize the interaction of neutrons with the cables. The LMR-400 cables have a higher bandwidth than RG-142 cables but much higher sensitivity to neutron-induced signals.<sup>144</sup> This two-cable solution is a compromise between high bandwidth and neutron-induced signal sensitivity. All HYNBT channels are biased at  $-750$  V using a bias-T (Picosecond Pulse Labs, model 5531). The signals from the HYNBT CVD diamond detectors are recorded by three channels of a 3-GHz, 10-GS/s, Tektronix TDS-694 oscilloscope.<sup>139</sup> The OMEGA optical fiducial pulse train is recorded on the fourth oscilloscope channel using a fast photodiode to provide a time reference with respect to the laser pulse. The fiducial analysis and fitting procedure are described in Ref. 135.

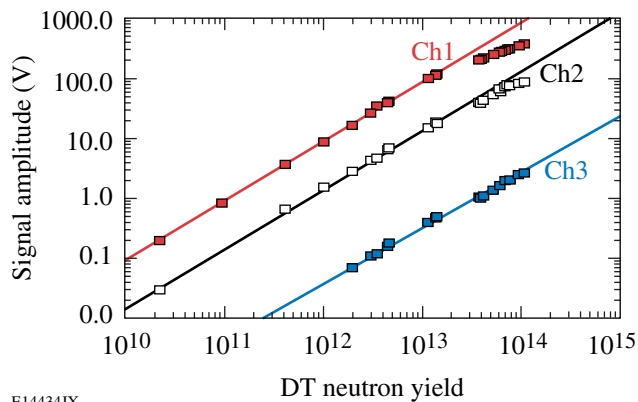
The HYNBT has been tested on OMEGA for both DT and D<sub>2</sub> implosions. Figure 2.68 shows a typical oscilloscope trace for a shot yielding  $4.4 \times 10^{12}$  DT neutrons. Since the HYNBT is biased by a negative high voltage, the signals from CVD diamonds are positive and then inverted during analysis. The measured signals were fit by a convolution of a Gaussian and an exponential decay, as described in detail in Ref. 135. The time constant of the exponential decay (0.5 ns in Fig. 2.68) represents the carriers' collection time in the CVD diamond wafer. At a constant bias voltage, the time constant depends on the thickness and diameter of the CVD wafer. It needs to be determined once and can then be used for the analysis of all subsequent data. All other fit parameters are determined for every shot to account for trigger shifts and changes in bang time and ion temperature. The time of the pulse is defined to be the center of the Gaussian part of the fit. Figure 2.69 shows the signal amplitudes of all three HYNBT channels as a function of the DT neutron yield. The straight lines are linear fits to the data for each channel. The signal from the first HYNBT channel saturates above 100 V and the second channel saturates above 80 V. At a yield of  $1 \times 10^{15}$  the third channel will have a signal of  $\sim 20$  V and will not be saturated. The three HYNBT channels can thus measure the neutron bang time in DT implosions over the yield range from  $1 \times 10^{10}$  to  $1 \times 10^{15}$ . For D<sub>2</sub> implosions, the bang time can be measured for neutron yields above  $3 \times 10^{10}$ .

The timing accuracy of the HYNBT was studied by measuring the time difference among channels. The time difference between two channels recorded during two shot days with DT yields varying from  $8.4 \times 10^{12}$  to  $3.5 \times 10^{13}$  had an rms of 13 ps (Ref. 136). The HYNBT was tested five times during 2005 and in all cases demonstrated internal time resolution better than 20 ps. The timing calibration of the HYNBT bang time relative to the OMEGA laser pulse was established by cross calibration against the NTD (Sec. 2.5.8.3). A good correlation between the two detectors was observed with an rms difference of 40 ps.



Shot 42120  
E14431JX

Figure 2.68  
Channel-2 HYNBT signal for shot 42120  
with a DT neutron yield of  $4.4 \times 10^{12}$ .



E14434JX

Figure 2.69  
Signal amplitude of the HYNBT channels  
as a function of DT neutron yield.

Only the first HYNBT channel is sensitive enough for  $D_2$  implosions on OMEGA. The first channel has been cross calibrated against the NTD. EMP mitigation measures applied during the HYNBT design have reduced the EMP noise level about ten times relative to the NBT.<sup>135</sup> For all shots on OMEGA the EMP noise level in the HYNBT is below 4 mV.

More details about this work are found in Ref. 136.

#### 2.5.8.5 Neutron magnetic recoil spectrometer

Measurement of the compressed fuel areal density  $\rho R$  is fundamental to understanding any implosion. Charged-particle diagnostics (Sec. 2.5.1) have been used extensively for determining  $\rho R$  for a wide range of implosions, but these methods are accurate only when  $\rho R \lesssim 200 \text{ mg/cm}^2$  and will fail for areal densities of 300 to 2000  $\text{mg/cm}^2$ , expected in NIF implosions. A unique high-resolution neutron spectrometer, known as a magnetic recoil spectrometer (MRS) because of its operating principle, has thus been designed as part of LLE's collaboration with the Plasma Science and Fusion Center at MIT. This type of spectrometer<sup>145–147</sup> is currently operational only on the Joint European Torus and has never been installed on a laser facility. An MRS is being built for OMEGA and a nearly identical instrument will be built for the NIF.

The spectrometer,<sup>148–150</sup> shown schematically in Fig. 2.70(a), measures the spectra of neutrons between 6 and 32 MeV. The  $\rho R$  can be inferred from the ratio of downscattered neutrons  $Y_{ds}$  (1.9 to 14.1 MeV) to the yield  $Y_n$  of primary neutrons (14.1 MeV). The areal density is proportional to the ratio  $Y_{ds}/Y_n$ :

$$\rho R \approx \frac{(2\gamma + 3)m_p}{(\gamma\sigma_d + \sigma_t)} \frac{Y_{ds}}{Y_n}, \quad (2.5.9)$$

where  $\gamma$  is the ratio of the deuteron and triton number densities,  $m_p$  is the proton mass, and  $\sigma_d$  and  $\sigma_t$  are the total  $nd$  and  $nt$  elastic-scattering cross sections, respectively. The energy range 6 to 10 MeV was selected for the MRS down-scattered neutron measurements partly to avoid the low-energy tail of the primary neutron spectrum. The total cross sections used in Eq. (2.5.9) must then be replaced by the effective elastic cross sections for generating down-scattered neutrons in this energy range.

The spectrometer has three basic components. The first is a CH (or CD) foil to produce recoil protons (or deuterons) from incident neutrons. The second is a magnet for energy dispersion and focusing of forward-scattered recoil particles onto a detector plane. This focusing provides a clear mapping between position in the plane and the energy of the proton (or deuteron), and thus the energy of the neutron that scattered it. The third is the detector, which records the position of each recoil particle and is insensitive to various sources of background; CR-39 nuclear track detectors<sup>52</sup> will be used for this in coincidence mode.<sup>151</sup> Several options are available for configuring the MRS even after the component positions are set: the foil composition determines whether proton or deuteron recoils are being used, and the foil area and thickness can be adjusted to change the energy resolution and detection efficiency.

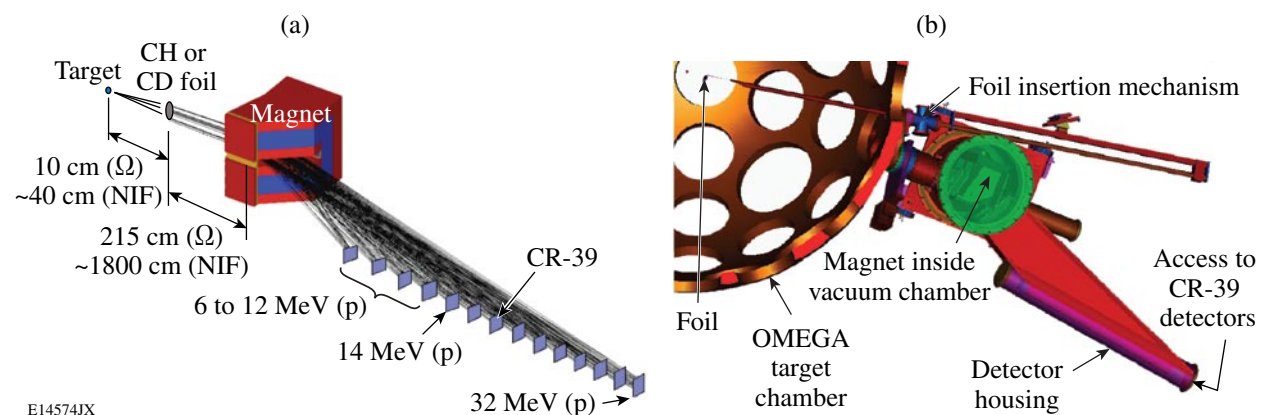


Figure 2.70

(a) Principle of the magnetic recoil spectrometer (MRS), which will be used to determine the areal density ( $\rho R$ ), the ion temperature ( $T_i$ ), and the absolute neutron yield with high accuracy, first at OMEGA and then at the NIF. Forward-scattered protons from a CH foil (or deuterons from a CD foil) are momentum analyzed and focused by the magnet onto the detector. (b) Concept for the implementation of the MRS system on OMEGA.

The nature of the spectra to be measured is illustrated in Fig. 2.71, which shows simulations for a cryogenic DT implosion at OMEGA with  $\rho R \approx 130 \text{ mg/cm}^2$  (Ref. 152), a NIF “P<sub>6</sub> fizzle” with  $\rho R \sim 1000 \text{ mg/cm}^2$  (Ref. 153), and an ignited capsule with  $\rho R \sim 1500 \text{ mg/cm}^2$  (Ref. 153). The MRS should be able to reliably measure all of these spectra.

The instrument measures the spectra of neutrons between 6 and 32 MeV, covering all essential details of the three simulations shown in Fig. 2.71. For a high-yield implosion on the NIF, a second estimate of the fuel  $\rho R$  can be independently made from tertiary neutrons in the range 20 to 32 MeV [Sec. 2.5.1.1(e)], allowing a self-consistency check with the  $\rho R$  measured from scattered primary neutrons. This will be important for understanding NIF fizzes on the verge of igniting.

The MRS that will be installed on OMEGA is a prototype for the NIF. The most expensive component, a 500-lb magnet, has been manufactured (by Dexter Magnetic Technologies<sup>154</sup>) and characterized. LLE will engineer the interface of the prototype to OMEGA [Fig. 2.70(b)], and MIT will be responsible for detector/software development and system calibration.

The prototype MRS system is similar to the system planned for implementation on the NIF except for some rescaling of distances. The magnet, the core of the spectrometer, is virtually identical for both systems. Well before 2010 OMEGA experiments will verify that all the necessary elements of the MRS are functioning correctly, including the detector, the full system integration, the analysis programs, the instrument calibration, and the final instrument qualification.

On the NIF, the MRS is expected to measure  $\rho R$  from 300 to 2000  $\text{mg/cm}^2$  in the yield range from  $1 \times 10^{15}$  to  $1 \times 10^{19}$  with accuracy better than 10%. For cryogenic DT implosions on OMEGA with an areal density of 100  $\text{mg/cm}^2$  and a yield of  $1 \times 10^{13}$ , the signal-to-background ratio of the MRS is estimated to be  $\sim 10$  and the inferred areal density should be accurate to approximately 10%. For areal densities substantially above 200  $\text{mg/cm}^2$ , the MRS will be the only diagnostic able to measure the  $\rho R$ ; its utility will be unique and vital to implosion studies within the National Ignition Campaign.

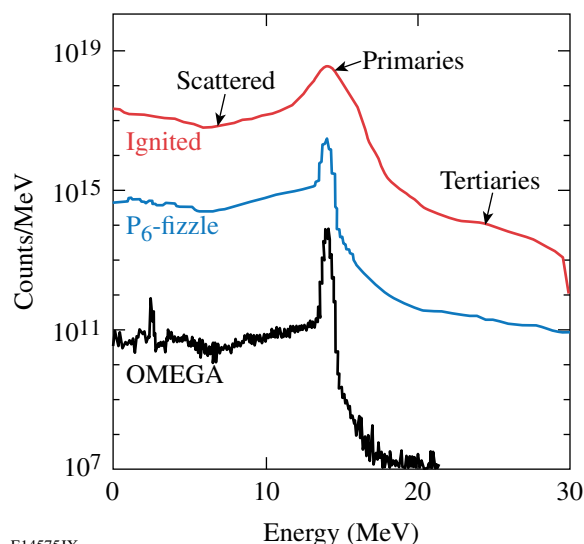
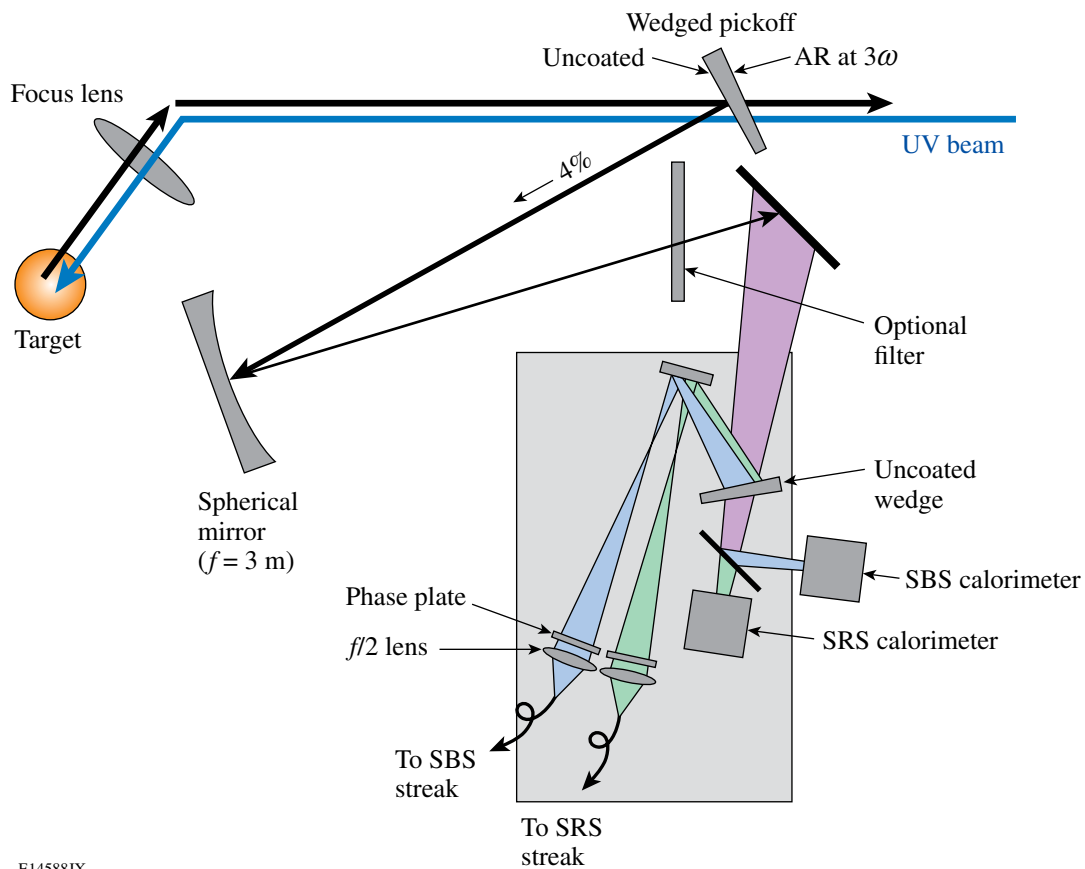


Figure 2.71  
Simulated neutron spectra that could be measured by the MRS. The three spectra are for an ignited implosion with  $\rho R \sim 1500 \text{ mg/cm}^2$ , a NIF “P<sub>6</sub> fizzle” with  $\rho R \sim 1000 \text{ mg/cm}^2$ , and an OMEGA cryogenic DT implosion with  $\rho R \approx 130 \text{ mg/cm}^2$ . In each case, the MRS will accurately measure  $\rho R$ ,  $T_i$ , and the absolute yield.

### 2.5.9 Full-Aperture Backscatter Stations

Over the past three years, three full-aperture backscatter stations (FABS) have routinely operated on OMEGA. These stations are used to characterize the light backscattered from the target through focusing lenses. The information obtained from these stations is critical for the understanding of laser–plasma interaction experiments<sup>155,156</sup> and the interpretation of target implosion experiments and is required for detailed comparisons with code simulations.

The FABS (Fig. 2.72) measures backscattered light energies and temporally resolved spectra in the regions of stimulated Raman scattering (SRS,  $\lambda = 400$  to  $700$  nm) and stimulated Brillouin scattering (SBS,  $\lambda = 351 \pm 1$  nm). All of the light collected by the focus lenses of beams 25 and 30 is



E14588JX

Figure 2.72  
Layout of one of the full-aperture backscatter stations (FABS). Light scattered by the target is collected by the focus lens of one of the OMEGA beams. A planar reflection from an uncoated surface of a glass wedge directs 4% of the scattered light to calorimeters and fibers connected to spectrometers and streak cameras for the analysis of stimulated Brillouin scattering (SBS, around 351 nm) and stimulated Raman scattering (SRS, between 400 and 700 nm).

diagnosed, as is 351-nm light sampled from the H17 diagnostic port. The instruments in the FABS have been designed and implemented in collaboration with LLNL. LLNL has installed the third FABS station for 527-nm interaction experiments, in which beam 25 is converted to the second harmonic and diverted to enter the target chamber through port P9. This FABS station is a replica of the other two, except that the streak-camera channels and calorimeters are filtered to cover the range of 520 to 1060 nm.

The SBS (351 nm) calorimeters have been cross-calibrated with a through-the-tank shot at low beam energy and with a large-aperture reference calorimeter placed behind the wedged pickoff in Fig. 2.72. The SRS (400 to 700 nm) calorimeters have been calibrated using measured electrical calibration constants for the calorimeters and measured transmission and reflection coefficients for all optical components between the calorimeters and the target. Typical energy measurements with the SRS calorimeters have uncertainties of 5% to 10%. For large energy reflections from the target, an optional neutral density filter protects the optical components of the FABS.

The temporally resolved SBS and SRS data are coupled into 435- $\mu$ m-diam gradient-index light fibers using  $f/2$  lenses and holographic scatter plates (phase plates), as shown in Fig. 2.72. The fibers are  $\sim 10$  m long and are coupled into two spectrometer–streak-camera systems, one each for SRS and SBS. The SBS and SRS signals from FABS25 and FABS30 are time-multiplexed onto two S20 streak cameras. The SBS streak camera uses the new, high-performance ROSS streak system (Sec. 2.5.3), and the SRS camera will soon use the same system.

A group-velocity correction is applied to the SRS spectra since the blue part of the spectrum arrives  $\sim 3$  ns after the red part. No such correction is required for the SBS spectra. The spectral and temporal resolutions are  $\Delta\lambda \approx 0.04$  nm and  $\Delta t \sim 80$  ps for SBS, and  $\Delta\lambda \approx 9$  nm and  $\Delta t \sim 100$  ps for SRS.

A fiducial comb consisting of eight 527-nm pulses spaced at 548 ps is simultaneously added to the streak camera photocathode to allow absolute timing of the scattered-light spectra relative to the main laser pulse and to calibrate the time axis.

Typical data obtained with the SBS channel are shown in Fig. 2.73 for a spherical implosion.<sup>157</sup> The raw, multiplexed data are shown in Fig. 2.73(a) and separate single-channel analyses are shown in Fig. 2.73(b). A scattered component at the laser wavelength ( $\lambda_L = 351$  nm) is seen through the focus lenses but not the H17 diagnostic port and is due to light transmitted past the target (“blow-by”). The time-resolved data are cross-calibrated with the time-integrated scattered-light calorimeter measurements for FABS25 and FABS30. Streaked data such as that presented here allow quantitative analysis and comparison with hydrodynamic simulations; for example, the time-varying blue shift seen here provides information on the rate of expansion of the coronal plasma. While the data of Fig. 2.73 show no obvious evidence for SBS, many long-scale-length plasma experiments in planar geometry have provided clear evidence of SBS.

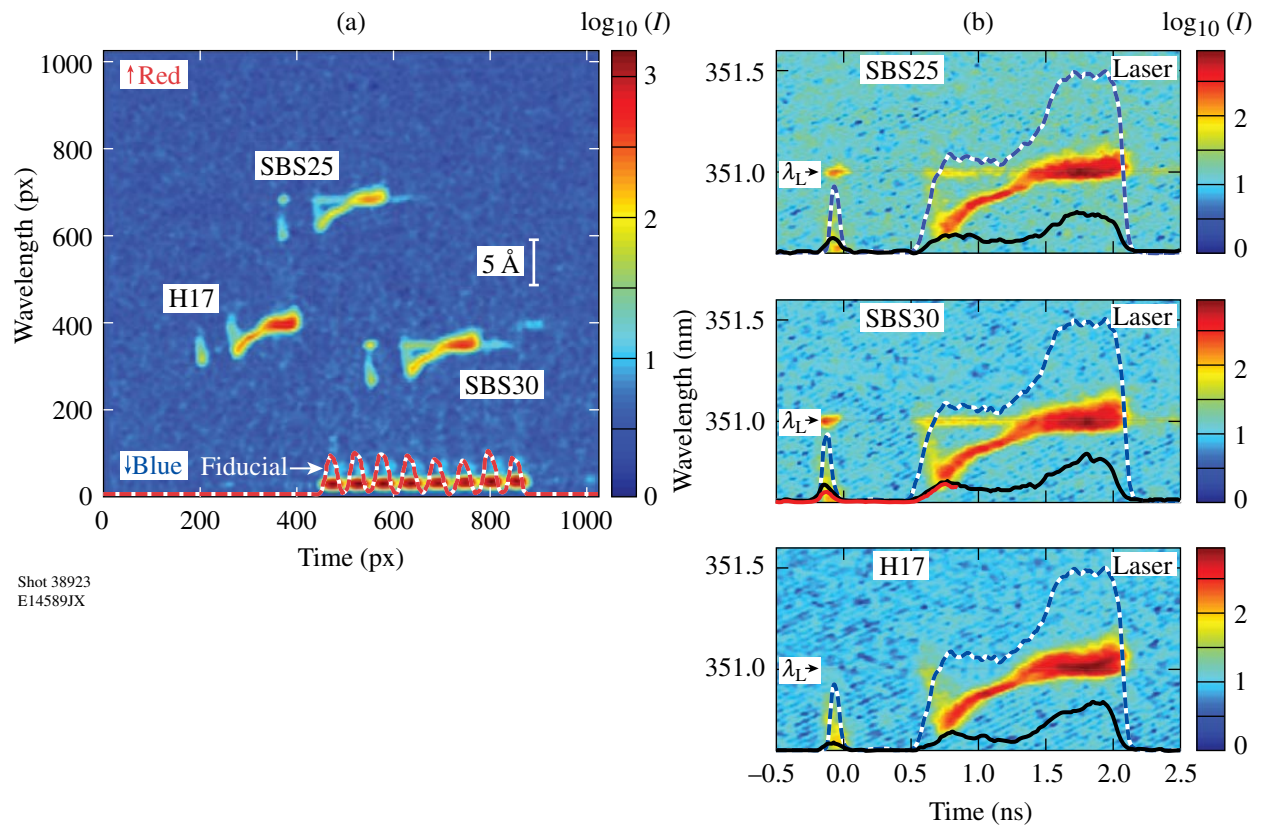


Figure 2.73

(a) Multiplexed temporally and spectrally resolved records of scattered light from a spherical target implosion on OMEGA (shot 38923). Two channels correspond to scattered-light measurements through the focus lenses of beams 25 and 30, while the third channel records light observed between the focusing lenses through the hex diagnostic port H17. The signal intensity ( $I$ ) is displayed on a logarithmic scale, and the time scale is calibrated using a series of fiducial pulses with a separation of 548 ps. (b) Analysis of the individual channels, along with the incident laser pulse measured for beam 40 (blue-and-white dashed lines) and the scattered power integrated over all wavelengths (black), both on a linear scale.

Similar multiplexed time-resolved spectral data (Fig. 2.74) are obtained for the two SRS channels. The reduced data shown in Fig. 2.74(b) are presented on a common color scale for easier quantitative comparison of the signals, one of which (SRS-30) represents SRS sidescattering while the other (SRS-25) represents SRS backscattering. The suppression of the SRS signals by the middle of the laser pulse indicates changing plasma conditions

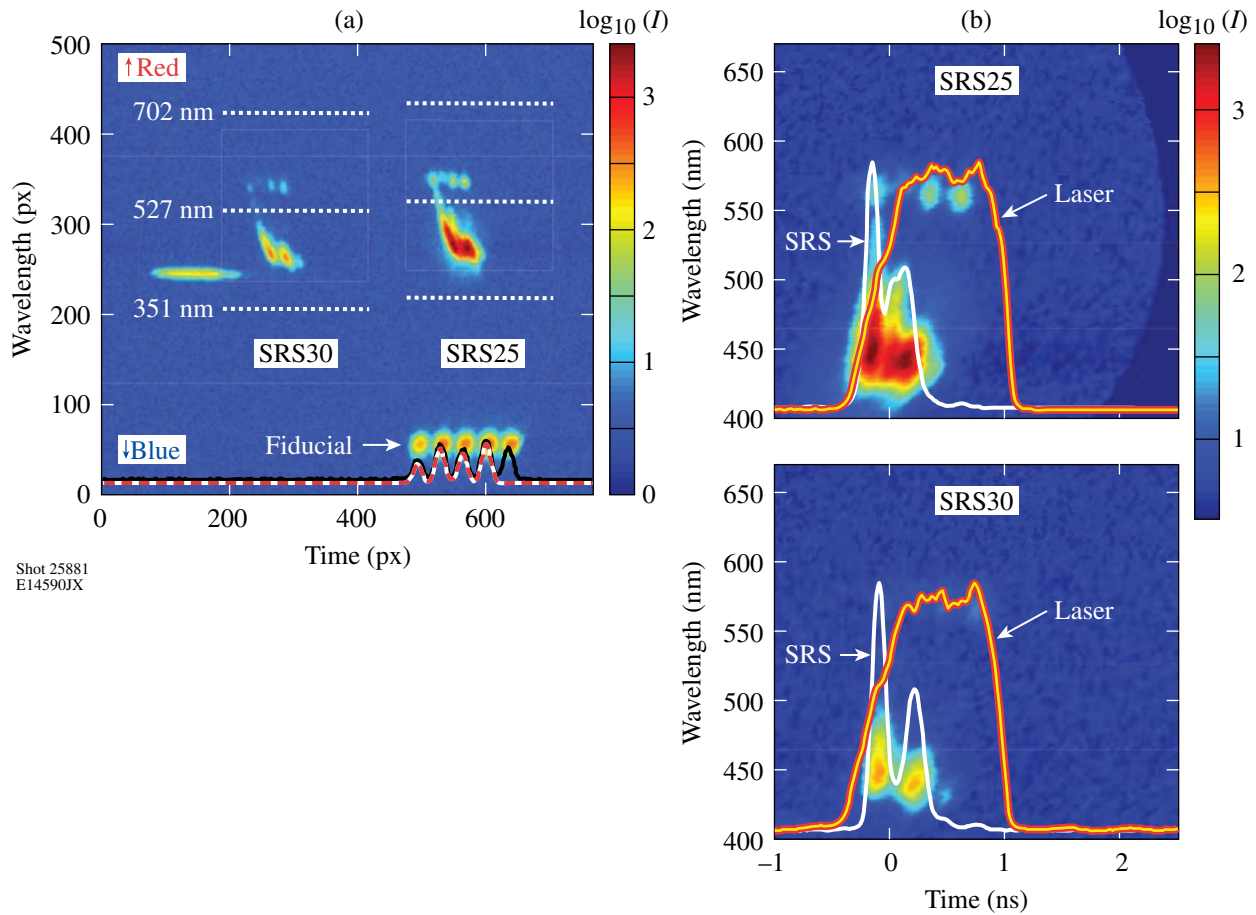


Figure 2.74

(a) Multiplexed SRS streak camera record for OMEGA long-scale-length plasma shot 25881. (b) Detailed reductions of the SRS records for FABS25 and FABS30. The data are corrected for group-velocity dispersion in the 10-m optical fiber between the FABS stations and the spectrometer. The incident laser pulse (orange) and the spectrally integrated SRS signal (white) are given on a linear scale. The SRS emission is suppressed at later times.

### 2.5.10 Near-Backscatter Imaging

Two cameras have been installed on OMEGA for the purpose of near-backscatter imaging (NBI).

The cameras are designed to measure light scattered by the target into the vicinity of the focus lenses of beams 25 and 30. This light may be 351-nm light reflected from the target, or it may be the result of nonlinear processes such as stimulated Brillouin scattering (SBS), stimulated Raman scattering (SRS), or cross-beam energy transfer. This light is not measured by the full-aperture backscatter station (FABS, Sec. 2.5.9).

The physical layout of the NBI system is shown in Fig. 2.75. It is similar to the NBI system implemented on Nova.<sup>158</sup> In some circumstances, laser light scattered by the target is directed back toward the laser but extends beyond the incident beam aperture and strikes a scatter plate surrounding the focus lens. Light reflected off the scatter plate is imaged onto two time-integrating cameras, one (SBS-NBI) filtered for  $351 \pm 10$  nm and the other (SRS-NBI) filtered for 400 to 710 nm. The cameras are operated in air inside re-entrant tubes in the OMEGA target chamber.

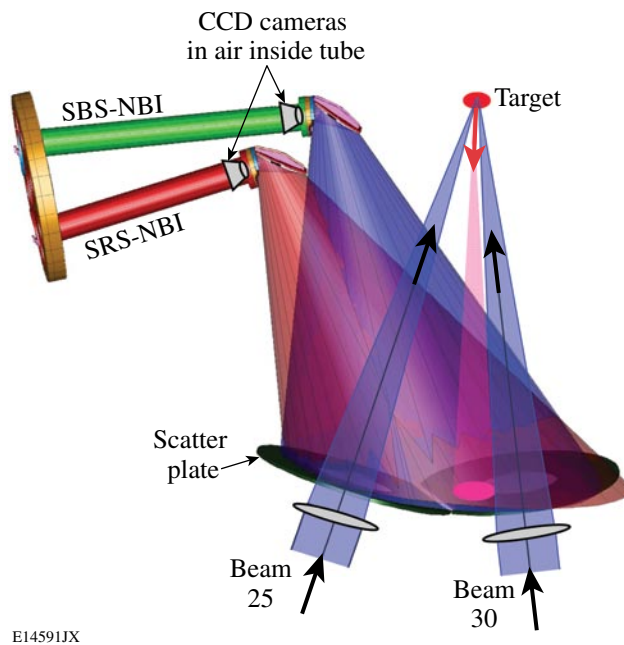


Figure 2.75  
Experimental layout of the SBS and SRS near-backscatter-imaging (NBI) channels in the OMEGA target chamber. White, painted scatter plates surround beams 25 and 30, which pass unimpeded through the central holes in the plates. A directed backscatter beam is shown schematically in pink, striking the scatter plate outside the central hole. The two NBI cameras, filtered for SBS ( $351 \text{ nm} \pm 10 \text{ nm}$ ) and SRS (400 to 710 nm), photograph the time-integrated image of the scattered light from the scatter plates. The cameras are located in air inside re-entrant tubes.

A typical raw CCD image is shown in Fig. 2.76(a). This shows a highly directed beam of scattered light, a fraction of which is diagnosed by the FABS. To provide a quantitative analysis [Fig. 2.76(b)], the images of each scatter plate are corrected for geometrical distortion as the oblique observation angle and varying image distances cause significant magnification changes across the image of each plate. The flat-fielding analysis also incorporates appropriate corrections for the angles of incidence and observation at each point on the scatter plates. Since the field of view of the camera extends to angles well beyond  $10^\circ$  from the optical axis, additional flat-field corrections are applied. In separate experiments the scatter plates have been found to be within a few percent of Lambertian without any noticeable specular component. In contrast, sand-blasted Al plates that were originally installed on OMEGA showed a strongly forward-directed scattering distribution following a  $\cos^3\theta$  distribution, where  $\theta$  is the angle from specular. This rendered quantitative analysis of the data problematic.

The NBI image analysis requires calibrations that are carried out separately for the SBS (351 nm) and SRS (400 to 700 nm) channels. For calibration at 351 nm, a low-energy OMEGA beam was reflected by an uncoated fused-quartz plate inside the target chamber, located at  $\sim 15$  cm past focus, and directed toward one of the scatter plates. The known amount of beam energy striking the plate then allowed the determination of an appropriate calibration constant. Alternative calibration schemes are being developed by LLNL.

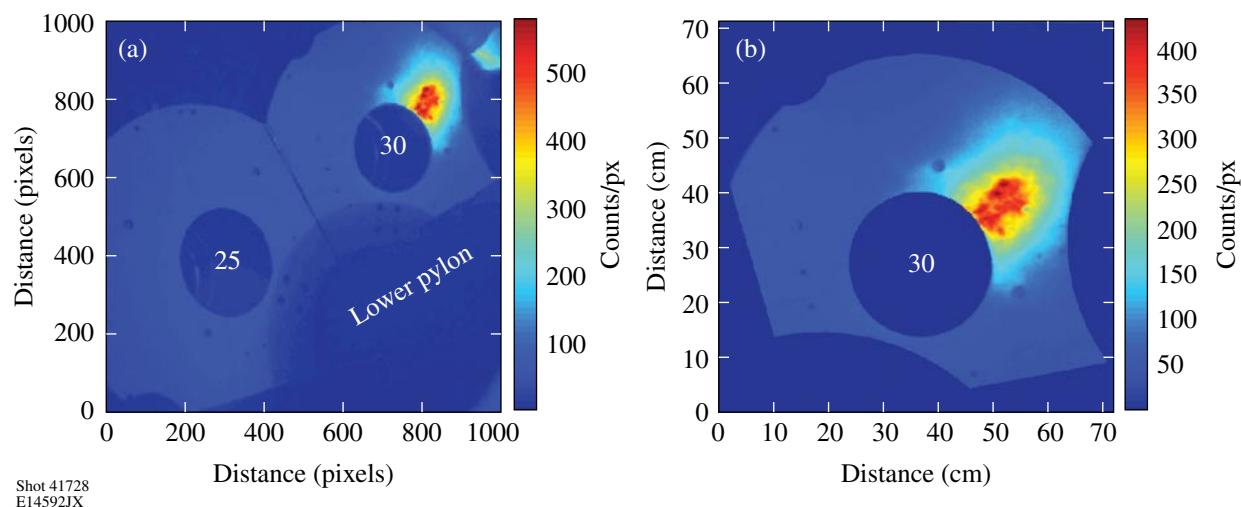


Figure 2.76

NBI images from the SBS channel for OMEGA shot 41728. (a) Raw image with geometrical image distortion due to the oblique viewing angle. (b) Image of the beam-30 NBI plate corrected for geometrical image distortion. The intensity is also corrected for the scattering characteristics of a Lambertian scatter plate at the appropriate angles of incidence and observation and the field angle of the camera. Cut-outs and shadowed regions of the scatter plates are blocked out in (b).

A variant of this procedure has been used for the SRS calibration. A low-power, 532-nm cw laser was piped through a light fiber to target chamber center and directed toward one of the NBI scatter plates. An absolutely calibrated photodiode embedded in the scatter plate measured the local laser fluence. An SRS calibration constant was then derived from intensity contour plots for the calibration image and the known fluence at the diode location.

### 2.5.11 X-ray Backlighter Capabilities

X-ray radiography continues to be a valuable diagnostic tool for characterizing high-energy-density plasmas. Many experiments, including studies of laser imprinting, the growth of perturbations due to the Rayleigh–Taylor instability, and jet propagation in low-density media, have used large-area x-ray backlighters. In this geometry the object is placed between the x-ray source and an x-ray imager, and the area of the backlighter spot is typically a little bigger than the area of the object. Primary x-ray imagers are variants of pinhole cameras with the pinhole providing spatial resolution of the x-ray absorption. X-ray microscopes (Sec. 2.5.2.3) are also used, with the spatial resolution being provided by the x-ray optics.

The signal-to-noise ratio, uniformity, and field of view of these radiographs are limited by the size and uniformity of the emission from the large-area backlighters. An alternate radiographic technique, point-projection backlighting,<sup>159,160</sup> has thus been developed for use on the OMEGA laser. This uses the backlighter itself as the imaging device. The concept of point-projection backlighting is not new, but its development and use on OMEGA have increased substantially over the past few years.

A schematic of a point-projection backlighter is shown in Fig. 2.77. A point source of x rays casts a shadow of the plasma being characterized onto a large-format x-ray detector. Encoded into the shadow data is the transmission through the plasma along the path from the x-ray source to the detector. The signal-to-noise ratio, uniformity, and field of view of the measurement are no longer

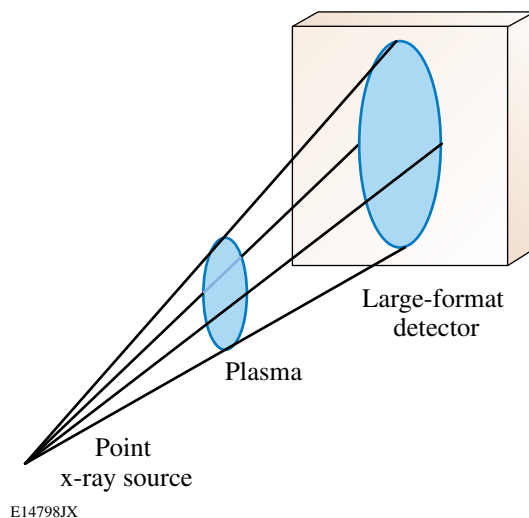


Figure 2.77

Schematic of a point-projection backlighter. The point x-ray source casts an image onto the detector from x rays that pass through the plasma being radiographed. The image is magnified by the ratio of the distance of the detector from the source to the distance of the plasma from the source.

limited by the uniformity of a large-area backlighter; they are limited only by the uniformity of x-ray emission into the solid angle subtended by the detector and self-emission from the object being radiographed. The spatial resolution is defined by the spatial size of the x-ray emitter just as the size of a pinhole defines the spatial resolution of a pinhole camera.

Two point-projection backlighter configurations are shown in Fig. 2.78. Both configurations use a foil as an x-ray emitter and a substrate with a pinhole to limit the spatial extent of the x rays reaching the detector. Figure 2.78(a) shows the simplest scheme, where the x-ray emission foil is mounted directly onto the pinhole substrate with the laser beams needed to create the x rays incident on the rear surface. This geometry requires that the x-ray emission foil be transparent to the x rays used for radiography. In Fig. 2.78(b), the x-ray emission foil is mounted to the pinhole substrate at a large enough angle so that the laser beams can illuminate the front surface of the x-ray emitter. The pinhole in the substrate must then be at an angle relative to the substrate surface. Both of these configurations have been used on OMEGA experiments and have proven to be valuable tools for diagnosing high-energy-density plasmas.

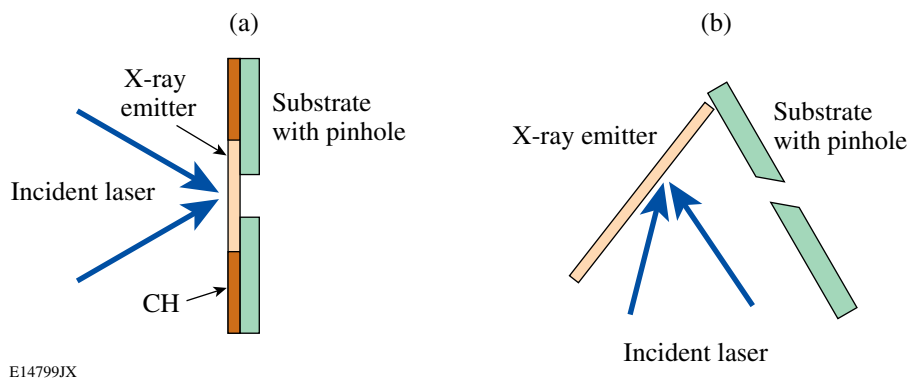


Figure 2.78

Two point-projection backlighter configurations. In (a) the laser beams are incident onto the rear surface of a target composed of an x-ray emitter bonded to a substrate with a pinhole. In (b) the laser is incident onto the front surface of the x-ray emitter with the substrate at an angle to the x-ray emitter. The pinhole in (b) is drilled at an angle relative to the substrate surface.

The rear-surface point-projection backlighter is limited to x-ray emitters for which the Lyman- $\alpha$  and/or helium- $\alpha$  lines from the laser illumination of the emission foil have lower energies than the nearest absorption edge. For K-shell emitters, this is true only for elements with  $Z$  greater than or equal to that of chlorine. This may be seen from Table 2.7, which lists common x-ray emitters for backlighting together with their K absorption edge and Lyman- $\alpha$  and helium- $\alpha$  emission energies. Chlorine is the lowest-atomic-number element whose helium- $\alpha$  emission has a lower energy than the K absorption edge. A thin emitter foil will thus be transparent to these x rays. The lowest-atomic-number element that is transparent to both the Lyman- $\alpha$  and the helium- $\alpha$  emissions is vanadium.

A point-projection backlighter with the geometry shown in Fig. 2.78(a) has been characterized with three different detectors: a single-strip x-ray framing camera, Kodak Biomax MS film, and an x-ray-sensitive CCD array. The backlighter assembly consisted of a 25- $\mu\text{m}$ -diam pinhole in the center of a 5-mm  $\times$  5-mm, 50- $\mu\text{m}$ -thick Ta foil with 100  $\mu\text{m}$  of CH on both foil faces. The x rays were emitted by a 200- $\mu\text{m}$ -diam, 5- $\mu\text{m}$ -thick V foil illuminated by 2 to 21 beams from the OMEGA laser in the direction toward the detector. The detector has a large open aperture protected by a 5- $\mu\text{m}$ -thick V foil, so any debris created by the pinhole assembly has the potential to damage the detector. The backlighter assembly shown in Fig. 2.78(a) has been shown to minimize shrapnel-like debris that could cause damage. Edge response data for all three detectors for a two-beam shot with a 1-ns, temporally flat pulse are shown in Fig 2.79. The data are fit very well with an error function, consistent with a Gaussian point spread function. There is little difference in the measured resolution for the three detectors. The equivalent full width at half maximum of the point-spread function for the framing camera, film, and CCD array are  $13 \pm 1 \mu\text{m}$ ,  $13 \pm 1 \mu\text{m}$ , and  $15 \pm 1 \mu\text{m}$ , respectively.

Examples of point-projection backlighter images are given in Secs. 2.15.1 and 2.12.1.5. Point-projection backlighting can also be applied to the phase-contrast imaging of high-energy-density plasmas. Small point sources are critical for this application.

Table 2.7: Common K-shell x-ray emitters with their K-edge, Lyman- $\alpha$ , and helium- $\alpha$  x-ray energies (in keV).

Element	K edge	Ly $\alpha$	He $\alpha$
Mg	1.303	1.4717	1.3432
Al	1.55898	1.7277	1.5883
Si	1.839	2.0043	1.8539
Cl	2.833	2.9585	2.7751
Sc	4.492	4.523	4.295
Ti	4.966	4.966	4.727
V	5.465	5.431	5.18
Fe	7.112	6.952	6.668
Ni	8.333	8.073	7.766
Cu	8.979	8.593	8.28
Zn	9.659	9.281	8.95

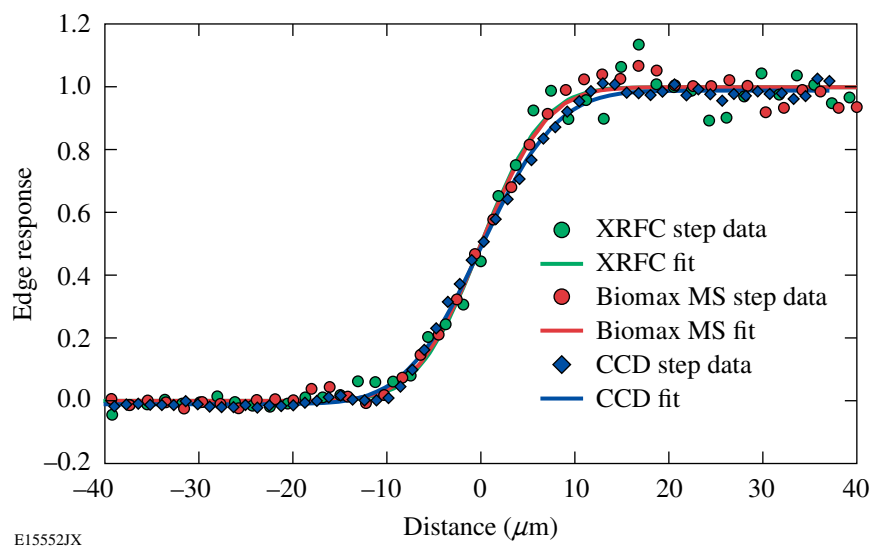


Figure 2.79

Spatial resolution of a V point-projection backlighter measured by recording an edge response for an x-ray framing camera (XRFC, green points), Kodak Biomax MS film (red points), and an x-ray-sensitive CCD array (blue points). The measured data were fit with error functions, assuming a Gaussian point-spread function.

### 2.5.12 Short-Pulse Backlighter Development

Ultrashort (<20 ps), bright x-ray backlighter sources in the 2-keV photon energy range will be provided by OMEGA EP to image cryogenic spherical implosions close to stagnation. Simulations have shown that ~2-keV x rays are optimum for the high-contrast radiography of imploded cores at the time of peak neutron production (typically with temperature ~1 keV and areal density  $\rho R \sim 200 \text{ mg/cm}^2$ ). A framing-camera gating time of ~20 ps is envisaged in order to minimize motional blurring and the contribution from target self-emission.

Preliminary experiments were performed on the Vulcan laser at the Rutherford Appleton Laboratory, UK, to measure aluminum K-shell x-ray emission in the 1.6- to 2.0-keV range. The ultrashort-pulse Vulcan 100 TW<sup>161</sup> and Petawatt<sup>162</sup> laser facilities were used to irradiate small aluminum foil targets. The *p*-polarized laser beams were focused at a 30° angle of incidence with *f*/3 off-axis parabolas to a spot size of ~10 μm in diameter on thin foils with an area of 100 × 100 μm<sup>2</sup>. The targets on the 100-TW facility were mounted as 20-μm-thick flags on carbon fibers of 6-μm diameter [Fig. 2.80(a)], while the targets on the Petawatt facility were suspended by two thin spider-silk fibers [Fig. 2.80(b)] to reduce the coupling of electron current into the target mount and to minimize thermal losses. The full short-pulse capability of the 100-TW facility (0.5 ps) was not used for these experiments; instead, the Vulcan laser produced a 14-ps pulse and a pulse energy of ~100 J, to result in a maximum on-target intensity of 1 × 10<sup>18</sup> W/cm<sup>2</sup>. For the experiments on the Petawatt facility, the laser had a 0.4-ps pulse duration and a pulse energy of ~530 J, resulting in 4 × 10<sup>20</sup> W/cm<sup>2</sup> on target at the tightest focus.

X-ray spectrometers equipped with potassium acid phthalate (KAP) crystals ( $2d = 26.63 \text{ \AA}$ ) recorded the plasma emission from the laser-irradiated side at a viewing angle of  $16^\circ$  with respect to the target normal. Figure 2.81(a) shows the results for two laser intensities using the 100-TW facility. The lower intensity of  $10^{16} \text{ W/cm}^2$  was obtained by defocusing the laser to a  $\sim 100\text{-}\mu\text{m}$  spot diameter while keeping the laser energy at  $\sim 100 \text{ J}$  and the pulse duration at  $14 \text{ ps}$ . The emission consists of the  $\text{He}_\alpha$  ( $1.59 \text{ keV}$ ) and  $\text{Ly}_\alpha$  ( $1.73 \text{ keV}$ ) transitions of the helium- and hydrogen-like ions and several

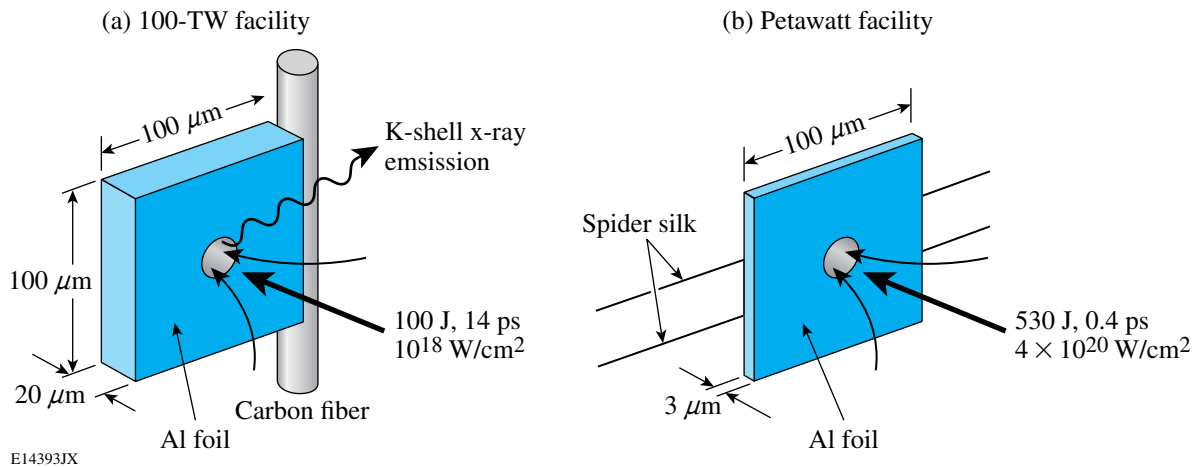


Figure 2.80

Aluminum foil targets with an area of  $100 \times 100 \mu\text{m}^2$ , (a) mounted as flags on carbon fibers for experiments on the 100-TW facility and (b) suspended by thin spider-silk fibers for experiments on the Petawatt facility of the Rutherford Appleton Laboratory Vulcan laser system. Ultrashort pulses were focused onto the foils and the Al K-shell emission was measured.

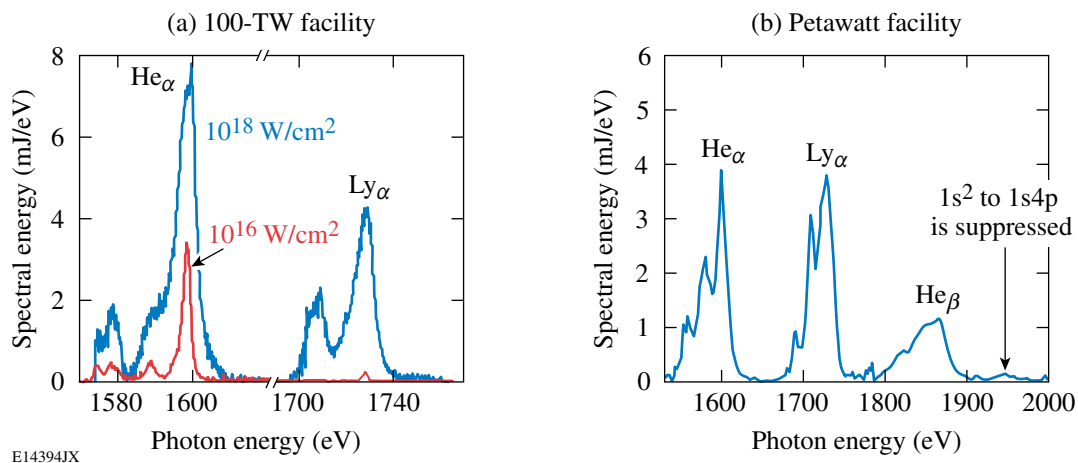


Figure 2.81

Aluminum K-shell emission from Vulcan experiments on (a) the 100-TW and (b) the Petawatt facilities. A larger spectral range was available in (b). Electron densities and temperatures of up to (a)  $n_e = 8 \times 10^{22} \text{ cm}^{-3}$  and  $T_e = 400 \text{ eV}$  and (b)  $n_e = 2 \text{ to } 4 \times 10^{23} \text{ cm}^{-3}$  and  $T_e = 500 \text{ to } 600 \text{ eV}$  are inferred.

satellite lines on the lower-energy side of each resonance line. For the higher laser intensity of  $10^{18}$  W/cm<sup>2</sup>, the spectral energies of the He<sub>α</sub> and Ly<sub>α</sub> lines are larger by factors of 2.5 and 10, respectively, and a significant increase in the spectral line widths is observed.

The radiated spectral energy densities in units of mJ/eV were estimated by using the detector quantum efficiency, filter transmissions, the crystal diffraction efficiency, and the solid angle of the spectrograph. The quantum efficiency was obtained from K<sub>α</sub> measurements in single-photon counting mode, making assumptions for the photon absorption probability in the CCD chip.<sup>163</sup> The absorption of an x-ray photon creates a certain number of free charge carriers proportional to the photon energy. K<sub>α</sub> measurements of various target materials yielded the value of 4.56-eV absorbed energy per count per pixel for the CCD detector. The absorption probability for 1.6- to 2.0-keV photons in a typical 20-μm-thick silicon depletion layer is in the range 75%–100%. Since the exact depletion-layer thickness is not known, a 100% absorption probability was assumed. Peak spectral energy densities of ~7 mJ/eV (He<sub>α</sub>) and ~4 mJ/eV (Ly<sub>α</sub>) were inferred assuming isotropic emission into a 4π solid angle. The absolute uncertainty is estimated to be a factor of 3 based on the fact that no absolute calibration of the spectrometers was performed.

Calculations with the commercially available *PrismSPECT* program<sup>164</sup> were performed to estimate the plasma conditions in the laser-heated foil targets. The plasmas were assumed to be in steady-state, nonlocal-thermodynamic-equilibrium conditions in slab geometry and to have a homogeneous density and electron temperature over a specified thickness. The temporally and spatially averaged electron temperature and density were found to be  $T_e = 300$  eV and  $n_e = 3 \times 10^{21}$  cm<sup>-3</sup> for the  $1 \times 10^{16}$  W/cm<sup>2</sup> measurement, while a strongly increased density of  $8 \times 10^{22}$  cm<sup>-3</sup> and a slightly higher temperature of 400 eV were inferred for  $1 \times 10^{18}$  W/cm<sup>2</sup> (Ref. 165). A possible explanation for the difference in density might be pre-plasma formation by a laser-pulse pedestal, induced by amplified spontaneous emission, that causes some ablation of the front layer before the main laser pulse impinges on the target. The main pulse then interacts with plasma at less than solid density and an increased density scale length. At laser intensities below  $1 \times 10^{18}$  W/cm<sup>2</sup> the ponderomotive force is probably insufficient to push the underdense plasma out of the beam path and the laser energy is mainly deposited below the critical density, while for higher intensities “hole boring” creates a channel in the preformed plasma and the laser energy is deposited in a near-solid-density plasma.

The result for a 3-μm-thick, spider-silk-mounted target that was irradiated on the Petawatt facility at  $4 \times 10^{20}$  W/cm<sup>2</sup> is shown in Fig. 2.81(b). Higher densities and temperatures are inferred with  $n_e \sim 2$  to  $4 \times 10^{23}$  cm<sup>-3</sup>, which is close to solid density ( $n_e = 7.8 \times 10^{23}$  cm<sup>-3</sup>), and  $T_e \sim 500$  to 600 eV. The overall spectral energy is slightly lower than for the 20-μm foil target, probably due to the smaller number of emitters in the thinner foil target. Rapid temporal changes in the density and temperature are expected in these highly transient short-pulse-laser-produced plasmas together with strong gradients in the longitudinal and radial directions. Isochoric heating of foil targets to a depth of ~15 μm with temperatures of up to 500 eV was recently reported<sup>166</sup> for solid-density foils and buried Al tracer layers irradiated on the Petawatt facility at intensities of ~ $10^{20}$  W/cm<sup>2</sup>. In contrast, a hot surface layer with a 2- to 3-keV electron temperature and a depth of 1 μm was observed<sup>167</sup> in the interaction of a 0.7-ps Petawatt laser beam with solid copper-foil targets at  $3 \times 10^{20}$  W/cm<sup>2</sup>. The

densities and temperatures inferred from the Al K-shell emission are close to the values reported in Ref. 167, showing that the bulk emission from the isochorically heated solid material dominates.

The measured time-integrated spectral energy densities are encouraging for the development of a short-pulse backlighter source. Assuming an emission time of  $\sim 20$  ps and a peak spectral energy density of  $7$  mJ/eV, this corresponds to a spectral power density of  $\sim 350$   $\mu\text{J}/(\text{eV}\cdot\text{ps})$  into  $4\pi$  steradians, which is a factor of  $\sim 3.5$  higher than the predicted self-emission in the 2-keV range of an imploded cryogenic target at stagnation. Absolute time-integrated measurements of the cryogenic target self-emission are underway to provide a better estimate. Simulations have shown that backlighter spectral power densities of  $800$   $\mu\text{J}/(\text{eV}\cdot\text{ps})$  are required to obtain high-contrast radiographs at stagnation. Improved estimates of the spectral power density will require measurement of the temporal evolution of the backlighter source. Such experiments are proposed for OMEGA EP.

### 2.5.13 Velocity Interferometry System for Any Reflector (VISAR)

The velocity interferometry system for any reflector (VISAR) diagnostic<sup>168</sup> was implemented on OMEGA by LLNL.<sup>169</sup> It detects the Doppler shift of a probe beam reflected off a moving surface, which may be a shock in a transparent medium or the rear target surface. Equation-of-state and shock-timing experiments use this diagnostic. To support these experiments, LLE took over responsibility for this diagnostic and optimized it to operate as a routine facility diagnostic. In the period October 2002 to May 2006 VISAR was used on over 800 target shots.

The VISAR system (Fig. 2.82) comprises three primary components: a probe laser, an imaging system, and two Mach-Zehnder interferometers. The probe laser is a Spectra Physics<sup>170</sup> frequency-doubled Nd:YAG laser that produces 8-ns pulses that can be stacked to provide a  $\sim 24$ -ns pulse. The

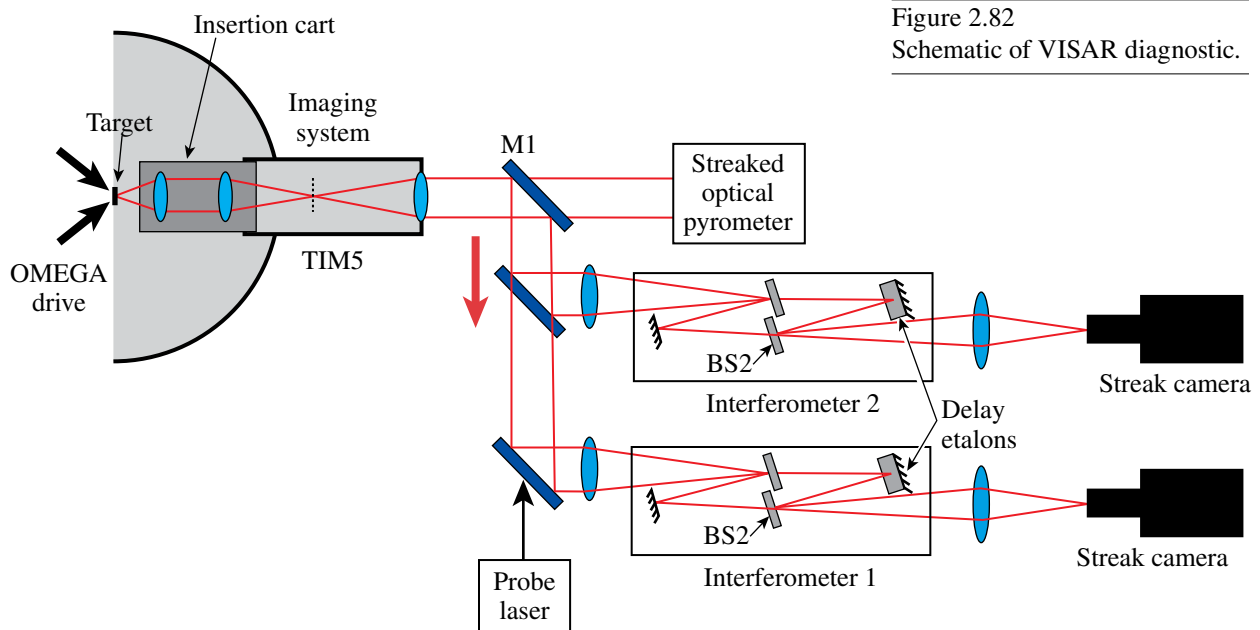


Figure 2.82  
Schematic of VISAR diagnostic.

probe laser is fiber-optically coupled to the rest of the VISAR system. The imaging system relays an image of the rear target surface to the output beamsplitters (BS2) of the interferometers. It also conveys the probe beam to and from the target. Each interferometer has an optical etalon (delay) in one leg, providing a comparison of the phases of the reflected probe beam signal at two different times. The result is a series of fringes (imposed onto the target image) whose displacements are proportional to the velocity of the rear surface, resolved in space along the face of the target transverse to the direction of shock propagation. These fringe patterns are detected with an optical streak camera to provide a record of velocity as a function of space and time, with  $\sim 5\text{-}\mu\text{m}$  spatial resolution and  $\sim 10\text{-}$  to  $50\text{-ps}$  temporal resolution, depending on the sweep speed. The second channel has a different velocity sensitivity to resolve the  $2\pi$  ambiguities that result when instantaneous velocity jumps (from shocks) are greater than one fringe period.

The detection of the shock-breakout time from opaque samples is possible with VISAR by simply monitoring the rear surface of the target. If the shock is weak, it will initiate movement of the surface that will be detected by VISAR. If the shock is strong, it will vaporize the surface and the expanding material will absorb the VISAR probe beam. In either case the arrival time of the shock is measured. The coating on the periscope mirror M1 is designed to transmit the self-emission from the target to the streaked optical pyrometer (Sec. 2.5.14), allowing simultaneous velocity and temperature measurements.

Two significant upgrades to this system have recently been implemented. The system now includes new ROSS streak cameras (Sec. 2.5.3), and an entirely new optical system has been installed to facilitate rapid installation and streamline operation. The new system has excellent performance and has decreased the diagnostic preparation time required for each shot.

A measure of the precision of the VISAR diagnostic is the correlation of the velocities deduced from the two channels. Figure 2.83 shows the velocity profiles recorded on an isentropic compression experiment that produces a slow, continuous target compression. This results in a rear-side velocity that increases over many nanoseconds. The excellent agreement between the two channels and its persistence for over 10 ns demonstrates the accuracy and stability of the system.

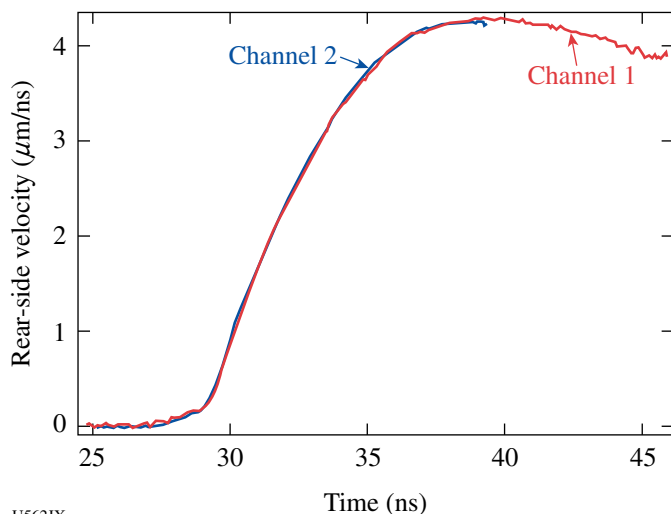


Figure 2.83  
Rear-side velocity from an isentropically compressed target measured by two VISAR channels.

### 2.5.14 Streaked Optical Pyrometer

Shocks driven by laser-produced plasmas on OMEGA typically have temperatures greater than 5000 K and produce optical emission. This emission is measured by the LANL streaked optical pyrometer,<sup>171</sup> which uses a Cassegrain telescope (optimized for 250-nm light) coupled to an optical streak camera. This system has been modified so that it can be used simultaneously with the VISAR system (Sec. 2.5.13). Referring to Fig. 2.82, the self-emission light in the 600- to 850-nm range leaks through one of the periscope mirrors (M1) and enters the streaked optical pyrometer. Correction optics compensate for the refractive VISAR telescope used at these wavelengths. The result is a system that provides simultaneous velocity (VISAR) and temperature measurements (streaked optical pyrometer) and has been extremely useful for equation-of-state and shock-timing experiments.

This arrangement has recently been enhanced by removing seven of the mirrors that were needed for the Cassegrain system. The new optical system (Fig. 2.84) is much simpler: it has an image relay (two lenses), two mirrors, a Dove prism (for image rotation), and an interference filter pack. This system has increased the sensitivity by a factor of six and enabled the detection of multiple wavelength bands (400 to 500 nm and 600 to 850 nm). The higher sensitivity allows a better detection of phase-transition (melt) signals, and the multiple wavelengths allow color-temperature measurements.

The responsivity of the pyrometer has been calibrated using a lamp whose calibration is traceable to a National Institute of Standards and Technologies standard. The lamp is placed in the OMEGA target chamber and viewed with a standard experimental configuration. Various narrowband filters are inserted to measure the spectral response. An initial guess for the system response was taken as the product of the published spectral response of the S20 photocathode and the measured transmission spectra of the wavelength-dependent optical elements. The spectral response curve was then adjusted to reproduce the spectroscopic measurements. For a Planckian source, this provides a relatively simple relation between the recorded signal and the brightness temperature of the body. The constants used to adjust the spectral response are updated to follow optical element changes and system degradation and are available for each experiment.

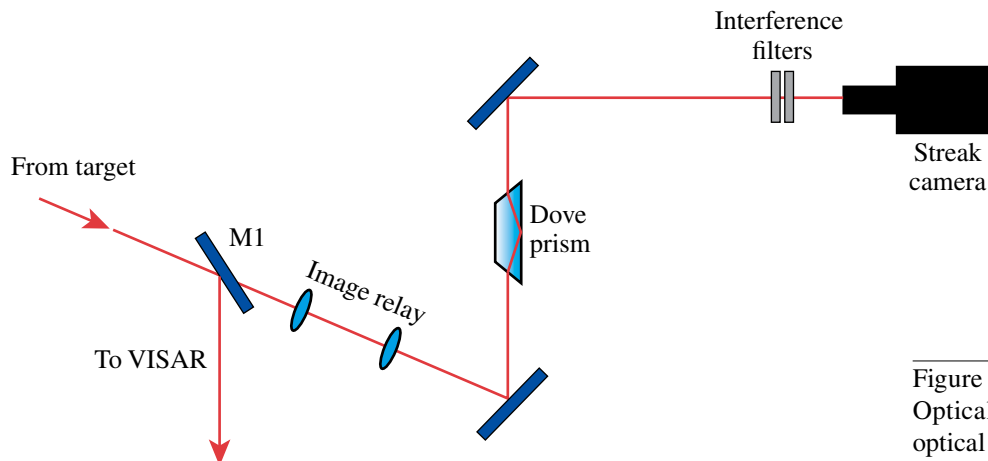


Figure 2.84  
Optical layout of the streaked optical pyrometer.

### 2.5.15 Cryogenic-Target Characterization Diagnostic

A cryogenic-target characterization diagnostic (CTCD) has been installed on OMEGA to permit evaluation of the integrity of the cryogenic D<sub>2</sub> or DT ice layers 50 ms prior to the shot. The layout of the diagnostic is shown in Fig. 2.85. A pulsed, ~50- $\mu$ s LED light source is piped through a 450- $\mu$ m light fiber to an OMEGA port. A magnified image of the fiber output is relayed to the target. After removal of the shroud and layering sphere <90 ms before shot time, the LED is fired and a shadowgraphic image of the target is formed on a CCD camera as shown in Fig. 2.85. This image is read out before the shot for subsequent analysis.

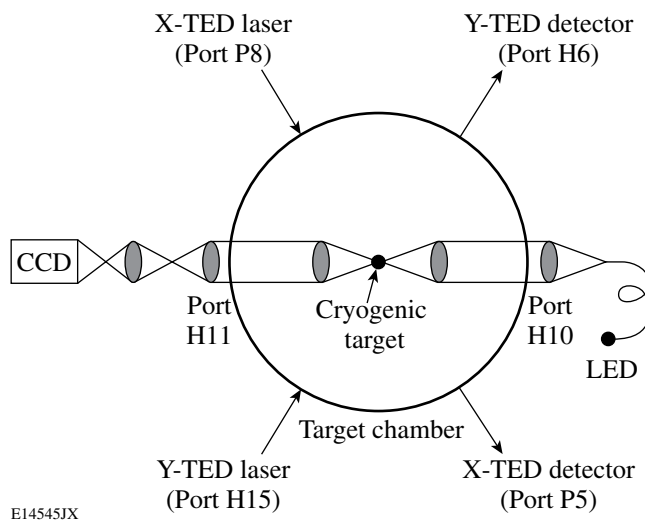


Figure 2.85

Schematic of the cryogenic-target characterization diagnostic (CTCD) on the OMEGA target chamber. A 627-nm, high-brightness LED illuminates the cryogenic target for ~50  $\mu$ s within ~50 to 100 ms prior to shot time. The target is imaged onto a CCD camera, yielding a shadowgraph. Two additional laser beams illuminate the target and are viewed in the target existence detectors X-TED and Y-TED.

A typical CTCD shadowgram is shown in Fig. 2.86(a). The four spider silks supporting the target are clearly visible as is the bright ring representing the DT ice layer of this target. The quality of these images is inferior to that obtained in the characterization station due to experimental constraints imposed by the OMEGA target chamber. However, these images still allow a basic assessment of the integrity of the targets to be made. They are sharp because of the short, 50- $\mu$ s, LED pulse.

Figure 2.87 shows the unwrapped shadowgraph of Fig. 2.86(a) in the vicinity of the target surface and the bright ring. Superposed on the figure are the positions of the target surface and the bright ring as determined by the image analysis software (black lines). Also shown (in red) are the target surface and bright ring locations as obtained before the shot in the target characterization station for approximately the same angle of observation. The close correspondence is indicative that the target has not undergone any significant change during its transport from the characterization station to the OMEGA target chamber, a process that typically takes between one and two hours and many target manipulations.

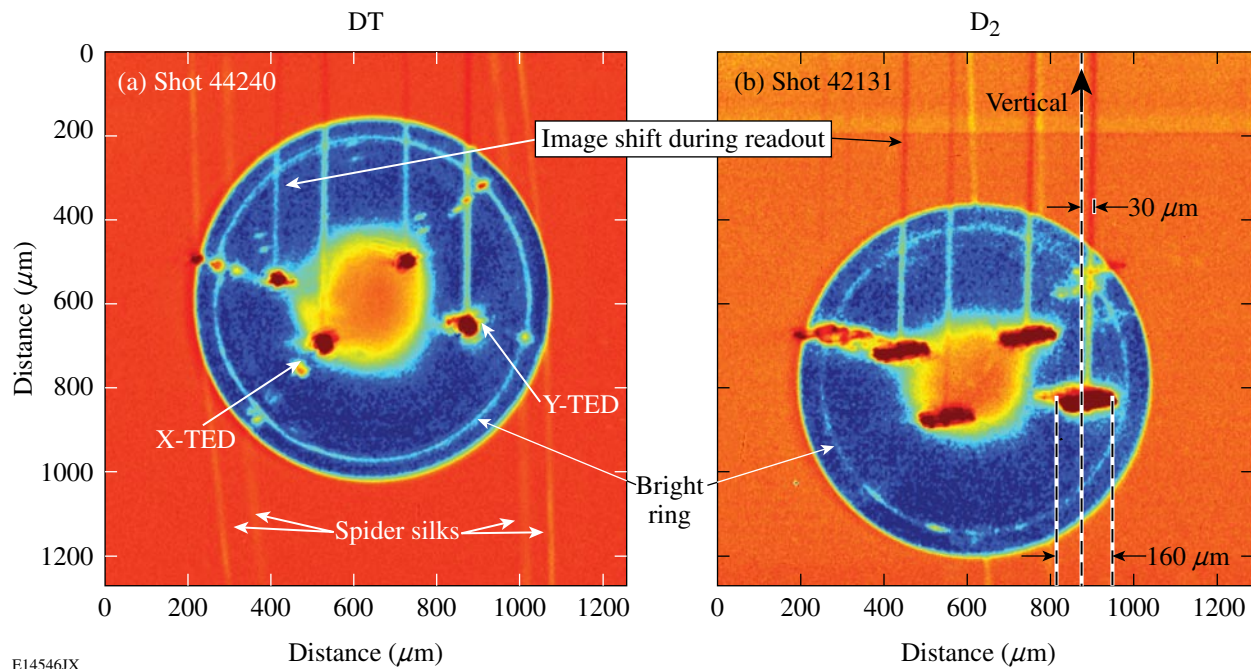


Figure 2.86

CTCD shadowgraphic images of cryogenic targets suspended by four spider silks, obtained using the 50- $\mu$ s LED pulse. The bright ring due to the ice layer is clearly visible, albeit with some breaks caused by defects in the ice layer. The bright dots are due to two cw laser beams (“X-TED” and “Y-TED”) reflecting off various surfaces of the target; their size provides an indication of target motion during the 10-ms integration time of the CCD camera. Target (a), a DT target, exhibits minimum vibrations ( $<10 \mu\text{m}$ ) while target (b), a D<sub>2</sub> target, suffers from very large ( $\sim 160 \mu\text{m}$ ) vibrations.

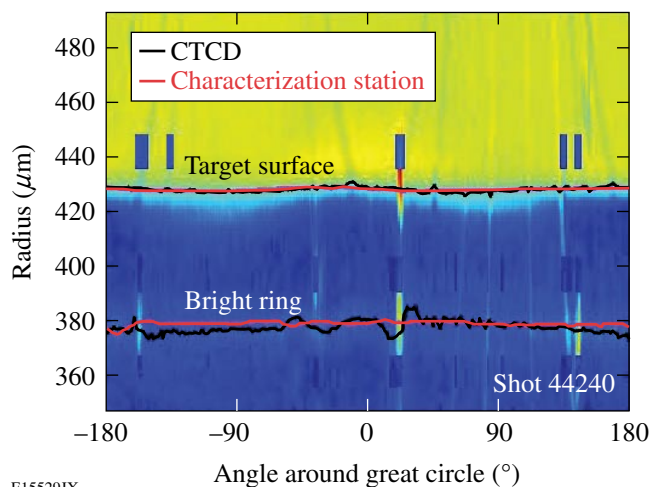


Figure 2.87

Unwrapped CTCD shadowgram of Fig. 2.5.27(a). Black lines indicate the locations of the bright ring and target edge obtained from the CTCD image. The red lines indicate the corresponding view obtained on the target characterization station, demonstrating that the target is essentially unchanged during its transport to the OMEGA target chamber.

Of particular significance in Fig. 2.86 are the bright dots aligned along two diameters and indicated as “X-TED” and “Y-TED.” They result from the target existence detector (TED), a system in which two cw, 1-mW, HeNe lasers illuminate the target from two directions (Fig. 2.85). In the absence of a target at target chamber center, detectors on the opposite side of the chamber detect the light from these lasers and prevent the OMEGA laser from firing. Reflections from the various surfaces of the cryogenic target give rise to the multitude of bright dots aligned on a diameter.

These bright dots provide information on the target vibration at shot time in two ways. First, the CCD camera (a DALSA<sup>172</sup> DALSTAR 1M30) integrates over ~10 ms. In the presence of vibrations this causes the HeNe laser to expose a larger area of the CCD. This is very apparent in Fig. 2.86(b), where the target vibrates over a distance of ~160  $\mu\text{m}$  perpendicular to the silks, while the target in Fig. 2.86(a) shows minimal vibration (<10  $\mu\text{m}$ ). Further information is provided by the faint vertical lines (“streaks”) through the bright dots. In the 2 ms subsequent to the 10-ms integration time of the CCD camera, the image is shifted, row by row (in the downward vertical direction of Fig. 2.86), to a storage location on the same chip. During this 2-ms interval the bright TED laser reflections continue to illuminate the target and reach the CCD, resulting in the streaks on the image. These streaks appear as straight lines in the vertical direction of the image if the target does not move during the 2-ms image transfer time [as in Fig. 2.86(a)]. However, if the target vibrates during the transfer, these lines can become curved. In the example of Fig. 2.86(b), the small deviation of the streak from the vertical (~30  $\mu\text{m}$  at the top of the target) indicates a vibration frequency well below 400 Hz.

The features described here have been observed frequently and have led to significant improvements in the target support system. Vibration-free images such as that shown in Fig. 2.86(a) are now routinely observed.

### 2.5.16 External-User–Developed Diagnostics

External users of OMEGA often develop, implement, and operate new diagnostic systems. The routine operation of many of these systems has been turned over to the OMEGA Experimental Operations Group. This section describes several of the external-user–developed diagnostics whose operational responsibility still rests with the originating user.

#### 2.5.16.1 HENEX (High-energy electronic x-ray diagnostic)

HENEX is an x-ray spectrometer developed by a team with participants from NRL, LLNL, NIST, and SFA Inc.<sup>173</sup> to record spectra in the energy range of 1.1 to 20.1 keV. HENEX has four reflection crystals with overlapping coverage of 1.1 to 10.9 keV and one transmission crystal covering the range of 8.6 to 20.1 keV. The spectral resolving power varies from approximately 2000 at low energies to ~300 at 20 keV. The spectrum of each crystal is recorded by a modified dental x-ray charge-coupled detector with a dynamic range >2500. This device has been used on OMEGA experiments and is a core diagnostic for x-ray spectroscopy on the NIF.

#### 2.5.16.2 TBD (Transmitted beam diagnostic)

LLNL has developed and fielded on OMEGA a transmitted beam diagnostic<sup>174</sup> to measure the fraction of a high-intensity second-harmonic interaction beam transmitted through an underdense

target. The TBD consists of an uncoated reflector, mounted near the target, that collects and reflects 4% of the transmitted light to a camera assembly outside the vacuum chamber. The TBD measures beam spray, beam deflection, and the absolute transmitted power. A third-harmonic TBD has recently been installed.

### **2.5.16.3 HRXI (High-resolution x-ray imaging)**

CEA has developed HRXI,<sup>175</sup> a high-spatial-resolution, time-resolved, x-ray imaging diagnostic, for OMEGA. It combines two state-of-the-art x-ray technologies developed in France: a high-resolution x-ray microscope (with an energy cutoff of ~6 keV) and a high-speed x-ray streak camera. The instrument achieves spatial and temporal resolutions of ~5  $\mu\text{m}$  and ~30 ps, respectively.

### **2.5.16.4 Dante**

Dante is a time-resolved x-ray spectrometer developed by LLNL and used on the Nova and OMEGA lasers.<sup>176,177</sup> This diagnostic measures the soft-x-ray power in a number of channels defined by the combination of filter edges. The detectors are planar vacuum x-ray diodes with Al, Ni, or Cr cathodes. High-speed (5 GHz) digitizers are used to time resolve the signals. The primary function of Dante is to measure the absolute, spectrally resolved, radiation flux from a hohlraum. The version of Dante installed on OMEGA has a total of 18 channels with nominal energies ranging from ~60 eV to ~15 keV. Precision calibration has been carried out using two beamlines [U3C (50 eV to 1 keV) and X8A (1 to 6 keV)] at the National Synchrotron Light Source.

### **2.5.16.5 DMX**

DMX<sup>178</sup> was developed by CEA as an x-ray spectrometer for eventual use on the NIF and LMJ.<sup>179</sup> It has 18 energy channels ranging from 50 eV to 20 keV. The softer bands (<1.5 keV) use a combination of mirrors and filters and a coaxial diode detector. The mirror/filter combination is designed to improve hard-x-ray rejection. The intermediate channels (from 1.5 keV to 5 keV) use only a filter and a coaxial diode. The highest-energy channels use a photoconductive detector (neutron-damaged GaAs) instead of an x-ray diode detector. The absolute x-ray response of the diodes and the relative transmissions of the mirror/filter combinations have been calibrated on a synchrotron beamline at the Laboratoire pour l'Utilisation du Rayonnement Electromagnetique in Orsay. DMX has been used for several hohlraum physics campaigns on OMEGA.

### **2.5.16.6 DEMIN (Detector micromegas for neutrons)**

DEMIN is a new neutron diagnostic developed by a team from CEA.<sup>180</sup> It has been designed to measure neutrons in the background of the high levels of gamma rays that are produced in ignition or near-ignition experiments. The detector couples a neutron-to-charged-particle converter to a micromegas (micro-mesh gaseous structure) detector.<sup>181,182</sup> The version developed for use on OMEGA was designed to carry out 12- to 17-MeV neutron spectroscopy of secondary neutrons. Based on tests performed on OMEGA, the  $\gamma$ -ray background is sufficiently suppressed by this device to allow measurements of secondary as well as tertiary neutrons in future experiments on OMEGA, the NIF, and the LMJ.<sup>179</sup>

## **2.6 TARGET FABRICATION** (Under construction)

## 2.7 REFERENCES

1. "A Novel Energy Measurement System for the OMEGA Laser," *LLE Review Quarterly Report* **63**, 110, Laboratory for Laser Energetics, University of Rochester, Rochester, NY, LLE Document No. DOE/SF/19460-91, NTIS Order No. DE96000767 (1995).
2. T. J. Kessler, Y. Lin, J. J. Armstrong, and B. Velazquez, "Phase Conversion of Lasers with Low-Loss Distributed Phase Plates," in *Laser Coherence Control: Technology and Applications*, edited by H. T. Powell and T. J. Kessler (SPIE, Bellingham, WA, 1993), Vol. 1870, p. 95.
3. Y. Lin, T. J. Kessler, and G. N. Lawrence, "Design of Continuous Surface-Relief Phase Plates by Surface-Based Simulated Annealing to Achieve Control of Focal-Plane Irradiance," *Opt. Lett.* **21**, 1703 (1996).
4. T. J. Kessler, Y. Lin, L. S. Iwan, W. P. Castle, C. Kellogg, J. Barone, E. Kowaluk, A. W. Schmid, K. L. Marshall, D. J. Smith, A. L. Rigatti, J. Warner, and A. R. Staley, "Laser Phase Conversion Using Continuous Distributed Phase Plates," in *Second Annual International Conference on Solid State Lasers for Application to Inertial Confinement Fusion*, edited by M. L. André (SPIE, Bellingham, WA, 1997), Vol. 3047, p. 272.
5. S. Skupsky, R. W. Short, T. Kessler, R. S. Craxton, S. Letzring, and J. M. Soures, "Improved Laser-Beam Uniformity Using the Angular Dispersion of Frequency-Modulated Light," *J. Appl. Phys.* **66**, 3456 (1989).
6. S. Skupsky and R. S. Craxton, "Irradiation Uniformity for High-Compression Laser-Fusion Experiments," *Phys. Plasmas* **6**, 2157 (1999).
7. Y. Kato, K. Mima, N. Miyanaga, S. Arinaga, Y. Kitagawa, M. Nakatsuka, and C. Yamanaka, "Random Phasing of High-Power Lasers for Uniform Target Acceleration and Plasma-Instability Suppression," *Phys. Rev. Lett.* **53**, 1057 (1984).
8. "OMEGA Phase Conversion with Distributed Phase Plates," *LLE Review Quarterly Report* **33**, 1, Laboratory for Laser Energetics, University of Rochester, Rochester, NY, LLE Document No. DOE/DP/40200-65 (1987).
9. J. A. Menapace, S. N. Dixit, F. Y. Genin, and W. F. Brocious, "Magnetorheological Finishing for Imprinting Continuous-Phase Plate Structures onto Optical Surfaces," in *Laser-Induced Damage in Optical Materials: 2003*, edited by G. J. Exarhos, A. H. Guenther, N. Kaiser, K. L. Lewis, M. J. Soileau, and C. J. Stolz (SPIE, Bellingham, WA, 2003), Vol. 5273, p. 220.
10. H. G. Ahlstrom, "Lawrence Livermore National Laboratory Laser Fusion Program," Lawrence Livermore National Laboratory, Livermore, CA, UCRL-87114 (1982).

11. S. P. Regan, J. A. Marozas, J. H. Kelly, T. R. Boehly, W. R. Donaldson, P. A. Jaanimagi, R. L. Keck, T. J. Kessler, D. D. Meyerhofer, W. Seka, S. Skupsky, and V. A. Smalyuk, "Experimental Investigation of Smoothing by Spectral Dispersion," *J. Opt. Soc. Am. B* **17**, 1483 (2000).
12. S. P. Regan, J. A. Marozas, R. S. Craxton, J. H. Kelly, W. R. Donaldson, P. A. Jaanimagi, D. Jacobs-Perkins, R. L. Keck, T. J. Kessler, D. D. Meyerhofer, T. C. Sangster, W. Seka, V. A. Smalyuk, S. Skupsky, and J. D. Zuegel, "Performance of 1-THz-Bandwidth, Two-Dimensional Smoothing by Spectral Dispersion and Polarization Smoothing of High-Power, Solid-State Laser Beams," *J. Opt. Soc. Am. B* **22**, 998 (2005).
13. T. R. Boehly, V. A. Smalyuk, D. D. Meyerhofer, J. P. Knauer, D. K. Bradley, R. S. Craxton, M. J. Guardalben, S. Skupsky, and T. J. Kessler, "Reduction of Laser Imprinting Using Polarization Smoothing on a Solid-State Fusion Laser," *J. Appl. Phys.* **85**, 3444 (1999).
14. A. Cok, "Optimization of Polar-Direct-Drive Beam Profiles for Initial NIF Targets," *2006 Summer Research Program for High School Juniors at the University of Rochester's Laboratory for Laser Energetics*, University of Rochester, Rochester, NY (2006) (unpublished).
15. Zygo Corporation, Middlefield, CT 06455.
16. J. D. Moody, L. Divol, S. H. Glenzer, A. J. MacKinnon, D. H. Froula, G. Gregori, W. L. Kruer, L. J. Suter, E. A. Williams, R. Bahr, and W. Seka, "Experimental Studies of Simultaneous 351 nm and 527 nm Laser Beam Interactions in a Long Scalelength Plasma," in *Inertial Fusion Sciences and Applications 2003*, edited by B. A. Hammel, D. D. Meyerhofer, J. Meyer-ter-Vehn, and H. Azechi (American Nuclear Society, La Grange Park, IL, 2004), p. 218.
17. S. H. Glenzer, P. Arnold, G. Bardsley, R. L. Berger, G. Bonanno, T. Borger, D. E. Bower, M. Bowers, R. Bryant, S. Buckman, S. C. Burkhart, K. Campbell, M. P. Chrisp, B. I. Cohen, C. Constantin, F. Cooper, J. Cox, E. Dewald, L. Divol, S. Dixit, J. Duncan, D. Eder, J. Edwards, G. Erbert, B. Felker, J. Fornes, G. Frieders, D. H. Froula, S. D. Gardner, C. Gates, M. Gonzalez, S. Grace, G. Gregori, A. Greenwood, R. Griffith, T. Hall, B. A. Hammel, C. Haynam, G. Heestand, M. Henesian, G. Hermes, D. Hinkel, J. Holder, F. Holdner, G. Holtmeier, W. Hsing, S. Huber, T. James, S. Johnson, O. S. Jones, D. Kalantar, J. H. Kammerschroer, R. Kauffman, T. Kelleher, J. Knight, R. K. Kirkwood, W. L. Kruer, W. Labiak, O. L. Landen, A. B. Langdon, S. Langer, D. Latray, A. Lee, F. D. Lee, D. Lund, B. MacGowan, S. Marshall, J. McBride, T. McCarville, L. McGrew, A. J. Mackinnon, S. Mahavandi, K. Manes, C. Marshall, J. Menapace, E. Mertens, N. Meezan, G. Miller, S. Montelongo, J. D. Moody, E. Moses, D. Munro, J. Murray, J. Neumann, M. Newton, E. Ng, C. Niemann, A. Nikitin, P. Opsahl, E. Padilla, T. Parham, G. Parrish, C. Petty, M. Polk, C. Powell, I. Reinbachs, V. Rekow, R. Rinnert, B. Riordan, M. Rhodes, V. Roberts, H. Robey, G. Ross, S. Sailors, R. Saunders, M. Schmitt, M. B. Schneider, S. Shiromizu, M. Spaeth, A. Stephens, B. Still, L. J. Suter, G. Teitbohl, M. Tobin, J. Tuck, B. M. Van Wonterghem,

- R. Vidal, D. Voloshin, R. Wallace, P. Wegner, P. Whitman, E. A. Williams, K. Williams, K. Winward, K. Work, B. Young, P. E. Young, P. Zapata, R. E. Bahr, W. Seka, J. Fernandez, D. Montgomery, and H. Rose, "Progress in Long Scale Length Laser-Plasma Interactions," *Nucl. Fusion* **44**, S185 (2004).
18. C. Niemann, L. Divol, D. H. Froula, G. Gregori, O. Jones, R. K. Kirkwood, A. J. MacKinnon, N. B. Meezan, J. D. Moody, C. Sorce, L. J. Suter, R. Bahr, W. Seka, and S. H. Glenzer, "Intensity Limits for Propagation of 0.527  $\mu\text{m}$  Laser Beams Through Large-Scale-Length Plasmas for Inertial Confinement Fusion," *Phys. Rev. Lett.* **94**, 085005 (2005).
  19. D. H. Froula, P. Davis, L. Divol, J. S. Ross, N. Meezan, D. Price, S. H. Glenzer, and C. Rousseaux, "Measurement of the Dispersion of Thermal Ion-Acoustic Fluctuations in High-Temperature Laser Plasmas Using Multiple-Wavelength Thomson Scattering," *Phys. Rev. Lett.* **95**, 195005 (2005).
  20. S. H. Glenzer, D. H. Froula, S. Ross, C. Niemann, N. Meezan, and L. Divol, "Characterization of High-Temperature Laser-Produced Plasmas Using Thomson Scattering," Lawrence Livermore National Laboratory, Livermore, CA, UCRL-PROC-215698 (2005).
  21. W. R. Donaldson, M. Millecchia, and R. Keck, "A Multichannel, High-Resolution, UV Spectrometer for Laser-Fusion Applications," *Rev. Sci. Instrum.* **76**, 073106 (2005).
  22. R. S. Craxton, "High Efficiency Frequency Tripling Schemes for High Power Nd:Glass Lasers," *IEEE J. Quantum Electron.* **QE-17**, 1771 (1981).
  23. D. Eimerl, J. M. Auerbach, C. E. Barker, D. Milam, and P. W. Milonni, "Multicrystal Designs for Efficient Third-Harmonic Generation," *Opt. Lett.* **22**, 1208 (1997).
  24. A. Babushkin, R. S. Craxton, S. Oskoui, M. J. Guardalben, R. L. Keck, and W. Seka, "Demonstration of the Dual-Tripler Scheme for Increased-Bandwidth Third-Harmonic Generation," *Opt. Lett.* **23**, 927 (1998).
  25. Y. R. Shen, *The Principles of Nonlinear Optics* (Wiley, New York, 1984), p. 324.
  26. R. Kekre, "Tuning Multiple Triplers Using a UV Spectrometer," *2003 Summer Research Program for High School Juniors at the University of Rochester's Laboratory for Laser Energetics*, University of Rochester, Rochester, NY, LLE Report No. 332, LLE Document No. DOE/SF19460-526 (2004).
  27. J. H. Kelly, L. J. Waxer, V. Bagnoud, I. A. Begishev, J. Bromage, B. E. Kruschwitz, T. J. Kessler, S. J. Loucks, D. N. Maywar, R. L. McCrory, D. D. Meyerhofer, S. F. B. Morse, J. B. Oliver, A. L. Rigatti, A. W. Schmid, C. Stoeckl, S. Dalton, L. Folsbee, M. J. Guardalben, R. Jungquist, J. Puth, M. J. Shoup III, D. Weiner, and J. D. Zuegel, "OMEGA EP: High-Energy Petawatt Capability for the OMEGA Laser Facility," *J. Phys. IV France* **133**, 75 (2006).

28. L. J. Waxer, D. N. Maywar, J. H. Kelly, T. J. Kessler, B. E. Kruschwitz, S. J. Loucks, R. L. McCrory, D. D. Meyerhofer, S. F. B. Morse, C. Stoeckl, and J. D. Zuegel, "High-Energy Petawatt Capability for the OMEGA Laser," *Opt. Photonics News* **16**, 30 (2005).
29. J. Murray, "A Walk Through the National Ignition Facility," *ICF Quarterly Report*, **7**, 95, Lawrence Livermore National Laboratory, Livermore, CA, UCRL-LR-105821-97-3 (1997).
30. I. N. Ross, P. Matousek, M. Towrie, A. J. Langley, and J. L. Collier, "The Prospects for Ultrashort Pulse Duration and Ultrahigh Intensity Using Optical Parametric Chirped Pulse Amplifiers," *Opt. Commun.* **144**, 125 (1997).
31. Time-Bandwidth Products AG (TBP), CH-8005 Zurich, Switzerland.
32. E. B. Treacy, "Optical Pulse Compression with Diffraction Gratings," *IEEE J. Quantum Electron.* **QE-5**, 454 (1969).
33. J. A. Armstrong, N. Bloembergen, J. Ducuing, and P. S. Pershan, "Interactions Between Light Waves in a Nonlinear Dielectric," *Phys. Rev.* **127**, 1918 (1962).
34. V. Bagnoud, M. J. Guardalben, J. Puth, J. D. Zuegel, T. Mooney, and P. Dumas, "High-Energy, High-Average-Power Laser with Nd:YLF Rods Corrected by Magnetorheological Finishing," *Appl. Opt.* **44**, 282 (2005).
35. Koheras A/S, DK-3460 Birkerod, Denmark.
36. M. D. Skeldon, "A High-Bandwidth Electrical Waveform Generator Based on an Aperture-Coupled Stripline," *Rev. Sci. Instrum.* **71**, 3559 (2000).
37. Kentech Instruments Ltd., South Moreton, Didcot, Oxfordshire, OX11 9AG, UK.
38. Spectral Instruments, Tucson, AZ 85745.
39. Acton Research Corporation, Acton, MA 01720.
40. Greenfield Technology, Ferme des Arpentis, 91430 Vauhallan, France.
41. A. DeJager, "Optical Time Domain Reflectometry for the OMEGA EP Laser," *2005 Summer Research Program for High School Juniors at the University of Rochester's Laboratory for Laser Energetics*, University of Rochester, Rochester, NY, LLE Report No. 343 (2006).
42. J. M. McMahon, J. L. Emmett, J. F. Holzrichter, and J. B. Trenholme, "A Glass-Disk-Laser Amplifier," *IEEE J. Quantum Electron.* **QE-9**, 992 (1973).

43. B. M. Van Wonterghem, J. R. Murray, J. H. Campbell, D. R. Speck, C. E. Barker, I. C. Smith, D. F. Browning, and W. C. Behrendt, "System Description and Initial Performance Results for Beamlet," *ICF Quarterly Report*, **5**, 1, Lawrence Livermore National Laboratory, Livermore, CA, UCRL-LR-105821-95-1, NTIS Order No. DE95017171 (1994).
44. E. Grasz, D. Silva, M. McDaniel, D. Tiszauer, A. Rowe, and S. Yakuma, "Transport and Handling," *ICF Annual Report 1997*, Lawrence Livermore National Laboratory, Livermore, CA, UCRL-LR-105821-97-3, 214 (1998).
45. LLE's first use of water-cooled flash lamps in a disk amplifier is described in M. J. Lubin, J. M. Soures, and L. M. Goldman, "Large-Aperture Nd:Glass Laser Amplifier for High-Peak-Power Application," *J. Appl. Phys.* **44**, 347 (1973).
46. The fill factor,  $f$ , is defined such that the product of  $fF_{\text{peak}}$  and the beam aperture equals the integral of the fluence  $F$  over the aperture, where  $F_{\text{peak}}$  is the peak fluence.
47. Richardson Electronics, LaFox, IL 60147.
48. R. A. Zacharias, E. S. Bliss, S. Winters, r. A. Sacks, M. Feldman, A. Grey, J. A. Koch, C. J. Stolz, J. S. Toeppen, L. Van Atta, and B. W. Woods, "Wavefront Control of High-Power Laser Beams in the National Ignition Facility," in *Advanced High-Power Lasers*, edited by M. Osinski, H. T. Powell, and K. Toyoda (SPIE, Bellingham, WA, 2000), Vol. 3889, p. 332.
49. C. E. Barker, B. M. Van Wonterghem, J. M. Auerbach, R. J. Foley, J. R. Murray, J. H. Campbell, J. A. Caird, D. R. Speck, and B. W. Woods, "Design and Performance of the Beamlet Laser Third-Harmonic Frequency Converter," in *Solid State Lasers for Application to Inertial Confinement Fusion (ICF)*, edited by W. F. Krupke (SPIE, Bellingham, WA, 1995), Vol. 2633, p. 398.
50. P. J. Wegner, J. M. Auerbach, C. E. Barker, S. C. Burkhart, S. A. Couture, J. J. DeYoreo, R. L. Hibbard, L. W. Liou, M. A. Norton, P. A. Whitman, and L. A. Hackel, "Frequency Converter Development for the National Ignition Facility," Lawrence Livermore National Laboratory, Livermore, CA, UCRL-JC-129725 (1998).
51. See [http://www.lle.rochester.edu/05\\_omega/05\\_02\\_documentation/05\\_documentation.html](http://www.lle.rochester.edu/05_omega/05_02_documentation/05_documentation.html) (2007).
52. F. H. Séguin, J. A. Frenje, C. K. Li, D. G. Hicks, S. Kurebayashi, J. R. Rygg, B.-E. Schwartz, R. D. Petrasso, S. Roberts, J. M. Soures, D. D. Meyerhofer, T. C. Sangster, J. P. Knauer, C. Sorce, V. Yu. Glebov, C. Stoeckl, T. W. Phillips, R. J. Leeper, K. Fletcher, and S. Padalino, "Spectrometry of Charged Particles from Inertial-Confinement-Fusion Plasmas," *Rev. Sci. Instrum.* **74**, 975 (2003).

53. M. J. Moran, "Detector Development for  $\gamma$ -Ray Diagnostics of D-T Fusion Reactions," *Rev. Sci. Instrum.* **56**, 1066 (1985).
54. F. H. Séguin, C. K. Li, J. A. Frenje, D. G. Hicks, K. M. Green, S. Kurebayashi, R. D. Petrasso, J. M. Soures, D. D. Meyerhofer, V. Yu. Glebov, P. B. Radha, C. Stoeckl, S. Roberts, C. Sorce, T. C. Sangster, M. D. Cable, K. Fletcher, and S. Padalino, "Using Secondary-Proton Spectra to Study the Compression and Symmetry of Deuterium-Filled Capsules at OMEGA," *Phys. Plasmas* **9**, 2725 (2002).
55. T. E. Blue and D. B. Harris, "The Ratio of D-T and D-D Reactions as a Measure of the Fuel Density-Radius Product in Initially Tritium-Free Inertial Confinement Fusion Targets," *Nucl. Sci. Eng.* **77**, 463 (1981).
56. H. Azechi, N. Miyanaga, R. O. Stapf, K. Itoga, H. Nakaishi, M. Yamanaka, H. Shiraga, R. Tsuji, S. Ido, K. Nishihara, Y. Izawa, T. Yamanaka, and C. Yamanaka, "Experimental Determination of Fuel Density-Radius Product of Inertial Confinement Fusion Targets Using Secondary Nuclear Fusion Reactions," *Appl. Phys. Lett.* **49**, 555 (1986).
57. M. D. Cable and S. P. Hatchett, "Neutron Spectra from Inertial Confinement Fusion Targets for Measurement of Fuel Areal Density and Charged Particle Stopping Powers," *J. Appl. Phys.* **62**, 2233 (1987).
58. H. Azechi, M. D. Cable, and R. O. Stapf, "Review of Secondary and Tertiary Reactions, and Neutron Scattering as Diagnostic Techniques for Inertial Confinement Fusion Targets," *Laser Part. Beams* **9**, 119 (1991).
59. S. Kurebayashi, J. A. Frenje, F. H. Séguin, J. R. Rygg, C. K. Li, R. D. Petrasso, V. Yu. Glebov, J. A. Delettrez, T. C. Sangster, D. D. Meyerhofer, C. Stoeckl, J. M. Soures, P. A. Amendt, S. P. Hatchett, and R. E. Turner, "Using Nuclear Data and Monte Carlo Techniques to Study Areal Density and Mix in D<sub>2</sub> Implosions," *Phys. Plasmas* **12**, 032703 (2005).
60. V. Yu. Glebov, D. D. Meyerhofer, C. Stoeckl, and J. D. Zuegel, "Secondary-Neutron-Yield Measurements by Current-Mode Detectors," *Rev. Sci. Instrum.* **72**, 824 (2001).
61. S. Skupsky and S. Kacenjar, "Measuring Fuel  $\rho R$  for Inertial Fusion Experiments Using Neutron Elastic-Scattering Reactions," *J. Appl. Phys.* **52**, 2608 (1981).
62. H. Nakaishi, N. Miyanaga, H. Azechi, M. Yamanaka, T. Yamanaka, M. Takagi, T. Jitsuno, and S. Nakai, "Fuel Areal Density Measurement of Laser-Imploded Targets by Use of Elastically Scattered Protons," *Appl. Phys. Lett.* **54**, 1308 (1989).
63. C. K. Li, F. H. Séguin, D. G. Hicks, J. A. Frenje, K. M. Green, S. Kurebayashi, R. D. Petrasso, D. D. Meyerhofer, J. M. Soures, V. Yu. Glebov, R. L. Keck, P. B. Radha, S. Roberts, W. Seka, S. Skupsky, C. Stoeckl, and T. C. Sangster, "Study of Direct-Drive, Deuterium-Tritium Gas-

- Filled Plastic Capsule Implosions Using Nuclear Diagnostics at OMEGA,” *Phys. Plasmas* **8**, 4902 (2001).
64. D. D. Meyerhofer, J. A. Delettrez, R. Epstein, V. Yu. Glebov, V. N. Goncharov, R. L. Keck, R. L. McCrory, P. W. McKenty, F. J. Marshall, P. B. Radha, S. P. Regan, S. Roberts, W. Seka, S. Skupsky, V. A. Smalyuk, C. Sorce, C. Stoeckl, J. M. Soures, R. P. J. Town, B. Yaakobi, J. D. Zuegel, J. Frenje, C. K. Li, R. D. Petrasso, D. G. Hicks, F. H. Séguin, K. Fletcher, S. Padalino, C. Freeman, N. Izumi, R. Lerche, T. W. Phillips, and T. C. Sangster, “Core Performance and Mix in Direct-Drive Spherical Implosions with High Uniformity,” *Phys. Plasmas* **8**, 2251 (2001).
  65. P. B. Radha, S. Skupsky, R. D. Petrasso, and J. M. Soures, “A Novel Charged-Particle Diagnostic for Compression in Inertial Confinement Fusion Targets,” *Phys. Plasmas* **7**, 1531 (2000).
  66. J. A. Frenje, C. K. Li, F. H. Séguin, S. Kurebayashi, R. D. Petrasso, J. M. Soures, J. Delettrez, V. Yu. Glebov, D. D. Meyerhofer, P. B. Radha, S. Roberts, T. C. Sangster, S. Skupsky, and C. Stoeckl, “Measurements of Fuel and Shell Areal Densities of OMEGA Capsule Implosions Using Elastically Scattered Protons,” *Phys. Plasmas* **9**, 4719 (2002).
  67. D. R. Welch, H. Kislev, and G. H. Miley, “Tertiary Fusion Neutron Diagnostic for Density-Radius Product and Stability of Inertial Confinement Fusion,” *Rev. Sci. Instrum.* **59**, 610 (1988).
  68. “Nuclear Diagnostics for High-Density Implosions,” *LLE Review Quarterly Report* **69**, 46, Laboratory for Laser Energetics, University of Rochester, Rochester, NY, LLE Document No. DOE/SF/19460-152, NTIS Order No. DE97004432 (1996).
  69. R. D. Petrasso, C. K. Li, M. D. Cable, S. M. Pollaine, S. W. Haan, T. P. Bernat, J. D. Kilkenny, S. Cremer, J. P. Knauer, C. P. Verdon, and R. L. Kremens, “Measuring Implosion Symmetry and Core Conditions in the National Ignition Facility,” *Phys. Rev. Lett.* **77**, 2718 (1996).
  70. “D-<sup>3</sup>He Protons as a Diagnostic for Target  $\rho R$ ,” *LLE Review Quarterly Report* **73**, 15, Laboratory for Laser Energetics, University of Rochester, Rochester, NY, LLE Document No. DOE/SF/19460-212 (1997).
  71. C. K. Li, F. H. Séguin, J. A. Frenje, R. D. Petrasso, J. A. Delettrez, P. W. McKenty, T. C. Sangster, R. L. Keck, J. M. Soures, F. J. Marshall, D. D. Meyerhofer, V. N. Goncharov, J. P. Knauer, P. B. Radha, S. P. Regan, and W. Seka, “Effects of Nonuniform Illumination on Implosion Asymmetry in Direct-Drive Inertial Confinement Fusion,” *Phys. Rev. Lett.* **92**, 205001 (2004).
  72. F. H. Séguin, C. K. Li, J. A. Frenje, S. Kurebayashi, R. D. Petrasso, F. J. Marshall, D. D. Meyerhofer, J. M. Soures, T. C. Sangster, C. Stoeckl, J. A. Delettrez, P. B. Radha, V. A.

- Smalyuk, and S. Roberts, "Measurements of  $\rho R$  Asymmetries at Burn Time in Inertial-Confinement-Fusion Capsules," *Phys. Plasmas* **9**, 3558 (2002).
73. C. K. Li, D. G. Hicks, F. H. Séguin, J. A. Frenje, R. D. Petrasso, J. M. Soures, P. B. Radha, V. Yu. Glebov, C. Stoeckl, D. R. Harding, J. P. Knauer, R. L. Kremens, F. J. Marshall, D. D. Meyerhofer, S. Skupsky, S. Roberts, C. Sorce, T. C. Sangster, T. W. Phillips, M. D. Cable, and R. J. Leeper, "D<sup>3</sup>-He Proton Spectra for Diagnosing Shell  $\rho R$  and Fuel  $T_i$  of Imploded Capsules at OMEGA," *Phys. Plasmas* **7**, 2578 (2000).
74. C. K. Li, F. H. Séguin, J. A. Frenje, R. D. Petrasso, R. Rygg, S. Kurebayashi, B. Schwartz, R. L. Keck, J. A. Delettrez, J. M. Soures, P. W. McKenty, V. N. Goncharov, J. P. Knauer, F. J. Marshall, D. D. Meyerhofer, P. B. Radha, S. P. Regan, T. C. Sangster, W. Seka, and C. Stoeckl, "Capsule-Areal-Density Asymmetries Inferred from 14.7-MeV Deuterium-Helium Protons in Direct-Drive OMEGA Implosions," *Phys. Plasmas* **10**, 1919 (2003).
75. D. G. Hicks, C. K. Li, R. D. Petrasso, F. H. Séguin, B. E. Burke, J. P. Knauer, S. Cremer, R. L. Kremens, M. D. Cable, and T. W. Phillips, "Design of an Electronic Charged Particle Spectrometer to Measure  $\rho R$  on Inertial Fusion Experiments," *Rev. Sci. Instrum.* **68**, 589 (1997).
76. D. G. Hicks, "Charged Particle Spectroscopy: A New Window on Inertial Confinement Fusion," Ph.D. thesis, Massachusetts Institute of Technology, 1999.
77. C. K. Li, F. H. Séguin, J. A. Frenje, S. Kurebayashi, R. D. Petrasso, D. D. Meyerhofer, J. M. Soures, J. A. Delettrez, V. Yu. Glebov, P. B. Radha, F. J. Marshall, S. P. Regan, S. Roberts, T. C. Sangster, and C. Stoeckl, "Effects of Fuel-Shell Mix Upon Direct-Drive, Spherical Implosions on OMEGA," *Phys. Rev. Lett.* **89**, 165002 (2002).
78. C. K. Li, F. H. Séguin, J. A. Frenje, R. D. Petrasso, J. A. Koch, P. A. Amendt, S. P. Hatchett, S. W. Haan, and N. Izumi, "Using Charged Particles to Measure  $\rho R$  and  $\rho R$  Asymmetries for Indirect-Drive Implosions," *Bull. Am. Phys. Soc.* **48**, 57 (2003).
79. J. A. Frenje, C. K. Li, F. H. Séguin, J. Deciantis, S. Kurebayashi, J. R. Rygg, R. D. Petrasso, J. Delettrez, V. Yu. Glebov, C. Stoeckl, F. J. Marshall, D. D. Meyerhofer, T. C. Sangster, V. A. Smalyuk, and J. M. Soures, "Measuring Shock-Bang Timing and  $\rho R$  Evolution of D<sup>3</sup>He Implosions on OMEGA," *Phys. Plasmas* **11**, 2798 (2003).
80. C. Stoeckl, V. Yu. Glebov, S. Roberts, T. C. Sangster, R. A. Lerche, R. L. Griffith, and C. Sorce, "Ten-Inch Manipulator-Based Neutron Temporal Diagnostic for Cryogenic Experiments on OMEGA," *Rev. Sci. Instrum.* **74**, 1713 (2003).
81. R. A. Lerche and R. L. Griffith, "Resolution Limitations and Optimization of the LLNL Streak Camera Focus," in *High Speed Photography, Videography, and Photonics V*, edited by H. C. Johnson (SPIE, Bellingham, WA, 1987), Vol. 832, p. 266.

82. C. Stoeckl, R. E. Bahr, B. Yaakobi, W. Seka, S. P. Regan, R. S. Craxton, J. A. Delettrez, R. W. Short, J. Myatt, A. V. Maximov, and H. Baldis, "Multibeam Effects on Fast-Electron Generation from Two-Plasmon-Decay Instability," *Phys. Rev. Lett.* **90**, 235002 (2003).
83. Goodfellow Corporation, Berwyn, PA 19312.
84. W. R. Donaldson, R. Boni, R. L. Keck, and P. A. Jaanimagi, "A Self-Calibrating, Multichannel Streak Camera for Inertial Confinement Fusion Applications," *Rev. Sci. Instrum.* **73**, 2606 (2002).
85. R. A. Lerche, D. W. Phillion, and G. L. Tietbohl, "25 ps Neutron Detector for Measuring ICF-Target Burn History," *Rev. Sci. Instrum.* **66**, 933 (1995).
86. C. K. Li and R. D. Petrasso, "Charged-Particle Stopping Powers in Inertial Confinement Fusion Plasmas," *Phys. Rev. Lett.* **70**, 3059 (1993).
87. V. Yu. Glebov, C. Stoeckl, S. Roberts, T. C. Sangster, J. A. Frenje, R. D. Petrasso, R. A. Lerche, and R. L. Griffith, "Proton Temporal Diagnostic for ICF Experiments on OMEGA," to be published in *Review of Scientific Instruments*. See also *LLE Review Quarterly Report* **96**, 230, Laboratory for Laser Energetics, University of Rochester, Rochester, NY, LLE Document No. DOE/SF/19460-509, NTIS Order No. PB2006-106668 (2003).
88. P. Kirkpatrick and A. V. Baez, "Formation of Optical Images by X-Rays," *J. Opt. Soc. Am.* **38**, 766 (1948).
89. F. J. Marshall, T. Ohki, D. McInnis, Z. Ninkov, and J. Carbone, "Imaging of Laser-Plasma X-Ray Emission with Charge-Injection Devices," *Rev. Sci. Instrum.* **72**, 713 (2001).
90. F. J. Marshall, J. A. Delettrez, R. Epstein, R. Forties, R. L. Keck, J. H. Kelly, P. W. McKenty, S. P. Regan, and L. J. Waxer, "Direct-Drive-Implosion Experiments with Enhanced Fluence Balance on OMEGA," *Phys. Plasmas* **11**, 251 (2004).
91. R. A. Forties and F. J. Marshall, "In-Situ Characterization of High-Intensity Laser Beams on OMEGA," *Rev. Sci. Instrum.* **76**, 073505 (2005).
92. T. C. Sangster, J. A. Delettrez, R. Epstein, V. Yu. Glebov, V. N. Goncharov, D. R. Harding, J. P. Knauer, R. L. Keck, J. D. Kilkenny, S. J. Loucks, L. D. Lund, R. L. McCrory, P. W. McKenty, F. J. Marshall, D. D. Meyerhofer, S. F. B. Morse, S. P. Regan, P. B. Radha, S. Roberts, W. Seka, S. Skupsky, V. A. Smalyuk, C. Sorce, J. M. Soures, C. Stoeckl, K. Thorp, J. A. Frenje, C. K. Li, R. D. Petrasso, F. H. Séguin, K. A. Fletcher, S. Padalino, C. Freeman, N. Izumi, J. A. Koch, R. A. Lerche, M. J. Moran, T. W. Phillips, and G. J. Schmid, "Direct-Drive Cryogenic Target Implosion Performance on OMEGA," *Phys. Plasmas* **10**, 1937 (2003).

93. J. D. Kilkenny, P. Bell, R. Hanks, G. Power, R. E. Turner, and J. D. Wiedwald, "High-Speed Gated X-Ray Images," *Rev. Sci. Instrum.* **59**, 1793 (1988).
94. D. K. Bradley, J. Delettrez, P. A. Jaanimagi, F. J. Marshall, C. P. Verdon, J. D. Kilkenny, and P. Bell, "X-Ray Gated Images of Imploding Microballoons," in *High Speed Photography, Videography and Photonics VI*, edited by G. L. Stradling (SPIE, Bellingham, WA, 1988), Vol. 981, p. 176.
95. P. M. Bell, J. D. Kilkenny, G. Power, R. Bonner, and D. K. Bradley, "Multiframe X-Ray Images from a Single Meander Stripline Coated on a Microchannel Plate," in *Ultrahigh Speed and High Speed Photography, Photonics, and Videography VII*, edited by G. L. Stradling (SPIE, Bellingham, WA, 1989), Vol. 1155, p. 430.
96. J. D. Kilkenny, "High Speed Proximity Focused X-Ray Cameras," *Laser Part. Beams* **9**, 49 (1991).
97. D. K. Bradley, P. M. Bell, J. D. Kilkenny, R. Hanks, O. Landen, P. A. Jaanimagi, P. W. McKenty, and C. P. Verdon, "High-Speed Gated X-Ray Imaging for ICF Target Experiments," *Rev. Sci. Instrum.* **63**, 4813 (1992).
98. D. K. Bradley, P. M. Bell, O. L. Landen, J. D. Kilkenny, and J. Oertel, "Development and Characterization of a Pair of 30–40 ps X-Ray Framing Cameras," *Rev. Sci. Instrum.* **66**, 716 (1995).
99. V. A. Smalyuk, T. R. Boehly, L. S. Iwan, T. J. Kessler, J. P. Knauer, F. J. Marshall, D. D. Meyerhofer, C. Stoeckl, B. Yaakobi, and D. K. Bradley, "Fourier-Space Image Processing for Spherical Experiments on OMEGA," *Rev. Sci. Instrum.* **72**, 635 (2001).
100. R. E. Turner, O. L. Landen, D. K. Bradley, S. S. Alavarez, P. M. Bell, R. Costa, J. D. Moody, and D. Lee, "Comparison of Charge Coupled Device vs Film Readouts for Gated Micro-Channel Plate Cameras," *Rev. Sci. Instrum.* **72**, 706 (2001).
101. M. C. Richardson, R. S. Marjoribanks, S. A. Letzring, J. M. Forsyth, and D. M. Villeneuve, "Spectrally Discriminating Time-Resolved and Space-Resolved X-Ray Plasma Diagnostics," *IEEE J. Quantum Electron.* **QE-19**, 1861 (1983).
102. F. J. Marshall, M. M. Allen, J. P. Knauer, J. A. Oertel, and T. Archuleta, "A High-Resolution X-Ray Microscope for Laser-Driven Planar-Foil Experiments," *Phys. Plasmas* **5**, 1118 (1998).
103. F. J. Marshall and J. A. Oertel, "A Framed Monochromatic X-Ray Microscope for ICF," *Rev. Sci. Instrum.* **68**, 735 (1997).
104. F. J. Marshall and Q. Su, "Quantitative Measurements with X-Ray Microscopes in Laser-Fusion Experiments," *Rev. Sci. Instrum.* **66**, 725 (1995).

105. F. J. Marshall, J. A. Delettrez, R. Epstein, and B. Yaakobi, "Diagnosis of Laser-Target Implosions by Space-Resolved Continuum Absorption X-Ray Spectroscopy," *Phys. Rev. E* **49**, 4381 (1994).
106. F. J. Marshall and G. R. Bennett, "A High-Energy X-Ray Microscope for Inertial Confinement Fusion," *Rev. Sci. Instrum.* **70**, 617 (1999).
107. F. J. Marshall, J. A. Oertel, and P. J. Walsh, "Framed, 16-Image, Kirkpatrick–Baez Microscope for Laser–Plasma X-Ray Emission," *Rev. Sci. Instrum.* **75**, 4045 (2004).
108. J. Carbone, J. J. Zarnowski, M. Pace, S. Czebiniak, and R. Carta, "Megarad and Scientific CIDs," in *Solid State Arrays and CCD Cameras*, edited by C. N. Anagnostopoulos, M. M. Blouke, and M. P. Lesser (SPIE, Bellingham, WA, 1996), Vol. 2654, p. 131.
109. PHOTONIS, 19106 Brive, France.
110. P. A. Jaanimagi, R. Boni, D. Butler, S. Ghosh, W. R. Donaldson, and R. L. Keck, "The Streak Camera Development Program at LLE," in *26th International Congress on High-Speed Photography and Photonics*, edited by D. L. Paisley, S. Kleinfelder, D. R. Snyder, and B. J. Thompson (SPIE, Bellingham, WA, 2005), Vol. 5580, p. 408.
111. Sydor Instruments, Rochester, NY 14623.
112. R. Boni and P. Jaanimagi, "System for Photometric Calibration of Optoelectronic Imaging Devices Especially Streak Cameras," U.S. Patent No. 6,642,499 (19 July 1999).
113. Photek Ltd., St. Leonards-on-Sea, United Kingdom.
114. Magnetic Shield Corporation, Bensenville, IL 60106.
115. A. Offner, "Unit Power Imaging Catoptric Anastigmat," U.S. Patent No. 3,748,015 (24 July 1973).
116. D. H. Kalantar, P. M. Bell, R. L. Costa, B. A. Hammel, O. L. Landen, T. J. Orzechowski, J. D. Hares, and A. K. L. Dymoke-Bradshaw, "Characterization of X-Ray Streak Cameras for Use on Nova," in *22nd International Congress on High-Speed Photography and Photonics*, edited by D. L. Paisley and A. M. Frank (SPIE, Bellingham, WA, 1997), Vol. 2869, p. 680.
117. O. Gotchev, V. N. Goncharov, J. P. Knauer, T. R. Boehly, T. J. B. Collins, R. Epstein, P. A. Jaanimagi, and D. D. Meyerhofer, "Test of Thermal Transport Models Through Dynamic Overpressure Stabilization of Ablation-Front Perturbation Growth in Laser-Driven CH Foils," *Phys. Rev. Lett.* **96**, 115005 (2006).

118. H. Shiraga, S. Fujioka, P. A. Jaanimagi, C. Stoeckl, R. B. Stephens, H. Nagatomo, K. A. Tanaka, R. Kodama, and H. Azechi, "Multi-Imaging X-Ray Streak Camera for Ultrahigh-Speed Two-Dimensional X-Ray Imaging of Imploded Core Plasmas," *Rev. Sci. Instrum.* **75**, 3921 (2004) (invited).
119. J. Delettrez, R. Epstein, M. C. Richardson, P. A. Jaanimagi, and B. L. Henke, "Effect of Laser Illumination Nonuniformity on the Analysis of Time-Resolved X-Ray Measurements in UV Spherical Transport Experiments," *Phys. Rev. A* **36**, 3926 (1987).
120. S. P. Regan, J. A. Delettrez, F. J. Marshall, J. M. Soures, V. A. Smalyuk, B. Yaakobi, V. Yu. Glebov, P. A. Jaanimagi, D. D. Meyerhofer, P. B. Radha, W. Seka, S. Skupsky, C. Stoeckl, R. P. J. Town, D. A. Haynes, Jr., I. E. Golovkin, C. F. Hooper, Jr., J. A. Frenje, C. K. Li, R. D. Petrasso, and F. H. Séguin, "Shell Mix in Compressed Core of Spherical Implosions," *Phys. Rev. Lett.* **89**, 085003 (2002).
121. S. P. Regan, J. A. Delettrez, R. Epstein, P. A. Jaanimagi, B. Yaakobi, V. A. Smalyuk, F. J. Marshall, D. D. Meyerhofer, W. Seka, D. A. Haynes, Jr., I. E. Golovkin, and C. F. Hooper, Jr., "Characterization of Direct-Drive-Implosion Core Conditions on OMEGA with Time-Resolved Ar K-Shell Spectroscopy," *Phys. Plasmas* **9**, 1357 (2002).
122. C. Stoeckl, V. Yu. Glebov, D. D. Meyerhofer, W. Seka, B. Yaakobi, R. P. J. Town, and J. D. Zuegel, "Hard X-Ray Detectors for OMEGA and NIF," *Rev. Sci. Instrum.* **72**, 1197 (2001).
123. B. Yaakobi, C. Stoeckl, W. Seka, J. A. Delettrez, T. C. Sangster, and D. D. Meyerhofer, "Measurement of Preheat Due to Fast Electrons in Laser Implosions of Cryogenic Deuterium Targets," *Phys. Plasmas* **12**, 062703 (2005).
124. B. Yaakobi, C. Stoeckl, T. R. Boehly, R. S. Craxton, D. D. Meyerhofer, and W. D. Seka, "Measurement of Preheat Due to Fast Electrons in Laser Implosions," in *26th European Conference on Laser Interaction with Matter*, edited by M. Kalal, K. Rohlena, and M. Siñor (SPIE, Bellingham, WA, 2001), Vol. 4424, p. 392.
125. L. T. Hudson, A. Henins, R. D. Deslattes, J. F. Seely, G. E. Holland, R. Atkin, L. Marlin, D. D. Meyerhofer, and C. Stoeckl, "A High-Energy X-Ray Spectrometer Diagnostic for the OMEGA Laser," *Rev. Sci. Instrum.* **73**, 2270 (2002).
126. J. F. Seely, R. D. Deslattes, Jr., L. T. Hudson, G. E. Holland, R. Atkin, D. D. Meyerhofer, and C. Stoeckl, "X-Ray Spectra in the 12- to 60-keV Energy Range from Plasmas Produced by the OMEGA Laser," in *Applications of X Rays Generated from Lasers and Other Bright Sources II*, edited by G. A. Kyrala and J.-C. J. Gauthier (SPIE, Baltimore, MD, 2001), Vol. 4504, p. 198.

127. J. F. Seely, L. Goray, D. L. Windt, B. Kjornrattanawanich, Y. Uspenskii, and A. V. Vinogradov, "Extreme Ultraviolet Optical Constants for the Design and Fabrication of Multilayer-Coated Gratings," in *Optical Constants of Materials for UV to X-Ray Wavelengths*, edited by R. Soufli and J. F. Seely (SPIE, Bellingham, WA, 2004), Vol. 5538, p. 43.
128. J. F. Seely, C. A. Back, C. Constantin, R. W. Lee, H.-K. Chung, L. T. Hudson, P. Szabo, A. Henins, G. E. Holland, and R. Atkin, "Hard X-Ray Spectra from Laser-Generated Plasmas Recorded by the HENEX Spectrometer in the 1 keV–40 keV Energy Range," in *Laser-Generated, Synchrotron, and Other Laboratory X-Ray and EUV Sources, Optics, and Applications II*, edited by G. A. Kyrala, J.-C. J. Gauthier, C. A. MacDonald, and A. M. Khounsary (SPIE, Bellingham, WA, 2005), Vol. 5918, p. 59180M.
129. B. Yaakobi, F. J. Marshall, and D. K. Bradley, "Pinhole-Array X-Ray Spectrometer for Laser-Fusion Experiments," *Appl. Opt.* **37**, 8074 (1998).
130. B. Yaakobi, V. A. Smalyuk, J. A. Delettrez, F. J. Marshall, D. D. Meyerhofer, and W. Seka, "Measurement of Areal Density Modulation of Laser-Imploded Shells Through *K*-Edge Imaging," *Phys. Plasmas* **7**, 3727 (2000).
131. B. Yaakobi, V. A. Smalyuk, J. A. Delettrez, R. P. J. Town, F. J. Marshall, V. Yu. Glebov, R. D. Petrasso, J. M. Soures, D. D. Meyerhofer, and W. Seka, "Spherical Implosion Experiments on OMEGA: Measurements of the Cold, Compressed Shell," in *Inertial Fusion Sciences and Applications 99*, edited by C. Labaune, W. J. Hogan, and K. A. Tanaka (Elsevier, Paris, 2000), p. 115.
132. L. A. Welser, R. C. Mancini, J. A. Koch, S. Dalhed, R. W. Lee, I. E. Golovkin, F. Marshall, J. Delettrez, and L. Klein, "Processing of Multi-Monochromatic X-Ray Images from Indirect Drive Implosions at OMEGA," *Rev. Sci. Instrum.* **74**, 1951 (2003).
133. J. A. Koch, T. W. Barbee, Jr., N. Izumi, R. Tommasini, R. C. Mancini, L. A. Welser, and F. J. Marshall, "Multispectral X-Ray Imaging with a Pinhole Array and a Flat Bragg Mirror," *Rev. Sci. Instrum.* **76**, 073708 (2005).
134. V. A. Smalyuk, V. N. Goncharov, J. A. Delettrez, F. J. Marshall, D. D. Meyerhofer, S. P. Regan, and B. Yaakobi, "Evolution of Shell Nonuniformities Near Peak Compression of Spherical Implosion," *Phys. Rev. Lett.* **87**, 155002 (2001).
135. C. Stoeckl, V. Yu. Glebov, J. D. Zuegel, D. D. Meyerhofer, and R. A. Lerche, "Wide-Dynamic-Range 'Neutron Bang Time' Detector on OMEGA," *Rev. Sci. Instrum.* **73**, 3796 (2002).
136. V. Yu. Glebov, C. Stoeckl, T. C. Sangster, C. Mileham, S. Roberts, and R. A. Lerche, "High-Yield Bang Time Detector for the OMEGA Laser," *Rev. Sci. Instrum.* **77**, 10E712 (2006).

137. V. Yu. Glebov, C. Stoeckl, T. C. Sangster, S. Roberts, G. J. Schmid, R. A. Lerche, and M. J. Moran, "Prototypes of National Ignition Facility Neutron Time-of-Flight Detectors Tested on OMEGA," *Rev. Sci. Instrum.* **75**, 3559 (2004).
138. G. J. Schmid, R. L. Griffith, N. Izumi, J. A. Koch, R. A. Lerche, M. J. Moran, T. W. Phillips, R. E. Turner, V. Yu. Glebov, T. C. Sangster, and C. Stoeckl, "CVD Diamond as a High Bandwidth Neutron Detector for Inertial Confinement Fusion Diagnostics," *Rev. Sci. Instrum.* **74**, 1828 (2003).
139. Tektronix, Inc., Beaverton, OR 97077.
140. H. Brysk, "Fusion Neutron Energies and Spectra," *Plasma Phys.* **15**, 611 (1973).
141. V. Yu. Glebov, C. Stoeckl, T. C. Sangster, S. Roberts, R. A. Lerche, and G. J. Schmid, "NIF Neutron Bang Time Detector Prototype Test on OMEGA," *IEEE Trans. Plasma Sci.* **33**, 70 (2005).
142. Harris International, New York, NY 10036.
143. C. Stoeckl, J. A. Delettrez, J. H. Kelly, T. J. Kessler, B. E. Kruschwitz, S. J. Loucks, R. L. McCrory, D. D. Meyerhofer, D. N. Maywar, S. F. B. Morse, J. Myatt, A. L. Rigatti, L. J. Waxer, J. D. Zuegel, and R. B. Stephens, "High-Energy Petawatt Project at the University of Rochester's Laboratory for Laser Energetics," *Fusion Sci. Technol.* **49**, 367 (2006).
144. V. Yu. Glebov, R. A. Lerche, C. Stoeckl, G. J. Schmid, T. C. Sangster, J. A. Koch, T. W. Phillips, C. Mileham, and S. Roberts, "Progress with CVD Diamond Detectors for ICF Neutron Time-of-Flight Applications," presented at ICOPS 2005, International Conference on Plasma Sciences, Monterey, CA, 20–23 June 2005 (Paper 10281).
145. J. Källne and H. Enge, "Magnetic Proton Recoil Spectrometer for Fusion Plasma Neutrons," *Nucl. Instrum. Methods Phys. Res.* **A311**, 595 (1992).
146. R. J. Leeper, G. A. Chandler, G. W. Cooper, M. S. Derzon, D. L. Fehl, D. L. Hebron, A. R. Moats, D. D. Noack, J. L. Porter, L. E. Ruggles, J. A. Torres, M. D. Cable, P. M. Bell, C. A. Clower, B. A. Hammel, D. H. Kalantar, V. P. Karpenko, R. L. Kauffman, J. D. Kilkenny, F. D. Lee, R. A. Lerche, B. J. MacGowan, M. J. Moran, M. B. Nelson, W. Olson, T. J. Orzechowski, T. W. Phillips, D. Ress, G. L. Tietbohl, J. E. Trebes, R. J. Bartlett, R. Berggren, S. E. Caldwell, R. E. Chrien, B. H. Failor, J. C. Fernández, A. Hauer, G. Idzorek, R. G. Hockaday, T. J. Murphy, J. Oertel, R. Watt, M. Wilke, D. K. Bradley, J. Knauer, R. D. Petrasso, and C. K. Li, "Target Diagnostic System for the National Ignition Facility," *Rev. Sci. Instrum.* **68**, 868 (1997).
147. J. Frenje, "Instrumentation for Fusion Neutron Measurements and Experimentation at JET," Ph.D. thesis, Uppsala University, 1998.

148. J. A. Frenje, K. M. Green, D. G. Hicks, C. K. Li, F. H. Séguin, R. D. Petrasso, T. C. Sangster, T. W. Phillips, V. Yu. Glebov, D. D. Meyerhofer, S. Roberts, J. M. Soures, C. Stoeckl, K. Fletcher, S. Padalino, and R. J. Leeper, "A Neutron Spectrometer for Precise Measurements of DT Neutrons from 10 to 18 MeV at OMEGA and the National Ignition Facility," *Rev. Sci. Instrum.* **72**, 854 (2001).
149. R. Petrasso, Supplemental Proposal to Nuclear Probing of Dense Plasmas—Stewardship Science Academic Alliances Program, Grant #DE-FG03-03NAS00058, request for Purchase of the Magnet for a Magnetic-Recoil Spectrometer for  $\rho R$  and  $T_i$  Measurements of Warm and Cryogenic OMEGA Implosions, and for Warm, Fizzle, and Ignited NIF Implosions, submitted to R. Schneider, U.S. Department of Energy, 24 September 2003.
150. J. A. Frenje, D. T. Casey, C. K. Li, F. H. Séguin, J. R. Rygg, R. D. Petrasso, V. Yu. Glebov, D. D. Meyerhofer, T. C. Sangster, C. Stoeckl, J. M. Soures, P. Song, S. Hatchett, and S. Haan, "A Magnetic Recoil Spectrometer (MRS) for  $\rho R$  and  $T_i$  Measurements of Warm and Cryogenic OMEGA Implosions, and for Warm, Fizzle, and Ignited NIF Implosions," to be submitted to Review of Scientific Instruments.
151. D. T. Casey, J. A. Frenje, C. K. Li, J. R. Rygg, F. H. Séguin, R. D. Petrasso, V. Yu. Glebov, B. Owens, D. D. Meyerhofer, T. C. Sangster, P. Song, S. Haan, S. Hatchett, R. Lerche, M. Moran, O. L. Landen, D. C. Wilson, R. Leeper, and R. Olson, "Diagnosing Cryogenic DT Implosions at OMEGA and the NIF Using Magnetic Recoil Spectrometry (MRS)," *Bull. Am. Phys. Soc.* **51**, 142 (2006).
152. S. Hatchett, Lawrence Livermore National Laboratory, private communication (2004).
153. S. W. Haan, Lawrence Livermore National Laboratory, private communication (2004).
154. Dexter Magnetic Technologies Inc., Hicksville, NY 11801.
155. A. J. Martin, R. J. Simms, and R. B. Jacobs, "Beta Energy Driven Uniform Deuterium-Tritium Ice Laser in Reactor-Size Cryogenic Inertial Fusion Targets," *J. Vac. Sci. Technol. A* **6**, 1885 (1988).
156. W. Seka, R. S. Craxton, R. L. Keck, J. P. Knauer, D. D. Meyerhofer, S. P. Regan, C. Stoeckl, B. Yaakobi, R. E. Bahr, D. Montgomery, H. Baldis, and R. Kirkwood, "Laser-Plasma Interaction Diagnostics for ICF Fusion Research," in *Advanced Diagnostics for Magnetic and Inertial Fusion*, edited by P. E. Stott, A. Wootton, G. Gorini, E. Sindoni, and D. Batani (Kluwer Academic/Plenum Publishers, New York, 2002), p. 27.
157. W. Seka, V. N. Goncharov, J. A. Delettrez, D. H. Edgell, I. V. Igumenshchev, R. W. Short, A. V. Maximov, J. Myatt, and R. S. Craxton, "Time-Dependent Absorption Measurements in Direct-Drive Spherical Implosions," *Bull. Am. Phys. Soc.* **51**, 340 (2006).

158. R. K. Kirkwood, C. A. Back, M. A. Blain, D. E. Desenne, A. G. Dulieu, S. H. Glenzer, B. J. MacGowan, D. S. Montgomery, and J. D. Moody, "Imaging Backscattered and Near to Backscattered Light in Ignition Scale Plasmas," *Rev. Sci. Instrum.* **68**, 636 (1997) (invited).
159. J. Workman, J. R. Fincke, P. Keiter, G. A. Kyrala, T. Pierce, S. Sublett, J. P. Knauer, H. Robey, B. Blue, S. G. Glendinning, and O. L. Landen, "Development of Intense Point X-Ray Sources for Backlighting High Energy Density Experiments," *Rev. Sci. Instrum.* **75**, 3915 (2004) (invited).
160. D. K. Bradley, O. L. Landen, A. B. Bullock, S. G. Glendinning, and R. E. Turner, "Efficient, 1-100-keV X-Ray Radiography with High Spatial and Temporal Resolution," *Opt. Lett.* **27**, 134 (2002).
161. C. N. Danson, J. Collier, D. Neely, L. J. Barzanti, A. Damerell, C. B. Edwards, M. H. R. Hutchinson, M. H. Key, P. A. Norreys, D. A. Pepler, I. N. Ross, P. F. Taday, W. T. Toner, M. Trentelman, F. H. Walsh, T. B. Winstone, R. W. W. Wyatt, "Well Characterized  $10^{19}$  W cm<sup>2</sup> Operation of Vulcan—An Ultra-High Power Nd:Glass Laser," *J. Mod. Opt.* **45**, 1653 (1998).
162. C. N. Danson, P. A. Brummitt, R. J. Clarke, J. L. Collier, B. Fell, A. J. Frackiewicz, S. Hancock, S. Hawkes, C. Hernandez-Gomez, P. Holligan, M. H. R. Hutchinson, A. Kidd, W. J. Lester, I. O. Musgrave, D. Neely, D. R. Neville, P. A. Norreys, D. A. Pepler, C. J. Reason, W. Shaikh, T. B. Winstone, R. W. W. Wyatt, and B. E. Wyborn, "Vulcan Petawatt—An Ultra-High-Intensity Interaction Facility," *Nucl. Fusion* **44**, S239 (2004).
163. H.-S. Park, D. M. Chambers, H.-K. Chung, R. J. Clarke, R. Eagleton, E. Giraldez, T. Goldsack, R. Heathcote, N. Izumi, M. H. Key, J. A. King, J. A. Koch, O. L. Landen, A. Nikroo, P. K. Patel, D. F. Price, B. A. Remington, H. F. Robey, R. A. Snavely, D. A. Steinman, R. B. Stephens, C. Stoeckl, M. Storm, M. Tabak, W. Theobald, R. P. J. Town, J. E. Wickersham, and B. B. Zhang, "High-Energy  $K\alpha$  Radiography Using High-Intensity, Short-Pulse Lasers," *Phys. Plasmas* **13**, 056309 (2006).
164. "SPECT3D Imaging & Spectral Analysis Suite, Getting Started," Prism Computational Sciences, Inc., Madison, WI, Report No. PCS-R-041, Ver. 3.0 (2002).
165. W. Theobald, C. Stoeckl, T. C. Sangster, J. Kuba, R. Snavely, M. H. Key, R. Heathcote, D. Neely, and P. Norreys, "X-Ray Line Emission Spectroscopy of 100-TW Laser-Pulse-Generated Plasmas for Backlighter Development of Cryogenic Implosion Capsules," *Bull. Am. Phys. Soc.* **49**, 103 (2004).
166. R. G. Evans, E. L. Clark, R. T. Eagleton, A. M. Dunne, R. D. Edwards, W. J. Garbett, T. J. Goldsack, S. James, C. C. Smith, B. R. Thomas, R. Clarke, D. J. Neely, and S. J. Rose, "Rapid Heating of Solid Density Material by a Petawatt Laser," *Appl. Phys. Lett.* **86**, 191505 (2005).

167. W. Theobald, K. Akli, R. Clarke, J. Delettrez, R. R. Freeman, S. Glenzer, J. Green, G. Gregori, R. Heathcote, N. Izumi, J. A. King, J. A. Koch, J. Kuba, K. Lancaster, A. J. MacKinnon, M. Key, C. Mileham, J. Myatt, D. Neely, P. A. Norreys, H.-S. Park, J. Pasley, P. Patel, S. P. Regan, H. Sawada, R. Shepherd, R. Snavely, R. B. Stephens, C. Stoeckl, M. Storm, B. Zhang, and T. C. Sangster, "Hot Surface Ionic Line Emission and Cold K-Inner Shell Emission from Petawatt-Laser-Irradiated Cu Foil Targets," *Phys. Plasmas* **13**, 043102 (2006).
168. L. M. Barker and R. E. Hollenbach, "Laser Interferometer for Measuring High Velocities of Any Reflecting Surface," *J. Appl. Phys.* **43**, 4669 (1972).
169. P. M. Celliers, D. K. Bradley, G. W. Collins, D. G. Hicks, T. R. Boehly, and W. J. Armstrong, "Line-Imaging Velocimeter for Shock Diagnostics at the OMEGA Laser Facility," *Rev. Sci. Instrum.* **75**, 4916 (2004).
170. Spectra-Physics, A Division of Newport Corporation, Mountain View, CA 94039.
171. J. A. Oertel, T. J. Murphy, R. R. Berggren, J. Faulkner, R. Schmel, D. Little, T. Archuleta, J. Lopez, J. Verlarde, and R. F. Horton, "Multipurpose 10 in. Manipulator-Based Optical Telescope for OMEGA and the Trident Laser Facility," *Rev. Sci. Instrum.* **70**, 803 (1999).
172. DALSA, Waterloo, Ontario, Canada, N2V 2E9.
173. J. Seely, C. Back, R. Deslattes, L. Hudson, G. Holland, P. Bell, and M. Miller, "Hard X-Ray Spectrometers for the National Ignition Facility," *Rev. Sci. Instrum.* **72**, 2562 (2001).
174. C. Niemann, G. Antonini, S. Compton, S. H. Glenzer, D. Hargrove, J. D. Moody, R. K. Kirkwood, V. Rekow, J. Satariano, C. Sorce, W. Armstrong, R. Bahr, R. Keck, G. Pien, W. Seka, and K. Thorp, "Transmitted Laser Beam Diagnostic at the OMEGA Laser Facility," *Rev. Sci. Instrum.* **75**, 4171 (2004).
175. Ph. Troussel, B. Meyer, R. Reverdin, B. Angelier, G. Lidove, P. Salvatore, and A. Richard, "Wolter-Like High Resolution X-Ray Imaging Microscope for Rayleigh Taylor Instabilities Studies," *Rev. Sci. Instrum.* **76**, 063707 (2005).
176. H. N. Kornblum, R. L. Kauffman, and J. A. Smith, "Measurement of 0.1–3-keV X-Rays from Laser Plasmas," *Rev. Sci. Instrum.* **57**, 2179 (1986).
177. K. M. Campbell, F. A. Weber, E. L. Dewald, S. H. Glenzer, O. L. Landen, R. E. Turner, and P. A. Waide, "OMEGA Dante Soft-X-Ray Power Diagnostic Component Calibration at the National Synchrotron Light Source," *Rev. Sci. Instrum.* **75**, 3768 (2004).

178. J. L. Bourgade, B. Vilette, J. L. Bocher, J. Y. Boutin, S. Chiche, N. Dague, D. Gontier, J.-P. Jadaud, B. Savale, R. Wrobel, and R. E. Turner, "DMX: An Absolutely Calibrated Time-Resolved Broadband Soft X-Ray Spectrometer Designed for MJ Class Laser-Produced Plasma," *Rev. Sci. Instrum.* **72**, 1173 (2001) (invited).
179. M. L. Andre, "Laser Megajoule Project Status," in *Inertial Fusion Sciences and Applications 99*, edited by C. Labaune, W. J. Hogan, and K. A. Tanaka (Elsevier, Paris, 2000), p. 32.
180. M. Houry, E. Delagnes, D. Riz, B. Canaud, L. Disdier, F. Garaude, Y. Giomataris, V. Yu. Glebov, Ph. Legou, Ph. Rebourgeard, and C. Sangster, "DEMIN: A Neutron Spectrometer, Micromegas-Type, for Inertial Confinement Fusion Experiments," *Nucl. Instrum. Methods Phys. Res. A* **557**, 648 (2006).
181. Y. Giomataris, P. Rebourgeard, J. P. Robert, and G. Charpak, "Micromegas: A High-Granularity Position-Sensitive Gaseous Detector for High Particle-Flux Environments," *Nucl. Instrum. Methods Phys. Res. A* **376**, 29 (1996).
182. G. Charpak, J. Derre, Y. Giomataris, and Ph. Rebourgeard, "Micromegas, a Multipurpose Gases Detector," *Nucl. Instrum. Methods Phys. Res. A* **478**, 26 (2002).



## 3. Proposal Information

Applications for facility use and financial grants from DOE are welcome from any qualified U.S. university, laboratory, or company. The preparation and submission of NLUF proposal documents is governed by the requirements described in the Research Announcement (call for proposals) issued by the DOE/NNSA Albuquerque Operations Office. This office issues the call for proposals, screens and accepts the proposals, and forwards all responsive proposals to NLUF for technical evaluation.

### 3.1 PROPOSAL PREPARATION

This section provides supplemental information to assist potential users in preparing NLUF proposals. Proposals to conduct experiments at NLUF are a request for allocation of laser beam time and, if proposed, a request for DOE financial (grant) assistance. The most important part of the proposal is the technical description and justification of the proposed experiment. The proposal should contain clear statements indicating the purpose of the experiment, the method, and the results expected.

It is mandatory that each proposal specifically state the required number of OMEGA shots, the required OMEGA laser and diagnostic configurations, the required theoretical and computational support, and the required target specifications and quantity. The principal investigators are expected to communicate with the DOE target contractor (GA) during formulation of the proposal to obtain estimates of the effort required to provide targets for the proposed experiments. A Proposal Summary sheet (see Appendix C), identifying the experiment requirements must accompany each proposal to use the NLUF. In cases where either the requested target quantity or specifications cannot be obtained within the target fabrication support contractor resources allotted to NLUF, the user must include funding for target support within his/her proposal. Similarly, if the prospective user requires computational support from LLE, such support must be costed in the proposal.

Potential applicants who intend to include in their proposal any information considered proprietary are cautioned to refer to the instructions in the DOE Research Announcement regarding the marking and protection of such data.

Separate technical and cost proposals are required for applicants seeking financial support from DOE/NNSA. Specific guidance on the format and content of each document will be provided in the DOE/NNSA Research Announcement.

### 3.2 FACILITY REQUIREMENTS

Proposals must clearly describe the specific requests for the facility, including laser and diagnostics configurations and target requirements, and contain a detailed discussion of the

background, justification, techniques, measurement accuracy, and expected results. Each of these items is critical in evaluating the proposal.

Proposals which are incomplete or not responsive to the requirements set forth in the DOE/NNSA Research Announcement will be returned. Potential users are encouraged to contact the NLUF manager for technical discussions during the proposal formulation process. This assures that important questions, such as the engineering practicality of the experiment, the equipment and target fabrication resources required, and cost factors are addressed at an early stage.

Inquiries on the use of the facility may be addressed as follows:

Manager  
National Laser Users' Facility  
Laboratory for Laser Energetics  
250 East River Road  
Rochester, NY 14623-1299  
(585) 275-3866

Telephone inquiries may be directed to either to the NLUF Manager or the Administrative Liaison.

### **3.3 INSTITUTIONAL COLLABORATIONS**

The proposal must clearly identify all collaborations that are required to carry out the proposed work. A formal confirmation from an authorized representative of the collaborating institution must accompany the proposal.

### **3.4 PROPOSAL SUBMISSION**

All NLUF proposals must be submitted in response to the DOE/NNSA Research Announcement (call for proposals), which is issued on or about the beginning of the calendar year. No proposals will be accepted directly by the NLUF or LLE.

### **3.5 PROPOSAL REVIEW**

Evaluation of applications will be conducted using a merit-review process in accordance with the criteria set forth in the DOE call for proposals. The scientific peer review panel (Steering Committee) is appointed by the President of the University of Rochester, with DOE approval. Members of the panel include outstanding scientists from education and government, each with demonstrated achievement in the scientific community. The terms of appointment for members are staggered so that part of the membership is renewed for each review.

Final selections for grant awards are made by a designated DOE official in consultation with the scientific peer review panel, based on technical merit, cost, and funding availability. The user research grants are issued and administered by the DOE Oakland Operations Office.

### **3.6 FINANCIAL SUPPORT FOR USER EXPENSES**

Along with the technical proposal requesting access to the NLUF, applicants may request financial (grant) assistance from DOE. Researchers requesting financial support from DOE must submit a separate cost proposal as described in the DOE call for proposals. The budget information submitted to DOE should include personnel costs, supplies and materials, other direct costs (including travel to the University of Rochester), indirect costs, target-fabrication costs, theoretical support, and equipment costs.



## 4. Policies

### 4.1 USER RESEARCH GRANTS

User research grants are negotiated between the user and DOE's Oakland Operations Office. DOE will notify those users that are approved for funding. This notification takes place after the Steering Committee has reviewed the proposals and made its recommendation to DOE.

### 4.2 SAFETY

LLE is designed to allow many kinds of activities, ranging from fabrication and experimentation to seminars and tours. From the viewpoint of safe work practices, however, LLE must be considered first and foremost an open laboratory environment; accordingly, all of the potential safety and health hazards of a benchtop lab must be assumed to exist.

Only by practicing safety will the risk of accidents be minimized. This is the responsibility of each user, regardless of activities. Unsafe work practices cannot be tolerated, whether they result from a failure to observe written policies and procedures, or from a failure to use prudent judgment. Unsafe actions by a user may, among other things, result in termination of an experiment.

Users must comply with all relevant safety policies and procedures in place at the UR/LLE.

All materials to be employed in experiments that are unusual, e.g., hazardous metals and all targets, must be pre-approved by UR/LLE before they are brought to the facility.

### 4.3 TARGET DESIGNS

Proposed targets must be reviewed by LLE and declared "system safe."

If a user is concerned about the safety of a particular activity, the matter is to be directed immediately to the attention of the Facility Manager.

### 4.4 SCHEDULING OF EXPERIMENTS

The scheduling process for OMEGA and OMEGA EP experiments is detailed in Appendix A (LLE INST 3000F). The facility users should note the timeline itemized in Table 4.1 with respect to the scheduling of facility shots.

A Shot Request Form (SRF) is required for each shot to be taken on OMEGA. The user is responsible for completing these forms. The SRF's must be completed via computer; access is available through the LLE home page at [www.lle.rochester.edu](http://www.lle.rochester.edu). The user should contact the NLUF

Manager to obtain instructions and the pertinent password to access the SRF's via the web site.

Table 4.1: NLUF experiment timeline.

Time	Event/Required Action
~May of solicitation year	DOE/NNSA notification to NLUF grantees.
June of each year	Facility Advisory and Scheduling Committee meets to set Annual Schedule.
4 months prior to scheduled experiment	Submit target request forms (TRF's) to target contractor (GA) [or make alternative target fabrication arrangements].
2 months prior to scheduled shots	Submit detailed experimental proposal and draft SRF's to FASC.
2 weeks prior to shots	Fill out shot request forms (SRF's) and participate in pre-shot configuration review at LLE (or by VTC). Also submit pre-shot briefing viewgraphs to NLUF manager for week-in-advance shot briefing.
2 working days prior to shots	Provide target metrology data to OMEGA/OMEGA EP Experimental Group Leader.

In the event that a user is not prepared to conduct an experiment when scheduled or the laser system is unavailable (for whatever reason) when scheduled, an attempt to reschedule the experiment to a later date will be made. However, the users must bear in mind that the OMEGA schedule is very tight and there is not much flexibility to reapportion shot time if the assigned time is not used as originally scheduled.

#### 4.5 POST-SHOT EVALUATION

There are several post-shot key reporting requirements for all external users of the OMEGA and OMEGA EP facilities. These are itemized in Table 4.2. Of particular importance is the requirement for a post-shot "critique" of the experiment. The review of proposals for the continuation of ongoing work at NLUF and for new experiments takes into consideration the technical performance and timely reporting of previous work performed at NLUF by the user.

Table 4.2: NLUF User reporting requirements.

Time	Report/Briefing	Receiver
On shot day	Complete experimental effectiveness rating (a 0, 0.5, or 1.0 point system) to indicate initial assessment of experimental success in meeting objectives.	Shot Director
1 day after shot day	A brief summary of progress toward experimental objectives.	NLUF Manager
1 week after shot day	A detailed critique on all aspects of experiment.	Engineering Division Director
October of each year	A brief summary of progress made toward achieving program objectives. This is published in the LLE Annual Report.	NLUF Manager
Upon completion of grant/effort proposal	Final report.	DOE/NNSA and NLUF Manager

#### **4.6 PHOTOGRAPHIC DATA/DARKROOM POLICY**

LLE maintains a darkroom for the purpose of processing films used in OMEGA experiments. This darkroom is available for photographic use by qualified users only. A qualified user is one who has demonstrated darkroom capability and understanding and has obtained permission to use the darkroom from the darkroom manager.

#### **4.7 PUBLICATIONS**

It is the University of Rochester's policy that the results of the research conducted on its campuses be freely published. This policy also applies to the publication of a description of the user's experiment and the results of that experiment. To protect the interests of users and the University, a delay in publication consistent with this policy may be made upon written request.

The users' facility is also under obligation to report on work conducted at the facility.

To address these objectives, the users' facility produces an annual summary of users' research. Each user agrees to furnish and authorize the users' facility to reproduce (1) the abstract of the user's research as contained in the proposal and (2) a brief report of the annual progress or the results of the experiment. The report is to be submitted by the user to the NLUF manager no later than six weeks following the completion of each fiscal year.

#### **4.8 ACKNOWLEDGMENTS**

A specific acknowledgment on all abstracts, reports, and publications of the research performed at the users' facility is required with the following sentence on the title or first page:

"The research and materials incorporated in this work were partially developed at the National Laser Users' Facility at the University of Rochester's Laboratory for Laser Energetics, with financial support from the U.S. Department of Energy under Cooperative Agreement DE-FC52-92SF19460."

Investigators should also add acknowledgments for any other contracts that support this research, including any DOE research contracts.

#### **4.9 RESTRICTED DATA**

It is the policy of the University of Rochester that classified research will not be conducted as part of the DOE-funded program at the NLUF. Accordingly, a user must not submit any proposal that requires the use of or is likely to generate security classified data, including DOE-restricted data. In the unforeseen event that it becomes necessary to use such data for the performance of a user's experiment, the University reserves the right to stop the work; to terminate, without liability, any further requirement to operate the users' facility for that experiment; and to hold the data for disposition under applicable law.

If, while at the user's facility, a user realizes or suspects that restricted data is being generated, the matter must be brought immediately to the attention of the Director of LLE.

#### **4.10 SECURITY**

All personnel, including users and visitors, are required to wear University of Rochester identification badges while in the building. A key and key card are required for access to the building during nonworking hours. Keys, key cards, and ID badges may be requested from the Administrative Liaison. Please note that all foreign nationals visiting the laboratory must receive approval from DOE/NNSA. Requests for foreign visitors must be submitted to the Administrative Liaison at least 60 days in advance of the proposed visit.

#### **4.11 SMOKING**

LLE facilities must be maintained in a very clean environment. For this reason, smoking is not permitted within the main building or its adjoining structures.

#### **4.12 WEB SITE**

The UR/LLE maintains a web site ([www.lle.rochester.edu](http://www.lle.rochester.edu)) that contains an NLUF page and OMEGA facility schedule.

## 5. Travel and Housing Information

### 5.1 HOTELS AND HOUSING

For short visits, several hotels are located within a reasonable distance. Reservations are made by the user directly. (See map on LLE web site.)

### 5.2 AIRPORT

The Greater Rochester International Airport serves the metropolitan area. American, Jet Blue, Continental, United, Delta, Northwest, USAir, and other airlines have flight connections at the airport.

The airport is within ten minutes of the users' facility. For short visits, taxicab transportation is readily available. Car rentals are arranged at the airport.

### 5.3 MAP

A map of the access routes to LLE is shown below.



**Appendix A**

**Laser Facility Organization and Regulation Manual**

**Part I**



**Part I**  
**Concept of Operations and Scheduling**

1000	Laser Facility Overview
1001	OMEGA Governance Plan
1002	Science Program Advisory Committee
1003	FASC Roles and Responsibilities
1004	Experimental Proposals and Principal Investigator Roles and Responsibilities
1005	Laser Facility Operations Overview
1006	Laser Facility Manager
1007	Laser System Scientist
1008	Cryogenic and Tritium Facility Manager

## **1000 Laser Facility Overview**

OMEGA is a multikilijoule-class laser facility located at the University of Rochester's Laboratory for Laser Energetics (UR/LLE). The OMEGA Laser Facility includes the 60-beam compression laser system, the four-beam extended performance (EP) laser, and the cryogenic target handling system. The laser systems can be operated independently, with separate scientific objectives for each, or jointly with the combined capabilities addressing a single requirement.

The OMEGA compression laser system is a 60-beam neodymium glass laser that is frequency converted to deliver up to 30 kJ of 351-nm light on target. This system is capable of conducting fully diagnosed direct-drive or indirect-drive target physics experiments, including direct-drive planar or spherical cryogenic experiments. The system is designed to operate on a 1-h shot cycle and will nominally deliver 1000 shots per year in single-shift operations.

The OMEGA EP Laser System consists of four beams, two that have both long- and short-pulse capability and two that have only long-pulse capability. The short-pulse beams deliver 1- to 100-ps pulses at energies up to 2.6 kJ per beam to either the OMEGA compression target chamber or the auxiliary OMEGA EP target chamber. The long-pulse beams deliver 1- to 10-ns pulses at energies up to 6.5 kJ per beam to the auxiliary OMEGA EP target chamber. When coupled to the OMEGA target chamber, the OMEGA EP system will support short-pulse backlighting and fast-ignition experiments. When coupled to the auxiliary target chamber, the system will be capable of fully diagnosed high-energy, high-intensity planar experiments. The system is designed to operate on a 2-h shot cycle and will nominally deliver 450 shots per year in single-shift operations.

The OMEGA Cryogenic Target Handling System (CTHS) is capable of filling, layering, and characterizing cryogenic DD and DT spherical targets and DD planar targets. It delivers and positions these targets in the target chamber and supports them at the target

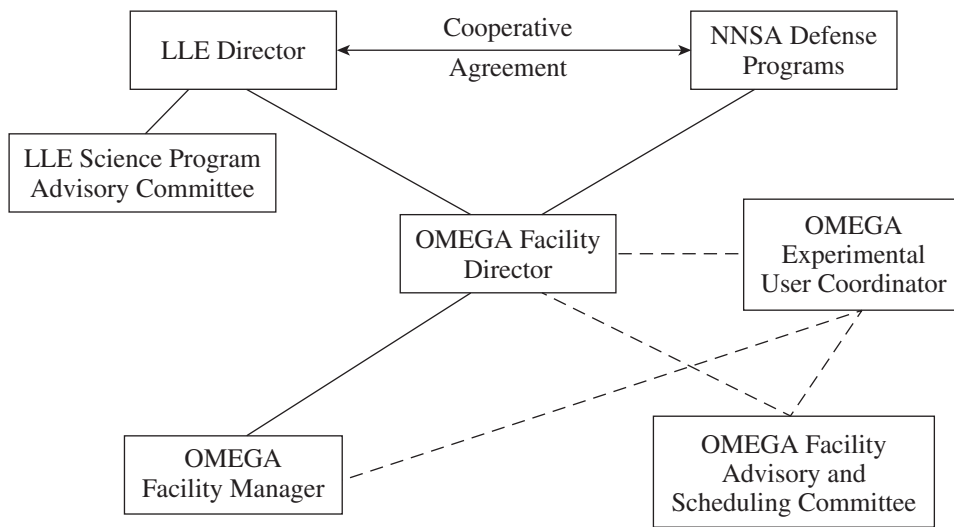
chamber center until they are shot. The OMEGA EP system will be limited to planar DD targets.

The OMEGA Laser Facility is funded by the Department of Energy (DOE) and is housed in the University of Rochester–owned Laboratory for Laser Energetics’ facility located on the South Campus of the University of Rochester. The facility is operated under a Cooperative Agreement between the Department of Energy and UR/LLE. Under this Agreement the UR/LLE also operates the National Laser Users’ Facility (NLUF). Shots are made available to NLUF users on the OMEGA Laser Facility; however, the NLUF users are funded by DOE outside of the DOE–UR/LLE Cooperative Agreement.

**1001 OMEGA Governance Plan**

**1.1 Introduction**

The OMEGA Governance Plan covers the process by which the OMEGA Laser Facility, including OMEGA EP, is governed to determine the allocation of system time, schedule user experiments, and ensure that users’ current and future requirements are presented to the OMEGA Facility Director. This governance plan does not cover the line-management functions of the OMEGA Facility Director to operate and maintain OMEGA and OMEGA EP. The organization for OMEGA Governance is outlined in Fig. I-1.



E15619JX

Figure I-1

### **1.1.1 LLE Director**

The LLE Director is responsible for the overall direction of the laboratory to ensure that National Nuclear Security Administration (NNSA) program goals are supported. He is responsible for appointing the OMEGA Facility Director.

- The LLE Director is selected by the President and approved by the Board of Trustees of the University of Rochester in consultation with NNSA and is appointed for a five-year renewable term.
- The LLE Director reports administratively to the University of Rochester's Provost. Programmatically, the LLE Director consults with the NNSA Assistant Deputy Administrator Office for Inertial Confinement Fusion.
- The LLE Director approves and publishes the annual OMEGA fiscal-year shot schedule three months prior to the start of the fiscal year and certifies that it fulfills the guidance provided by NNSA.

### **1.1.2 OMEGA Facility Director**

The OMEGA Facility Director is responsible for defining the overall OMEGA facility use that maximizes the benefit to the national stockpile stewardship and ignition programs and balances security priorities with broader scientific, technological, and economic competitiveness goals.

### **1.1.3 OMEGA Facility Advisory and Scheduling Committee (FASC)**

This committee recommends OMEGA system time allocation, promotes an effective user community, and reviews the facility's overall effectiveness for users.

### **1.1.4 LLE Science Program Advisory Committee**

This committee advises the LLE Director on major policy issues, balance of program use, use strategy, availability, and future capabilities of OMEGA. It advises on LLE's inertial confinement fusion (ICF) science program direction.

### **1.1.5 OMEGA Experimental User Coordinator**

The Experimental Coordinator is the single point of contact for all non-LLE Principal Investigators (PI's). He/she is the liaison between the PI and the OMEGA support staff for technical information and user support for planning and conducting experiments on OMEGA. The user coordinator is appointed by the Experimental Division Director.

### **1.1.6 OMEGA Laser Facility Manager**

The OMEGA Laser Facility Manager is responsible for the overall operation and operational readiness of the OMEGA Laser System, including the OMEGA compression and OMEGA EP facilities.

## **1.2 OMEGA System Time Availability, Programmatic Allocation, and User Support**

### **1.2.1 System Time Availability**

There are three principal uses of OMEGA: ignition physics, weapons physics, and basic science. The allocation of system shot time to users will be based on NNSA's programmatic needs and available shot time. The number of shots depends on the type of shots, system availability, experimental effectiveness, and funding levels.

The OMEGA Laser Facility Manager is responsible for the overall operation of OMEGA, including ensuring that system availability and experimental effectiveness are optimized. The Laser Facility Manager will provide the following to the OMEGA Facility Director, the OMEGA Facility Advisory and Scheduling Committee, and the LLE Science Program Advisory Committee:

- Monthly report on the number of target shots scheduled and completed by user, including the experimental effectiveness of each shot. A yearly summary report will be provided.
- Monthly report of OMEGA system availability, including an analysis of the contribution to system nonavailability. A yearly summary report will be provided.
- An annual projection of the system time available based on the expected funding.

### **1.2.2 Programmatic Allocation**

The OMEGA Facility Advisory and Scheduling Committee (FASC) will recommend system time allocations as described in Sec. 1003 following guidance on program balance. In FY08 the system time allocation was 50% for the National Ignition Campaign (NIC), 20% for weapons physics, 25% for basic science (NLUF and Laboratory), and 5% for contingency. Contingency will be assigned to make up system time lost due to unavailability and/or additional urgent requirements. The FASC will advise the LLE Director and OMEGA Facility Director on changes to the guidance for program balance.

### **1.2.3 OMEGA User Support**

The OMEGA Facility Director has fiscal responsibility for operation of the facility and is responsible for ensuring that all appropriate support functions are provided. Standard capabilities required for users to conduct experiments supplied by the facility include:

- Experimental support, including facility diagnostics, operations data processing and access, standard phase plates, and polarization rotators. An on-site target contractor provides support for national laboratories and

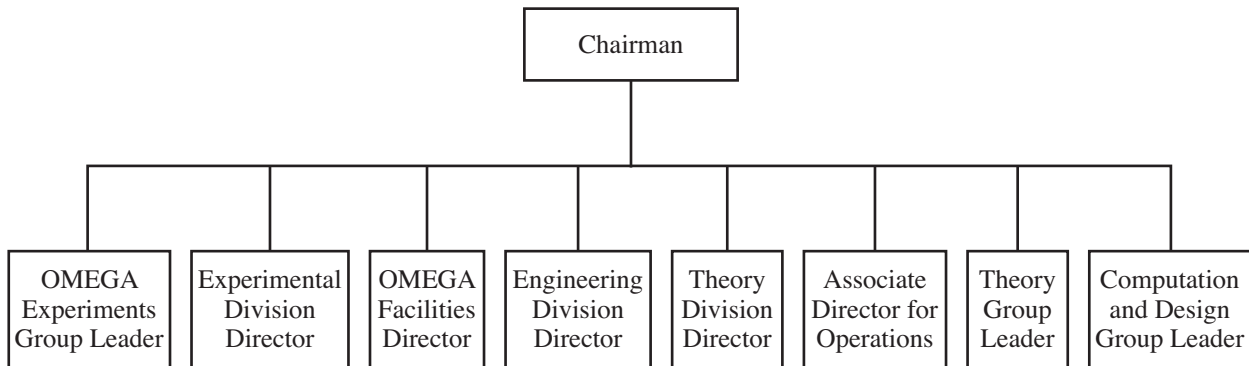
- Administrative support including badging, safety training, facility orientation, data archiving and retrieval, Shot Request Form (SRF) administration and preparation assistance, working areas and logistic support, and computer network connections.
- Engineering support to field/adapt user-supplied diagnostics.
- Technical information and support for planning and conducting user experiments.

### **1002 Science Program Advisory Committee**

LLE's Science Program Advisory Committee advises the LLE Director on significant policy matters relating to LLE's scientific program and OMEGA's use and capabilities planning. The organization of this committee is shown in Fig. I-2; its chairman is appointed by the Laboratory Director. Its specific responsibilities include the following:

- Make recommendations to the OMEGA Facility Advisory and Scheduling Committee as to LLE experiments to be performed and their relative priorities.
- Formulate LLE's annual Work Plan.
- Formulate and maintain up-to-date long-range program plans of five and ten years.
- Advise on major changes to the overall balance of facility use that may be required.
- Recommend actions needed to resolve issues of inadequate system time or financial resources to meet programmatic requirements.
- Recommend policy with respect to international collaboration and use of OMEGA.
- Review major proposals that significantly add or change facility capabilities and advise on the merits of such additions or changes relative to cost (including the cost of the system time).
- Brief or provide a written report of its recommendations to the LLE Director and other LLE Division Directors. If a consensus view is not reached within the committee, all views will be represented.
- Develop LLE's Annual Self-Assessment.

OMEGA Scientific Program Advisory Committee



G7138J2

Figure I-2

**1003 FASC Roles and Responsibilities**

**3.1 Responsibilities**

The Facility Advisory and Scheduling Committee formulates the annual facility schedule, reviews experimental proposals for compatibility and safety, and evaluates facility availability and experimental effectiveness. The FASC recommends the annual facility schedule and represents the needs of the users to the LLE Director and OMEGA Facility Director.

**3.1.1 Annual Scheduling Meeting**

The full FASC meets in June of each year to formulate the one-year OMEGA facility schedule for the upcoming fiscal year. Additionally, the FASC reviews facility availability and effectiveness for the previous year and recommends notional shot allowances for the fiscal year after next. Specific responsibilities include:

- Recommend shot allocations for the set of experimental proposals submitted by the OMEGA user groups for the upcoming fiscal year using the following criteria:
  - Consistency of experimental goals and NNSA’s programmatic requirements and the likelihood of the experimental goals being achieved.
  - The uniqueness of OMEGA to perform the experiment or a recommendation that the experiment be performed by another facility.
  - The impact of the experiment on the facility, e.g., potential for system damage, environmental issues, etc.

- Review programmatic requirements for the fiscal year after next and make a recommendation for total system time required and the overall program balance.
- Review user requests for facility modifications and recommend appropriate action to the LLE Director and OMEGA Facility Director.
- Review the OMEGA availability and experimental effectiveness for the past year and recommend appropriate lessons learned to the LLE Director and OMEGA Facility Director.
- Review existing experimental capabilities such as diagnostics and information availability, and recommend improvements where warranted.
- Review policy for experimental data ownership, access, and security issues.

**3.1.1.1 Membership** The FASC committee members are appointed by the host institution and approved by the LLE Director. The membership is summarized below.

Number of Members	Subcommittee	Source
8	Ignition Physics	LLNL, LANL, LLE (5), SNL
2	Weapons Science	LLNL, LANL
2	Basic Science	NLUF Manager (1) University Community (1)

The committee membership will serve for a term determined by the host institution. The term should nominally be for at least two years. The committee chairman will be the OMEGA Facility Director.

The basic science subcommittee consists of the NLUF manager and a representative of the university users' committee appointed by the LLE Director. Basic science consists of the NLUF and Laboratory basic science programs. Laboratory means the National Laboratories (LLNL, LANL, and SNL) and LLE (including the Fusion Science Center represented through LLE). An NLUF Technical Evaluation Panel is appointed separately as defined by the NLUF management program contained in the UR/LLE-DOE Cooperative Agreement. This committee meets biennially to review NLUF proposals and recommends to NNSA the proposals to fund and their shot allocations. The recommendations of this committee are represented by the NLUF Manager at the FASC. While the NLUF programmatic funding is provided separately by NNSA, the programmatic funding for Laboratory basic science is provided by the individual laboratory and system time is provided by the facility. The Laboratory basic science program will be administered by the NLUF Manager who will issue a yearly solicitation for proposals. The

Laboratory Basic Science Review Committee members will be approved by the LLE Director and will consist of members from the user laboratories (one each) as well as at least two independent members. This committee will peer review all proposals on merit and make a recommendation to the LLE Director of proposals in rank order including a recommended system time allocation.

**3.1.1.2 Committee Procedures** The procedures that govern the annual schedule formulation process and facility review are outlined in this section. This process will be initiated each year by the OMEGA Facility Director issuing relevant guidance and a planning timeline.

- The subcommittees meet in the early spring to review proposals and recommend system time requirements in time to provide an input to the draft annual facility schedule and support the annual FASC meeting held in June each year.
- The OMEGA Facility Director collects the inputs from the subcommittees, evaluates facility impact, and formulates a draft of the fiscal-year schedule for review at the annual FASC meeting. The subcommittee chairman will present proposals for system time to the FASC, including the results of proposal ranking and recommending experiments that should be scheduled.
- The full committee will meet in closed session to evaluate the input of the subcommittees and recommend a balanced program that meets the guidance provided by NNSA. If there is inadequate system time to fulfill all requests, the committee will recommend the “split” among the three areas and require the subcommittees to reduce the requests to meet the allocation. The full committee will recommend the fiscal-year schedule that includes 5% contingency to the LLE Director for approval.
- The committee will complete the reviews identified in Sec. 3.1.1 and report the results to the LLE Director and OMEGA Facility Director.

**3.1.1.3 User Requirements** Each laboratory is responsible for formulating an experimental program to fulfill its campaign objectives. Proposals for experiments from selected PI’s are formulated to meet those program objectives. Proposals that are not in support of program objectives should not be submitted. Members of participating laboratories cannot be PI’s on NLUF proposals. Proposals from outside entities [for example, proposals resulting from international agreements (e.g., CEA, AWE)], will go through the same process as all other proposals. Proposal content and PI responsibilities are detailed in Sec. 1004.

### **3.1.2 Fiscal Year After Next First-Quarter Schedule**

A provisional first-quarter schedule will be developed in April of each year. The planning for this will be initiated by LLE at least two months in advance, and the scheduling meeting will be via video teleconference. This will allow the identification of target requirements early to ensure that first-quarter experiments can be supported. While this schedule is provisional, it is envisioned that it will be adopted with little or no revision during the normal annual June OMEGA Scheduling and Advisory Committee meeting. The recommended notional system time allocations for the upcoming fiscal year should be used as guidance in arriving at this provisional first-quarter schedule. Section 3.1.1 procedures should be used in developing this schedule.

### **3.1.3 Biweekly FASC Meetings**

A subcommittee of the FASC consisting of the LLE members of the FASC, the Laser Facility Manager, the Experimental Operations Group Leader, and the Laser System Scientist meet biweekly to administer the facility schedule and monitor its effectiveness (other, non-LLE committee members are welcome to attend this meeting if available on site). Specific responsibilities include:

- Review experimental proposals submitted by Principal Investigators two months in advance for system and experimental compatibility and safety. Approve or recommend changes to the proposals.
- Review experimental critiques submitted by Principal Investigators and propose corrective actions to the Facility Director where warranted.
- Evaluate the current and planned activities on the system presented by the Laser Facility Manager.
- Evaluate the experimental diagnostic performance and progress in implementing new/modified diagnostics presented by the Experimental Operations Group Leader.
- Review the status of submitted proposals and critiques.
- Review recommended schedule changes and, in consultation with users, formulate schedule changes to accommodate user requests where possible.
- Assign system contingency time to make up for lost experimental time or to perform new, high-priority experiments.
- Conduct a running review of the system schedule to determine the ability to perform previously approved experiments, especially those dependent on system or diagnostic upgrades.
- Ensure that the facility schedule is kept current and posted on LLE's web site.

## 1004 Experimental Proposals and Principal Investigator Roles and Responsibilities

With respect to the laser facility, PI's are those individuals responsible for proposing experiments to be conducted on the OMEGA Laser System.

### 4.1 Principal Investigator Orientation

Principal investigators must complete an OMEGA familiarization before conducting their first experiment. This familiarization should be scheduled through the Laser Facility Manager at least three months prior to the PI's first scheduled experiment. The familiarization will include the following:

- Briefing on OMEGA and /or OMEGA EP capabilities,
- Review of PI responsibilities including SRF preparation,
- Safety briefing,
- Tour of OMEGA/OMEGA EP,
- Observation of operations, preferably with an experimental PI,
- Target metrology and positioning requirements, and
- Briefing on diagnostic procedures.

### 4.2 Experimental Proposal

Once an experiment is scheduled by the FASC, the PI is responsible for submitting a proposal template and SRF's, coordinating experimental and laser requirements, monitoring the experimental execution, and writing a critique of the execution of the experiment within one week of its performance. Principal investigators are responsible for submitting an electronically transmitted experiment proposal template to the FASC that amplifies and extends the information submitted prior to scheduling the experiment. This template and accompanying SRF's, target request forms (TRF's), and VISRAD files must be received at least two months prior to the conduct of the experiment and will initiate the preparation phase for the experiment.

#### 4.2.1 Proposal Template Instructions

**4.2.1.1** Date of experiment, AM or PM, experiment title, principal investigator names, and applicable facility (OMEGA, OMEGA EP, or both)

**4.2.1.2** Summary of the experiment's objectives.

**4.2.1.3** Laser and diagnostic requirements for the experiment. The input for this should include experimental configuration name and a draft SRF and a request identification (RID) number for each experimental configuration. Any non-LLE supported diagnostics or unqualified diagnostics should be separately identified.

**4.2.1.4** Type and number of targets including number of spares.

- Identify the target request form (TRF) number for each configuration, if available.
- A sample of complex targets (defined as other than a simple flat-foil, spherical direct-drive capsule, or plain hohlraum) must be delivered to LLE at least one week prior to the scheduled experiment. This will allow testing the positioning of the target and developing accurate target-positioning procedures and reticules by placing the target at target chamber center (TCC) when TCC time is available. Indicate on the proposal if targets are complex and include the number of targets ordered for each configuration.
- Targets must be metrologized prior to delivery at LLE and verified after arrival at LLE using LLE's Powel scope. Metrology data will be available to the Experimental Operations Group no later than two full working days prior to the day of shots.
- Target, target support, and target shield mass must be minimized to preclude either shrapnel or vapor-deposition degradation of optics. Generally this means that flat targets should be no larger than the beam spot size plus 100  $\mu\text{m}$ , support structures should be of minimum mass to securely support the target, and shields should be of a minimum area and thickness.

**4.2.1.5** A VISRAD file that shows the target including the mount stalks and the beams intercepting the target. (Use of the software program, VISRAD, enhances visualization and importation of data to the SRF.) The file name must be formatted "<RID Number>-<PI Name>.vww," e.g., for targets corresponding to RID 12345 and PI surname of Heeter, the file name is "12345-Heeter.vww." VISRAD files must be submitted as attachments to the proposal.

**4.2.1.6** Quantity (shot count) of target shots proposed.

**4.2.1.7** Identification of diagnostics planned for use on the experiment that are not qualified for use on OMEGA/OMEGA EP. Non-qualified diagnostics are those that have not completed facility qualification per LLE Instruction 7700 and are not generally selectable on the SRF.

**4.2.1.8** Laser-energy transport considerations (OMEGA only)

- A. Estimate laser-energy transmission through target:  
Significant transmission of laser light through a target can cause damage to the opposed beam optics of the OMEGA compression facility. A beam transmitted through an underdense target can have significant spatial modulation. The potential for such damage is increased when a distributed phase plate is used in a beam. To assess the potential for such damage, the PI is required to state the estimated

level of laser-beam transmission through the target (including blow-through) for the proposed experimental configuration. The basis of this estimate can be a simulation of the laser–target interaction or data from an experiment that closely simulates the proposed experimental configuration. No experiment will be approved unless such an estimate is provided in the template submitted for approval to the OMEGA FASC two months prior to the scheduled shot day. Beam dumps or calorimeters can be installed in opposing beams to increase the maximum acceptable energy transmission (for up to six beams). The following matrix shows the maximum allowable blow-through under various scenarios:

DPP in either target or opposing beam?	Beam block (in opposing beam?)	Maximum acceptable energy transmission
Yes	No	20 J
Yes	Yes	200 J
No	No	100 J
No	Yes	300 J

- B. Estimated laser-energy backscatter from the target  
Significant backscatter from a target can cause damage to the beamline optics. To prevent damage, the estimated backscatter energy must not exceed 140 J.
- C. Estimated laser energy reflected from the target  
Significant laser energy reflected from a flat target can be directed into other beam ports and damage beamline optics. To reduce the reflected energy and prevent damage, the maximum angle of incidence of a laser beam on a flat target must not exceed 65°.

**4.2.1.9** Special shot-schedule considerations associated with experiment.

**4.2.1.10** Campaign configuration variables. Include all shot parameters such as pulse shapes, beam energies, beam delays, diagnostic setup, etc. that will be varied during the campaign.

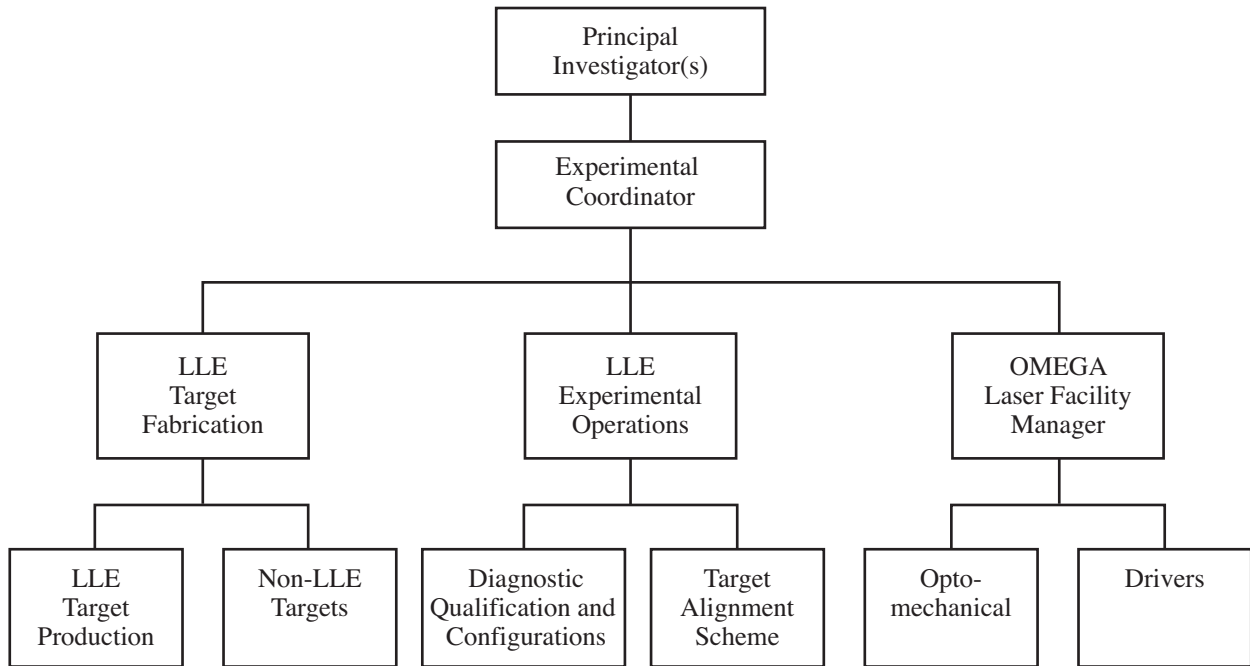
**4.2.2** The proposal template (see Table I-1) will be reviewed by the FASC to ensure that the experiment’s requirements are consistent with the capabilities of the Laser Facility.

Experiment Proposal Template (Table 1-I)

<b>4.2.1.1</b>		General:      Date of Experiment:		<input type="checkbox"/> AM	<input type="checkbox"/> PM	
		A. Experiment Title:				
		B. Principle Investigators:				
		C. Facility:		<input type="checkbox"/> OMEGA	<input type="checkbox"/> OMEGA EP	
<b>4.2.1.2</b>		Summary of Experiment Objectives:				
Experimental Specifications and Laser/Diagnostic Requirements:						
<b>4.2.1.3</b> SRF		<b>4.2.1.4</b> Targets			<b>4.2.1.5</b> VISRAD Filename (RID-PI Name.vrw) (Submit files with proposal)	<b>4.2.1.6</b> # of Target Shots
Experimental Configuration Name	Example RID #	TRF #	Complex Yes	No	Quantity	
			<input type="checkbox"/>	<input type="checkbox"/>		
			<input type="checkbox"/>	<input type="checkbox"/>		
			<input type="checkbox"/>	<input type="checkbox"/>		
			<input type="checkbox"/>	<input type="checkbox"/>		
			<input type="checkbox"/>	<input type="checkbox"/>		
<b>4.2.1.7</b> Identify all diagnostics required that are not qualified						
Diagnostic Name			Description			
<b>4.2.1.8</b>		Energy Transport Considerations				
		A. Estimated laser transmission through target (OMEGA only):				
		B. Estimated backscatter energy is less than 140 J				
		C. For flat targets, verify maximum angle of incidence is less than 65°				
		<div style="text-align: right;"> <u>    </u> J  <input type="checkbox"/>  <input type="checkbox"/> </div>				
<b>4.2.1.9</b>		Special considerations:				
<b>4.2.1.10</b>		Campaign configuration variables:				

**4.3 Principal Investigator Responsibilities**

Once the principal investigator’s experiment has been scheduled, it will become the PI’s responsibility to interface (via the Experimental Division liaison representative for user experiments) with the assigned experimental coordinator, and ultimately with the Laser Facility Manager, the Experimental Operations Group, the Optomechanical System Group, and the LLE Target Fabrication Group (while keeping the experimental coordinator and liaison representative informed) to ensure that the experimental and laser system requirements are coordinated and understood (see Fig. I-3). If a principal investigator uses targets and/or diagnostics not provided by LLE resources, or requires a pulse shape that is not in the LLE inventory, the PI must coordinate those respective requirements through the corresponding LLE groups to ensure that, at the time the experiment is to be conducted, issues associated with availability or compatibility of those non-LLE-provided resources have been resolved.



G7140aJ1

Figure I-3

**4.3.1 Experiment Reviews**

**4.3.1.1** Approximately two weeks prior to commencing the experiment, the PI, or designee, will conduct a comprehensive review of the detailed requirements for their upcoming campaign. This review is for the mutual benefit of the laser and experimental operations group leaders and the scientists involved with the laser and diagnostic systems. If changes have been

made since the two month submission, the PI shall submit an updated VISRAD model of the targets and revised SRF's that define each unique shot configuration prior to this meeting. (See Sec. 4010 "Shot Request Forms and Administration" for more on the forms.)

**4.3.1.2** All new diagnostics must be fully qualified two full weeks before the date of the experiment.

**4.3.1.3** Final Shot Request Forms shall be submitted to the Laser Facility Manager by the close of business on the Monday prior to the week of target shots. The Laser Facility Manager shall be notified of subsequent changes prior to the initiation of the shot by the operations crew. Any special requirements for set up of the diagnostics for the first shot should be clearly indicated: for example, modifications to the ten-inch manipulator set-up sheets.

**4.3.1.4** By two working days before the shots, the PI will provide target metrology results for all targets to the Experimental Operations Group Leader.

**4.3.1.5** For each shot day of the campaign, the PI will support the shift briefings as appropriate. During the actual execution of the experiments, the principal investigator will act as an advisor to the LLE Shot Director and may be called upon to render advice on whether to proceed with planned experiments in the event of abnormal system performance. The Shot Director is in charge of the overall laser and target systems during a shot series. If issues associated with safety (personnel or equipment) arise during an experimental sequence, the Shot Director can abort that shot or even the whole series if warranted.

**4.3.1.6** Submit the Shot Effectiveness Form prior to the shot after next.

### **4.3.2 Experimental Critiques**

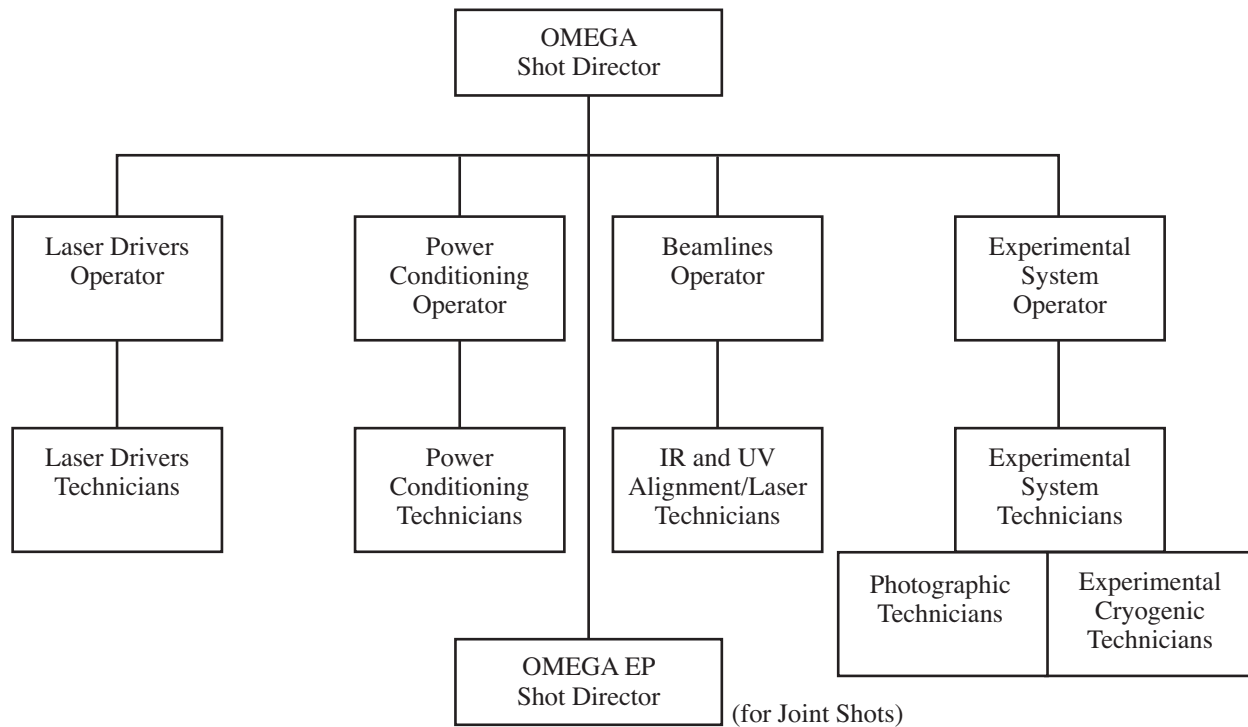
Once the experiment (or sub-series of the experiment) has been conducted, it is the responsibility of the principal investigator to provide to the FASC [within one week after the experiment (or sub-series) has been conducted] a written critique of the performance of the experiment and facility. The following items should be included:

- Problems encountered
  - Laser
  - Experimental diagnostics
  - Experimental
  - Target
- Suggestions for improvements
- Positive feedback

**1005 Laser Facility Operations Overview**

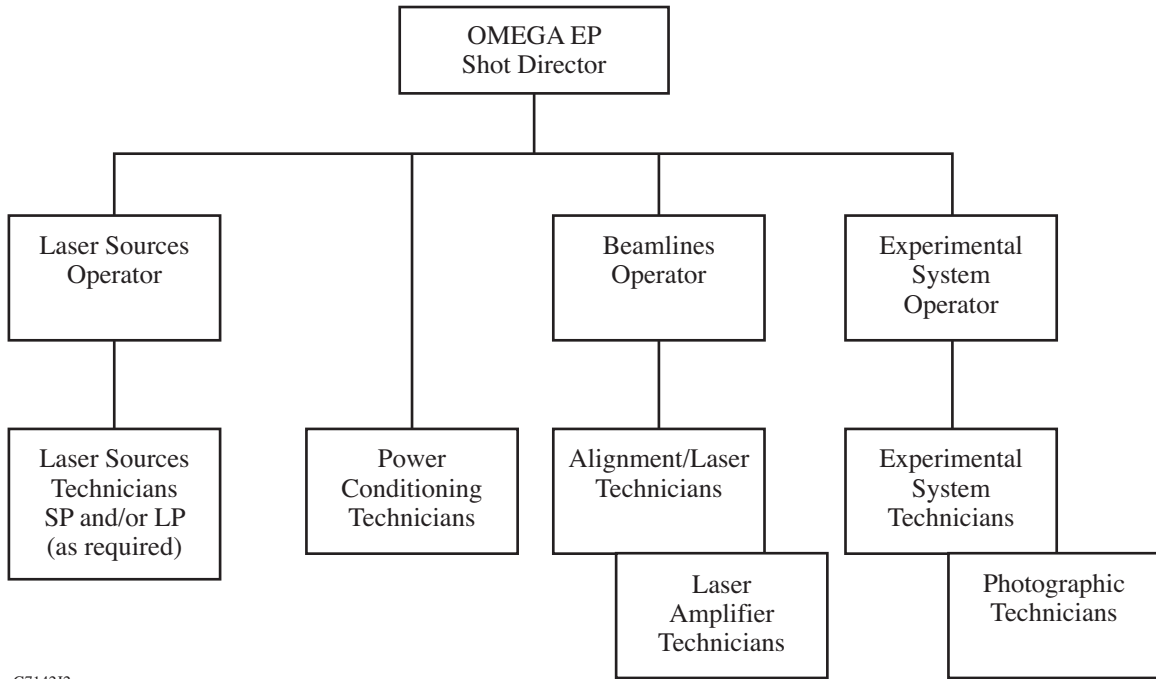
All aspects of OMEGA shot operations are under the direction and control of the OMEGA Facility Operations organization shown in Fig. I-4. OMEGA and OMEGA EP may be operated independently, with separate scientific objectives for each system, or jointly with the combined capabilities addressing a single requirement. For certain high-yield shots, the opposite facility will have to be in closed access even though the facilities are operating independently. The Shot Director(s) are under the overall direction of the Laser Facility Manager, who heads up the OMEGA Shot Operations watch organization. For joint OMEGA and OMEGA EP operations, the OMEGA EP Shot Director reports to the OMEGA Shot Director. This watch organization will directly control the actual shot operations and will be responsible for safety, shot execution, and data collection.

The CTHS, Tritium Filling Station (TFS), Tritium Removal Systems (TRS), and cryogenic Cart Maintenance Room (CMR) are operated by qualified watchstanders under the direction and control of the Cryogenic and Tritium Facility Manager (see Fig. I-5). The CTHS target chamber insertion and positioning systems are operated through the OMEGA facility watch organization (see Fig. I-4).



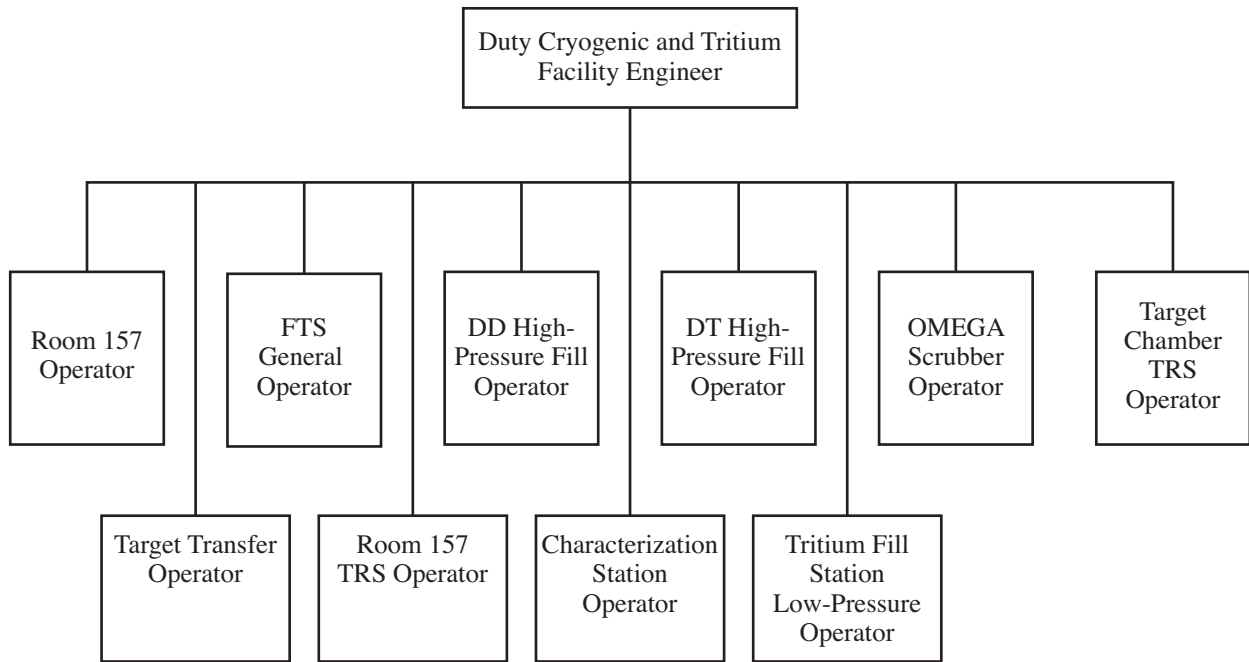
G7141J2

Figure I-4(a): OMEGA watch organization.



G7142J2

Figure I-4(b): OMEGA EP watch organization.



G7143J2

Figure I-5: CTHS organization.

The full OMEGA/OMEGA EP shot watch organization (excluding CTHS filling, layering, and characterization watches), unlike the divisional administrative organization, is operative only during shot operations. Personnel qualified for and assigned to these watches during specific periods of time may come from any of the Laboratory's divisions. While assigned to a watch, however, they report to and are directed by the Shot Director until relieved.

For shot operations, the watch organization shown in Fig. I-4 must be manned to the extent detailed in Sec. 2021. During non-shot periods (maintenance and/or scheduled system modifications or upgrades) only the Shot Director will be stationed.

System corrective and preventive maintenance will be scheduled and performed by the existing Laboratory administrative divisional organization. Divisional responsibilities for services (e.g., mechanical design, electronics design, computer software, etc.) and equipment/systems are detailed below. Where equipment and systems cross divisional lines, one lead Division is assigned the overall responsibility. Corrective and preventive maintenance will be scheduled in consonance with the Laser System Schedule approved by the FASC. Scheduled divisional maintenance will be approved by the Group Leader designated by the Division Director. The Laser Facility Manager, or Cryogenic and Tritium Facility Manager, as appropriate, or person appointed by them will review, track, and monitor the scheduling and completion of all key scheduled maintenance actions.

To ensure the operational readiness of the OMEGA/OMEGA EP Laser Facilities, including laser, target, cryogenic targets, and building support systems, the placing of major equipment or systems (those that would prevent completing a fully diagnosed target shot) out of commission will be controlled by the OMEGA Shot Operations watch organization under the direction of the Laser Facility Manager or the CTHS organization under the direction of the Cryogenic and Tritium Facility Manager as appropriate. The divisional representative will obtain permission from the on-watch Shot Director or Cryogenic and Tritium Facility Manager as appropriate prior to placing a major equipment or system out of commission. The return of equipment and systems to commission after maintenance will also be reported to the Shot Director or Cryogenic and Tritium Facility Manager as appropriate. The Shot Director and Cryogenic and Tritium Facility Manager will maintain a log for their areas of responsibility indicating the current status of equipment placed out of commission. Separate logs for the OMEGA compression facility, the OMEGA EP facility, and the CTHS facility will be maintained.

OMEGA Laser Facility service and equipment responsibilities are as follows:

OMEGA Facility Division

Services

Clean room (Laser Bay and Target Bay)

Film processing

Equipment/Systems

Alignment sensor packages

Blast window assemblies, distributed phase plates, distributed polarization rotators

Cryogenic Target Handling System  
Deformable mirrors  
De-ionized water and glycol cooling systems (including controls, indications, and purification)  
Experimental control and data acquisition  
Experimental target diagnostic peripherals (e.g., nose cones, filters, pin holes, etc.)  
Focus lens subassembly  
Frequency conversion  
Grating compression chamber and beam transport tubes and associated vacuum systems  
Grounding system  
Hardware Timing System  
Infrared alignment  
Interlock system (door interlocks, motion detectors, warning light and alarm controls, and dump system)  
Laser amplifiers  
Laser amplifier structures (service cranes, etc.)  
Laser beamline diagnostics (HED spectrograph, UV transport calibration, beam timing, pulse shape, and pulse contrast)  
Laser control system (including interfaces, cabling, card cages, neuron modules, cable converters, and PLC subsystems *less* SUN workstations and displays, alignment video system)  
Laser drivers—main, SSD, backlighter, and fiducial for OMEGA and short and long pulse for OMEGA EP (oscillators and pulse shaping)  
Laser optomechanical elements (alignment sensors, polarization control optics, mirrors, beam splitters, flip-in devices, spatial filters, and path-length adjusters)  
Nitrogen purge system  
Off-axis parabola inserter  
Optics  
Parabola alignment diagnostic  
Periscope mirror assembly  
Plasma-electrode Pockels cell (PEPC)  
Power conditioning including PEPC power conditioning  
Radiation detection system  
Radio communication system  
Short-pulse alignment  
Spatial filters  
Spatial-filter vacuum systems  
Structures (end mirror target mirror, target area, spatial filter, etc.)  
Target chambers and associated vacuum systems  
Target positioning  
Target viewing  
Tritium Filling Station (TFS)

Tritium Removal Systems (TRS)  
Ultraviolet alignment

Engineering Division

Services

Electronics design  
Electronics Shop  
Machine Shop  
Mechanical design  
Optical Fabrication Shop  
Optical Manufacturing Shop  
Software development and maintenance

Experimental Division

Services

Film digitizing  
Target production

Equipment/Systems

Experimental target diagnostics  
Laser diagnostics (streak cameras and HED's)  
Targets

Theory Division

Services

Computing and networking

Equipment/Systems

Alignment video system  
Control system software  
Imaging software  
(Non-LON) network wiring and hub equipment  
PC's  
SUN workstations and displays

Administration Division

Services

Accounting  
Administrative services  
Facility improvements  
Personnel services  
Purchasing

Equipment/Systems

De-ionized water and glycol pumps, motors, and heat exchangers

- Electrical distribution (switch gear, motor control centers, power panels, breakers, distribution to connected equipment, emergency diesel generators, and distribution to PCU's)
- Heating, ventilation, air-conditioning system, and DDC system
- Pneumatic air and nitrogen systems
- Public address system
- Target/Laser Bay 10-T cranes
- Target Bay elevator

### **1006 Laser Facility Manager**

The Laser Facility Manager is responsible for the overall operation and operational readiness of the OMEGA Laser System including the OMEGA compression and OMEGA EP facilities. The Laser Facility Manager reports to the OMEGA Facility Director. The LFM has a support staff of an Associate LFM and an Operations Analyst for OMEGA and OMEGA EP. The LFM has the following specific responsibilities: (Note: The LFM may delegate authority to the OMEGA or OMEGA EP Associate LFM to act for him as he deems appropriate.)

- Manage the OMEGA Laser Facility to ensure that it is fully ready to execute the schedule of experiments proposed by the FASC and approved by the LLE Director.

- Direct laser facility operations to ensure operations are conducted effectively and safely.

- Directly supervise the OMEGA and OMEGA EP Shot Directors to ensure that he/she fulfills his/her responsibilities in operating the applicable facility.

- Coordinate the preparation and submission of written procedures covering shot operations to the OMEGA Facility Director for approval. Approve written change notices as required to clarify or amend these procedures in advance of the approval of a formal revision by the OMEGA Facility Director.

- Manage and control all laser facility maintenance to ensure safety and operational readiness.

- Make recommendations regarding the procurement of all laser facility services, operating equipment spares and supplies, and system upgrade components.

- Be responsible for the overall system configuration control and management in close coordination with System Engineering.

- Directly manage watchstander training and qualification and certify the qualification of the Shot Directors.

- Serve as a member of the OMEGA FASC and provide this committee with a periodic report of system status and the status of completing scheduled experimental operations.

- Approve the laser facility watchbills.

Maintain a list of laser facility qualified and proficient watchstanders.

Administer the Work Authorization Procedure requirements.

Administer facility access requirements and procedures.

Provide daily written directions for laser facility operations in the Laser Facility Manager's Day Order Books. Separate books for OMEGA and OMEGA EP will be maintained.

### **1007 Laser System Scientist**

The Laser System Scientist is responsible for the safe propagation of the laser in each laser system. The Laser System Scientist reports to the OMEGA Facility Director and has the following responsibilities:

Support the preparation, qualification, and operation of the laser in close coordination with the Laser Facility Manager and Shot Directors. He/she is normally available on site during daily system qualification, short-pulse operations, and when precision of unique energy balance is required. When not on site he/she should normally be accessible by pager and phone.

Qualify the laser-beam spatial profile at the start of daily shot operations.

Maintain the system energy balance and specify the system setup for unique energy balance conditions specified by experimental principal investigators.

Qualify the laser for short-pulse and picket-pulse operations and approve the pulse shape and energy settings for each shot.

Analyze system performance.

Advise the Laser Facility Manager and Shot Director during any abnormal laser conditions including directing the suspension of operations if deemed necessary.

### **1008 Cryogenic and Tritium Facility Manager**

The Cryogenic and Tritium Facility Manager is responsible for the overall operation and operational readiness of the CTHS, TFS, TRS's, and CMR [collectively included in the Cryogenic and Tritium Facility (CTF)]. The Cryogenic and Tritium Facility Manager reports to the OMEGA Facilities Division Director and has the following specific responsibilities:

Manage the CTHS to ensure the reliable delivery of cryogenic targets of acceptable quality to the OMEGA compression facility to execute the schedule of experiments proposed by the FASC and approved by the Director of LLE.

Manage the TFS to ensure room-temperature DT targets are supplied to the OMEGA compression facility.

Direct facility operations to ensure that they are conducted effectively and safely.

Directly supervise the CTHS, TFS, TRS, and CMR operators to ensure that they fulfill their responsibilities.

Coordinate the preparation and maintenance of written procedures covering CTHS, TFS, TRS, and CMR operations. Approve written change notices as required to clarify or amend these procedures in advance of the approval of a formal revision by the OMEGA Facilities Division Director.

Manage and control all CTHS, TFS, TRS, and CMR maintenance to ensure operational readiness.

Make recommendations regarding the procurement of all services, operating equipment spares and supplies, and system upgrade components.

Be responsible for the overall CTF system configuration control and management. Coordinate all control system modifications including ensuring OMEGA Laser Facility Manager approves applicable changes.

Directly manage watchstander training and qualification and certify the qualification of all CTHS and TRS watchstanders.

Maintain a list of qualified and proficient CTF watchstanders.

Maintain the tritium inventory and a log of radioactive material.

Ensure that all radiological safety procedures are followed and report any radiological incidents to the LLE Radiation Safety Officer.

Ensure compliance with all procedural requirements of this LFORM; the Laser Facility Manual, Vol. IV, Operating Procedures; the LLE Radiological Controls Manual; and other LLE Instructions.

Control of system status including placing systems and equipment out-of-commission for maintenance and/or testing, maintaining the Equipment Status Log (Sec. 4004), and approving system/equipment Tagouts/Lockouts (Sec. 4005). NOTE: Where systems interface with the OMEGA facility, the facility Equipment Status Log and Tagout system under the purview of the Shot Director should be used.

Ensure that qualified watchstanders (Sec. 2023) are stationed in accordance with the posted watchbill (Sec. 2022) prior to conducting CTHS or TRS operations.

Ensure a CTHS, TFS, TRS, and CMR Facility Log is maintained to document operations.

Conduct prewatch and watch briefings as required.

Approve and inspect all radioactive material shipments received in and transferred out of the CTF.

Keep the OMEGA Facility Director, appropriate Group Leaders, and others, as appropriate, informed of system status and problems. As a minimum the following will be reported:

Failure to have targets ready for scheduled experiments (OMEGA Experiments Group Leader and Laser Facility Manager).

Failure of equipment that disrupts operations (applicable Division Director and Group Leader).

Any release of tritium above normal (LLE Radiation Safety Officer).

Accident or incident that causes personnel injury or significant equipment damage (applicable Division Director, Laboratory Safety Officer, and applicable Functional Safety Officer). Additionally, incident investigation and reporting in accordance with LLEINST 6950 should be completed.

## **Appendix B**

### **Glossary of Acronyms**



## ACRONYMS

$2\omega$	Second harmonic
$4\omega$	Fourth harmonic
ACSL	Aperture-coupled strip line
ASP	Alignment sensor package
AWE	Atomic Weapons Establishment
AWG	Arbitrary waveform generator
BWA	Blast window assembly
CCD	Charge-coupled device
CEA	Commissariat à l'Énergie Atomique
CEQC	Critical Equipment Qualification Checklist
CID	Charge-injection device
CLARA	Crystal large-aperture ring amplifier
CPS	Charged-particle spectrometer
CTCD	Cryogenic-target characterization diagnostic
CTHS	Cryogenic Target Handling System
CVD	Chemical vapor deposition
DEMIN	Detector micromegas for neutrons
DI	Deionized
DOE	Department of Energy
DPP	Distributed phase plate
DPR	Distributed polarization rotator
DTRA	Defense Threat Reduction Agency
EMI	Electromagnetic interference
EMP	Electromagnetic pulse
EMS	End-mirror structure
EP	Extended performance
FABS	Full-aperture backscatter station
FASC	Facility Advisory and Scheduling Committee
F-ASP	Stage-F alignment sensor package
FCC	Frequency conversion crystal
FLAS	Focus lens assembly
FWHM	Full width at half maximum
GCC	Grating compressor chamber

GMXI	Gated monochromatic x-ray imager
HED	Harmonic energy detector
HED	Harmonic energy diagnostic
HENEX	High-energy electronic x-ray diagnostic
HPGe	High-purity germanium
HRXI	High-resolution x-ray imaging
HT	Tritium gas
HTO	Tritiated water
HTS	Hardware Timing System
HXRD	Hard-x-ray detector
HYNBT	High-yield neutron bang time
IR	Infrared
IRAT	Infrared alignment table
KAP	Potassium acid phthalate
KB	Kirkpatrick–Baez
KD*P	Deuterated potassium dihydrogen phosphate
KDP	Potassium dihydrogen phosphate
LANL	Los Alamos National Laboratory
LARA	Large-aperture ring amplifier
LBO	Lithium triborate
LDRD	Laboratory-directed research and development
LiNbO <sub>3</sub>	Lithium niobate
LLE	Laboratory for Laser Energetics
LLNL	Lawrence Livermore National Laboratory
MCP	Microchannel plate
MCTS	Moving Cryostat Transfer Cart
MRS	Magnetic recoil spectrometer
MTG	Master timing generator
NBI	Near-backscatter imaging
NBT	Neutron bang time
Nd:YLF	Nd-doped yttrium lithium fluoride
NIF	National Ignition Facility
NLUF	National Laser Users' Facility
NNSA	National Nuclear Security Administration
NRL	Naval Research Laboratory
NTD	Neutron temporal diagnostic

nTOF	Neutron time of flight
OIP	OMEGA intercommunication protocol
OMA	Optical multichannel analyzer
OPCPA	Optical parametric chirped-pulse amplification
OPD	Optical path difference
OR	Oscillator Room
OTIS	OMEGA Transport Instrumentation System
PAD	Parabola alignment diagnostic
PCE	Power Conditioning Executive
PCU	Power conditioning unit
PEPC	Plasma-electrode Pockels cell
PFN	Pulse-forming network
PGR	Pulse Generation Room
PILC	Preionization and lamp check
pm	Picometer
PMA	Periscope mirror assembly
PMT	Photomultiplier tube
POL	Polarizer
POTTS	Precision Optical Timing and Triggering System
PTD	Proton temporal diagnostic
regen	Regenerative amplifier
RFG	Reference frequency generator
SBS	Stimulated Brillouin scattering
SD	Shot Director
SE	Shot Executive
SNL	Sandia National Laboratory
SPDP	Short-pulse diagnostic package
SRF	Shot Request Form
SRRS	Stimulated rotational Raman scattering
SRS	Stimulated Raman scattering
SSD	Smoothing by spectral dispersion
TB	Target Bay
TBD	Transmitted beam diagnostic
TC	Target chamber
TCC	Target chamber center
TC-TRS	Target Chamber Tritium Removal System

TED	Target existence detector
THz	Terahertz
TIM	Ten-inch manipulator
TMS	Target mirror structure
UV	Ultraviolet
UVAT	UV alignment table
VISAR	Velocity interferometry for any reflector
WRF	Wedge-range filter

## **Appendix C**

### **National Laser Users' Facility Proposal Summary Sheet**



## National Laser Users' Facility Proposal Summary Sheet

<b>Principal Investigator:</b> (Name, Institution, and Address)	
<b>Title of Proposed Project:</b>	
<b>Project Objective:</b>	
<b>Approach:</b>	
<b>Number of Students Involved</b> Graduate(s): Undergraduate(s):	
<b>Facility Requirements:</b>	
<b>Target Fabrication Contractor Support Request</b> 1.0 Minimum support required (\$) 2.0 Planned support request (\$)	
<b>Target Types:</b>	
<b>Number of Shots:</b>	
<b>Diagnostic Development:</b>	
<b>Equipment Required:</b>	
<b>User Provided Equipment:</b>	
<b>COMMENTS:</b>	

## **Appendix D**

### **FY06 Laser Facility Report**



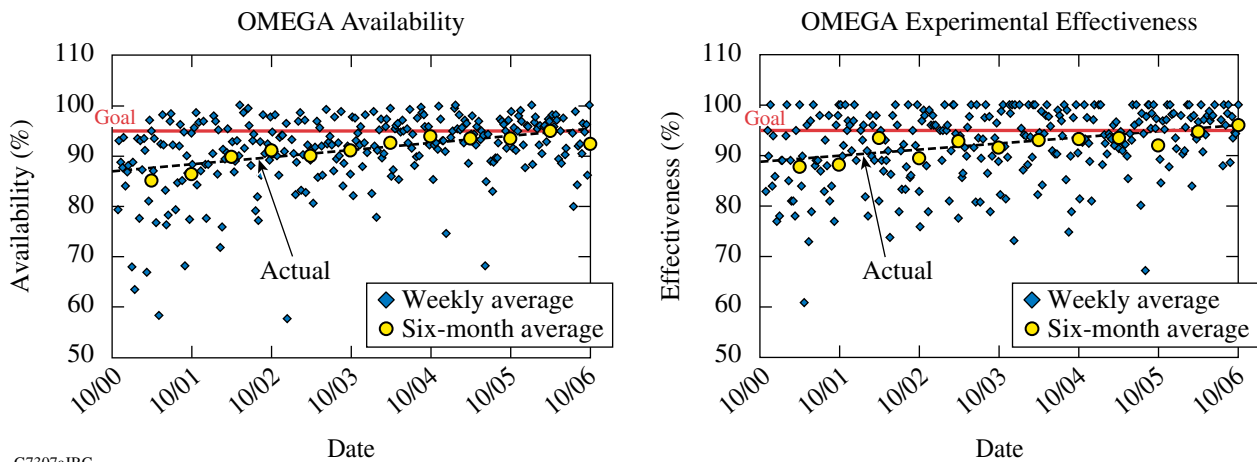
# FY06 Laser Facility Report

During FY06 the OMEGA Facility conducted 1394 target shots for a variety of users. Shaped-pulse cryogenic DT implosions highlighted the development of direct-drive cryogenic capability. A total of 12 D<sub>2</sub> and 15 DT direct-drive cryogenic target implosions were performed (see Table 108.VII). OMEGA Availability and Experimental Effectiveness averages for FY06 were 93.3% and 95.3%, respectively (see Fig. 108.56). Highlights of other achievements for FY06 include the following:

- The first of a series of direct-drive, ignition-scaled cryogenic targets containing tritium were imploded in February 2006. LLE achieved a DOE milestone in March by imploding two layered DT cryogenic targets containing tritium. The first high-yield, direct-drive, ignition-scaled, 50% DT cryogenic implosion was achieved in June 2006—the first time that such a target was imploded on an ICF facility. OMEGA is now fully capable of fielding high-tritium-fraction cryogenic

Table 108.VII: The OMEGA target shot summary for FY06.

Laboratory	Planned Number of Target Shots	Actual Number of Target Shots	IDI NIC	DDI NIC	Total NIC	Non-NIC
LLE	724	714	201	497	698	16
LLNL	325	348	243	0	243	105
LANL	121	125	54	0	54	71
NLUF	120	122	0	0	0	122
CEA	40	49	0	0	0	49
SNL	24	30	30	0	30	0
NWET	6	6	0	0	0	6
Total	1360	1394	528	497		369



G7307aJRC

Figure 108.56  
OMEGA Availability and Experimental Effectiveness data from FY01 to FY06.

targets and has the infrastructure in place to support the corresponding radiological issues.

- A full set of 42 new indirect-drive-ignition distributed phase plates (IDI DPP's) were designed and fabricated for National Ignition Campaign (NIC) experiments on OMEGA. The phase plates produce an elliptical far field ( $200\ \mu\text{m} \times 300\ \mu\text{m}$ ) at normal incidence and a nearly circular spot at the plane of the laser entrance hole (LEH) and can be oriented for use in both pent and hex configurations. Hohlraum energetics experiments using IDI DPP's were successfully conducted in August, completing a DOE milestone for the National Ignition Campaign. The primary objective of these experiments is to study the effect of laser-beam smoothing with phase plates on the radiation temperature and scattering losses of the hohlraum.
- Low-adiabat, high-contrast pulse shapes are required for OMEGA ignition-scaled cryogenic DT target experiments. Such pulse shapes are typically characterized by a narrow picket pulse on top of a low-intensity foot pulse, followed by a high-intensity drive pulse. The new front end on OMEGA—the integrated front-end source (IFES)—is a highly stable optical-pulse-generation system based on fiber amplification of an optical signal that is temporally carved from a continuous-wave fiber laser. The use of fiber-optic lasers and amplifiers and waveguide temporal modulators makes IFES ideally suited for producing reliable, stable pulse shapes. Recent experiments on OMEGA have required >100:1-contrast-ratio pulse shapes. The electrical waveform that drives the waveguide modulators to shape the pulse is produced using LLE's aperture-coupled-strip-line (ACSL) technology. The shape is designed to precompensate the temporal distortions in the laser due to amplifier gain saturation and nonlinear conversion in the frequency-conversion crystals (FCC's). Figure 108.57 shows (on a logarithmic scale) the design template and the measured ultraviolet laser pulse produced on target by OMEGA for pulse shape LA279901P. The match between the designed and measured shapes is excellent, particularly in the following critical pulse parameters: the picket energy, the >100:1-contrast foot, and the rising edge of the drive pulse.
- A year-long project to upgrade the active-shock-breakout (ASBO) diagnostic was completed in April 2006. The upgrade

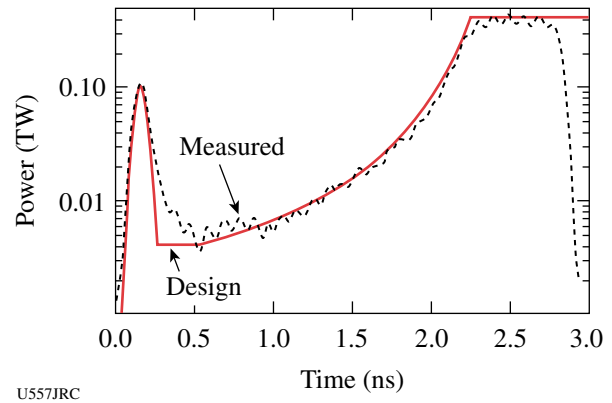


Figure 108.57

OMEGA single-beam pulse shape from low-adiabat cryogenic target implosions (shot #42966) using pulse shape LA279901P.

enables high-precision measurements and ease of operation for equation-of-state (EOS) and shock-timing experiments. Using the existing system as a baseline, the upgrade incorporates a new optical layout that uses the Rochester Optical Streak System (ROSS) streak cameras as detectors for the two velocity interferometer system for any reflector (VISAR) channels. The result is an outstanding optical device that provides excellent performance and smooth operation using the accurately calibrated ROSS cameras. Many experiments are using the new ASBO system. CCD camera data-acquisition capability for x-ray framing cameras was extended to TIM's 4 and 5 and is now available on all TIM's.

- The OMEGA EP short-pulse beam-transport tube was installed during an extended maintenance week in June 2006. The beam-transport tube connects the OMEGA EP grating compression chamber located within the OMEGA EP Target Bay to port P9 on the OMEGA target chamber. Significant structural modifications within the OMEGA target area were required to facilitate the installation of the short-pulse beam tube including target bay platform structural modifications, modifications required to facilitate access to OMEGA UV transport optics, and the addition of two Target Bay jib cranes. Facility modifications planned for FY07 include the relocation of TIM 2 from port H7 to port H3, installation of the off-axis parabola in port H7, and installation of the OMEGA EP transport mirrors on the east side of the OMEGA target chamber.

## **Appendix E**

### **National Laser Users' Facility and External Users' Programs**



## National Laser Users' Facility and External Users' Programs

During FY06, 680 target shots were taken on OMEGA for external users' experiments, accounting for 48.8% of the total OMEGA shots for the year. The external users during this year included seven collaborative teams participating in the National Laser Users' Facility (NLUF) program and many collaborative teams from the National Laboratories (LLNL, LANL, and SNL) and the Commissariat à l'Énergie Atomique (CEA) of France. Some of this work is highlighted in this section.

### NLUF Program

In FY06, the Department of Energy (DOE) issued a solicitation for NLUF grants for the period of FY07–FY08. A total of 12 proposals were submitted to DOE for the NLUF FY07/08 program. An independent DOE Technical Evaluation Panel comprised of Prof. Ani Aprahamian (University of Notre Dame), Dr. Steven Batha (LANL), Dr. Ramon Leeper (SNL), Prof. Howard Milchberg (University of Maryland), and Dr. Robert Turner (LLNL) reviewed the proposals on 18 April 2006 and recommended that six of the twelve proposals receive DOE funding and shot time on OMEGA in FY07–FY08. Table 108.VIII lists the successful proposals.

### FY06 NLUF Experiments

FY06 was the second of a two-year period of performance for the NLUF projects approved for the FY05–FY06 funding and OMEGA shots. Six of these NLUF projects were allotted OMEGA shot time and received a total of 122 shots on OMEGA in FY06. Some of this work is summarized in this section.

#### *Isentropic Compression Experiments (ICE) for Measuring EOS on OMEGA*

Principal Investigators: Y. M. Gupta and J. R. Asay (University of Washington)

This experimental effort is geared toward developing new areas of high-pressure research. The aim of the FY06 shots was to continue development of techniques to generate high-accuracy, quasi-isentropic, equation-of-state data. This will make possible, for the first time, "cold" stress-density loading curves for standard materials at loading rates up to ten times higher than possible with other methods in the Mbar regime. For the FY05 NLUF allocation, a platform was developed to produce high-accuracy and high-pressure stress-strain data on aluminum.<sup>1</sup> This was the first such data to be measured with a

Table 108.VIII: FY07–FY08 NLUF Proposals.

Principal Investigator	Affiliation	Proposal Title
R. P. Drake	University of Michigan	Experimental Astrophysics on the OMEGA Laser
R. Falcone	University of California, Berkeley	X-Ray Compton Scattering on Compressed Matter
P. Hartigan	Rice University	Laboratory Experiments on Supersonic Astrophysical Flows Interacting with Clumpy Environments
R. Jeanloz	University of California, Berkeley	Recreating Planetary Core Conditions on OMEGA—Techniques to Produce Dense States of Matter
R. Mancini	University of Nevada, Reno	Multiview Tomographic Study of OMEGA Direct-Drive Implosion Experiments
R. D. Petrasso, C. K. Li	Massachusetts Institute of Technology	Monoenergetic Proton Radiography of Laser/Plasma-Generated Fields and ICF Implosions

laser driver and was taken with ramp compression timescales more than ten times faster than had previously been possible. A stiffer response of aluminum was observed than had been previously observed at slower ramp compression experiments on the Z facility at Sandia National Laboratory. In addition, it was observed that the elastic–plastic transition is much larger than expected from previous work at Z. This points to a strong rate dependence in the material strength. The new high-strain-rate data provided by these experiments are being used to benchmark models that incorporate time dependence being developed at Washington State University (WSU).

On 26 April 2006, 14 shots were performed on isentropic compression targets. The ICE-EOS package, as shown in Fig. 108.58, consists of a Au hohlraum, a plastic reservoir followed by a vacuum gap, and a triple-stepped Ta target. Fifteen beams from the OMEGA laser at  $0.35\text{-}\mu\text{m}$  wavelength, containing a combined energy of 5 kJ in a 2-ns temporally flat pulse, are focused symmetrically onto the inner walls of the Au hohlraum (1.7-mm LEH, 2.2-mm diameter, 1.7-mm length). This confined high-Z geometry results in a near-blackbody distribution of thermal x rays ( $T_h \sim 120\text{ eV}$ ) with uniform temperature gradients over a spatial region close to the diameter of the hohlraum. The hohlraum is attached to a  $25\text{-}\mu\text{m}$ -thick Be foil glued to a  $180\text{-}\mu\text{m}$ -thick, 12% Br-doped polystyrene foil ( $\text{C}_8\text{H}_6\text{Br}_2$ ). The x-ray field within the hohlraum launches an ablatively driven shock through the foil. The initial region of planarity is expected to approach the diameter of the hohlraum and can extend over millimeters. The Bromine dopant absorbs high-energy Au M-band x rays ( $\sim 2$  to  $5\text{ keV}$ ) generated within the hohlraum, which otherwise could preheat the Ta step sample. After breakout from the rear-surface shock, heating and momentum cause the Br-CH to dissociate and unload across a  $600\text{-}\mu\text{m}$  vacuum gap. Transit across the vacuum gap causes the mass-density gradients along the target axis to relax as a function of distance from the original Br-CH/vacuum-gap interface. The unloading Br-CH monotonically loads up against the Ta sample, and the imparted momentum launches a ramp stress wave through the material. The temporal profile of the compression wave may be shaped by varying the size of the vacuum gap, the density of the reservoir, or the temperature within the hohlraum. In the FY06 experiments the main targets consisted of  $25/40/55/70\text{ }\mu\text{m}$  Ta or W. A significant change in the target design from the previous campaigns in FY05 was the inclusion of a Be ablator and  $1\text{-}\mu\text{m}$  CH liner on the inner wall of the Au hohlraum. The purpose of this modification was to keep the hohlraum open for  $\sim 80\text{ ns}$  to facilitate future on-axis radiography experiments that would diagnose material properties (e.g., material strength) during compression. In this context an “open” hohlraum means no on-axis, line-of-sight Au content that would

serve to absorb the flash x-ray photons used for radiography. Be has a high-ablation velocity, and its inclusion (1) increases the x-ray ablative shock pressure into the sample for a given input laser energy and (2) serves to fill the hohlraum rapidly and thus acts as a filler, which delays the on-axis stagnation of the cylindrically converging Au hohlraum material. The  $1\text{-}\mu\text{m}$ -CH liner serves to further tamp the hohlraum collapse. The primary goal of the FY06 NLUF shots was to use this planar drive to extract a single-shot series of equation-of-state (EOS) data for Ta and W up to peak pressures in excess of 1 Mbar.

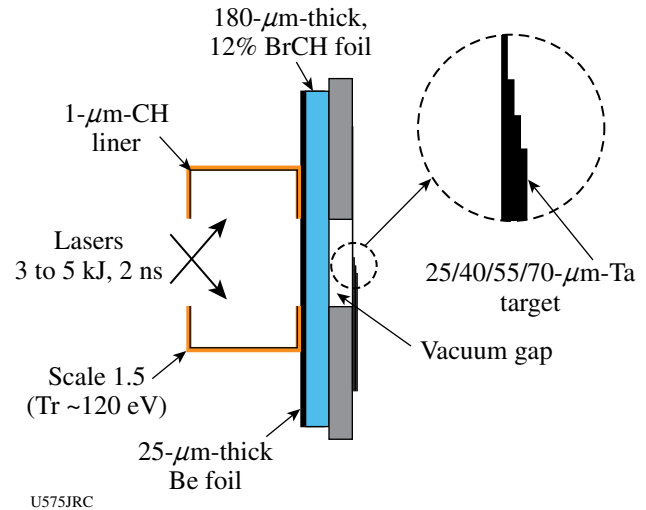


Figure 108.58

Schematic of ICE–EOS target package. The inclusion of a Be ablator and a 1-mm CH liner material serves to keep the hohlraum open for  $\sim 100\text{ ns}$ , as was verified in a separate radiography campaign.

The time history of the Ta/vacuum interface acceleration is recorded with a line-imaging velocity interferometer [velocity interferometry system for any reflector (VISAR)] with two channels set at different sensitivities. The time-resolved fringe movement recorded by a streak camera is linearly proportional to the velocity of the reflecting surface, which in this case is the Ta/vacuum interface. This allows an accurate measurement of the free-surface velocity as a function of time. The streak camera output of the VISAR for the target conditions described in Fig. 108.58 is shown in Fig. 108.59. The recently upgraded LLE VISAR provides a greater target field of view than had previously been possible, thereby allowing the use of four separate steps on a single shot for the first time, which ultimately increases the accuracy of the equation-of-state measurement.

The VISAR image provides spatial resolution at the target plane over  $\sim 800\text{ }\mu\text{m}$  and temporal resolution of the interferometer fringe displacement over a 30-ns time window. A planar

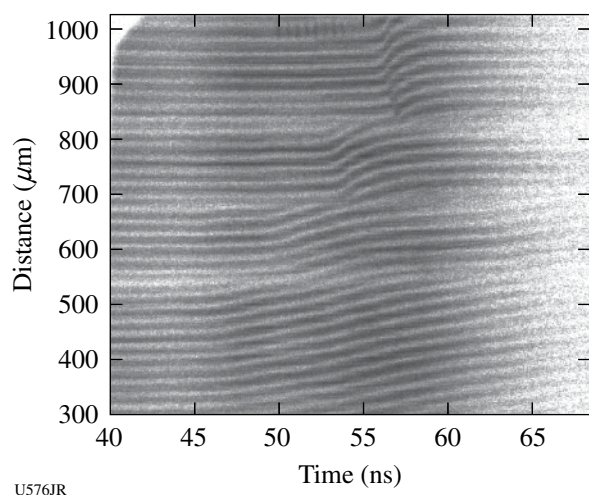


Figure 108.59  
VISAR streak record for target conditions described in Fig. 108.58.

drive was observed across the field of view with smooth ramp unloading from the 25-, 40-, 55-, and 70- $\mu\text{m}$ -Ta samples at progressively later times. The velocity sensitivity (set by the resolving element within the VISAR) is  $0.995 \text{ km s}^{-1}$  fringe shift $^{-1}$ . Using Fourier analysis and after deconvolving the data for temporal and spatial distortions within the streak camera, the time-resolved free-surface velocity ( $U_{\text{FS}}$ ) profile for each Ta thickness (Fig. 108.60) can be extracted. There is a very pronounced elastic-plastic precursor wave on all steps. An

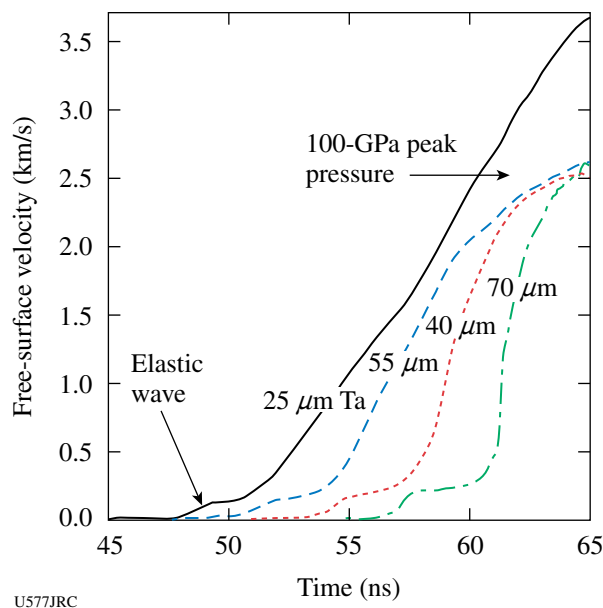


Figure 108.60  
Free-surface velocity profile deduced from the data in Fig. 108.59.

increase in this elastic-plastic wave as a function of Ta thickness/ramp rise time is observed. This is an important observation that points to a rate dependence in the material response. Analysis of this data is ongoing.

Using the iterative analysis technique described by Rothman *et al.*,<sup>2</sup> the free-surface velocity profiles in Fig. 108.60 can be used to generate a path through stress-density space up to 1 Mbar (Ref. 1). In future experiments techniques will be developed to shape the pressure profile of the ramp compression wave by using graded density reservoir materials.<sup>3</sup> This will increase the shock-up distance within the target, which in turn will facilitate larger step heights resulting in lower error bars. In addition, the use of graded density reservoirs is expected to increase the accessible peak pressure on OMEGA to greater than 4 Mbar.

### Laser-Plasma Interactions in High-Energy-Density Plasmas

Principal Investigator: H. Baldis (University of California, Davis)

High-temperature hohlraums (HTH) are designed to reach high radiation temperatures by coupling a maximum amount of laser energy into a small target in a short time. These 400- to 800- $\mu\text{m}$ -diam gold cylinders fill rapidly with hot plasma during irradiation with multiple beams in 1-ns laser pulses. The high-Z plasmas are dense, (electron density  $n_e/n_c \sim 0.1$  to 0.4), hot (electron temperature  $T_e \sim 10 \text{ keV}$ ), and bathed in a high-temperature radiation field (radiation temperature  $T_{\text{rad}} \sim 300 \text{ eV}$ ). Here the critical density  $n_c$  equals  $9 \times 10^{21}/\text{cm}^3$ . The laser beams heating this plasma are intense ( $\sim 10^{15}$  to  $10^{17} \text{ W/cm}^2$ ). The coupling of the laser to the plasma is a rich regime for laser-plasma interaction (LPI) physics. The LPI mechanisms in this study include beam deflection and forward scattering. To understand the LPI mechanisms, the plasma parameters must be known. An L-band spectrometer is used to measure the electron temperature. A ride-along experiment is to develop the x-radiation emitted by the thin back wall of the half-hohlraum into a thermal radiation source.

Figure 108.61 shows the experimental setup. About twenty laser beams in three cone angles are incident into a 600- $\mu\text{m}$ -diam, 660- $\mu\text{m}$ -long half-hohlraum. The side walls of the hohlraum are gold, usually 20  $\mu\text{m}$  thick. The back wall is thin,  $\sim 1 \mu\text{m}$  of gold or 1  $\mu\text{m}$  of gold overcoated with 1  $\mu\text{m}$  of parylene. The high- and intermediate-angle beams are focused at the center of the laser entrance hole (LEH), but the low-angle beams are focused  $\sim 250$  to 400  $\mu\text{m}$  in front of the LEH to avoid hitting the back wall. An LPI probe beam is incident almost normal to the hohlraum axis and aimed to an interaction region,

which is the plasma that is 200  $\mu\text{m}$  in front of the LEH. The transmission and forward scatter of this beam are measured with the temporally and spectrally resolved spectrometers and calorimeters in the full-aperture backscatter (FABS) diagnostic. Because of the laser-beam configuration on the OMEGA laser, one can use FABS to measure the forward-scattered light from opposing beams. If the beam is deflected, it falls onto the NBI plate. A time-averaged image of this deflection is recorded by the NBI camera. The L-band spectrometer views the plasma in the LEH region. The x-radiation emitted by the thin back wall can be used to heat a physics target. To characterize this source, the heating of a witness placed  $\sim 400 \mu\text{m}$  outside the back wall (Fig. 108.61) was measured.

Beam deflection is measured with the NBI plate. Figure 108.62 shows images of the NBI plate as a function of LPI

probe-beam intensity for two independent interaction beams. As the intensity increases, the beam deflection increases (the cross marks the center of the beam). The LPI beam is "bent" by the plasma flowing out of the target. Beam deflection occurs when the ponderomotively induced density depressions in the plasma move downstream and carry the light refracted into them. The images from NBI 25 and NBI 30 correspond to interaction beams B46 and B61, traversing the plasma at angles  $31^\circ$  and  $9^\circ$ , respectively, with respect to the normal to the axis of symmetry of the hohlraum. The beam deflections at  $5 \times 10^{15} \text{W/cm}^2$  are approximately  $15^\circ$  and  $7.2^\circ$ , respectively. This is the first observation of beam deflection as a function of laser intensity for different optical paths along the plasma.

Understanding the measured LPI mechanisms depends on knowing the plasma parameters. Radiation-hydrodynamics codes are used to predict the plasma conditions. These must be benchmarked by measurements of  $n_e$  and  $T_e$ . In highly charged gold, the  $3d \rightarrow 2p$  transitions of individual ionization states are separated by about 40 eV. If these lines can be resolved, the spectrum gives the distribution of the ionization states of gold. This, combined with models that predict the ionization state as a function of electron temperature, would give  $T_e$ .

The L-band spectrometer is designed to measure the  $3d \rightarrow 2p$  transitions in gold with high resolution. It is a transmission crystal spectrometer mounted to a single-strip framing camera. It captures a single-time and space-resolved, high-resolution spectrum. Figure 108.63(a) shows a measured spectrum. There is a group of lines, peaking at 10,100 eV, with half-width of about 250 eV. Simulated spectra [Fig. 108.63(b)] from the nonlocal thermodynamic equilibrium (NLTE) code *FLYCHK* (for  $\langle Z \rangle$  as a function of electron temperature) and *FLYSPEC* (for spectral lines) show similar features: a group of lines about 200 eV wide. The centroid moves to higher x-ray energy with higher electron temperature. A comparison of the data with simulation shows the measured electron temperature is  $\sim 7$  to 8 keV.

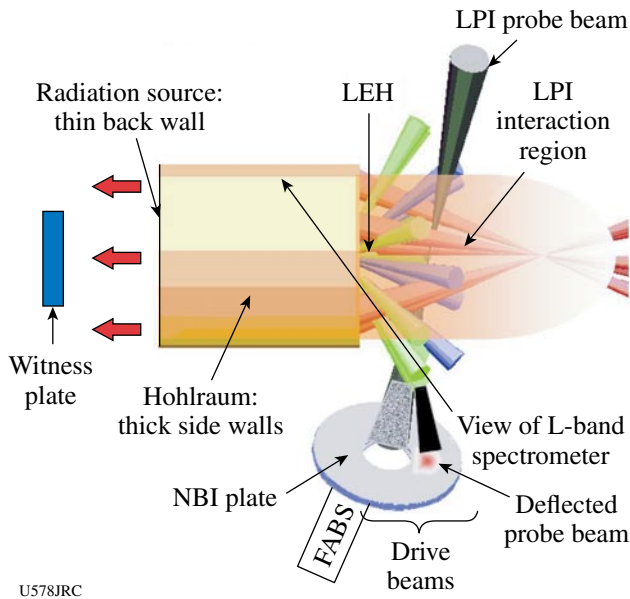
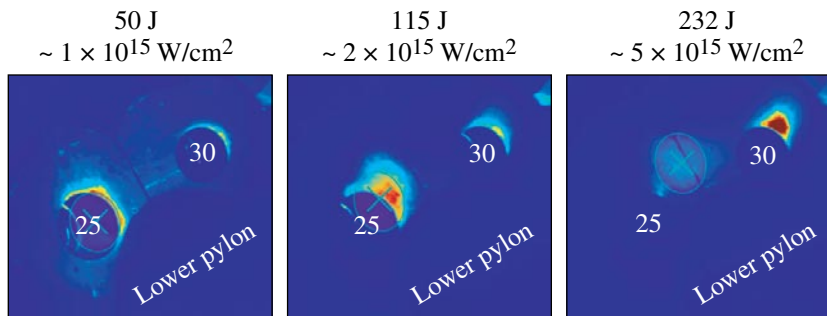


Figure 108.61  
Experimental setup of a hot hohlraum experiment.



U579JRC

Figure 108.62  
Images of NBI plates show beam deflection as a function of LPI probe-beam intensity.

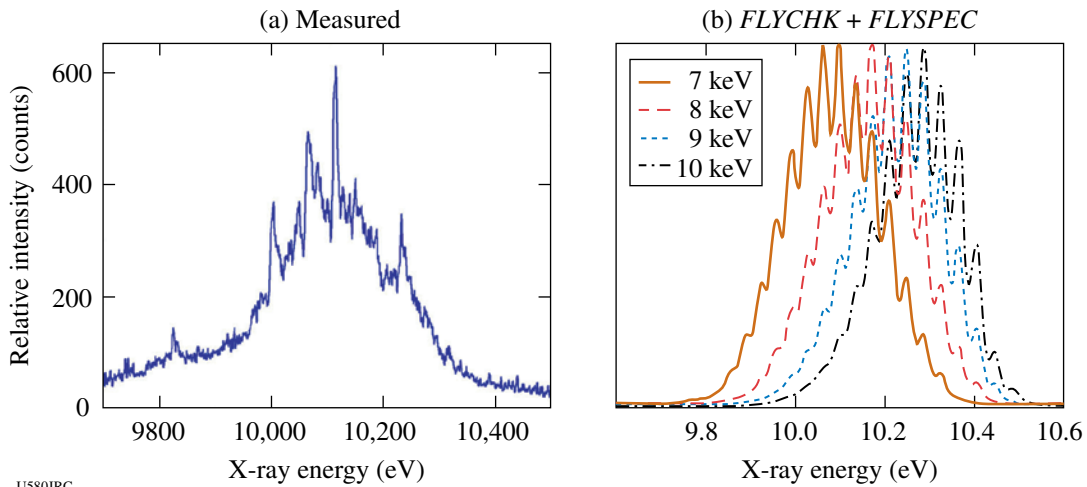


Figure 108.63  
 (a) L-band spectrometer measurement of  $3d - 2p$  transitions in Au. (b) Simulated spectra using the code *FLYCHK*.

Measured stimulated Brillouin forward scattering (SBFS) is shown in Fig. 108.64. The SBFS confirms the time at which the plasma reached the interaction region, by the transition from  $3\omega$  laser light to SBFS. The absence of  $3\omega$  light after 1 ns may indicate that the nonlinear beam deflection has shifted the beam toward the NBI plate, with the light missing the collecting lens. It is possible that the SBFS is *not* deflected because of its lower intensity.

The use of the back wall as a radiation source is demonstrated by using it to heat a Cr witness plate. The arrangement for the HTH half-hohlraum with a witness plate is shown in Fig. 108.65. Figure 108.65(a) shows a schematic of the target. The witness plate (WP) is mounted  $\sim 400 \mu\text{m}$  from the back wall, at an  $11^\circ$  tilt to the back wall so that the imaging diagnostic views the WP edge-on. The WP is a thin chromium foil

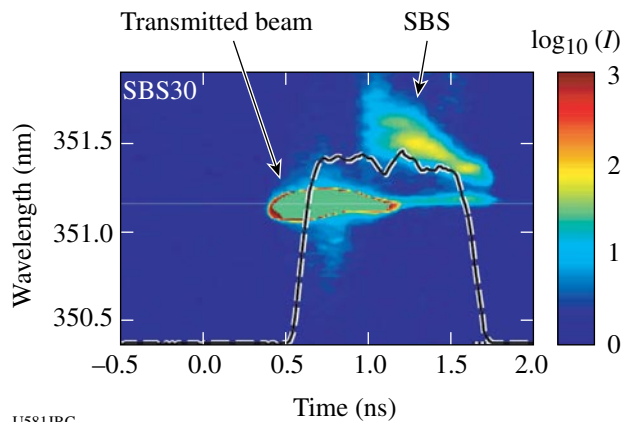


Figure 108.64  
 Streak camera image showing forward SBS.

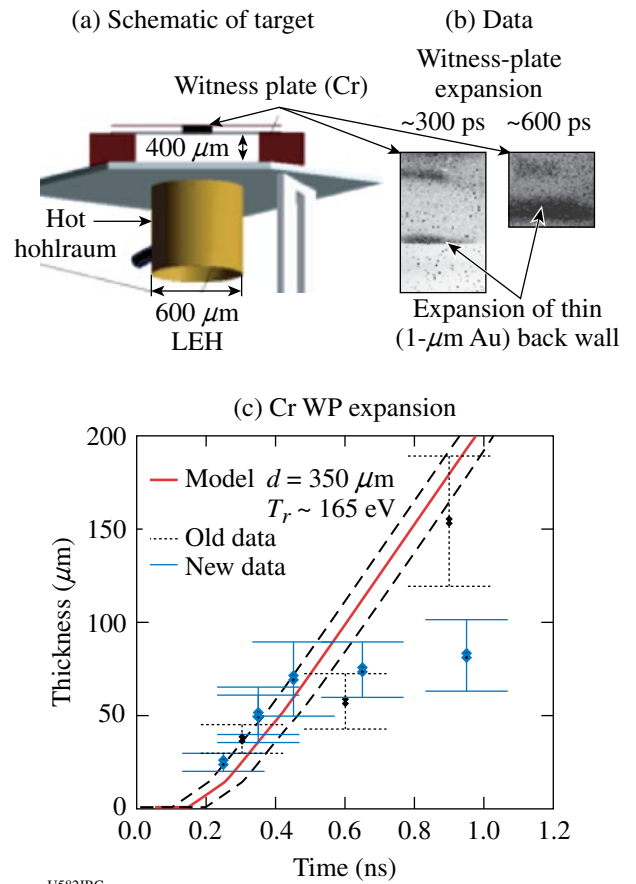


Figure 108.65  
 New radiation source: the thin back wall of an HTH half-hohlraum is used to heat a witness plate (WP). (a) The sketch of the target shows a WP mounted  $\sim 300 \mu\text{m}$  from the back wall at an  $11^\circ$  angle so it is viewed edge-on by the OMEGA diagnostic. (b) The data show a WP glowing after it has been heated by the back wall (also glowing). (c) The measured expansion of the Cr WP.

sandwiched in plastic (1  $\mu\text{m}$  on each side). Figure 108.65(b) shows the heated WP at two different times. Since these were taken on two different shots, the distance of the WP from the back wall is slightly different; however, the WP is clearly expanding as it is heated. Figure 108.65(c) shows the measured width of the WP as a function of time from several shots on several different days. The solid line is the predicted expansion from a radiation–hydrodynamic simulation, assuming the WP is heated solely by radiation from the back wall. The data are consistent with the simulation, which predicts the radiation temperature in the plate to be  $\sim 165$  eV.

The following additional measurements of plasma parameters in the LPI region have been performed: (a) the M-shell spectra of gold, (b) Raman backscatter, and (c)  $2\omega$  and  $4\omega$  Thomson scattering. These data are still being analyzed.

**Experimental Astrophysics on the OMEGA Laser**

Principal Investigator: R. P. Drake (University of Michigan)  
 Co-investigators: B. A. Remington, H. F. Robey, S. G. Glendinning, D. D. Ryutov, M. Herrmann, A. R. Miles, A. J. MacKinnon, B. E. Blue, and J. F. Hansen (LLNL); M. Koenig (LULI, Ecole Polytechnique, France); D. Arnett (University of Arizona); R. Rosner and T. Plewa (University of Chicago); J. Stone (Princeton University); S. Bouquet (CEA, France); J. P. Knauer and T. R. Boehly (LLE); Y. Zhang and J. Glimm (SUNY Stony Brook)

The OMEGA laser can address important issues in astrophysics because, through laser ablation, it can produce pressures of tens of Mbars over areas of square millimeters. Two such issues are the contribution of hydrodynamic instabilities to the structure in supernovae and the dynamics of radiative shock waves. After successfully creating collapsed radiative shock structures in both argon and xenon gas, an experiment was performed to Thomson-scatter light from the  $4\omega$  beam off of a shock front in argon gas.

In the experiment, ten smoothed beams of the OMEGA laser irradiate a 20- $\mu\text{m}$  beryllium disk with UV light at an irradiance of  $\sim 5 \times 10^{14}$  W/cm<sup>2</sup> for 1 ns. This launches the disk via ablation pressure at a high velocity into a 600- $\mu\text{m}$ -diam, 6-mm-long polyimide tube filled with 1.1 atm (0.001 g/cm<sup>3</sup>) of argon gas. This target had openings covered with 3000- $\text{\AA}$  polyimide facing the  $4\omega$  probe beam and the UV spectrometer and streak camera in TIM-2. The scattering volume was 3.7 mm from the initial drive disk position. The  $4\omega$  probe beam fired in a 2-ns pulse at 200 J, with a best-focus spot size of 100  $\mu\text{m}$ . The target axis for this experiment was parallel to the probed ion-acoustic waves.

Figure 108.66 shows spectral data from the first experiments to obtain Thomson-scattering data from a shock front. The signal lasted 300 ps, starting at 20.1 ns after the drive beams turned on. Before that, the signal was from the tail end of a destroyer beam blasting off the polyimide cover facing the collection diagnostic in TIM-2. The spectrum of the scattered light and a fit to the data are shown in Fig. 108.67. The overall spectrum is shifted in frequency by a Doppler shift, implying that the flow velocity of the shocked fluid is 110 km/s. Fits to the spectrum using the kinetic theory of Thomson scattering, combined with an evaluation of the average charge using an “average atom” model, give an ion temperature of 300 eV, an electron temperature of 250 eV, and an average charge of 13.7. These are sensible values for the argon near the shock front.

**Astrophysical Jets and HED Laboratory Astrophysics**

Principal Investigator: P. Hartigan (Rice University)

A variety of objects in the universe are surrounded by accreting disks of matter, and most of these systems drive highly collimated supersonic jets out the poles of these disks. Examples include jets from young stars, planetary nebulae, x-ray binaries, and black holes at the centers of active galaxies. The goal of this

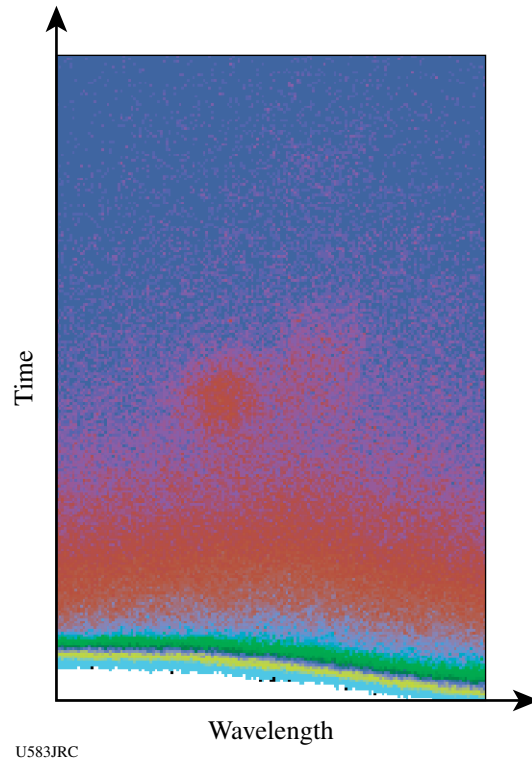
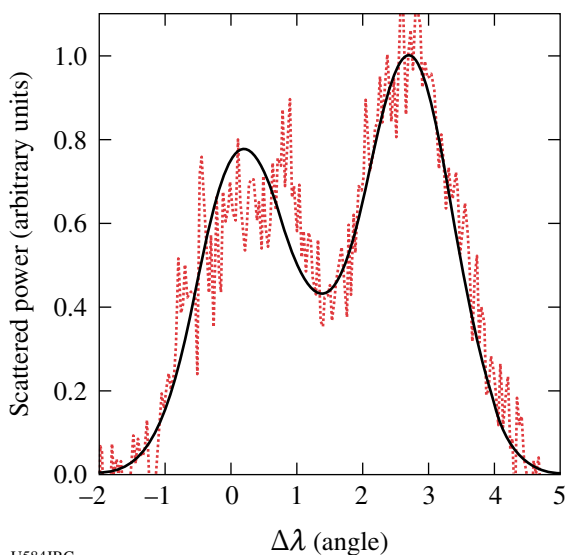


Figure 108.66  
 Streak camera data showing Thomson-scattered-light spectral evolution for collapsed radiative shock.



U584JRC

Figure 108.67  
Thomson-scattered spectrum and fit to the data for Fig. 108.66.

project is to create laboratory analogs of the jet phenomenon in the laboratory and follow what happens when such a jet interacts with an obstacle in the flow as it is observed to do in many astrophysical situations. An astrophysics fluid dynamics code (*AstroBEAR*) and the *RAGE* code at Los Alamos are both used to help design the experiment and interpret the results.

In the past year, two shot days were allotted for the project, and both succeeded in producing excellent images of shocks in the jet and the ball as the latter was being destroyed and entrained by the flow. The targets consisted of a dense ball

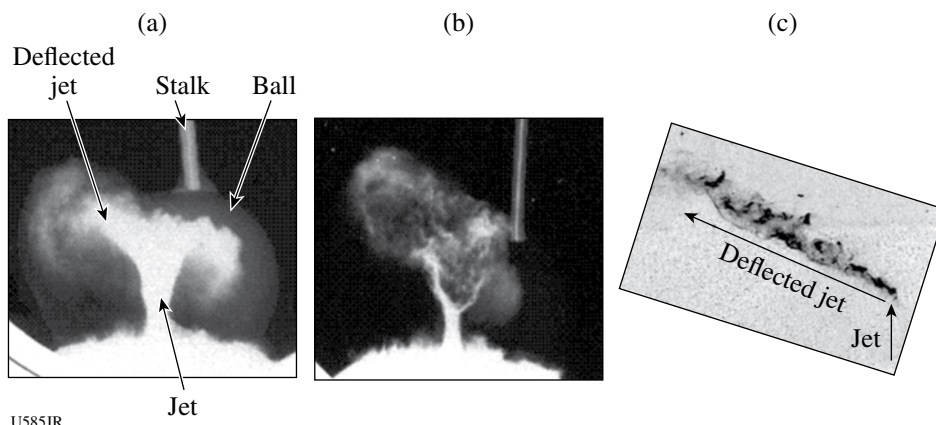
embedded at various offset distances (impact parameters) from the axis of the jet. The data set now includes a continuous range of impact parameters and times so we can follow the process as a function of these two variables. Sample images from the experiment are shown in the Fig. 108.68. Astrophysical observations of a deflected jet are scheduled for the end of November, and we will be comparing the new spectra from that effort with numerical datacubes of the *RAGE* and *AstroBEAR* simulations of the laser experiments to improve our understanding of the dynamics of these flows.

### Recreating Planetary Core Conditions on OMEGA

Principal Investigator: R. Jeanloz (University of California, Berkeley)

Significant technical as well as scientific breakthroughs in the NLUF high-pressure experiments on planetary fluids were made this past year. The approach that is used involves driving a laser-induced shock wave through a sample already precompressed in a diamond-anvil cell (Fig. 108.69). This combines the benefits of static and dynamic methods of high-pressure experiments, allowing the final pressure–volume–temperature ( $P$ – $V$ – $T$ ) state of the sample to be tuned across a broad range of thermodynamic conditions (Fig. 108.70). In fact, much-higher compressions, thus more-extreme interatomic interactions, are achieved through this approach than through traditional shock-wave (Hugoniot) measurements.

One of the major technical accomplishments of this program has been the significant improvement of the understanding of

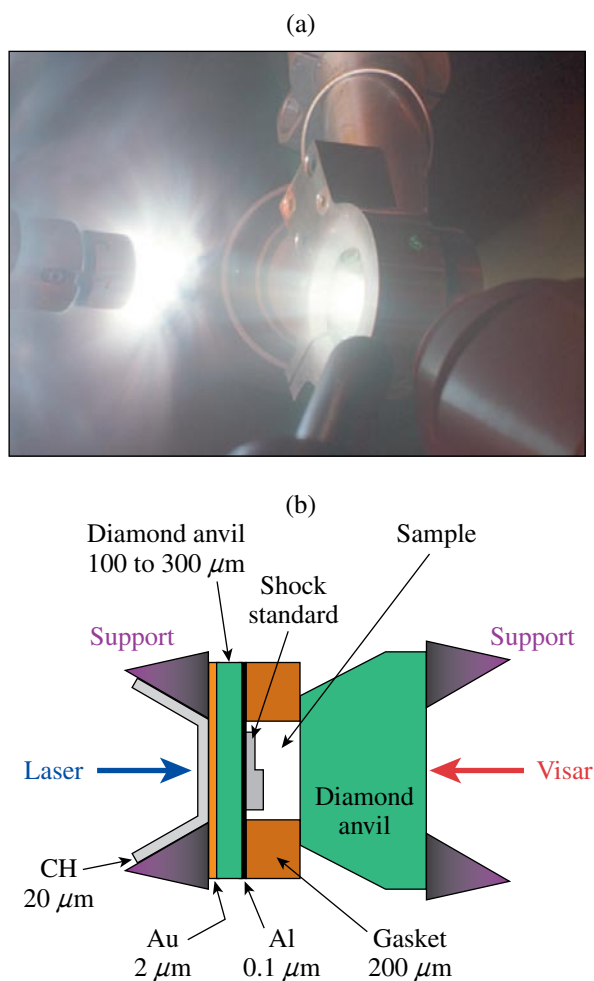


U585JR

Figure 108.68  
Deflected jets in the laboratory and in the universe. (a) OMEGA image of a jet deflecting from a ball located  $300\ \mu\text{m}$  from the axis of the jet, at 150 ns, taken with an Fe backlighter. Shocks are clearly visible in the ball and ahead of the deflected jet, which is starting to fragment. (b) Same as (a) with a  $350\text{-}\mu\text{m}$  offset at 200 ns and a Zn backlighter. (c) Hubble Space Telescope image of the deflected jet HH 110. The jet emerges from a young star off the bottom of the image and deflects off an opaque dark cloud of gas and dust.

the interferometry records obtained from the shock experiments (Fig. 108.71). Despite the use of antireflection coatings, the components in these experiments generate residual reflections that cause “ghost fringes” to appear in the VISAR records. This source of noise is now understood, to the point that the “ghost fringes” serve as internal calibrants for the records and a joint inversion of the records can be performed to obtain far better velocity resolution than previously thought possible.

In addition to equation-of-state measurements, one of the key measurements obtained from the VISAR records is the optical reflectivity of the shock front: it is possible to determine whether one is looking through the shock front or off its surface

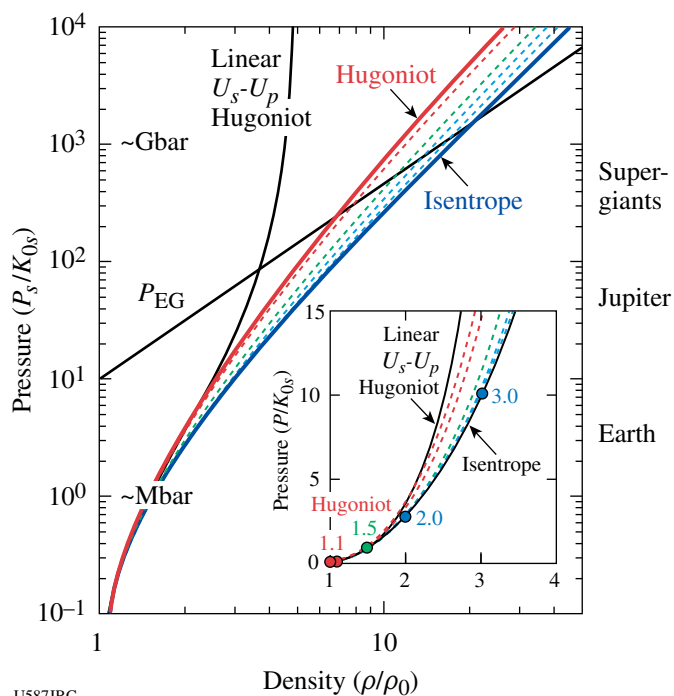


U586JRC

Figure 108.69

Photograph of (a) a loaded diamond cell subjected to laser-shock compression and (b) schematic cross section of the diamond cell. The diamond anvil of the entry (drive-laser) side must be thin in order to minimize attenuation of the shock front before it enters the sample. Diagnostics include velocity interferometry (using VISAR) as well as pyrometry (not shown).

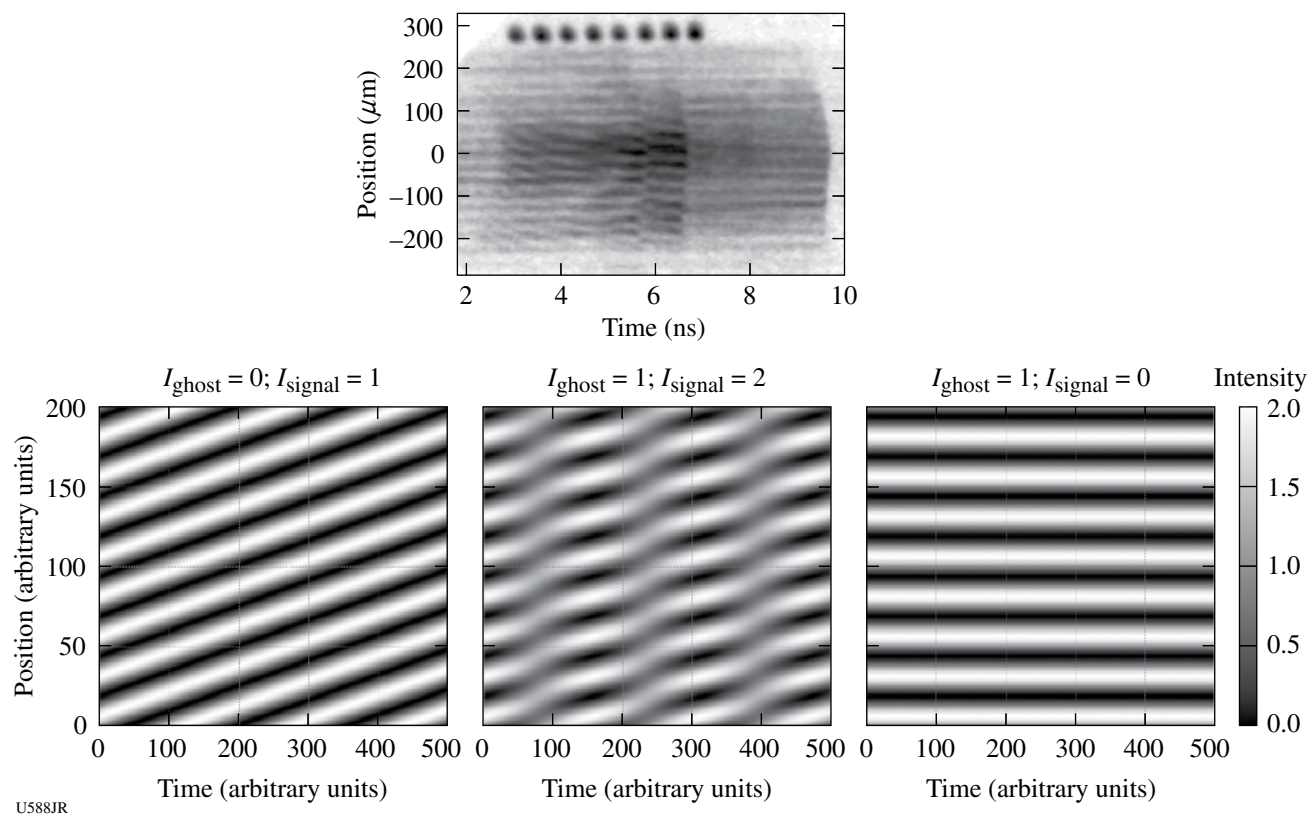
by the way the velocity fringes. The reflectivity at optical wavelengths can be converted to an equivalent of electrical conductivity, allowing us to determine the competing  $P$ - $T$  conditions under which helium becomes metallic (Fig. 108.72). This is important because the metallization conditions for helium, far more extreme than those for hydrogen, determine the depths at which hydrogen and helium—the primary constituents of giant planets—can behave as metallic alloys. Without such alloying, it is expected that helium separates from the much lighter hydrogen, and the gravitational energy released by this “differentiation” process is thought to be a major source of heat and internal evolution of giant-planetary interiors. Indeed, experiments now underway will allow the documentation of the enhanced reflectivity of hydrogen + helium mixtures (Fig. 108.73), promising to offer significant new constraints on models of planetary evolution and origins.



U587JRC

Figure 108.70

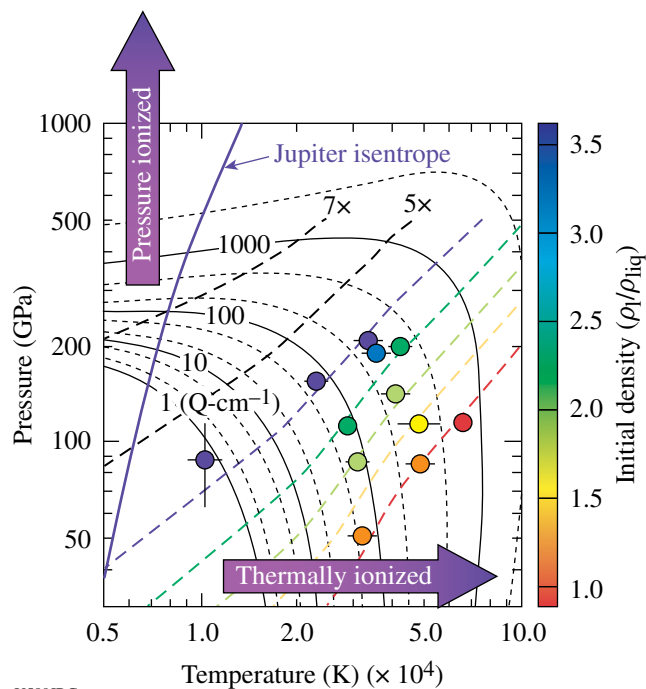
Pressure-density ( $P$ - $\rho$ ) equations of state, normalized by the zero-pressure bulk modulus ( $K$ ) and density illustrating the range of conditions that can be achieved between the single-shock Hugoniot and isentrope as a function of precompression by factors of 1.1, 1.5, 2.0, and 3.0 (see inset), all calculated from the Birch-Murnaghan<sup>4</sup> and Mie-Grüneisen<sup>5</sup> approaches assuming  $K'_0 = 4$ , a Grüneisen parameter varying as  $\gamma/\rho = \text{constant}$ , and  $\gamma_0 = 1.5$  (subscripts 0 and  $s$  indicate zero-pressure and isentropic conditions, respectively). The linear shock-velocity  $U_s$  versus particle-velocity  $U_p$  relationship, and the density dependence of the ideal electron-gas pressure ( $P_{EG}$ ) are shown for comparison, as are Mbar and Gbar pressures and planetary-center conditions (Earth, Jupiter, and supergiants) corresponding to a typical bulk-modulus value of 100 GPa ( $\approx 1$  Mbar). The inset shows the lower-pressure range on a linear plot.



U588JR

Figure 108.71

(Top) Velocity-interferometry (using VISAR) record from a laser-shock experiment on precompressed helium showing the presence of “ghost fringes” due to residual reflections from diamond and other surfaces. (Bottom) Simulations of the ghost fringes, from 100% signal (no ghost) on the left to 100% ghost (no signal) on the right; center panel shows a 2:1 intensity ratio for signal:ghost.



U589JRC

Figure 108.72

Reflectivity measurements as a function of pressure–temperature conditions achieved in helium (circles shaded according to the precompressed density  $\rho_1$  prior to shock loading) quantified in terms of equivalent electrical conductivity (solid and dotted contours). The data clearly probe the trade-offs between pressure and temperature in causing metallization (ionization), with predicted trajectories for different amounts of precompression indicated by the dashed lines and the model temperature distribution (isentrope) inside Jupiter shown for comparison.

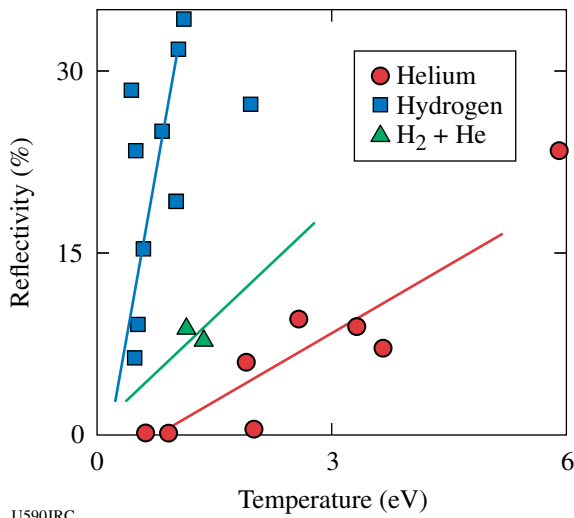


Figure 108.73 High-pressure reflectivity of hydrogen, helium, and hydrogen + helium mixtures under shock compression, shown as a function of Hugoniot temperature determined from pyrometry.

### Three-Dimensional Study of the Spatial Structure of Direct-Drive Implosion Cores on OMEGA

Principal Investigator: R. Mancini (University of Nevada, Reno)

The objective of this project is to study the three-dimensional (3-D) structure of the temperature and density spatial profiles of OMEGA direct-drive implosion cores using data from gated narrowband x-ray core images recorded along three quasi-orthogonal directions. To this end, this experiment uses plastic shell targets filled with deuterium gas and a tracer amount of argon for spectroscopic diagnostic purposes. Three identical multimono-chromatic imagers (MMI) have been designed, built, and fielded on OMEGA implosion experiments to perform observations along the lines of sight (LOS) of TIM-2, TIM-3, and TIM-4; this set of TIM's represents a quasi-orthogonal system of  $x$ - $y$ - $z$  Cartesian axes. The implosions were driven with 60 OMEGA beams, 23 kJ of UV energy, and a 1-ns square laser pulse. At the collapse of the implosion, the hot and dense core plasma achieved temperatures in the 1- to 1.5-keV range and electron number densities in the  $1 \times 10^{24} \text{ cm}^{-3}$  to  $2 \times 10^{24} \text{ cm}^{-3}$  range. X-ray K-shell line emission from the argon dopant is a suitable spectroscopy diagnostic for this temperature and density range.

Core images (recorded by MMI instruments) that are formed by a large array of 10- $\mu\text{m}$ -diam pinholes and reflected off a depth-graded  $\text{WB}_4\text{C}$  multilayer mirror with an average bilayer thickness of 15 Å yield narrowband x-ray images in the photon energy range from 3 to 5 keV. They have a magnification of 8.5,

provide spatial resolution of approximately 10  $\mu\text{m}$ , and record gated (framed) images characteristic of a 50-ps time interval. Indeed, these instruments record data with simultaneous space, time, and photon energy resolution. As an illustration of the data recorded by MMI, Figs. 108.74 and 108.75 display a time history of narrowband x-ray core images from OMEGA shot 42643 at the collapse of the implosion, based on the argon  $\text{Ly}_\beta$  ( $1s^2 2S-3p^2 P$ ,  $h\nu = 3936 \text{ eV}$ ) and  $\text{He}_\beta$  ( $1s^2 1S-1s2p^1 P$ ,  $h\nu = 3684 \text{ eV}$ ) line emissions. The photon energy narrowband of these images is given by the (mainly) Stark-broadening widths of the line shapes, which for the plasma conditions of these cores is 60 to 70 eV. Core dimensions are in the 60- to 100- $\mu\text{m}$  range. At early times, images recorded along both quasi-orthogonal directions show cores that are large and mostly round. For later times, one LOS shows a core shape that evolves into an oval shape, while the other LOS shows an object that remains more rounded but

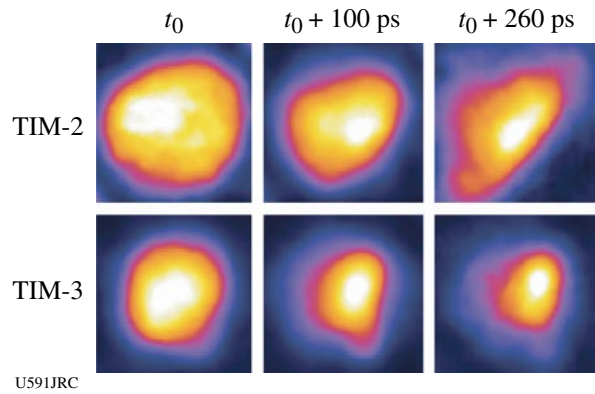


Figure 108.74 Gated argon  $\text{Ly}_\beta$  narrowband core images recorded along two quasi-orthogonal directions on OMEGA shot 42643.

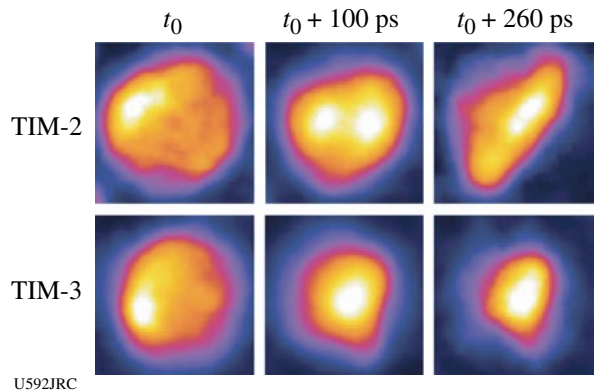


Figure 108.75 Gated argon  $\text{He}_\beta$  narrowband core images recorded along two quasi-orthogonal directions on OMEGA shot 42643.

getting smaller. Both observations suggest the evolution of a 3-D core from rounded to ellipsoidal shapes with a well-defined orientation in space. It is also interesting to observe the regions of greatest brightness associated with the  $Ly_{\beta}$  and  $He_{\beta}$  line emissions, which depends on both temperature and density conditions in the core. Detailed spectral modeling and analysis of the emissivity and opacity of the argon x-ray emission permit a reconstruction of spatial structure of the plasma. In this connection, Fig. 108.76 displays a temperature map based on the analysis of the second frame of data (i.e.,  $t_0 + 100$  ps) displayed in Figs. 108.74 and 180.75. The range of values of this spatial profile is consistent with the range of temperatures extracted from the analysis of data independently recorded with streaked spectrometers in the same experiment. Several analysis methods are currently being investigated that simultaneously consider data observed along several LOS's.

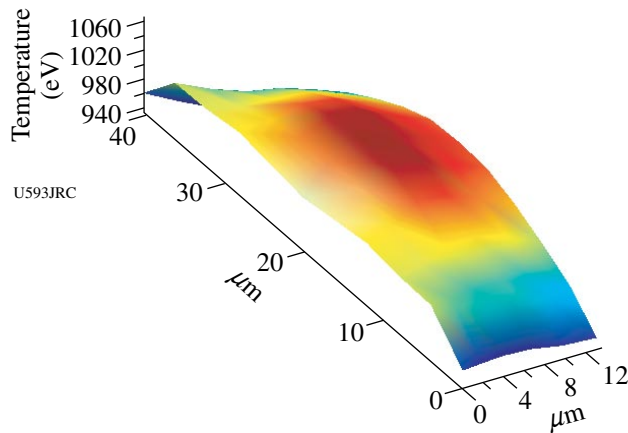


Figure 108.76  
Core temperature map for OMEGA shot 42643 extracted from TIM-2 data in Figs. 108.74 and 108.75 for  $t_0 + 100$  ps.

**Implosion Dynamics and Symmetry from Proton Imaging, Spectrometry, and Temporal Measurements**

Principal Investigators: R. D. Petrasso and C. K. Li (Massachusetts Institute of Technology)

As part of the MIT NLUF program, data was taken in an ongoing series of experiments using proton radiography to study transient  $E$  and  $B$  fields generated by the interaction of OMEGA laser beams with plastic foils. High-resolution, time-gated radiography images of a plastic foil driven by a  $10^{14}$ -W/cm<sup>2</sup> laser implied  $B$  fields of  $\sim 0.5$  MG and  $E$  fields of  $\sim 1.5 \times 10^8$  V/m. Simulations of these experiments with *LASNEX + LSP* have been performed and are in overall (though not exact) agreement with the data both for field strengths and for spatial distributions; this is the first direct experimental test of the laser-generated  $B$ -field package in *LASNEX*. The experiments also demonstrated that laser phase plates substantially reduce medium-scale chaotic field structure. The results have recently been published in *Physical Review Letters*<sup>6</sup> and in *Review of Scientific Instruments*.<sup>7</sup>

In each experiment, two plastic foils were illuminated by a single OMEGA laser beam, and a projection radiograph was made of each foil using a backlighter providing monoenergetic 14.7-MeV protons and a CR-39 area detector for image recording. One foil was perpendicular to the backlighter–detector direction, giving a face-on view of the resultant field structure, while the other foil was parallel to the backlighter–detector direction, giving a side-on view. The backlighter was formed by imploding a  $D^3He$ -filled, glass-shell capsule with 20 OMEGA laser beams (see Fig. 108.77). Since the burn duration of the  $D^3He$  implosion was short ( $\sim 150$  ps) relative to the 1-ns duration of the foil illumination, and the relative timing of the implosion and the foil illumination was adjustable, it was possible to record images at different times relative to the foil illumination.

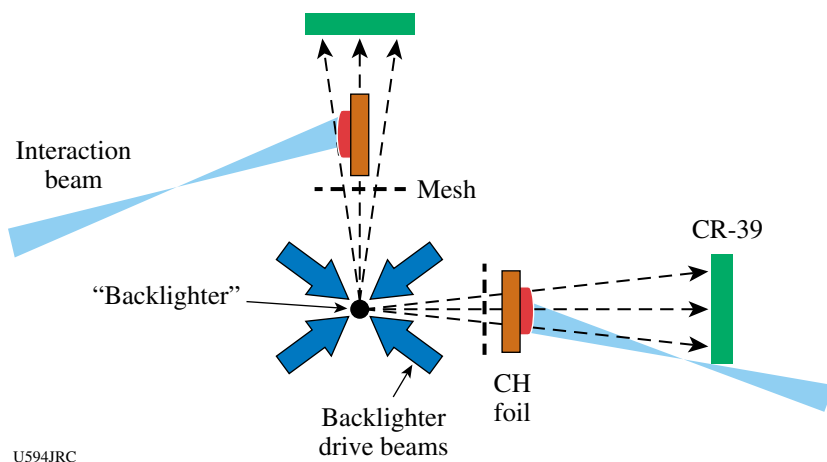


Figure 108.77  
Schematic illustration of experimental setup and the physical relationship between the proton backlighter (imploded  $D^3He$ -filled capsule), mesh, CH foils, CR-39 imaging detectors, and OMEGA laser beams. The distances of components from backlighter were 0.8 cm for mesh, 1 cm for foil, and 36 cm for detector. The hole-to-hole spacing in the mesh was  $150 \mu m$ .

The distortion in the mesh pattern at the detector shows how the proton trajectories were deflected through interaction with the fields generated by laser-plasma interaction at the foil. Sample images recorded at different times are shown in Fig. 108.78 (face-on) and Fig. 108.79 (side-on). These images have been analyzed in collaboration with LLNL and LLE to provide information about the time evolution of the field-induced distortion.<sup>6,7</sup>

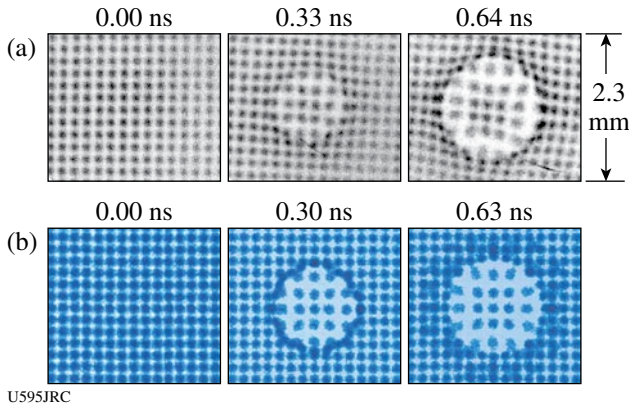


Figure 108.78  
 (a) Measured face-on  $D^3He$  proton images showing the effects of the  $B$  field generated by laser-plasma interactions at 0.0, 0.33, and 0.64 ns, respectively, after the interaction beam was turned on. The labeled dimensions of the image are scaled to the location of the foil. (b) Images simulated by *LASNEX* + *LSP* for the conditions that produced the experimental images shown in (a).

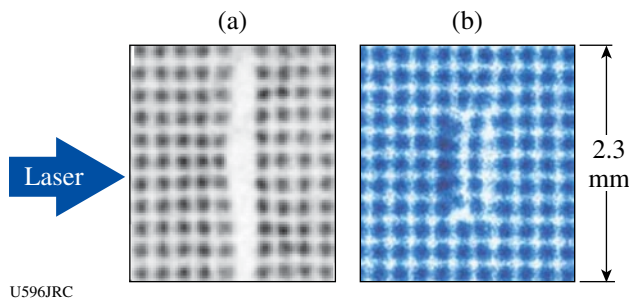


Figure 108.79  
 (a) Data and (b) simulation for the side-on images. The distortion in the center column of (a) resulted from the  $E$  field. The large separation between the two center columns of beamlets in (a) is due to attenuation by the CH foil, which is  $50 \mu m$  thick but 3 mm long in the direction parallel to the proton trajectories; this effect is not seen in (b) because proton-foil interactions were not modeled in the *LSP* simulation.

### FY06 LLNL OMEGA Experimental Programs

In FY06 LLNL led 354 shots on the OMEGA system. This total represents a shot rate of approximately 4% higher than nominal (340 shots scheduled for the year), an excellent

achievement when one considers that LLNL's programmatic needs frequently dictated difficult reconfigurations from one day to the next, especially during split days.

*National Ignition Campaign (NIC) Experiments:* One of the first experiments of the year was designed to examine the direct effects of laser-heated gas on an implosion capsule within a gas-filled hohlraum. Plastic hohlraums (to minimize radiation drive) and foam witness balls were used in a NIF-foot-scale experiment. The x-ray backlighting data are shown in Fig. 108.80. Arrows point to regions where there is a departure from spherical symmetry due to pressure from the laser-heated gas that filled the hohlraum.

Several shot days were devoted to the study of collective x-ray scattering from plasmons in warm (10 to 15 eV), dense ( $2$  to  $3 \times 10^{23}$  electrons/cm<sup>3</sup>) matter. By fitting the data to theoretical models, the electron density is obtained from the scattered x-ray data and found to be in agreement with simulations.

Throughout FY06 a number of laser-plasma interaction experiments were carried out, some in collaboration with CEA, using a gas-filled hohlraum arranged so that one OMEGA beam (beam 30) could be used as an on-axis probe. Spatially imaged Thomson scattering and a time-resolved transmitted beam diagnostic ( $3\omega$  TBD) were successfully fielded on OMEGA. Various experimental results are shown in Fig. 108.81 (electron and ion temperatures in the gas as a function of time), Fig. 108.82 (Brillouin scattering reduced as electron temperature increases), and Fig. 108.83 (Raman scattering measured as a function of density for fixed intensity). Experiments using a defocused beam with phase plates showed interaction instabilities decreasing with the average intensity, as predicted. Finally, a semiautomated mechanism for calibration of the near-backscatter plate was fielded and tested.<sup>8</sup>

An albedo (ratio of radiant energy emitted divided by radiant energy absorbed) experiment compared gold hohlraums and "cocktail" (mixtures of gold and uranium) 180-eV hohlraums and found, as predicted, a slight increase for the cocktail case.

In another collaboration with CEA, the OMEGA laser was used in the direct-drive configuration to illuminate spheres of gold, uranium, and a cocktail mixture to measure the conversion of laser energy into x-ray energy. Particular attention was given to obtaining detailed measurements in the 2- to 5-keV range.

An extensive series of experiments were performed for platform development, and use of that platform, for measuring the

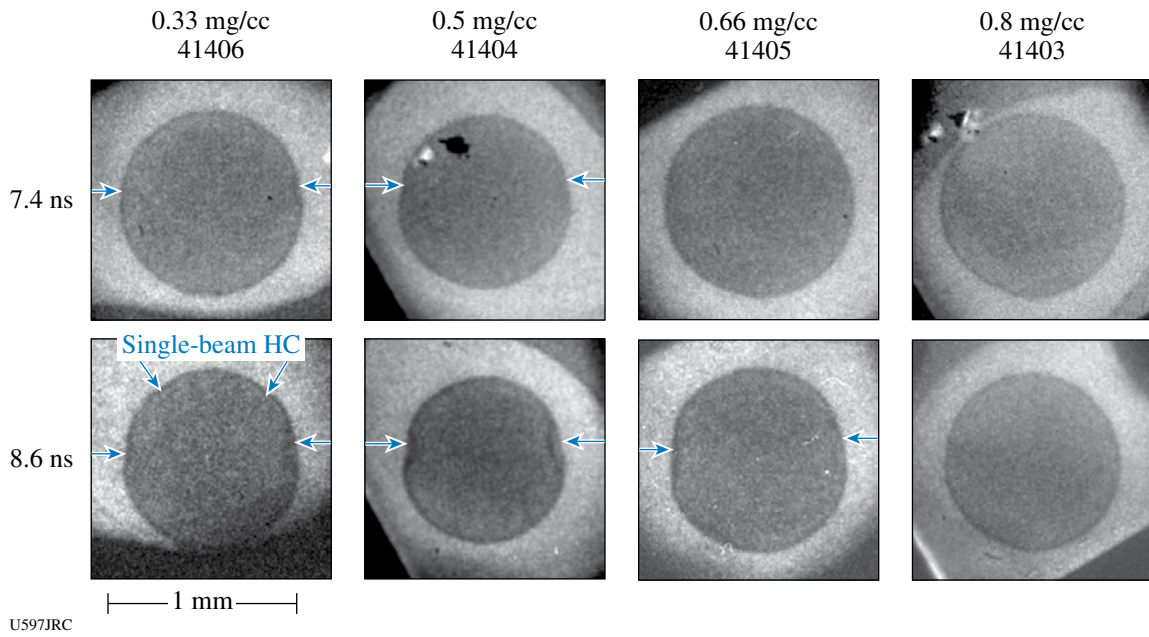


Figure 108.80 X-ray-backlit images of foam spheres, showing (arrows) effects of pressure from laser-heated hohlraum fill gas. Good backlighting foam-ball data were measured for the 0.3- to 0.8-mg/cc hohlraum fill range of interest for HC.

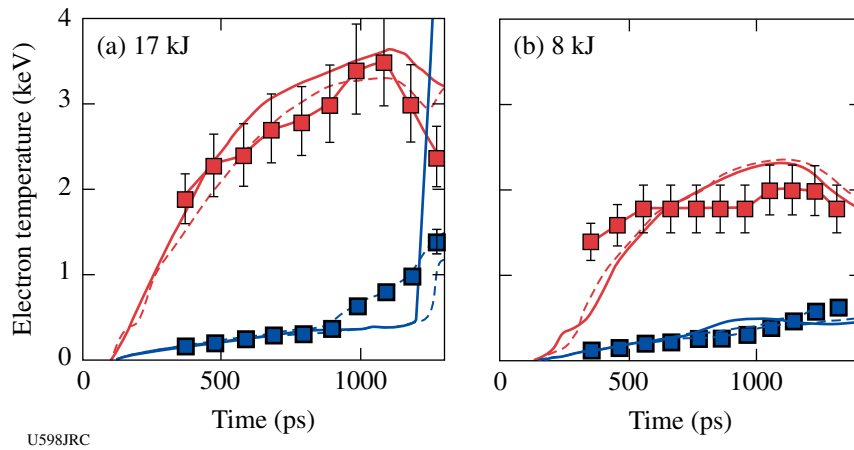


Figure 108.81 Electron temperature (open squares), ion temperature (dark squares), and simulations (solid lines) as a function of time along the laser beam path. The measured electron- and ion-temperature evolution validates the simulations of the plasma conditions along the interaction beam path.

Rayleigh–Taylor growth of ablator materials, being ablatively accelerated by x-ray drive. The planar ablator samples were mounted on the end of a one-ended hohlraum (“halfraum”). X-ray backlighting of the planar samples was used in both side-

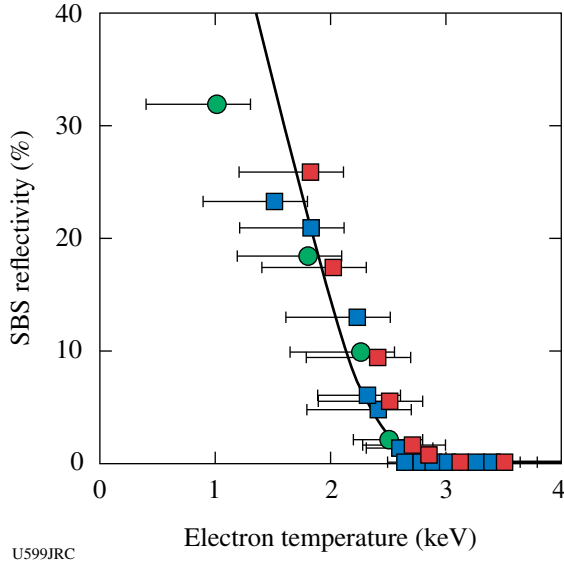


Figure 108.82 Measured SBS reflectivity (points) follows linear gain calculation (solid line) and drops with electron temperature, as predicted. Stimulated Brillouin scattering is reduced to zero for electron temperatures above 2.5 keV.

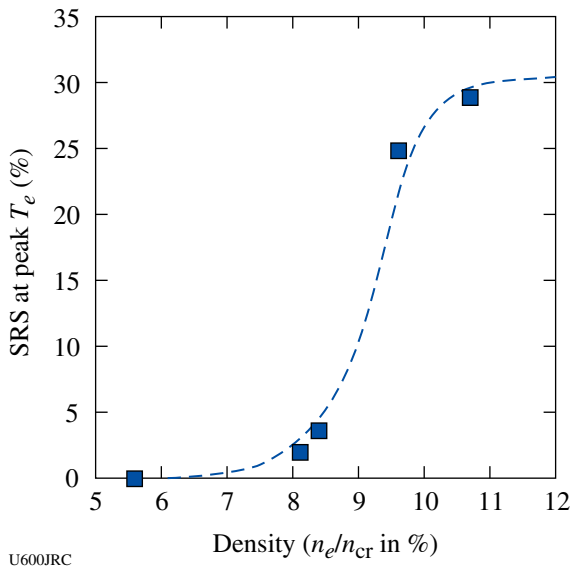


Figure 108.83 Density scaling of SRS at an intensity of  $1.5 \times 10^{15} \text{ W/cm}^2$ . Raman-scattering levels are consistent with linear gain calculations, varying with electron density for fixed laser intensity.

on and face-on geometry. The latter required imaging through the halfraum. Side-on images were obtained with both 2-D framing cameras and 1-D streak cameras, depending on the experiment. One goal is to be able to measure RT growth in Be from its inherent grain structure; this requires that the platform be capable of nearly 1000× growth, to increase the structure to observable size and simulate expected NIF conditions. Figure 108.84 shows face-on data for two materials, Be and diamond. The initially imposed 1-D perturbations have grown to measurable size. Figure 108.85 shows a summary of these results for diamond. Analysis and simulations are still ongoing to form a more complete understanding of the processes.

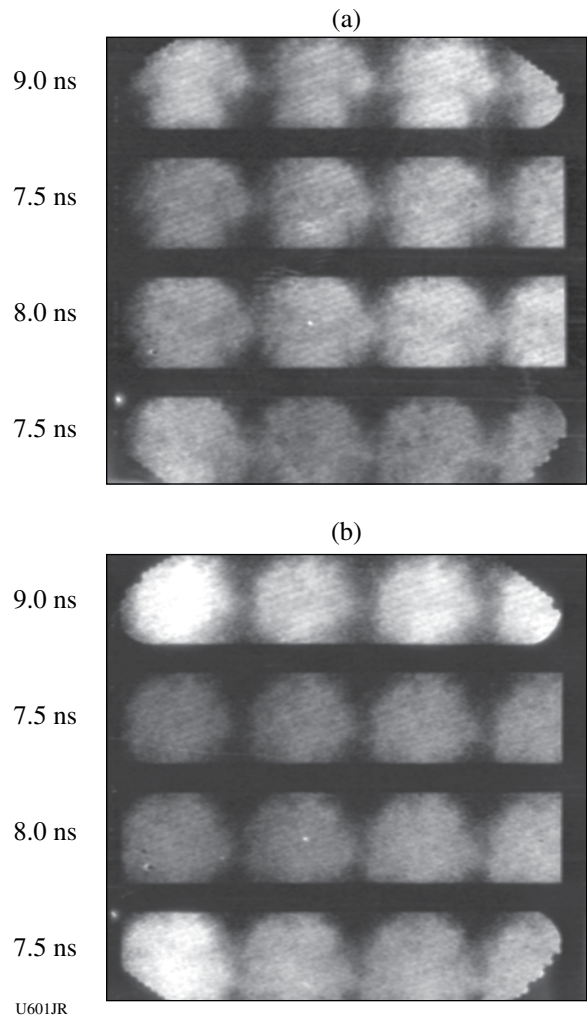
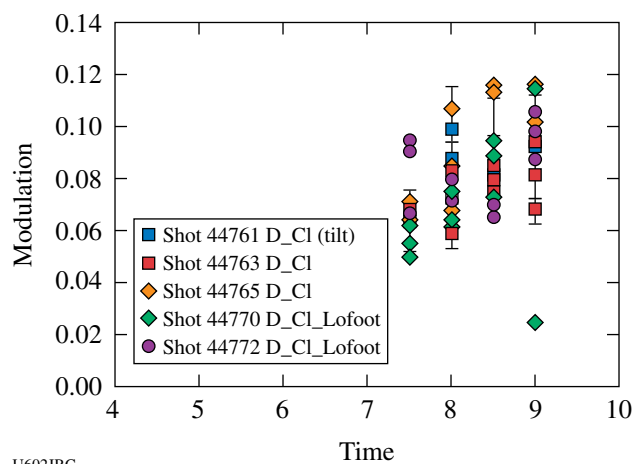


Figure 108.84 X-ray-backlit images of ablatively accelerated planar foils. Observation of large growth of 150-nm amplitude initial perturbations demonstrated (lines running diagonally lower left to upper right) for both (a) carbon (diamond) and (b) Be ablaters, as expected, based on previous CH(Ge) results.



U602JRC

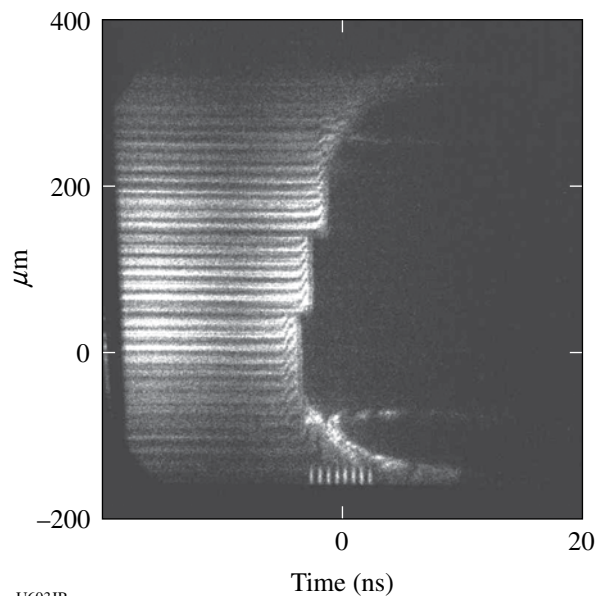
Figure 108.85

Modulation depth for diamond foils (see Fig. 108.84) for various times and laser drives.

A concern with gas-filled hohlraums is that they must, of necessity, have a window to contain the gas. Despite the fact that these windows are thin and low  $Z$ , they are the first objects irradiated by the laser beams, and they can generate x rays that may affect the capsule. To obtain quantitative data, Be step wedges (planar Be samples with three different thicknesses) were exposed to x rays produced by the interaction of the OMEGA laser with a thin plastic window. The resulting shock and preheating of the Be were measured with the active shock breakout (ASBO) diagnostic. An example of such data is shown in Fig. 108.86. The termination of the fringes (time runs left to right) coincides with the shock breaking out of the rear surface of the three steps (thickest step at top). Still other experiments used the ASBO, VISAR, and streaked optical pyrometer (SOP) to infer changes in the state—specifically, melting points—of Be and diamond, under varying levels of x-ray preheat and shock compression.

A series of implosion experiments modeled NIF fill tubes with a deliberately placed perturbation on the surface of the capsule. The inner layer of the capsule contained a mid- $Z$  (Ti) dopant. Under certain conditions, the perturbation resulted in a hydrodynamic jet of material moving through the imploded core. This jet was detected by the x-ray emission from the Ti dopant. While this experiment looked at the effect of the tube above the capsule, another experiment (“planar fill tube”), done in collaboration with LANL, investigated the effect of the fill hole using a planar analog. Initial experiments gave promising results using foams as a stand-in for solid DT and showed a jet of the indirectly driven ablator material propagating through the hole.

VISAR-1 Shot 44633



U603JR

Figure 108.86

ASBO data: shocks in Be driven by x rays from window. The abrupt turnoff of the reflected light (fringes) coincides with the time of shock breakout from the three different thicknesses of Be (thinnest at bottom).

One design for x-ray backlighters on the NIF looks like a peaked roof. Several OMEGA shots were carried out with this geometry to ascertain the x-ray conversion efficiency, and also the spatial uniformity, of this design. The results showed these targets capable of meeting the NIF specifications.

*High-Energy-Density Science (HEDS) Experiments:* Approximately one third of the LLNL OMEGA shots were for HEDS experiments.

One experiment used very small hohlraums to generate a thermal source of x rays at high photon energies, while at the same time examining the laser–plasma interaction issues associated with such targets. Figure 108.87 shows the x-ray spectra from the 10-keV region, along with model calculations for various thermal temperatures.

Late in FY06 LLNL executed a day of experiments using “double-shell” targets. This represented the culmination of extensive target fabrication work; x-ray tomographic images of the targets are shown in Fig. 108.88. The experiment used a variety of diagnostics, such as time-resolved x-ray backlighting, shown in Fig. 108.89. These data are now undergoing detailed analysis.

The nonlocal thermodynamic equilibrium (NLTE) experiments have as their goal the study and understanding of the radiative effects of high-Z (atomic number) dopants on implosions. Capsules containing deuterium, plus dopant gas, were directly driven by the OMEGA laser. Both spectroscopic x-ray and nuclear diagnostics were employed. Figure 108.90 shows the dramatic order-of-magnitude change in secondary neutrons (those arising as a result of tritium being generated in primary

nuclear fusion reactions) observed when a small amount of xenon is added. This is indicative of higher densities in the imploded fuel as a result of radiative cooling from the xenon.

Several experiments were carried out to prove the concept of an experimental platform for measuring x-ray opacities in warm, dense matter. These included the development of broadband soft-x-ray backlighters, point backlighters at higher energies, and a hohlraum drive to heat the samples to the desired conditions, along with the necessary diagnostics. These experiments will continue into FY07.

Dynamic hohlraums are directly driven, capsule-within-a-capsule targets. The idea is shown in Fig. 108.91; xenon gas within the outer capsule becomes hot and radiates, causing an x-ray-driven implosion of the inner, deuterium-containing capsule. Data obtained include x-ray-streaked images of the self-emitted x rays, multiple x-ray images, charged-particle information (collaboration with MIT), and multiple standard OMEGA neutron diagnostics. These data are currently being analyzed and compared with simulations.

We continued with our ICE (isentropic compression experiments) in FY06. Various improvements were made to targets, to increase planarity and temporal behavior of the shockless drive. Equation-of-state data were obtained for various materials.

The “shock-sphere” experiment conducted on OMEGA is an example of laboratory astrophysics. In this case, it is model-

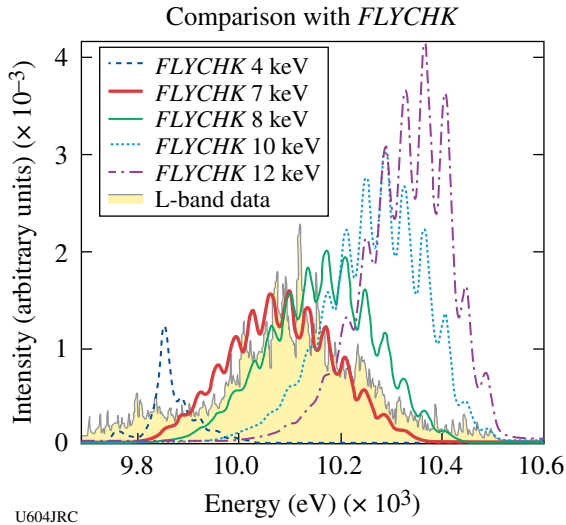


Figure 108.87 Spectroscopic data (gray, shaded area) from small, high-temperature hohlraum are best fit by model calculations (FLYCHK) between 7 and 8 keV (between thick and thin solid curves).

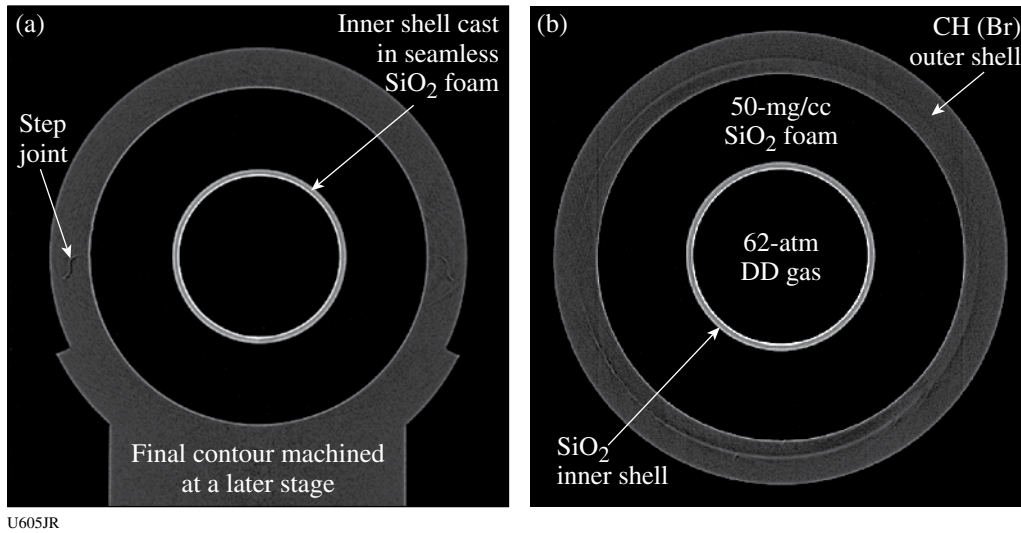


Figure 108.88 SiO<sub>2</sub> double-shell implosions. 3-D tomography of each double-shell capsule was performed to verify that all capsules meet all required specifications.

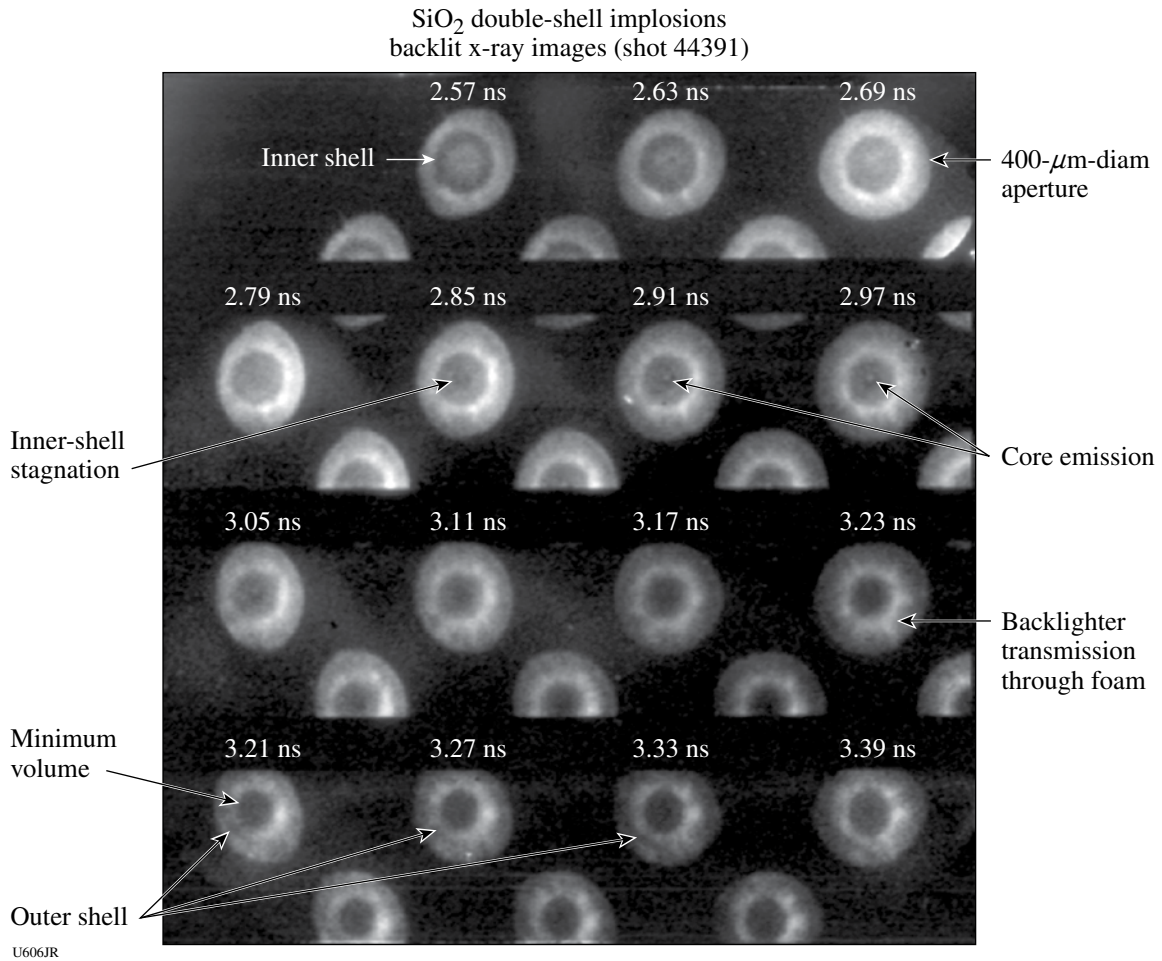


Figure 108.89  
Example of backlit x-ray images obtained from double-shell experiments.

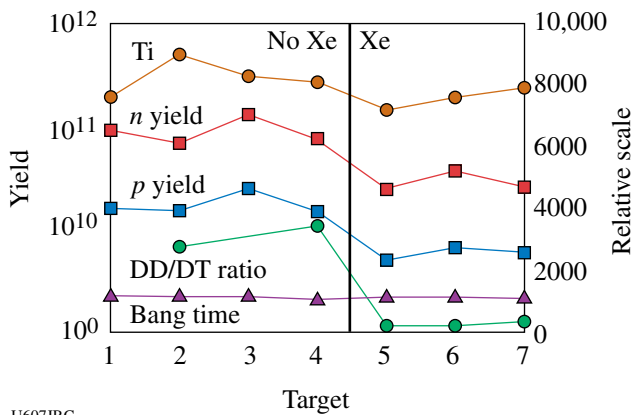


Figure 108.90  
Addition of Xe has a significant impact on implosion parameters in NLTE experiments, as shown by neutron data. Note the order-of-magnitude change in DT (secondary) neutrons, due to the radiative cooling by xenon atoms.

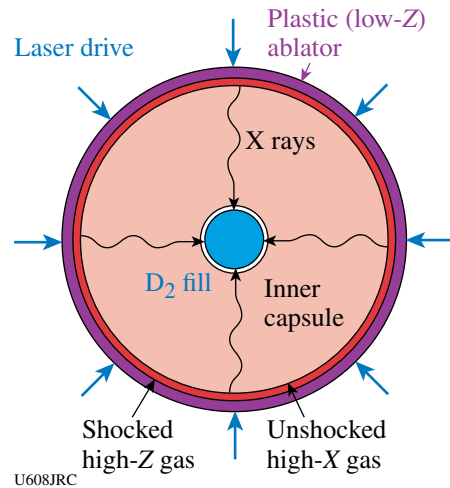


Figure 108.91  
Concept of “dynamic hohlraum;” Xe gas between shells produces x rays that ablatively implode inner shell.

ing the passage of a shock in low-density material past denser spherical objects and examining how the shock passage induces mixing of material into the interstellar medium. Figure 108.92 shows an example of the data. The laser-generated shock is moving toward the lower left, past the two spherical objects. (The grid is for diagnostic reference.) X-ray backlighting provides images at various times. On the right (at 12 ns) the shock is still visible, just to the right of the spheres. These data are being used to benchmark model calculations, which will then be applied to astronomical observations for comparison.

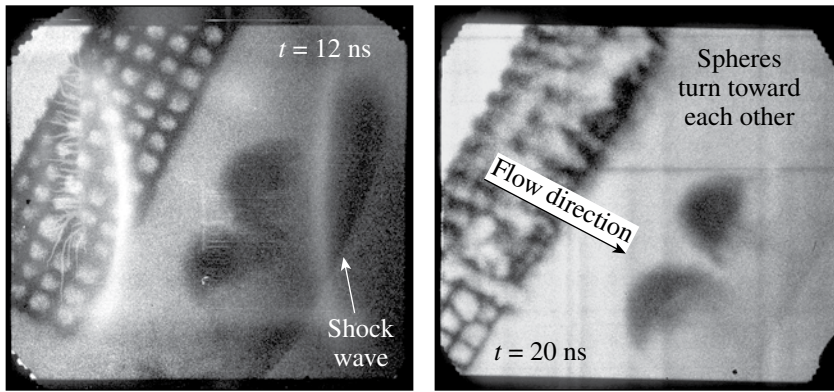
Another experiment looked at the propagation of “jets” into a low-density background material (“DDP experiment”), again using x-ray backlighting after lengthy (15- to 35-ns) time delays. The cell size of the low-density material (a copper foam) was

varied, and the results compared to simulations. Figure 108.93 shows a schematic of the experiment and an example of the data. As the jet of material moves upward, vortices form to the left and right (“roll up”), in agreement with hydrodynamic simulations.

Finally, another collaboration (CEA, NRL, and LLNL) used OMEGA shots for x-ray source and effects experiments. Various targets were investigated for their ability to produce copious x rays in the region around 10 keV, as shown in Fig. 108.94.

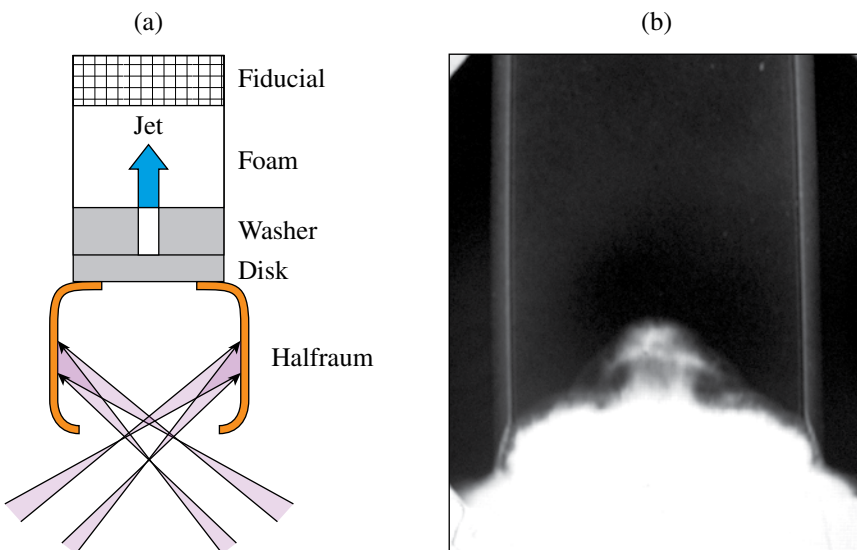
**FY06 LANL OMEGA Experimental Programs**

Los Alamos National Laboratory (LANL) successfully fielded a range of experiments on OMEGA during FY06 studying the physics relevant to inertial confinement fusion (ICF) and high-energy-density (HED) science in support of the national



U609JR

Figure 108.92  
X-ray-backlit images of shock (visible on right of the right-hand image, moving away from reference grid) and spheres imbedded in the low-density medium. Interacting clouds turn toward each other and eject material downstream after shock passage.



U610JRC

Figure 108.93  
(a) Layout of DPP experiment (x-ray backlighting not shown, perpendicular to page through the foam). (b) Data at 15 ns. Note the classic “roll up” of the upward-moving jet.

DMX spectra indicate 80 to 170 J/sphere at 10 keV and up to 6 kJ/sphere in the 1- to 3-keV band.

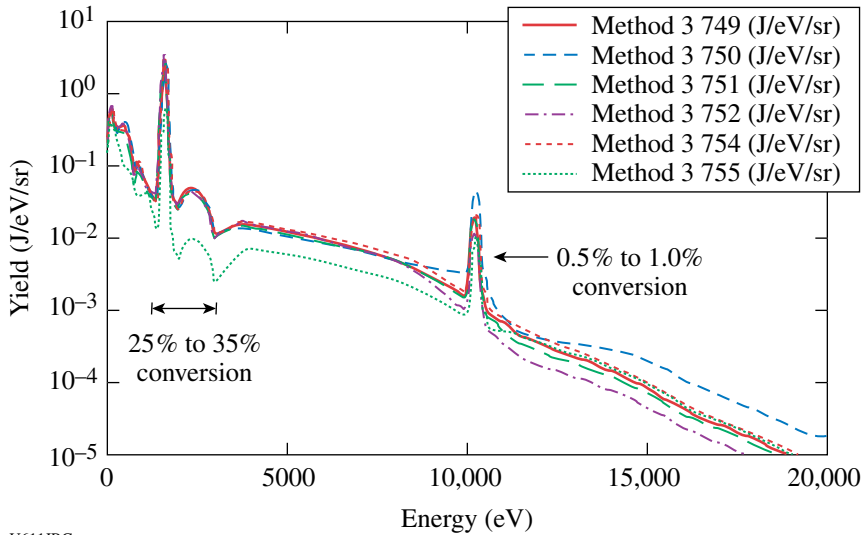


Figure 108.94  
Laser and target conditions that optimize the 10-keV x-ray output have been identified.

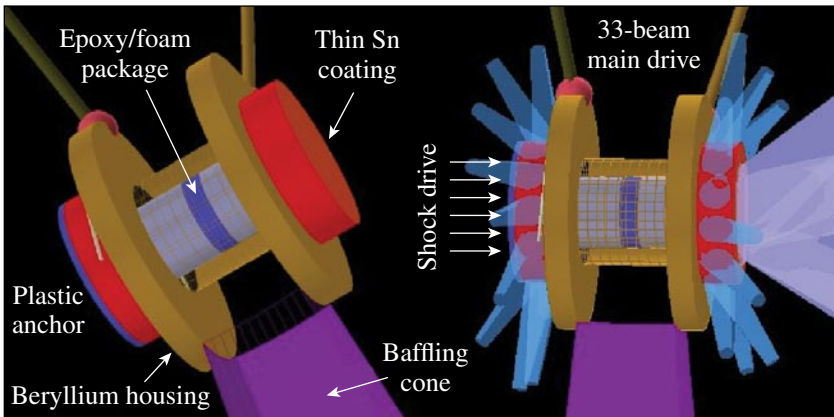
U611JRC

ignition effort. Many of these experiments were focused on developing underlying physics, diagnostics, and platforms for future experiments on the National Ignition Facility (NIF). LANL conducted a total of 125 target shots on OMEGA. Collaborations with LLNL, LLE, MIT, and AWE remain an important component of LANL's program on OMEGA. With the consolidation of ignition research in the United States into the National Ignition Campaign (NIC), healthy partnerships are required to achieve success in the national scientific objectives.

*Off-Hugoniot Heated Hydrodynamics:* The off-Hugoniot (OH) campaign continued in FY06 with three days of experiments. High-quality data were obtained on 37 of 39 system shots. These experiments studied material dynamics under heated and shocked conditions. In ignition capsules, defects,

arising from the manufacturing process, undergo significant evolution due to heating from Au M-band radiation prior to passage of the main shock. It has not been demonstrated that our hydrocodes accurately capture the physics of this interaction. The OH platform provides the means to study the complex interaction between shocks and heated material.

The OH platform utilizes a beryllium (Be) housing that is coated with a thin layer of tin (Sn). Inside the housing are layers of foam and epoxy. Thirty-three beams strike the tin and produce L-shell radiation that permeates throughout the package, heating the epoxy and foam (Fig. 108.95). A short time later, seven beams launch a strong shock into the foam. As the heated epoxy expands in the foam, the shock interaction with this system is radiographed onto Agfa-D7 film.



U612JRC

Figure 108.95  
The target configuration for the off-Hugoniot experiment. A beryllium housing filled with layers of epoxy and foam is heated by exciting Sn L-shell radiation. The evolution of the epoxy expanding into the foam is imaged via radiography.

An example of the improved data quality is shown in Fig. 108.95. Data from heat-only experiments [Fig. 108.96(a)] clearly show the epoxy expansion and shock in the foam. Moreover, the use of the calibrated D7 film allows complete resolution of the evolving density profiles. When a defect is heated and a strong shock is introduced [Fig. 108.96(b)], the residual density perturbations from the healing defect distort the shock front as it propagates through the epoxy. The resulting density profiles and spatial deformation of the shock front provide tight constraints for our ignition design hydrocodes like *RAGE* and *PETRA*.

*Inhomogeneous Radiation Flow:* Inhomogeneously mixed materials can occur in a variety of environments. Two examples are ICF capsules, where shell material mixes with the fuel and turbulent flows, and astrophysical systems, such as molecular clouds and star-forming regions, where density clumps can form. Models for the transport of radiation in inhomogeneously mixed

materials exist, each differing in the statistical treatment of the material mixtures. However, there is little experimental data to test these models. The inhomogeneous radiation flow experiment aims to provide data that can be used to test different models.

Figure 108.97 shows an overview of the experiment. A laser-driven hohlraum is heated to roughly 205 eV, which generates a temperature front. The temperature front propagates through gold-loaded foam, heating it. The soft-emission (~300 eV) of the heated foam is measured to determine the position of the radiation front. Two different gold-doped foams were examined: one loading with gold particles of diameters between 0.3 and 1.0 μm and another with very fine gold particles, diameters less than 0.1 μm.

Figure 108.98 displays preliminary measurements of the temperature-front position (circles) and the simulated trajectory

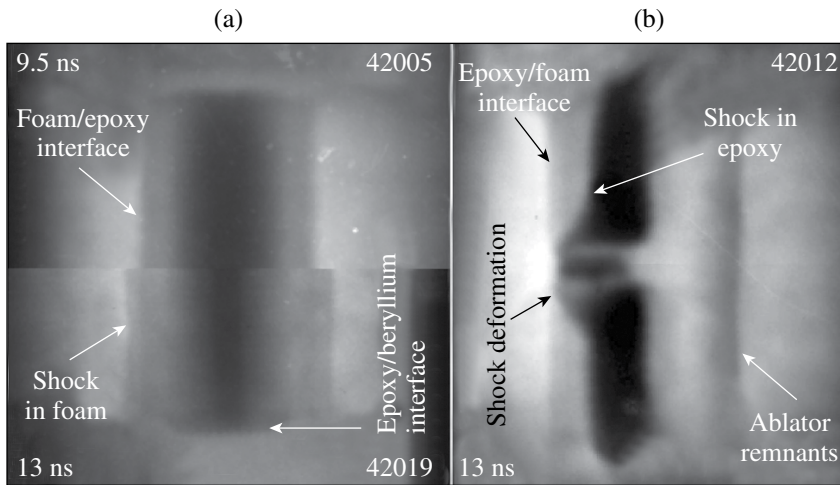


Figure 108.96  
 (a) Radiographs of a heated-only, epoxy disk at 9.5 and 13.0 ns after the onset of heating. The deformation in the beryllium/epoxy interface and the shock formed by the epoxy expansion are both clearly visible. (b) Data from a heated and shocked 37.5-μm rectangular gap.

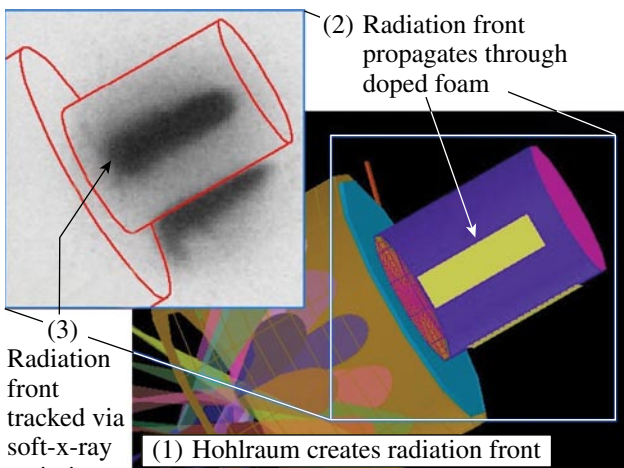


Figure 108.97  
 Sixteen beams heat a gold hohlraum that produces a radiation front that propagates through the foam. Diagnostic slits allow measurement of the front's progression.

U613JR

U614JRC

of the temperature front (solid line). The simulation appears to be in good agreement with the data.

**Beryllium Fill-Tube Defect Studies:** Be shells are impermeable to gaseous and liquid DT. To fill an ICF capsule with a Be shell, a fill tube is used. The fill tube is attached to the shell through a counter-bored fill hole. Fill tubes and fill-tube holes for Be ICF capsules inject shell material into the fuel perturbing the implosion. Mixing between the shell material and the fuel cools the fuel and degrades the efficiency of the ICF capsule.

As part of the LANL/LLNL NIC effort, experiments designed to quantify the amount of Be mass ejected by the jet formed by the fill-tube hole were conducted. These experiments were performed in planar geometry due to complications of fabricating and diagnosing in spherical geometry. This experiment focused on large-aspect-ratio (depth/diameter), from 2 to 20,

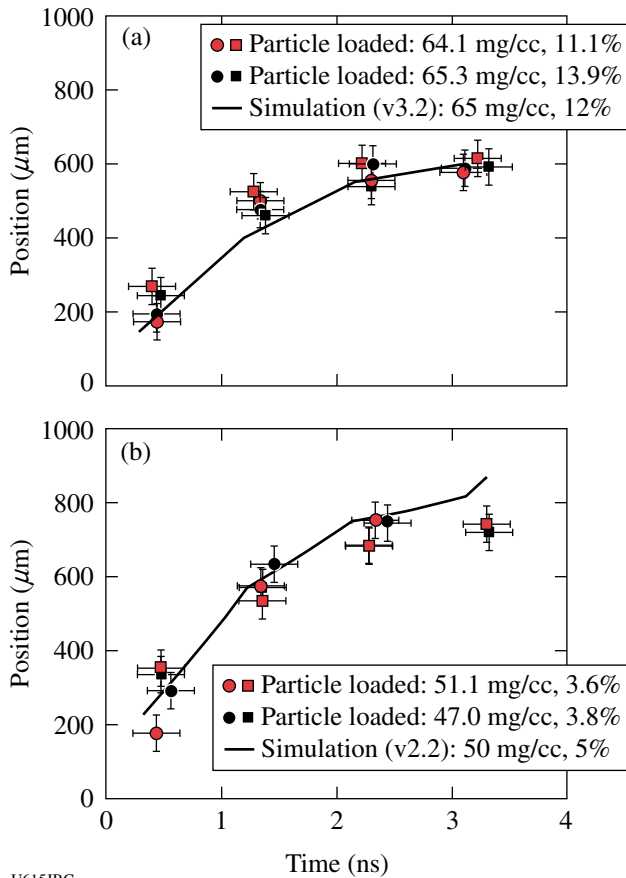


Figure 108.98 Simulations using NYM are in excellent agreement with the two cases examined: (top) 65-mg/cc foam with approximately 12% gold by weight and (bottom) 50-mg/cc foam with 5% gold by weight. [NYM simulations courtesy of M. Taylor (AWE).]

holes. The experimental configuration is shown in Fig. 108.99. A hohlraum is heated to 170- to 180-eV temperature. The temperature drive ablates and shocks the 100-μm-thick Be (3% Cu-doped) ablator. The shock ejects some material down the fill-tube hole and also propagates into the Be (3% Cu-doped) washer. The shock in the washer pushes material into the hole that jets into the foam.

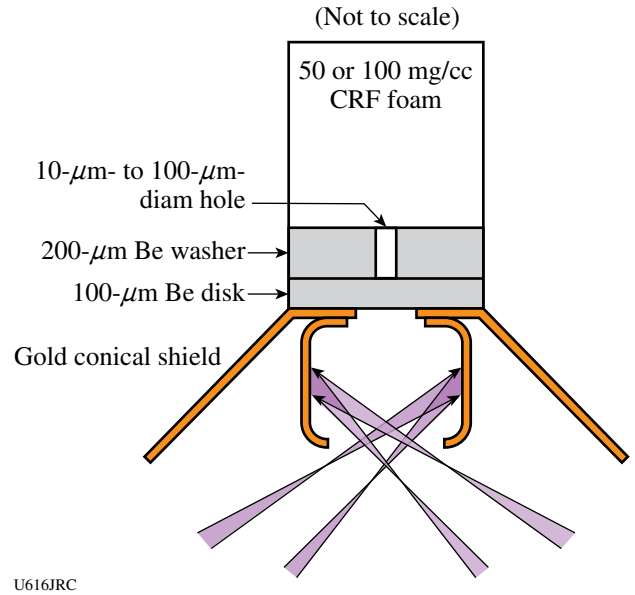


Figure 108.99 A heated gold hohlraum drives a shock into the beryllium disk, creating a jet as the Be is forced out the small hole at the bottom. The Be jet and disk are imaged from two orthogonal directions.

The mass of material jetted into the foam is measured with point-projection radiography at either 4.3 keV or 2.8 keV. Data have been obtained for jets formed by 100-, 50-, 40-, and 30-μm-diam holes. Figure 108.100 shows preliminary data of the jet formed by a 50-μm-diam fill-tube hole. The data were recorded with 4.3-keV x rays, 15 ns after the laser drive. The jet is roughly 170 μm across at the head and approximately 170 μm in length.

**High-Z Shell Implosions:** Two days of experiments studied the progression from non-LTE to LTE as the dopant gas concentration in a deuterium-filled capsule is increased. The presence of the high-Z dopants increases the radiation losses from the plasma, allowing the plasma to compress to a smaller volume. The physics of ignition and burn in high-Z capsules—specifically the effect of high-Z dopants on energy balance, equilibration, yield, and transport in implosions—is examined with measurements of yield,  $\rho R$ ,  $T_e$ ,  $T_i$ ,  $T_r$ , and implosion size.

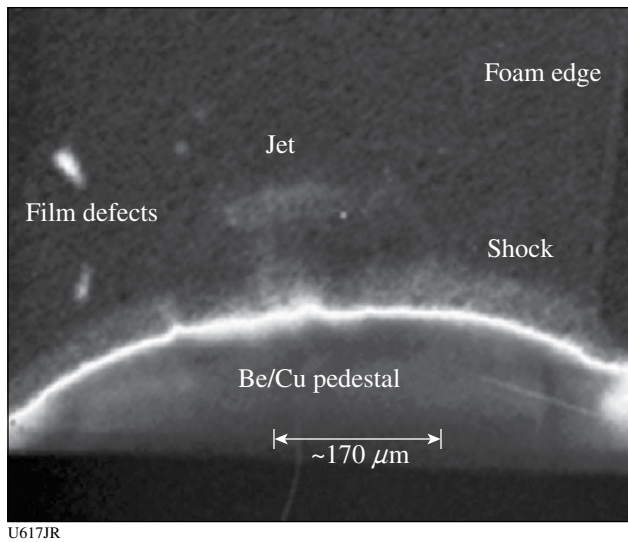


Figure 108.100

The jet caused by a 50- $\mu\text{m}$ -diam hole taken 15 ns after onset of the laser drive. Visible are the jet and the shock wave that has passed through the Be. The radiograph was obtained with 4.3-keV x rays.

These experiments used a 5- $\mu\text{m}$ -thick  $\text{SiO}_2$  spherical shell of 430- $\mu\text{m}$  radius, filled with 7 atm of deuterium and 3 atm of  $^3\text{He}$ . The  $^3\text{He}$  allows measurement of the proton spectrum from the  $\text{D}^3\text{He}$  reaction and thus determines the target's ion temperature and  $\rho R$ . Kr dopants were used as spectroscopic tracers to measure the electron temperature in the plasma from the helium lines. Variation of electron density is achieved by adjusting the Xe gas concentration. The experiments produced a wealth of data that is being used to determine how equilibrium is reached and to validate code calculations (Fig. 108.101).

*High-Z Dopant Impact in Stimulated Raman Scattering (SRS):* Experiments at the Helen laser observed a clear decrease in stimulated Raman backscattered (SRS) light when a small percentage,  $\sim 1\%$ – $2\%$ , of a high-Z dopant such as Ar or Xe was added to a CH-filled gas-bag target. This experimental observation prompted interest in the phenomenon, especially as a mitigation strategy for reducing SRS in NIF hohlraums. However, the exact physical mechanism of the high-Z dopant effects was unknown, especially the fact that only small amounts of high-Z dopant are required. Theoretical investigation of the effects of high-Z dopants on SRS at LANL found that the addition of high-Z dopants leads to beam spray of the laser via thermally enhanced forward stimulated Brillouin scattering (FSBS). This beam spray causes a reduction in SRS due to a reduction in the spatial coherence of the laser. Thermal effects due to inverse-Bremsstrahlung absorption of the laser have a  $Z^2$  dependence, meaning that a small amount of high-Z

material, compared to the background plasma Z, can have a large effect on the thermal response.

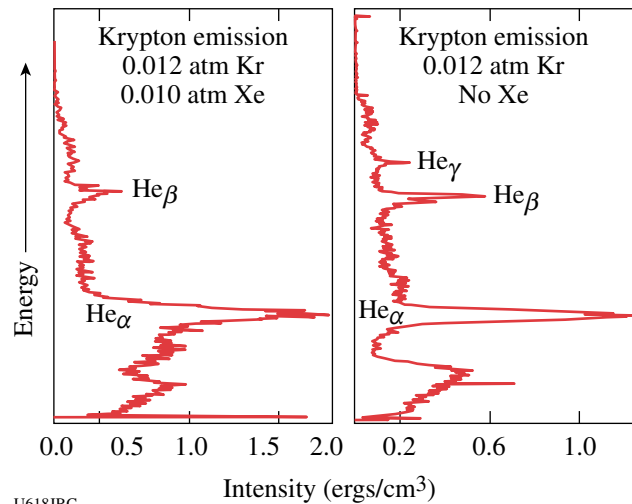
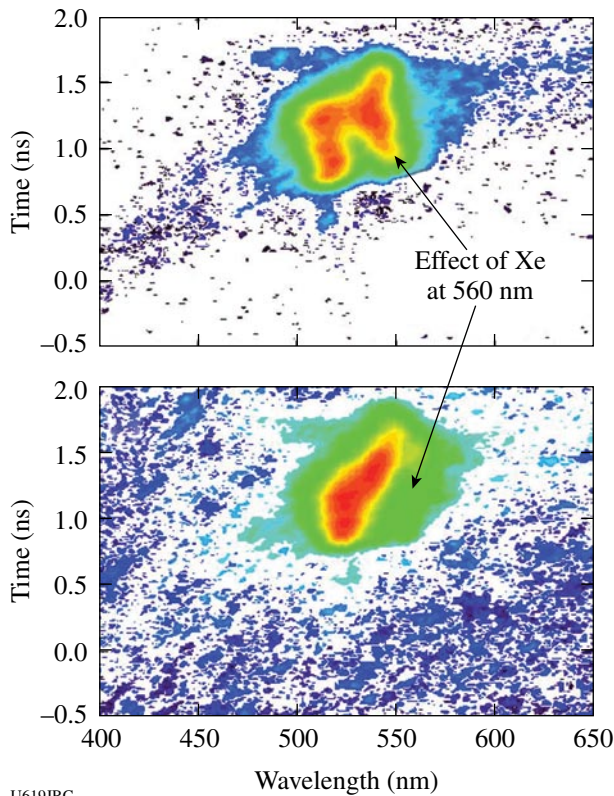


Figure 108.101

13- to 15-keV Krypton spectra of implosions doped (left) and undoped (right) with Xe. The enhanced cooling from Xe emission is observed by the reduction in  $\text{He}_\gamma$  and  $\text{He}_\beta$  emission of the Krypton spectra.

Through a strong collaboration by LANL, LLNL, and AWE, experiments were conducted at LLE using  $\text{C}_5\text{H}_{12}$  gas-filled hohlraum targets to validate theory. SRS was measured for various amounts of Xe dopant added to the hohlraum gas fill. As the percentage of Xe dopant exceeded  $\sim 5\%$ , SRS from the uniform interior hohlraum plasma region decreased. Figure 108.102 shows that the SRS reflectivity at wavelengths of  $\sim 550$  nm, corresponding to an electron density of  $n/n_c \sim 0.11$ , where  $n_c$  is the critical density for 351-nm light, is reduced with the addition of 8.7% Xe compared to that of 3.6% Xe early in the interaction-beam laser pulse. This is an indication that high-Z dopants may affect SRS. However, measurements of the beam spray for the transmitted beam did not change significantly between the two cases. Thus, it is inconclusive whether the effect is due to beam spray or another mechanism such as reabsorption of SRS light via inverse Bremsstrahlung. Interestingly, large amounts of SRS come from the plasma expanding from the hohlraum based on hydrodynamic simulations and the wavelength of SRS at  $\sim 520$  nm corresponding to an electron density  $n/n_c \sim 0.06$ .

In FY07 experiments, the laser intensity will be lowered to values closer to the critical onset intensity for SRS. The theory predicts a stronger effect of high-Z dopants at that intensity. In addition, the SRS reflectivity from the plasma expanding from the hohlraum should be decreased based on past experiments at the NOVA laser.

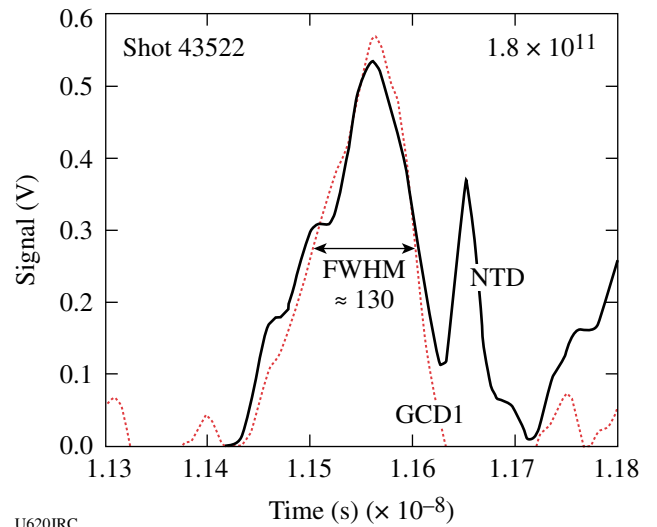


U619JRC

Figure 108.102

SRS spectra with (a) 3.6% and (b) 8.7% Xe dopant added to  $C_5H_{12}$  gas-filled hohlraums show a reduction in reflectivity at the interior electron density of  $n/n_c \sim 0.11$  ( $\sim 550$  nm). However, most of the SRS reflectivity comes from the plasma expanding from the hohlraum at a lower electron density,  $n/n_c \sim 0.06$  ( $\sim 520$  nm).

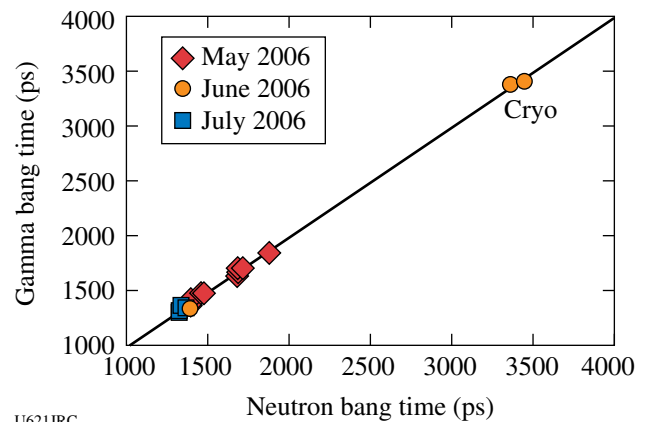
**Gas Cherenkov Detector Development:** The Gas Cherenkov Detector (GCD) is a collaborative effort between LANL, AWE, Photek, Inc., and NSTec to develop a fast “bang-time” diagnostic for NIF. The project benefited greatly from the multi-institutional diagnostic development efforts in FY06. Implementation of an ultrafast microchannel plate enhanced time response by a factor of 2.5 to better than 100 ps. This increased bandwidth enabled quality reaction histories of fusion burn using gammas (Fig. 108.103) to be obtained with speeds comparable to or exceeding that of the neutron temporal diagnostic (NTD). Moreover, bang-time measurements, i.e., the time of peak fusion reactivity, were achieved with a precision of 25 ps, when cross calibrated to NTD. This development should allow the gamma bang time/reaction history detector being planned for NIF to easily exceed the NIF system design requirement of 50 ps. The bang-time measurements, shown in Fig. 108.104, were obtained over a three-month period starting in May and ending with the 50/50 DT Cryo shots in July.



U620JRC

Figure 108.103

Gamma (GCD) and neutron reaction history (NTD) showing the consistency between burn history and peak neutron bang time.



U621JRC

Figure 108.104

Peak-neutron-bang-time measurements of GCD and NTD are consistent over a wide time window.

### FY06 Sandia National Laboratories OMEGA Experimental Programs

SNL carried out 30 shots on OMEGA in FY06 including the following experiments:

**Beryllium Ablation Rate Measurements in Planar Geometry:** For a successful NIF ignition experiment, the ablator mass remaining at the end of the capsule implosion must be in the range of 3%–5% of the original ablator mass. If too much of the ablator burns off, the DT fuel will be preheated and the required fuel  $\rho R$  cannot be achieved with the absorbed energy of the baseline ignition capsule. If too little of the ablator mass

burns off, the peak implosion velocity will be reduced and the hot-spot energy density will not be adequate for ignition. Thus, it is imperative that the mass ablation rate be known to high precision for the entire range of hohlraum temperatures encountered in the NIF ignition pulse shape. The experimental technique for ablation rate measurements in planar geometry is illustrated in Fig. 108.105 (details in Ref. 9). Basically, ablator samples are placed over an opening on the end of a halfraum. Laser beams enter through the LEH and provide the input power required to maintain the radiation field. The Dante array of K- and L-edge filtered photocathodes views the hohlraum wall through the LEH, and a time- and spectrally resolved measurement of the hohlraum radiation field is obtained from this data. An x-ray framing camera views the interior surface of the ablator sample, and the relative x-ray re-emission of the ablator versus the Au wall is determined. The streaked x-ray imager (SXI) diagnostic views the exterior surface of the ablator sample. The SXI employs an imaging slit, a transmission grating, an offset slit, and a streak camera to provide a highly time-resolved streaked image of the x-ray burnthrough flux on the exterior-facing side of the sample (as shown in Fig. 108.105). The combined information from these three measurements over a series of experiments is used to determine the mass ablation rate ( $\text{mg}/\text{cm}^2/\text{ns}$ ) as a function of hohlraum radiation temperature. In FY06, reduced-scale halfraums and increased SXI magnification were used to extend the ablation rate data for Be and Cu-doped Be into the 200- to 270-eV temperature range. As shown in Fig. 108.106, the measurements have been directly compared to the equivalent mass ablation rate in the baseline NIF ignition capsule calculations.<sup>10-12</sup>

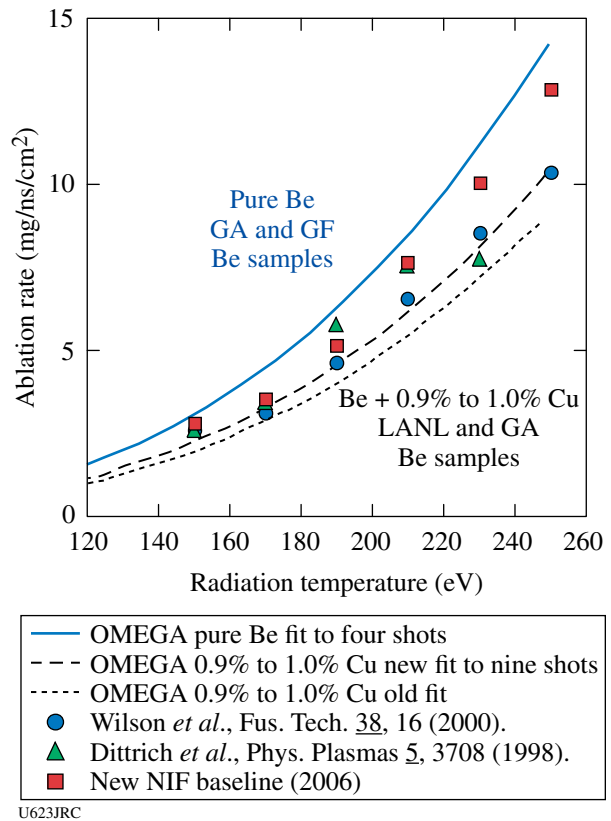


Figure 108.106 Ablation rate plotted as a function of radiation temperature from the OMEGA experiments (solid and dashed lines) and comparison to the baseline NIF capsule calculation. The range in the measured ablation rate seems to depend on view factor and spectrum as well as sample type and dopant concentration. Complete understanding of this data is work in progress.

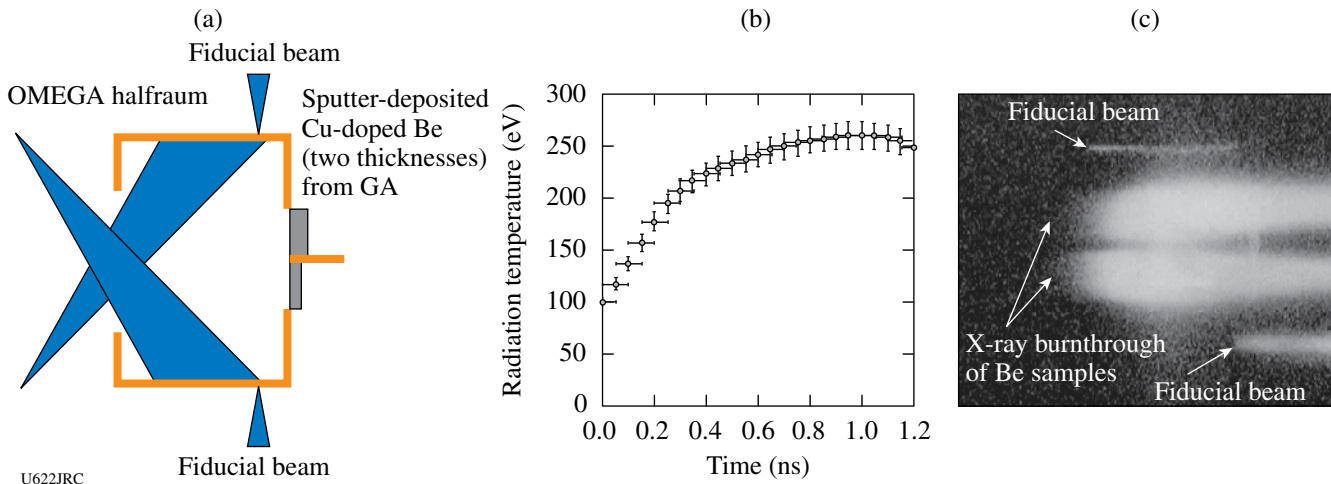


Figure 108.105 (a) Schematic of an ablation-rate measurement experiment. (b) DANTE-derived radiation temperature as a function of time. (c) Sample SXI streaked data showing burnthrough of Be samples.

*Beryllium X-Ray Burnthrough and Ablation-Rate Measurements in Convergent Geometry:* Since the ignition capsule's radius-time trajectory will vary with the shock-timing adjustments, it will be necessary to experimentally determine the burnthrough/no-burnthrough threshold of an imploding ablator shell and to iterate this burnthrough threshold measurement with the NIF shock-timing experiments. In FY06, SNL performed a series of experiments to develop a convergent ablation rate and burnthrough measurement technique. As illustrated in Fig. 108.107, the convergent burnthrough experiments are a logical extension of the planar ablation rate experiments. In the convergent experiments, a beryllium hemi-shell was mounted in a halfraum. The halfraum was larger than the sizes used in planar experiments, and specific beam-pointing adjustments were required to obtain acceptable capsule illumination symmetry ( $\pm 5\%$  in flux). An important diagnostic concern was that pinhole SXI imaging (rather than

slit imaging) was required for the convergent measurement, and a new technique was developed to verify the pointing and alignment accuracy to within  $\pm 50 \mu\text{m}$ . The SXI pinhole imaging setup is illustrated in Fig. 108.108, and the alignment verification technique is illustrated in Fig. 108.109. Key features of the burnthrough and no-burnthrough SXI streaks were verified in the FY06 experiments, and a preliminary unfold of convergent ablation rate was obtained from one of the experiments. Figure 108.110 shows an example x-ray streak image illustrating the spatial and time fiducials and an overlay of computationally simulated ablation-front and implosion features.

*VISAR Measurement of Hohlraum Radiation Temperature:* In FY05, a new technique for time-resolved measurement of hohlraum radiation temperature was successfully tested in a series of OMEGA experiments.<sup>13</sup> In FY05, we performed a series of experiments to extend the measurement techniques of Ref. 13 to situations in which shaped laser pulses have been used to produce sudden increases in the hohlraum radiation field, resulting in multiple shock fronts that converge within the quartz sample. As can be seen in Fig. 108.111, the interferometer technique appears to work well for this situation. Based on FY06 results, it is conceivable that a new series of Dante-interferometer calibration shots can be used to produce empirical relationships for the situation of multiply shocked quartz.

*Development of a NIF Shock-Timing Diagnostic:* The x-ray flux absorbed by an indirect-drive ICF capsule consists of a combination of blackbody x rays emitted from the high-Z hohlraum walls and higher-energy ( $>1 \text{ keV}$ ) x rays that originate in and near the hot, low-density plasma in which the laser light is absorbed. The high-energy photons can penetrate beyond the capsule. In previous LLE/SNL/LLNL collaborative experiments,<sup>14</sup> we found that, as hohlraum temperatures were increased beyond 135 eV, the ASBO window was preheated and became opaque. In the first half of FY06, the approach was to position the window completely out of the

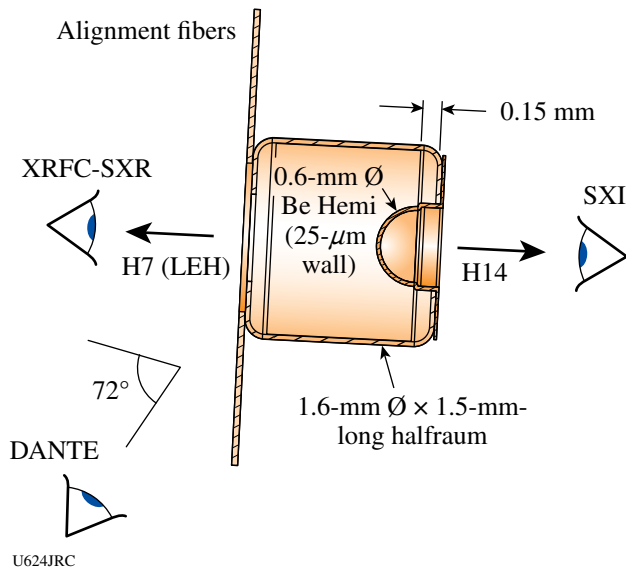


Figure 108.107  
Illustration of a convergent burnthrough experiment.

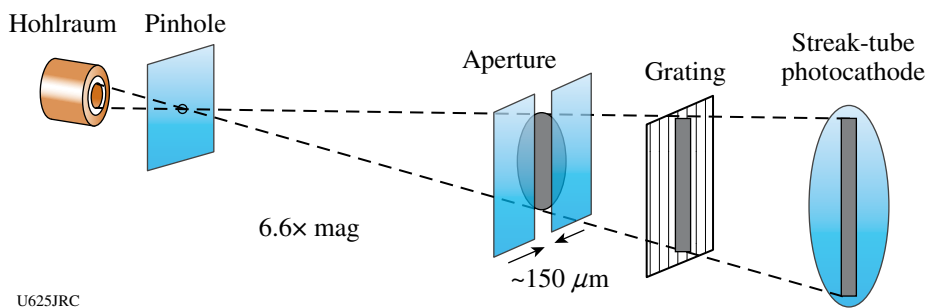


Figure 108.108  
Schematic showing SXI pinhole imaging setup.

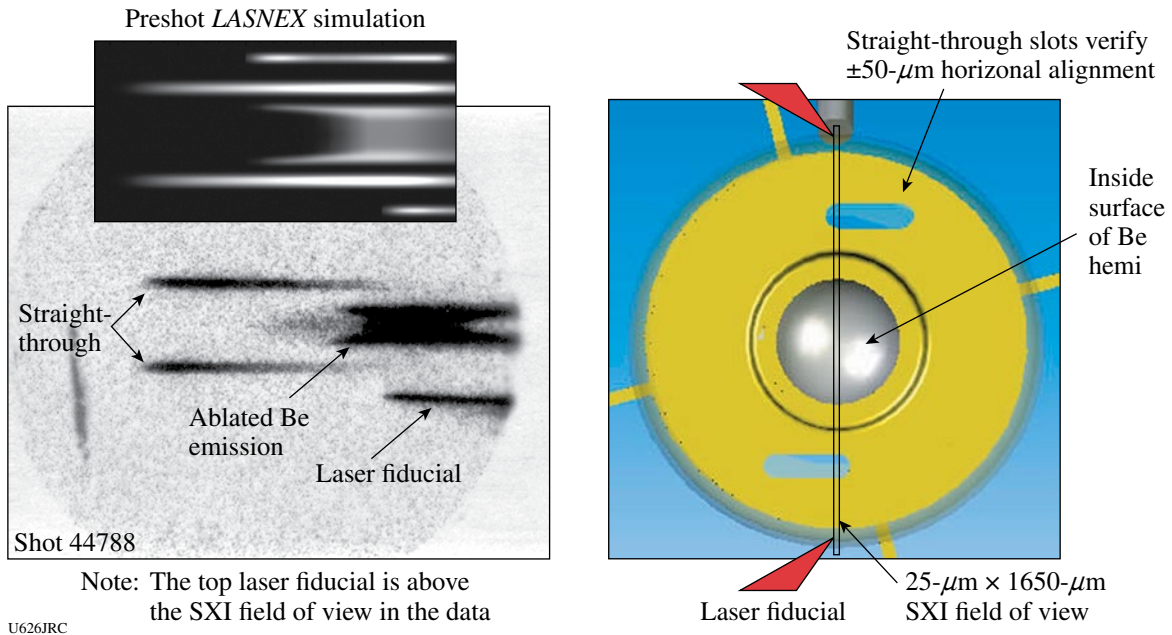


Figure 108.109  
Illustration of the alignment verification technique.

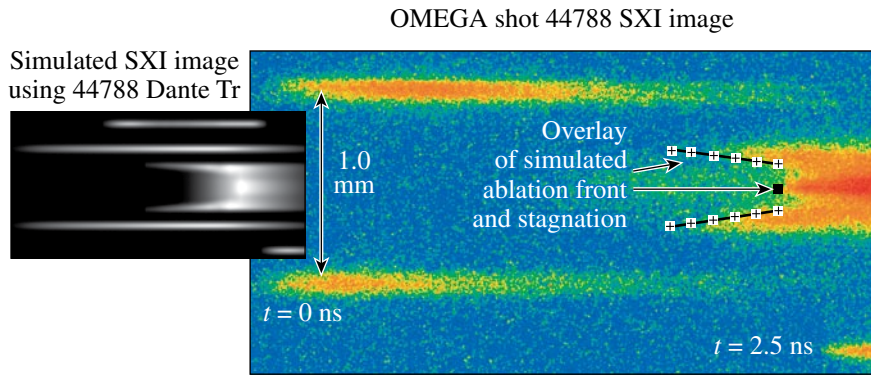


Figure 108.110  
Sample SCI data (right) and simulation from a convergent breakthrough experiment (left).

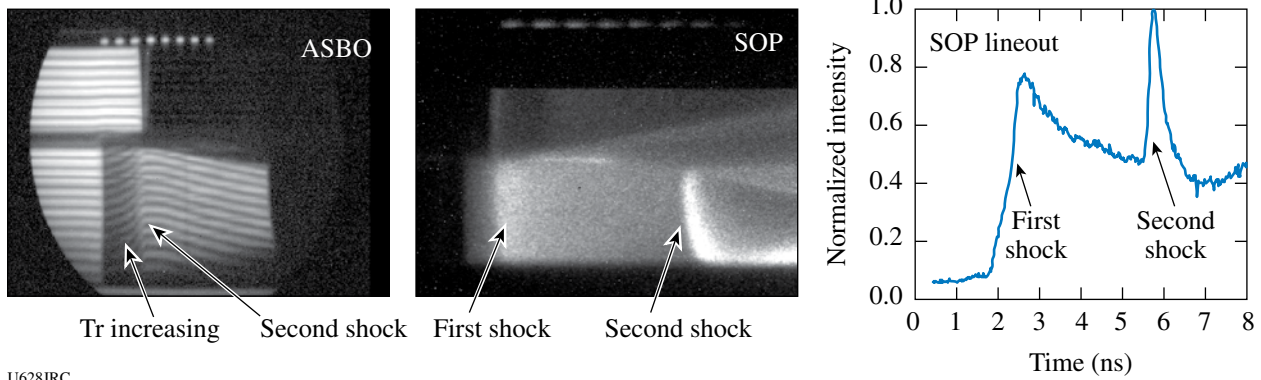


Figure 108.111  
Illustration of the VISAR technique to measure hohlraum radiation temperature.

line of sight of the laser spots in a halfraum geometry. This approach improved the situation and resulted in successful ASBO measurements for halfraum temperatures exceeding 140 eV (see Fig. 108.112). In late FY06, a series of experiments was started in which a NIF-like shock-timing geometry was tested. The first so-called "line-of-sight" hohlraum targets (Fig. 108.113) were designed and assembled at SNL. The targets worked well, but the experimental results indicated that further refinements in the design will be required for a successful shock-timing technique.

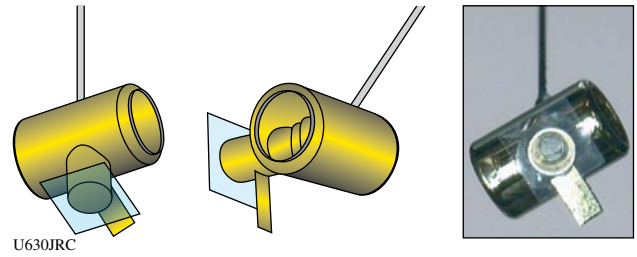
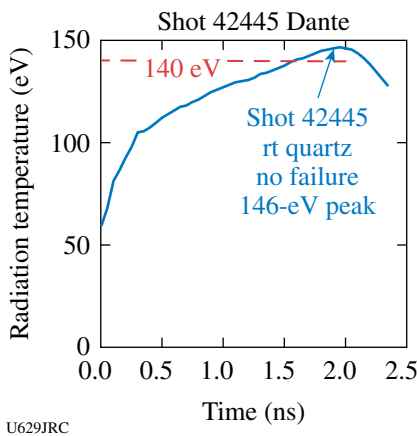
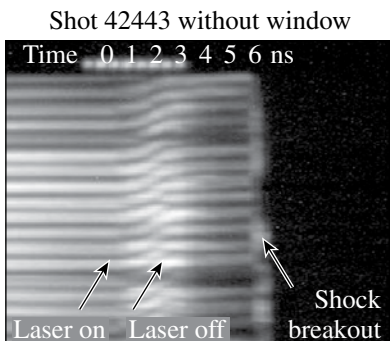
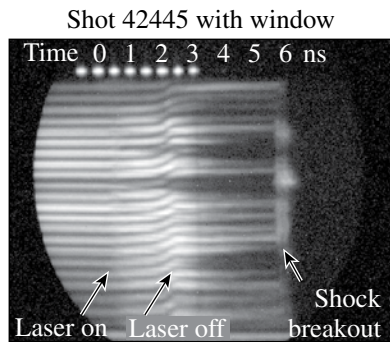


Figure 108.113  
Schematic of hohlraum used to test a NIF-like shock-timing geometry.



U629JRC

Figure 108.112  
Illustration of successful ASBO measurement in radiation fills exceeding 140 eV.

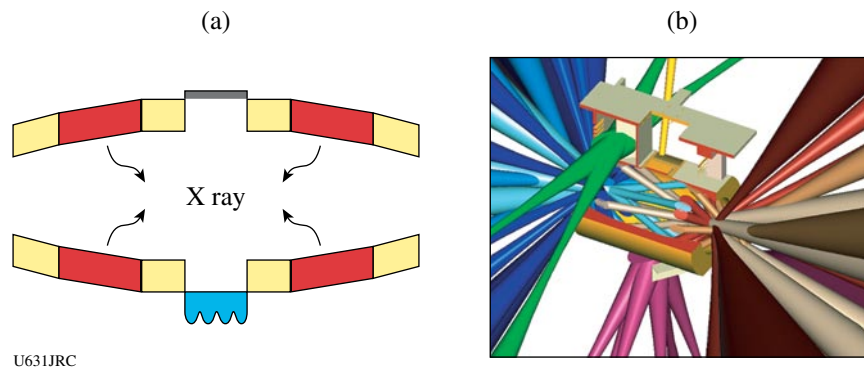
### FY06 CEA OMEGA Experimental Programs

In FY06, CEA carried out 49 target shots on OMEGA on several campaigns including studies of Rayleigh–Taylor instabilities in indirect-drive targets and the implementation of high-resolution x-ray imaging. Some of this work is outlined in this section.

*Rayleigh–Taylor Instabilities in Indirect Drive: Mode-Coupling Experiments:* Rayleigh–Taylor instabilities in indirect drive have been investigated by CEA on OMEGA since 2002 by using a rugby wall-shaped hohlraum.<sup>15</sup> Rugby hohlraums are, in fact, alternative designs for pre-ignition experiments with reduced energy on LMJ,<sup>16</sup> and the control of symmetry in a rugby hohlraum was also one of the goals of CEA FY06 symmetry experiments. A sketch of a rugby hohlraum is shown in Fig. 108.114 together with a diagram of the experimental configuration used for the RTI experiments. The cavity is heated with 40 beams (pulse shape PS26) in a three-cone (21°, 42°, and 59°) irradiation scheme. The 21° beams propagate across the hohlraum and are absorbed in the slanted part of the wall on the opposite side of the laser entrance hole. Dual-axis radiographies (side-on and face-on) are performed on each shot to measure the foil acceleration and the perturbation growth.

Previous experimental campaigns were devoted to the measurement of single-mode RT growth rate (wavelengths  $\lambda = 50$  and  $70 \mu\text{m}$ ) and the study of the feedout mechanism<sup>17</sup> in the case where the modulations were placed on the cold face [rear side, Fig. 108.114(a)] of the radiatively driven plastic foils.

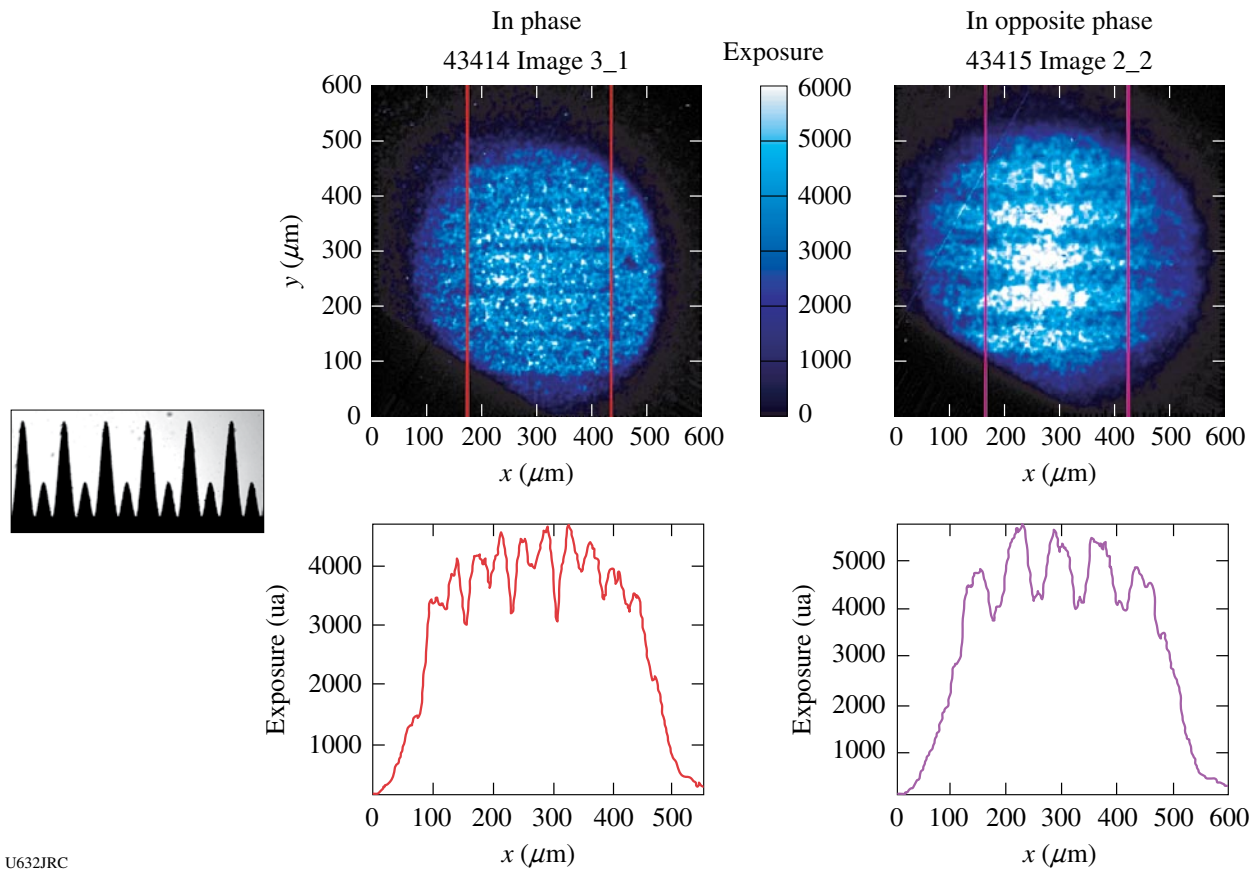
The FY06 campaign focused on mode coupling with germanium-doped foils (CHGe, 2.8% in atomic weight) modulated front side with a two-mode pattern ( $\lambda = 35$  and  $70 \mu\text{m}$ ). Depending on the relative phase between the two modes (in phase or in opposite phase), one or the other wavelength is predicted to become predominant during the growth. As illustrated in Fig. 108.115, if we compare two face-on pictures taken at the same time after  $t_0$  ( $t = 2.7$  ns), one sees clearly on the lineouts that



U631JRC

Figure 108.114

(a) Sketch of a rugby hohlraum. (b) Diagram of the configuration for RTI experiments. The  $21^\circ$  beams propagate across the cavity and are absorbed in the slanted part of the wall on the opposite side of the laser entrance hole.



U632JRC

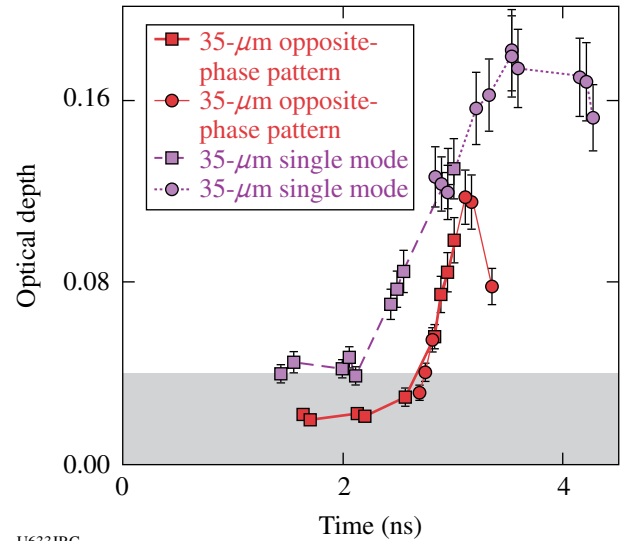
Figure 108.115

Lineouts across two face-on pictures taken at the same time ( $t = 2.7$  ns) for the two-mode patterns ( $\lambda = 35$  and  $70 \mu\text{m}$ ) under study. On the left, in phase pattern with the preponderant  $\lambda = 35\text{-}\mu\text{m}$  mode. On the right, the opposite phase pattern where  $\lambda = 70 \mu\text{m}$  predominates.

the  $\lambda = 35\text{-}\mu\text{m}$  mode overwhelms the  $\lambda = 70\text{-}\mu\text{m}$  mode for the in-phase case, and inversely for the opposite-phase pattern. As a consequence, the growth of the  $\lambda = 35\text{-}\mu\text{m}$  mode in the opposite-phase pattern is predicted to be delayed in time (due to a phase inversion) in comparison with a pure  $\lambda = 35\text{-}\mu\text{m}$  monomode. This trend is recovered in Fig. 108.116 on the plot showing the evolution of the optical depth versus time for both cases.

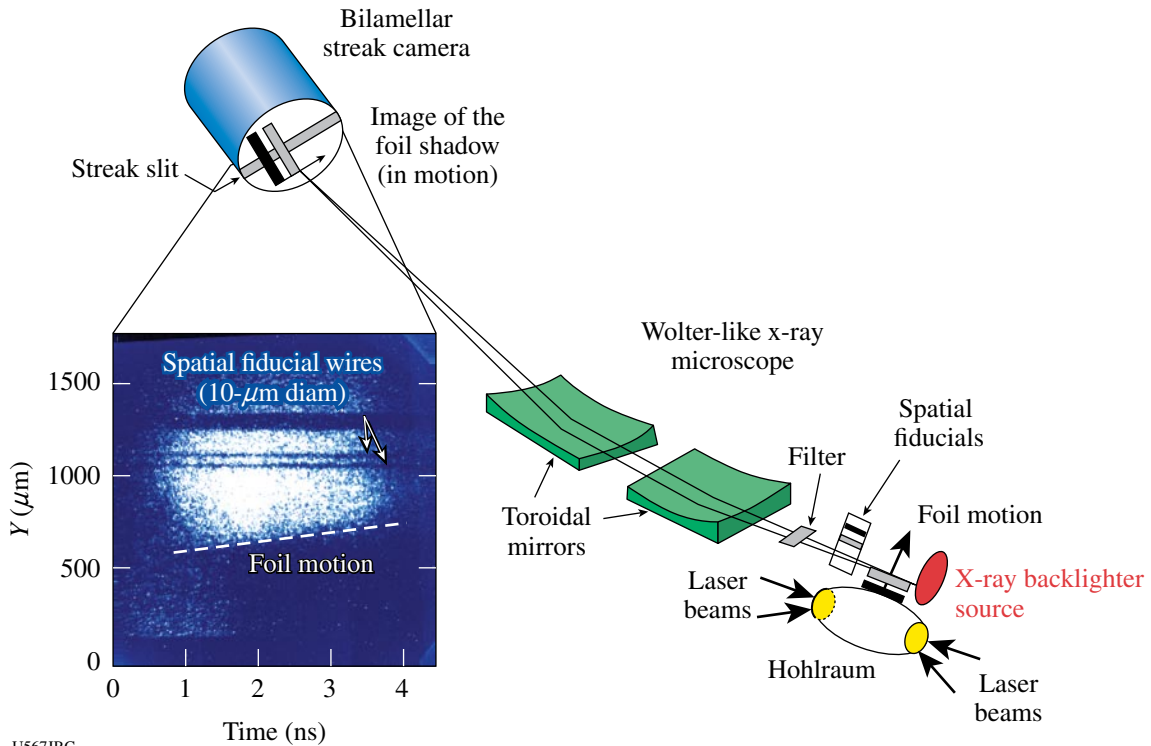
*High-Resolution X-Ray Imaging (HRXI):* For several years, Commissariat à l'Énergie Atomique in France (CEA/DIF Center<sup>18</sup>) has been developing HRXI, a high-resolution, time-resolved, x-ray imaging diagnostic. In FY06, HRXI was implemented and tested for the first time on OMEGA. HRXI combines two state-of-the-art technologies: a high-resolution x-ray microscope and a high-speed x-ray streak camera. The resulting instrument achieves a spatial and temporal resolution of  $\sim 5\ \mu\text{m}$  and  $\sim 30\ \text{ps}$ , respectively. The experimental configuration is shown in Fig. 108.117. The Wolter x-ray microscope for HRXI, used previously on Phebus experiments,<sup>19</sup> consists of two similar off-axis toroidal mirrors. The microscope had a focal length of 218 mm and a magnification ratio of 16. The mirrors were coated with a 30-nm Ni coating (energy cutoff  $\sim 6\ \text{keV}$ ). The microscope features an integrated visible-light

alignment system enabling the simultaneous projection of two crosses in the object plane and the image plane.



U633JRC

Figure 108.116 Growth (in optical depth) of the  $\lambda = 35\text{-}\mu\text{m}$  mode for the opposite phase pattern (solid symbols) and for a pure monomode perturbation (open symbols).



U567JRC

Figure 108.117 HRXI setup with a streaked image recorded during OMEGA shot 43418.

The streak camera includes a bilamellar-type streak tube,<sup>20</sup> which achieves both high temporal (30 ps) and spatial resolution (15 lp/mm). To match to the emitted x-ray backlighter spectrum used for these experiments (Ti foil emission near 4.8 keV), a transmission-mode photocathode was used with a thin CsI coating (10 nm) that was deposited on a self-sustaining CH foil of 800-nm thickness. The streak tube's P20 phosphor screen was read out with a cooled 1340 × 1300-pixel CCD with a 20- $\mu$ m pixel size.

HRXI was successfully tested for the first time on OMEGA during a joint CEA/DOE-LLE campaign on 27 April 2006. For these tests, HRXI recorded the acceleration of a thin, Ge-doped CH (45- $\mu$ m) foil driven by radiation from a rugby-wall-shaped hohlraum heated by 40 OMEGA beams with a 2-ns-time-duration, PS26 pulse shape. The foil was accelerated to a velocity of 60  $\mu$ m/ns. The inset in Fig. 108.117 shows a streak record of the motion of this thin foil in time using a 3-ns x-ray backlighter source. Three test objects were placed close to the foil to assess the spatial resolution of the diagnostic. Two 10- $\mu$ m-diam wires are clearly visible in the middle and along the streak image, leading to an actual estimated spatial resolution on the streaked image of less than 5  $\mu$ m.

## REFERENCES

1. R. F. Smith *et al.*, "Stiff Response in Aluminum Under Ultrafast Shockless Compression up to 110 Gpa," submitted to Physical Review Letters.
2. S. D. Rothman *et al.*, *J. Phys. D* **38**, 733 (2005).
3. R. F. Smith *et al.*, "Graded-Density Reservoirs for Accessing High Pressure Low Temperature Material States," to be published in *Astrophysics and Space Science*.
4. R. Jeanloz, *Geophys. Res. Lett.* **8**, 1219 (1981).
5. M. H. Rice, R. G. McQueen, and J. M. Walsh, *Solid State Phys.* **6**, 1 (1958).
6. C. K. Li, F. H. Séguin, J. A. Frenje, J. R. Rygg, R. D. Petrasso, R. P. J. Town, P. A. Amendt, S. P. Hatchett, O. L. Landen, A. J. Mackinnon, P. K. Patel, V. A. Smalyuk, T. C. Sangster, and J. P. Knauer, *Phys. Rev. Lett.* **97**, 135003 (2006).
7. C. K. Li, F. H. Séguin, J. A. Frenje, J. R. Rygg, R. D. Petrasso, R. P. J. Town, P. A. Amendt, S. P. Hatchett, O. L. Landen, A. J. Mackinnon, P. K. Patel, V. Smalyuk, J. P. Knauer, T. C. Sangster, and C. Stoeckl, *Rev. Sci. Instrum.* **77**, 10E725 (2006).
8. D. H. Froula *et al.*, *Phys. Plasmas* **13**, 052704 (2006).
9. R. E. Olson, R. J. Leeper, A. Nobile, J. A. Oertel, G. A. Chandler, K. Cochrane, S. C. Dropinski, S. Evans, S. W. Haan, J. L. Kaae, J. P. Knauer, K. Lash, L. P. Mix, A. Nikroo, G. A. Rochau, G. Rivera, C. Russell, D. Schroen, R. J. Sebring, D. L. Tanner, R. E. Turner, and R. J. Wallace, *Phys. Plasmas* **11**, 2778 (2003).
10. D. C. Wilson *et al.*, *Fusion Technol.* **38**, 16 (2000).
11. T. R. Dittrich *et al.*, *Phys. Plasmas* **5**, 3708 (1998).
12. S. W. Haan *et al.*, *Fusion Sci. Technol.* **49**, 553 (2006).
13. R. E. Olson *et al.*, *Rev. Sci. Instrum.* **77**, 10E523 (2006).
14. R. E. Olson, R. J. Leeper, G. A. Rochau, D. K. Bradley, P. M. Celliers, and T. R. Boehly, *J. Phys. IV France* **133**, 179 (2006).
15. A. Casner *et al.*, *J. Phys. IV France* **133**, 163 (2006).
16. J. Giorla *et al.*, *Plasma Phys. Control. Fusion* **48**, B75 (2006).
17. D. P. Smitherman *et al.*, *Phys. Plasmas* **6**, 932 (1999).
18. J. L. Bourgade *et al.*, CEA/DIF Center, Service SCEP, BP 12, Bruyères le Châtel, 91680, France.
19. Ph. Troussel *et al.*, *Rev. Sci. Instrum.* **76**, 063707 (2005).
20. A. Mens *et al.*, in *19th International Congress on High-Speed Photography and Photonics*, edited by B. Garfield and J. Rendell (SPIE, Bellingham, WA, 1990), Vol. 1358, pp. 315–328.